Experimental Studies on Mechanical, Thermal and Erosive Wear Characteristics of Granite Powder Filled Fiber Reinforced Polymer Composites for Wind Turbine Blade

PhD Thesis

MANOJ JANARDAN PAWAR
(Student ID: 2013RME9046)

DEPARTMENT OF MECHANICAL ENGINEERING
MALAVIYA NATIONAL INSTITUTE OF TECHNOLOGY, JLN MARG, JAIPUR-302017, India

2016

Experimental Studies on Mechanical, Thermal and Erosive Wear Characteristics of Granite Powder Filled Fiber Reinforced Polymer Composites for Wind Turbine Blade

A thesis submitted
in a partial fulfilment of the requirements for the award of the degree

DOCTOR OF PHILOSOPHY
in
ENGINEERING

by
MANOJ JANARDAN PAWAR
(Student ID: 2013RME9046)

Under the guidance of

Dr. AMAR PATNAIK
and
Prof. RAVINDRA NAGAR

DEPARTMENT OF MECHANICAL ENGINEERING
MALAVIYA NATIONAL INSTITUTE OF TECHNOLOGY,
JLN MARG, JAIPUR 302017, INDIA
2016

I dedicate this work to

My beloved younger brother

Late. Jayaram

(1986-2010)

Malaviya National Institute of Technology, Jaipur

Institute of National Importance, Established by the act of parliament

(Ministry of Human Resource Development)

CERTIFICATE

This is to certify that the thesis entitled "**Experimental Studies on Mechanical, Thermal and Erosive Wear Characteristics of Granite Powder Filled Fiber Reinforced Polymer Composites for Wind Turbine Blade**" submitted by **Pawar Manoj Janardan (ID No: 2013RME9046**) in partial fulfillment of the requirements for the award of **Doctor of Philosophy** in **Mechanical Engineering** to the **Malaviya National Institute of Technology, Jaipur** is an authentic record of research work carried out by candidate. To the best of my knowledge, the work incorporated in this thesis has not been submitted elsewhere for the award of any degree.

Manoj Janardan Pawar

Date: 23rd Dec 2016   ID No: 2013RME9046

This is to certify that the above statement made by the candidate is correct to the best of my knowledge and belief.

Dr. Amar Patnaik   **Prof. Ravindra Nagar**
Supervisor   Supervisor
Assistant Professor,   Dean Academic Affairs and Professor
Mechanical Engineering Department   Civil Engineering Department
M.N.I.T. Jaipur   M.N.I.T. Jaipur

The PhD viva voce examination of Mr. Manoj Janardan Pawar (2013RME9046) has been conducted by Oral Defense Committee (ODC) constituted by Dean (Academic Affairs) vide letter No: F4(P)Ph.D./Acad./MNIT/2016/1358 dated 14 Dec 2016 on Friday, 23rd Dec 2016. The ODC declares that the student has successfully defended the thesis during viva-voce examination

Dr. Rahul S. Mulik,   **Dr. Amar Patnaik**   **Prof. Ravindra Nagar**
External Examiner   **Supervisor**   **Supervisor**
  IIT Roorkee

ACKNOWLEDGEMENT

Date:

MNIT Jaipur   *Manoj Janardan Pawar*

ABSTRACT

Power generation utilizing wind is an energy source with minimum impact on environment and is also a best option where traditional energy distribution network does not reach. The overall performance of wind turbine system is significantly affected by performance of wind turbine blade. It is fact that failure of blade ultimately leads to overall breakdown of the system. Being the load-carrying member, superior mechanical performance of blade material is required to bear the static and dynamic forces to which a blade subjected. In view of this requirement polymer composites reinforced with long fibers can be best option due to their high specific strength, high stiffness, corrosion resistance and low density. Though, the glass and carbon fiber are the main reinforcement material for wind turbine blade, use of natural fiber also promoted as blade material for micro wind turbines. It is not feasible and economically reasonable to do parametric study by physically wind turbine blade testing in full scale.

The work in this thesis investigated the comparative analysis of glass, jute and carbon fiber loading on mechanical and erosive wear performance of epoxy based composites. Also study included the effect of inclusion granite powder waste in all the three compositions of fiber reinforced epoxy composites. The theoretical density of composite was calculated by applying rule of mixture and experimental density was calculated by applying Archimedes principle. From the difference between theoretical and experimental densities, the void fraction is calculated. The mechanical properties like tensile strength, flexural strength, inter-laminar shear strength and impact strength are evaluated experimentally confirming to ASTM standards. Fracture toughness of composites in mode-I is determined experimentally and validated numerical results by using ANSYS R14.5. The geometrical model of wind turbine blade of capacity 5 kW is developed in ANSYS Design modeller and performance is predicted in terms of stresses developed and tip deflection during flap-wise bending. The thermal and thermo-mechanical performance of the composites is studied through dynamic mechanical analysis, thermo-gravimetric analysis and thermal conductivity measurement respectively. The erosion rate of unfilled and granite powder filled polymer composites is experimentally determined in the environments of impact of sand particles along with water jet confirming to ASTM G73. The slurry erosion performance is further validated with the

results predicted using computational fluid dynamics tool; ANSYS Fluent. Similarly, solid particle erosion wear performance is evaluated by conducting tests according to ASTM G76.

The void fraction of composites depicted decrease with reinforcement of fiber. However, void fraction for granite powder filled GFRP composites show reverse in trend. Results depicted that significant improvement in tensile and flexural properties for unfilled glass and carbon epoxy composites up to 40 wt.% of fiber reinforcement. However, it is observed that 30 wt.% jute fiber reinforcement in unfilled polymer composites resulted in highest increase in tensile and flexural properties. Granite powder addition in to fiber reinforced polymer composites has slight improvement in mechanical performance up to 8 wt.% filler content and further the properties showed decline. The mechanical performance of 16 wt.% granite powder filled fiber epoxy composites is identical with unfilled composites. The fracture toughness of all the composites showed improvement owing to extrinsic and intrinsic toughening mechanism due to reinforcement of fiber and particulate filler respectively. The numerically predicted values of stress intensity factor are under estimated compared to experimental value due to deficiency in modelling of extrinsic and intrinsic toughening mechanism. The unfilled fiber reinforced epoxy composites depicted linear improvement in fracture toughness with increase in fiber loading due to formation of fiber-bridge with the faces of propagated crack. Granite powder particles present on the path of crack propagation resulted in to bifurcation or deviation of crack which absorbed the energy. Improvement in fracture toughness is observed for 8 to 16 wt.% granite powder addition. Still the value of fracture toughness for 24 wt.% granite powder reinforced polymer composites showed better fracture toughness compared to unfilled polymer composites.

Thermo-mechanical analysis of composites shows three distinct phases viz; glass phase, glass transition phase and rubbery phase. The storage modulus is greatly affected with reinforcement of fiber and particulate filler in glassy phase. The composites showed higher elastic response and lower viscous response in this phase. In transition phase the mobility of polymeric chain resulted in to decrease in stiffness and increase in viscous behavior of composites. In rubbery region composites neither have elastic properties nor viscous properties. With incorporation of fiber and filler materials glass transition temperature is affected marginally. The imperfect semicircle in Cole-Cole plots for most of the composites under investigation indicated heterogeneity of system. Thermo-mechanical performance of is in descending order for carbon epoxy, glass epoxy and jute epoxy composites respectively. Significant thermal degradation of composites is observed 300 to 400ºC for most composites. The residual content of glass and carbon composites found higher compared to jute epoxy

composites. Thermal conductivity of composite system is dependent on the thermal conductivity of constituent material. With reinforcement of glass and carbon fiber thermal conductivity of epoxy composites increased, whereas jute-epoxy composites illustrated thermal insulating behavior.

Granite powder filled fiber reinforced epoxy composites possess comparatively good potential for application like engineering structures in dusty environment in deserts subjected to erosive environment. The content of granite powder is to be decided sensibly keeping the strength and wear attack in mind. These composites, in general may also be strongly recommended for applications like wind turbine blades, pipe lines carrying water, light weight vehicles structures, etc. The steady state slurry erosion results for jute epoxy composites show better wear resistant behavior for 40 wt.% jute fiber loading. The granite filler content in the jute epoxy composite is played a major contribution for slurry erosion resistance concerned. Similarly, for unfilled and filled fiber epoxy composite reinforced with glass and carbon fiber showed improvement in slurry erosion resistance. The peak erosion rate is corresponds to 60 to 75º impingement angle which shows semi-ductile behavior of composites. The experimental results for slurry erosion rate are validated using computational fluid dynamics code. Solid particle erosion analysis for unfiled and granite powder filled fiber reinforced epoxy composites illustrated higher erosion rate than slurry erosion rate for corresponding composite. Improvement in solid particle erosion rate is observed with reinforcement of fiber and/or filler particles. In addition to steady state erosion wear, experiments are conducted according to Taguchi L_{16} orthogonal array approach for design of experiments. The results indicated that impact velocity and fiber or/and filler content influence the erosion wear rate significantly.

Finally, the calculation of ranking order of composites by using TOPSIS method for analysis of mechanical, physical, fracture and erosion wear behavior of unfilled and granite powder filled polymer composite is done and the sequence of ranking is ECG24 (Rank 1) > ECG16 (Rank 2) > EGG24 (Rank 3) >>……>> EJG24 (Rank 8) >>…… >> EJ10 (Rank 24). ECG24 (24 wt.% granite powder filled carbon epoxy composite) show the optimal performance among all unfilled and granite powder filled polymer composites considered in this study.

****

*****

<div align="right">

Chapter 1
INTRODUCTION
</div>

1.1 Back ground and motivation

In past few decades, the demand for energy development in wind energy sector has exponentially increased in the global market. The turbine blade has been the major section that subjected to failure first which leads to breakdown the total wind system. The materials used for wind turbine blade has been able to sustain wind loads along with gravitational load with minimum deformation. In view of these requirements, material with high strength and stiffness (as hybrid polymer composites) can be the best option for manufacturing of turbine blades. Hence, special emphasis was placed on mechanical and thermal properties, which are important considerations when selecting suitable polymeric materials for wind blade manufacturing. Wind turbine that has been located in environment containing plenty of dust, bugs, rain, sleet, snow or any other erosive air particulate, was more prone to erosion than a turbine erected in an area where these factors are not present. As wind mills have normally built in rural areas where, farmers turn the soil many times every year and also weather pattern changes are a common occurrence. A major problem in dusty environments was erosion of the leading edges of blades by wind carrying sand, which increases roughness and decreases aerodynamic performance [1]. This issue was serious and addressing towards the development of new erosion resistant material for wind turbine blades [2].

The efforts were started for micro-wind turbines with installation for educational reasons (at institutes or environment centres) and very small numbers of setups were existed especially in urban areas. Initially, wind turbines in the 2.5–20 kW were installed for awareness for green energy extracted by small wind turbines but recent work has started to focus on developing the micro (<1.5 kW) building integrated wind turbine [3]. Hence, small wind turbines are specially designed for built environment and can be located on buildings or on the ground next to buildings [4]. Generally, E-glass and carbon fiber reinforced polymer composites are the prime materials used for manufacturing of wind turbine blades. It is also well known that polymer and polymer based composites exhibit poor wear resistance as compared to metal and ceramic materials [5-7] but inclusion of ceramic materials as particulate filler in the fiber reinforced polymer composites, the wear resistance drastically improved as compared to unfilled fiber resin composites [8-10]. Studies [9-13] are available on solid particle erosion behavior of fiber reinforced polymer composites but there is limited

literature on slurry erosion of fiber reinforced polymer composites in environment of jet containing sand particles along with water.

However, most of the researchers as well as manufactures before going for any blade manufacturing and/or for experimental testing, they were initially tried to simulate the blade properties on CAD model, which helps the researcher as well as manufacturers the material feasibilities. The CAD model of turbine blade was generated using specification laid by National Advisory Committee for Aeronautics (NACA), NH1500. Finite element analysis response of blade was examined under different loads because of wind and gravitational forces [14, 15]. It was a challenging task to simulate the slurry erosion process using finite element codes. Chen et al. [16] constituted computational fluid dynamics (CFD)-based erosion prediction model and applied to geometries of elbows and plugged tees carrying oil. Three major components of comprehensive procedure were simulation of flow, particle tracking, and calculation of erosion. Again, dry and slurry erosion by using computational fluid dynamics (CFD) model was studied by Nguyen et al. [17-19] and they found that CFD model strongly supported the experimental results. Reports [20, 21] were also available on implementation of FLUENT code for assessment of erosion wear in different applications. The motion of the continuum phase was captured based on solving the three-dimensional Reynolds-Averaged Navier-Stokes (RANS) equations, while the kinematics and trajectory of the sand particles were evaluated by the discrete phase model (DPM).

The work reported in this thesis includes fabrication of unfilled and granite powder filled fiber reinforced polymer composites and to study their physical, mechanical, thermo-mechanical, and thermal behavior of test coupons as per ASTM standards. Further, part of thesis discussed on development of CAD model for actual blade dimensions with capacity of 5 kW wind turbine and numerically analyzing flap-wise bending response for different composite materials. This thesis also investigate the erosion wear performance of fabricated unfilled and granite powder filled fiber reinforced polymer composite in environment of impingement of dry sand and jet of water containing sand particles separately. Finally, the optimized composition is determined based on different performance defining criteria using multi criteria decision making method i.e. technique for order of preference by similarity to ideal solution. The outcomes of this research work would comprehensively lead us to the understanding of practical optimization of performance.

1.2 Thesis outline

The remainder of the thesis is outlined as follows

Chapter 2: Literature Review

The purpose of this chapter is to provide background information through past literature on the issues to be considered in the thesis and to emphasize the relevance of the present study. This chapter includes the key challenges and issues reported by numerous researchers on material for wind turbine blade. This chapter also summaries various issues available over a decade on physical, mechanical, thermo-mechanical, and erosion wear behavior of particulate filled polymer composites.

Chapter 3: Materials and Methods

This chapter describes the materials and methods used for the processing of all the composites under this investigation. It presents the details of the physical, mechanical, thermal, thermo-mechanical characterization and erosion wear tests which are carried out for the all the composites. The methodology related to the design-of-experiment technique based on Taguchi method is also presented in this part of the thesis.

Chapter 4: Physical, Mechanical and Fracture Analysis of Composites

This chapter comprises of three parts viz; Part I, Part II and Part III. Each part is dedicated for physical, mechanical and fracture analysis of unfilled and granite powder filled fiber reinforced polymer composite for glass fiber, jute fiber and carbon fiber respectively. This chapter also included an attempt to validate the experimentally obtained fracture toughness of composites with numerically predicted value using simulation software. Further, the mechanical performance of geometrical model of actual wind turbine blade is analyzed numerically in terms of flap-wise bending under aerodynamic and gravitational loads.

Chapter 5: Thermal and Thermo-Mechanical Analysis of Composites

This chapter is dedicated for thermal and thermo-mechanical characterization of unfilled and granite powder filled polymer matrix composites. Part I, Part II and Part III contain thermal and thermo-mechanical properties of glass epoxy composites, jute epoxy composites and carbon epoxy composites respectively. This chapter described the dynamic mechanical analysis (DMA), thermo-gravimetric analysis (TGA) and thermal conductivity measurement of composites. Attempt is made to predict the thermal conductivity of unfilled and particulate filled fiber reinforced polymer composites. The performance of composite is also evaluated during DMA by Cole-Cole plot, coefficient (C) and adhesion efficiency factor (A).

Chapter 6: Erosion Wear Behavior and Optimization of Composites

This chapter is divided in three parts: Part A deal with erosive wear behavior of composites subjected to impact of water jet containing sand particles both experimentally and numerically, Part B deal with solid particle erosion wear behavior of composites and Part C deal with ranking of composites using TOPSIS method.

Chapter 7: Summary and Conclusions

This chapter provided a comprehensive summary of the entire research presented in the thesis and clearly outlines the specific conclusions drawn from the work.

*****

Chapter 2
LITERATURE REVIEW

The purpose of literature review is to provide background information on the issues to be considered in this thesis and to emphasize the relevance of the present study. This chapter summarized the materials used for wind turbine blade and key issues reported by various researchers. Further, this chapter discussed various issues available over a decade on physical, mechanical, thermo-mechanical, thermal and erosive wear behavior of particulate filled fiber reinforced polymer composites. The topic briefly reviewed all the relevant literatures and found that still needs further research in order to improve the above said properties for structural applications. The past studies relevant to below mentioned points are discussed keeping in view of our research works:

- ❖ Wind turbine blade material: Issues and challenges
- ❖ Physical and mechanical characterization of polymer composites
- ❖ Fracture toughness analysis of polymer composites
- ❖ Thermal and thermo-mechanical characterization of polymer composites
- ❖ Erosive wear behavior of polymer composites
- ❖ Utilization of stone dust in various applications
- ❖ Implementation of design of experiment (DOE) and optimization technique

2.1 Wind turbine blade material, fabrication and testing: Issues and challenges

The world's growing appetite for wind energy is transforming wind blades into one of the hottest composite applications around. The huge build-up of wind-power generating capacity has raised a bumper crop of new plants for manufacturing these composite parts [22]. The fabrication technique used for polymeric wind turbine blade evolved over span of few decades. Initially, the wet winding technique was utilized for fabrication of blade structures then it shifted to vacuum infusion method. Further, advancement led to use of hand lay-up and pre-peg technique. Recent advancement in the manufacturing of wind turbine blade is automation in the fabrication technique [23].

Steel, aluminum, wood and composites were the most commonly used materials from 1970 to the end of the eighties. Although steel or aluminum might sound today like a strange choice of material, they were quite often used at an early stage of large wind turbine development, mainly because they were better characterized than their more modern alternatives. [24]. Eker et al. [25] investigated the use of composite material for wind turbine

blades. This research was based on theories of material science and wind technology. Author suggested that studies must be concentrated on stronger and more rigid fibers and more heat resistance, crack free and tough polymer matrix composite. Debnath et al. [26] discussed the viability, issues and challenges of utilization of natural fiber polymer composites for wind turbine blades. The issues related to primary manufacturing along with adhesive joining and machining of natural fiber reinforced polymer composites. Corbyn et al. [27] guided the manufacturing of fibre glass wing turbine blades. The manufactured blade is of 1.8m for a 1kW wind turbine. The two halves of blades are made separately using a number of layers of glass fibre mat and resin. Two separate halves are stuck together and fitted in to the mould and clamped together to ensure correct shape. An impressive number of different materials and manufacturing processes were used to build very large blades through federally funded projects. On the horizon of last fifteen years few representative studies carried out related to material and fabrication technique used in wind turbine blade manufacturing is presented in Table 2.1.

Table 2.1 Wind turbine blade material and fabrication

Year	Place	Material	Fabrication technique	Ref.
2015	Tbilisi, Georgia	Carbon + glass + basalt fiber + nanopowder (boron carbide, silicon carbide, zirconium diboride, oxide crystals $3Al_2O_3 \cdot 2SiO_2$, basalt powder) + Epoxy	Lay up	28
2013	Trondheim, Norway	Hybrid fibre [CRPF 50% + GRPF 50%] + Epoxy	----	29
2013	Denmark	Biobased fiber (jute, flax) + Epoxy	----	30
2012	Delft, Netherland	Carbon fibre UD/ Glass UD/ Hybrid + Epoxy	VARTM	31
2012	Guelph, Ontario, Canada	Glass fibre + Epoxy resin	Resin Injection Moulding	32
2012	Trondheim, Norway	Carbon/Glass fibre + Epoxy	Lay up	33
2010	Bozeman, MT, USA	Glass fibre + Epoxy/ Polyster/ Vnylester Fv= 0.4 to 0.6	Infusion/ VARTM	34
2009	Roskilde, Denmark	Bamboo fiber + Epoxy	Lay up	35
2003	Krikland, WA, USA	Carbon fibre/ Fibre glass + Epoxy	VARTM	36
2001	Copenhagen, Denmark.	Carbon fibre + Epoxy	----	37

Though the diverse types of materials and manufacturing techniques was used for wind turbine blades, some key issues and challenges related to wind turbine blade material are still exists such as;

1. Mechanical performance of material potentially developed for wind turbine blade [38, 39].

2. Improve the fracture toughness of composite with minimum penalties on the other properties [40, 41].

3. Performance of material subjected to simultaneous thermal and mechanical stresses [42].

4. CAD modeling and static mechanical analysis of wind turbine blade [15, 14].

5. Performance assessment of potential material against erosive environment in presence of air and water [43-45].

While developing new material for wind turbine blade the testing was suggested at various stages of development of material. The schematic of test pyramid is indicated in Figure 2.1. At the base of test pyramid vast number of static and cyclic mechanical tests of different alternative options was suggested on test coupon according to test standards. Based on results obtained from mechanical tests of coupon testing of blade connection and subcomponent testing was the next step. Finally, the full-scale blade test was conducted using the alternative option with optimum performance of mechanical and subcomponent testing. [45]. But it is quite difficult to actual manufacturing of wind turbine blade due to its shape and size. The blade geometry can be constructed using modeling software and the performance can be tested using analysis software under application of various loads [14, 15, 47 - 49]. This methodology saves time and cost of testing. The various material parameters can be optimized.
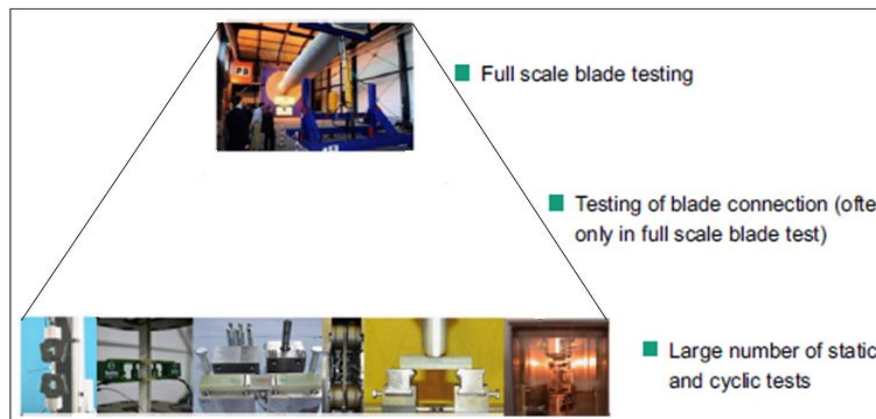
Figure 2.1 Schematic of test pyramid in wind turbine blade [45]

Wu et al. [15] developed a wind turbine blade geometry constructing interface in the study to facilitate the stress analysis using ANSYS. Based on the maximum principal stress failure criterion, the composite blade skin can be determined under a specified safety factor. A uniform stress loading on the blade can be derived with this design methodology. Qiao et

al. [47] developed a computer aided drafting (CAD) model of wind turbine blade by using Pro-E and MS Office-Excel. For simplified purposes, one aerofoil section was chosen to fit the thickness distribution, where the thickness of the blade was in reverse proportion with the radius of the rotor. Natarajan et al. [48] prepared the model of wind turbine blade for 10kW capacity by using CAD software CATIA. The material was CFRP to a large extent and aluminum was considered as reinforcement of the root section. Noticeable discrepancies were, however, observed in the strain results and in the deflections. Thus, more detailed modeling of this section will be conducted and confirmed by an experiment on a blade prototype. Rajadurai et al. [15] validated the experimental results of stresses developed and deflection of blade in flap-wise bending with finite element analysis results. The complex geometry of the composite blade is modeled utilizing ANSYS software. The response of the blade is examined under the specified drag, lift, axial, gravitational and centrifugal forces. A simple and reliable failure criterion is suggested for assessing the criticality of the blade under service loading conditions. Studies made in this paper are useful for optimum design of large size composite wind turbine blades.

2.2 Physical and mechanical characterization of polymer composites

Polymers are generally weak in strength alone, unless they are reinforced by strong and hard material in form of particulates or fibers. Development and fabrication of any particulate filled or fiber reinforced polymer matrix composite must be followed by physical and mechanical characterization in order to suit the requirements of application. Wang et al. [50] evaluated mechanical performance of alumina filled carbon fiber reinforced epoxy composites fabricated by vacuum assisted resin transfer moulding (VARTM) technique. Flexural properties of composite showed improvement up to 10 wt.% of filler addition and further decline the performance. Impact strength and fracture toughness of composites was linearly increase for addition of 15 wt.% of alumina as filler material. Pickering et al. [51] did comparative analysis of mechanical performance of randomly dispersed and aligned natural fiber reinforced polymer composites prepared through hand lay-up method. With increase in fiber loading the mechanical performance was improved. However, the composites reinforced with aligned fiber gave better mechanical performance compared to composites reinforced with randomly dispersed fiber. Petersen et al. [55] implemented hand lay-up and vacuum bagging method for fabrication of alumina tri-hydrate (ATH) (25 and 50 wt.% of resin) filled glass fiber reinforced polyester composites. Tensile strength was linearly decreased with from 120 MPa to 60 MPa with addition of 50 wt.% of ATH. However, flexural strength was

improved for 25 wt.% of filler addition and then decreased. The shear strength was remain unaffected up to 25 wt.% of filler and for 50 wt.% of filler, the value showed decline.

Braga and Magalhaes [53] fabricated hybrid composite reinforced with glass and jute fiber using hand lay-up method. Results showed superior performance of hybrid composite with increasing glass fiber loading. Khan et al. [54] comparatively characterized the mechanical performance of woven and non-woven jute fiber reinforced polymer composites. Woven jute polymer composite gave better mechanical performance than non-woven jute polymer composites. It was found that woven jute polymer composite showed identical properties in both wrap and weft direction. Also study was concluded that treatment of jute fiber with NaOH considerably improved the performance of composites. Hameed et al. [55] studied the influence of addition of epoxy modifiers on the tensile and flexural properties on glass epoxy composites. The glass fiber loading was varied up to 60 wt.%. Tensile strength was found to increase up to glass fiber loading 50 wt.% and beyond diminishes the performance. However, tensile modulus was linearly increased up to 60 wt.% of fiber loading. Flexural properties show similarity with tensile performance. Mechanical performance of unmodified epoxy was better than modified epoxy composites.

The inter-laminar shear strength (ILSS) of the carbon fiber/epoxy composites was investigated by He and Gao [56] and the results indicated that introduction of the $CaCO_3$ enhances ILSS. In particular, the addition of 4 wt% $CaCO_3$ leads to 36.6% increase in the ILSS for the composite. The results showed that the change of ILSS was primarily due to an increase of the epoxy matrix strength and an increase of the fiber/epoxy interface. The bifurcation of propagating cracks, stress transfer, and cavitation was deduced for the reasons of strengthening and toughening effect of $CaCO_3$ particles. Nayak et al. [57] studied effect of addition of different conventional filler particles on mechanical properties of glass epoxy composites. In this study epoxy resin was modified by Al_2O_3, SiO_2 and TiO_2 micro particles in glass fiber/epoxy composite to modify the mechanical properties. It is observed that mechanical properties like flexural strength, flexural modulus and ILSS were improved in case of SiO_2 modified epoxy composite compare to other micro modifiers. Alumina modified epoxy composite showed increase in hardness and impact energy compare to other modifiers.

Epoxy is modified with silicon dioxide filler particles with manual mixing and curing method by Ahmed et al. [58]. Neat epoxy showed better tensile strength and Young's modulus than composite with 5 wt% filler. Further addition of filler increases tensile strength and Young's modulus. With addition of filler increase in the hardness of particulate filled epoxy composite material was observed. Satapthy et al. [59] fabricated different sets of

unfilled and SiC filled jute epoxy composites using hand lay-up method. Hardness of Jute-epoxy-SiC particulate composites increased with an increase in reinforcement of fiber and/or particles. A gradual increase in both tensile strength as well as flexural strength with the fiber weight was noticed but, tensile and flexural strength found decreased with filler content. ILSS remained unaffected with fiber loading but improves with filler content. Alumina and SiC filled glass, carbon and Kevlar polyester composites were prepared by Abas et al. [60] with compression moulding technique and the performance is compared for mechanical properties. Flexural strength decreased with increasing volume fraction of reinforcement. Impact strength of composite found to be improved with increasing volume fraction of reinforcement. The values of hardness are increased with increasing volume fraction of both fibers and particles.

Kaundal et al. [61] varied glass fiber loading from 10 to 50 wt.% in polyester composites. Density of composite increased with increase in fiber content due to reduction in void content. With increase in the fiber loading the hardness value of all the composites increased. Impact energy of composite also increases with in fiber loading. Patnaik et al. [62] fabricated 0 to 20 wt.% varied SiC filled polyester composite reinforced with constant 50 wt.% glass fiber. It was noticed that as the content of SiC particles increases, both the tensile as well as bending strengths of the composite decline gradually but tensile modulus increased with SiC content. Hardness value of all filled composites found higher than unfilled glass epoxy composites one. Density decreased up to 10 wt.% of filler addition and further density remain unaffected. Zhao et al. [63] investigated effect of carbon fiber reinforcement on mechanical properties of graphene foam (GF)/polydimethylsiloxane (PDMS). The results depicted that mechanical performance of composite was observably improved. Reinforcement of 10 wt.% of carbon fiber in polymer composite cause increase in tensile strength and Young's modulus by 52% and 71% respectively compared with unreinforced composite. Scanning electron microscope images showed strong interfacial bonding between carbon fibers and matrix.

Yan et al. [64] studied use of natural fiber for polymer and cementitious composites. The effect of fiber treatment with 5 wt.% of NaOH solution on microstructure and mechanical properties of polymer composites were investigated. Microstructure study of alkali treated fiber showed much rougher fiber surface compared to untreated fiber. Tensile and flexural properties of treated fiber epoxy composites were improved by 17% and 16% respectively. This improvement in mechanical properties was attributed to improvement of adhesion at fiber-matrix interface due to alkali treatment which was clearly visible in SEM

micrographs. Performance of fiber reinforced concrete showed better performance compared to plain concrete. Essabir et al. [65] modified the palm fiber with alkali treatment and then reinforced in to polyethylene. Also clay particles were used as filler material to prepare hybrid composites. The morphological study showed that the alkali treatment of palm fiber enhanced their surface interaction with matrix. The tensile properties showed that composite reinforced with 1:1 ratio of fiber and filler material had best modulus and strength. Similarly, Boopalan et al. [66] investigated and compared the mechanical properties of raw jute and sisal fiber reinforced epoxy composites with alkali treated jute and sisal fiber reinforced epoxy composites. It was found that the sodium hydroxide treated jute and sisal fiber reinforced epoxy composites exhibited better mechanical properties than the raw jute and raw sisal fiber reinforced composites.

Chaichanawong et al. [67] prepared composites with different weight percentage (0-30 wt.%) of glass fiber reinforcement in polyamide matrix. Tensile test and flexural test were conducted based on ASTM D638-02a and ASTM D790-02, respectively. Yield strength, ultimate tensile strength and flexural strength of all specimens significantly decreased at the beginning stage of moisture absorption and then these mechanical properties were almost constant. In addition, ductility (%Elongation) of all specimens did not change at the beginning stage. However, ductility of all specimens significantly decreased in the third stage, and then their ductility were almost constant. Naresh et al. [68] studied effect of strain rate on tensile properties of glass-epoxy, carbon-epoxy and hybrid composites for aircraft wings experimentally and theoretically. Quasi-static tests were performed on Instron universal testing machine in accordance with ASTM D638. The results indicated that the tensile strength and tensile modulus of GFRP and hybrid composites increased and percentage of failure strain for GFRP, CFRP and Hybrid composites decreased with the increase in strain rate. However, tensile strength and tensile modulus of CFRP remains approximately constant.

Dong [69] presented flexural behavior of the glass and carbon fiber reinforced epoxy composites. Comparative study was conducted on two types of glass fiber and two types of carbon fiber. It is shown from the results that partial substitution of carbon fibers for glass fibers in high strength carbon fiber (e.g. T700S) reinforced composites improves the flexural strength, but partial substitution of carbon fibers for glass fibers in high modulus carbon fiber (e.g. P-100) reinforced composites does not improve the flexural strength. Bajracharya et al. [70] reinforced varying quantity of glass fibers (10 – 30 wt.%) with recycled thermoplastic material to produce new generation composite material. Intensive experimental studies were

then performed to characterize the tensile, compression and flexural properties of glass fiber reinforced mixed plastics composites. With reinforcement of 30 wt.% of glass fiber the tensile strength and elastic modulus was improved by 141% and 357% respectively. The best improvement was seen in the flexural properties due to the better orientation of the glass fibers in the longitudinal direction at the outer layers. The existing rule of mixture was modified considering randomness of fibers to reliably predict the strength properties of glass epoxy composites.

Dobah et al. [71] described the performance of woven jute polyester composites subjected to uniaxial and multi axial loading cases. Laminates with 25 wt.% of jute fiber content was fabricated using hand lay-up method. Performance of composite specimen for multi axial loading was inferior to the performance of uniaxial loading. Rahman et al. [72] studied mechanical performance of untreated and post fabrication treated polymer composites reinforced with raw, oxidized jute fiber. Post treated specimen demonstrated better performance compared to raw and oxidised one. Fiber loading of 30 wt.% showed optimum set of mechanical properties. Gopinath et al. [73] fabricated jute fiber reinforced polymer composites using two matrix materials viz; epoxy and polyester. Jute reinforced epoxy composites exhibited better mechanical performance than jute polyester composites. Athijayamani et al. [74] presented parametric analysis of bagasse fiber reinforced vinyl ester composites considering mechanical properties. The fabrication of composite laminated were carried out using Taguchi experimental design considering control parameters such as fiber length, fiber content, fiber diameter, NaOH concentration, and treatment duration. Results were analyzed to determine influence of each control parameter on tensile and flexural strength. Results revealed that fiber content was most significant parameter for mechanical properties and 40 wt.% fiber reinforced polymer composite exhibited higher value.

Manjunath et al. [75] fabricated and characterized glass epoxy composites filled with nano size alumina, nano size silica and micro size alumina trihydrate filler. Results showed that both the micro and nano filler act as a secondary reinforcement. The improvement in the mechanical properties was due to increase in adhesion and good dispersion of filler. The improved mechanical properties indicated that the glass fiber reinforced epoxy composites with particulate filler material is a good candidate for structural application. Merter et al. [76] prepared sets of polymer composites reinforced with compatible and incompatible glass fiber and investigated the mechanical properties. It was found that sizing applied to make glass fiber compatible have significant influence on the properties of polymer composite. The highest flexural properties (99.1 MPa flexural strength and 9.55 GPa flexural modulus) were

obtained from the composites reinforced with compatible (sized) glass fiber, due to better adhesion at the interface of glass fibers and polymer matrix. Motoc et al. [77] approached issued related to mechanical performance of hybrid (glass and carbon fiber) polymer composite for various content, orientation and stacking sequence of fiber. The results showed that composition containing highest carbon fiber content exhibited best mechanical performance in terms of tensile and flexural properties irrespective of orientation of fibers.

Harper et al. [78] presented a finite element method for predicting the mechanical performance of carbon fiber reinforced polymer composites. Fiber filaments were modelled using beam element representing large volume elements under investigation. The beams were attached to a regular grid of 2D element which represented matrix material. The predicted results for strength and stiffness for random and aligned fiber reinforced polymer composites were within 10% margin from experimental values for particular property. Medina at el. [79] focused on in-plain shear mechanical performance of carbon epoxy composites considering different weaving pattern. The laminates were manufactured using vacuum infusion process with unidirectional fabric in wrap direction, plain weave with balanced properties in wrap and weft direction and 2/2 twill weave with balanced properties in wrap and weft directions. The results showed that the weave structure have a very little effect on the in-plain shear properties of composites under considerations.

2.3 Fracture toughness analysis of polymer composites

Epoxy polymer belong to the class of thermosetting polymers are used as matrices for fiber reinforced composites and also as adhesives. However, they also come with an undesirable property of brittleness with low fracture resistance. Thus, the enhancement in fracture toughness has been a critical issue when it comes to their application and hence engineers have been working on the toughening of epoxies for several decades. Zhu and Joyce [80] presented a technical review of fracture toughness testing, evaluation and standardization for materials. The review described the most important fracture mechanics parameters: the elastic energy release rate G, the stress intensity factor K, the J integral, the crack-tip opening displacement (CTOD) and the crack-tip opening angle (CTOA). Attention was paid to guidelines on how to choose an appropriate fracture parameter to characterize fracture toughness for the material of interest, and how to measure the fracture toughness value defined either at a critical point or in a resistance curve format using laboratory specimens. In case of particulate filled FRP composites evaluation of stress intensity factor (K) or energy release rate (G) is most appropriate parameter

Launey and Ritchie [81] illustrated schematically the mutual competition between intrinsic mechanisms of damage which act ahead of the crack tip to demote crack advance and extrinsic mechanisms of crack-tip shielding that act mainly behind the crack tip to impede crack advance. Intrinsic toughening mechanism due to filler particle available on the path of crack and extrinsic toughening mechanism due to fiber bridge formed behind crack front is schematically presented in Figure 2.2. Brunner [82] discussed recent developments with the emphasis on experimental aspects of fracture toughness testing of FRP-composites in Mode I and Mode II. The stress intensity fracture (K) for FRP composites can be determined in tensile loading (opening) or shear loading (in plane).
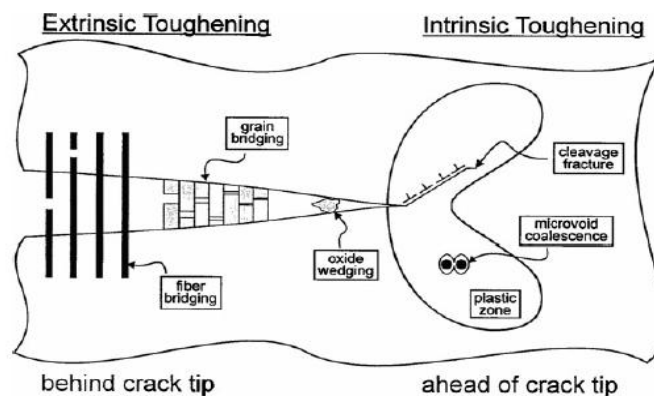
Figure 2.2 Schematic showing intrinsic and extrinsic toughening mechanisms [s45]

Acvi et al. [83], Ariken et al. [84] and Samanci et al. [85] studied fracture toughness in 3 point single edge notch bending mode for sand filled glass and steel fiber polyester composites. The ratio of crack length to width of specimen used was in the range of 0.1 to 0.7. The critical stress intensity factors K increased with increase in glass fiber ratio for all methods i.e. the initial notch depth method, the compliance technique and the J-integral methods. The critical stress intensity factors did not also change by increasing the notch-to-depth ratio. With increase in filler content the fracture toughness slightly decreased. However, with increase in fiber loading the toughness was observed to increase. Liu and Hughes [86] did comparative study of different densities in wrap and weft direction and different weave pattern of flax fiber on epoxy composites. The fracture test was conducted in compact tension mode with ratio of crack length to width of specimen from 0.45 to 0.55. The fracture toughness was observed identical in wrap and weft direction when wrap and weft density is similar. For different wrap and weft density the fracture toughness was recorded drastically different in wrap and weft direction. For weave pattern 1/1 the toughness was observed to be higher than that of 1/4, 1/6 and 1/10 pattern. Observations recommended use of plain weave pattern in order to obtain higher fracture toughness.

Perez et al. [87] modified polypropylene with $CaCO_3$ and SiO_2 and subjected to fracture toughness test in double end notch tension mode with crack length of 0.25 times of width of specimen on either sides. For PP/$CaCO_3$ composites, an increasing trend of stiffness with filler loading was found while a decreasing trend of strength, ductility and fracture toughness was observed. On the other hand addition of SiO_2 resulted in slightly improved fracture toughness of composite. Similarly, epoxy was toughened by Chandrasekaran [88] with addition of multi-walled carbon nano-tubes (MWCNT), graphite nano platelets (GNP) and thermally reduced graphene oxide (TRGO). Three point bend test was conducted with crack length of half of the width of specimen. For all the three fillers the fracture toughness is improved with increase in filler content. The toughening effect of TRGO is significant than GNP and MWCNT. TRGO increases bonding between filler and epoxy. The toughness was increased with increase in wt.% of GNP but starts to decrease with higher wt.% (2%). The polyethylene also modified by Lauke and Yun [89] with incorporation of micro sized silica and tested for crack resistance test. The crack resistance found to be decreased with increase in filler content. Theoretical modeling for the fracture toughness of particulate filled polymer composites was also presented by considering a simple geometrical model of particle–particle interaction in a regular particle arrangement.

De souza et al. [90] prepared the epoxy composites with compression moulding technique filled with barium glass, ytterbium trifluoride and aluminum silicate. At certain load level a crack initiated at the tip of initial sharp pre-crack. Further crack deflects between particles and due to higher dense particle the cracks formation turns to bridge formation as shown in Figure 2.3. Kusaka et al. [91] investigated mode-I fracture behavior of unidirectional carbon epoxy composites over wide range of loading rate. Fracture toughness of composites decreased with increase in loading rate indicating distinct rate sensitive transition.
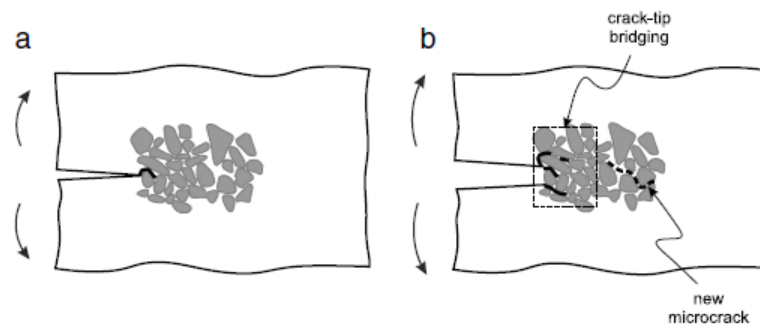
Figure 2.3 Crack deflection and bifurcation [90]

The mode I inter-laminar toughness and intra-laminar fracture toughness, and mode II inter-laminar shear fracture toughness of a thermoplastic and a toughened thermosetting polymer reinforced with aligned and cross-ply carbon fibers was investigated over a wide range of temperature. The nature of the fracture process and fracture resistance was explained qualitatively on the basis of measurements of toughness, crack-tip and crack-wake events, and post-mortem fractographic analysis [92]. Both the theoretical and experimental approaches was utilized for fracture analysis and damage tolerance estimation. The analysis was based on combination of J integral method and theory of nonlinear fracture mechanics. The critical values of fracture toughness were determined from the examination of notched specimen subjected to tensile and bending mode [93]. Coal gangue powder filled polypropylene composites modified with maleic anhydride grafted polypropylene were prepared. The value of fracture toughness was decreased considerably at 5 wt.% content of coal gangue and then improved noticeably with increasing filler content. Modified composite with 5 wt.% of maleic anhydride grafted polypropylene, the fracture toughness was higher compared to base polypropylene coal gangue composite. It was attributed to significant improvement in crack resistance in necking and fracture [94].

Zhang et al. [95] investigated experimentally fracture behavior in mode I and mode II for glass epoxy composites. Crack propagation was observed by video extensometer in addition to visual observation. Strain energy release rate were obtained from experimental method as well as 3D finite element method. Ayatollahi et al. [96] studied effect of multi walled carbon nanotubes on epoxy composite with emphasis on fracture toughness under bending and shear loading conditions. Several finite element (FE) analyses were performed to determine appropriate shear loading boundary conditions for a single-edge notch bend specimen (SENB) and an equation was derived for calculating the shear loading fracture toughness from the fracture load. It was seen that the increase in fracture toughness of nano-composite depends on the type of loading. Sun et al. [97] used a global-local multi-scale finite element model with effective homogeneous material properties for samples in tension mode. For epoxy composites filled with various volume fractions of SiO_2 particles, the simulation results for effective fracture toughness and critical strain energy release rate showed good agreement with past study. It is demonstrated that the finite element model can be used to efficiently study the toughness mechanisms.

Miura et al. [98] presented study of delamiation fracture behavior of woven glass fiber reinforced polymer composites. Mixed mode fracture tests were carried with six point bending mode. Also, a three dimensional finite element analysis was performed to determine

critical strain energy release rate at the onset of delamination. Reis [99] studied the effect of surface treatment by NaOH on fracture properties of natural fiber reinforced polymer composites. Epoxy and unsaturated polyester resin were used as matrix for preparing the composites. For comparison, unreinforced and untreated sisal fiber reinforced polymer mortars were also studied. From the results it was observed that untreated fiber reinforced polymer composites have higher fracture properties than other composites. Perez et al. [100] investigated effect of wood flour addition up to 30 wt.% on fracture properties of polymer composites. Reliable fracture toughness data that will be useful for structural applications were obtained. Although reduced ductility and toughness were observed for the composites respect to the matrix, in the case of modified composites, environmentally friendly stiffer materials were obtained with cost saving without sacrificing strength. Czabaj and Ratcliffe [101] measured intra-laminar and inter-laminar mode-I fracture toughness of carbon epoxy composites. Intra-laminar fracture toughness exhibited more extensive fiber bridging and rapidly increasing resistance curve as compared to inter-laminar fracture. Observations of initiation and propagation of intralaminar and interlaminar fracture, and the measurements of fracture toughness, were consistent with fractographic analysis using scanning electron microscopy.

Fracture behavior of polymer composites was investigated using Single Edge Notched Bending (SENB) specimens. The fracture tests were conducted on specimens with notch inclined at different angles under static loading at room temperature.the experimental data was analysed using linear-elastic fracture mechanics. 3D finite element model were developed for simulating fracture behavior of the SENB specimen. It was found that besides modes I and II, there was also insignificant mode III component of the critical strain energy release rate. The simulations were showed critical strain energy release rate decreased with increasing the notch inclination [102]. Kushvaha et al. [103] studied effect of shape and volume fraction of filler material on fracture behaviour of polymer composites. Experiments were conducted on pre-notched glass epoxy composite specimens in mode-I. the crack initiation and propagation was recorded using high speed camera. The results showed a pronounced improvement in crack initiation toughness for rod-shaped fillers producing _145% increase over unfilled epoxy at 15% volume fraction with flakes and spherical fillers showing 97% and 67% improvement, respectively. Jajam et al. [104] investigated synergistic effect of reactive multi-walled carbon nano tubes on fracture of hybrid epoxy composites. The crack-tip deformation histories and fracture parameters for stationary and growing cracks

are extracted. Crack initiation toughness was improved in modified epoxy relative to neat resin. The dynamic crack toughness value was found to be lower than static counterpart.

Nekhlaoui et al. [105] prepared two systems of composites polypropylene/clay and compatibilized polypropylene/caly with clay content varying from 5 to 30 wt.%. Clay addition markedly enhances the plastic work of fracture (We) and reduces the specific plastic work (Bwp). Gouda et al. [106] used liquid reactive rubber to improve the fracture toughness of epoxy composite laminates. Results showed that liquid rubber in small quantity (15 − 22 gsm) improved critical energy release rate up to 140% in mode-I and 32% in mode-II loading. Matthews et al. [107] developed wide range of fracture analysis to quantify the stress field at the crack tip. In this paper an expression of instantaneous evaluation of J-Integral is compared to finite element results. Wan et al. [108] investigated the fracture toughness (critical stress intensity factor) of epoxy composites filled with graphene oxide (GO), silane functionalized GO. With filling of GO the stress intensity factor was improved and with silane treatment of GO the vale was further improved.

Silva et al. [109] produced nanoclay and MWCNT filled glass fiber epoxy composites using vacuum moulding process in order enhance the fracture toughness. Tests were performed in mode I, II and mixed mode to determine critical strain energy release rate. Significant improvement was observed in fracture toughness for all loading modes by incorporation of nanoclay whereas; MWCNT resulted in moderate improvement in to fiber epoxy composites. Boyina et al. [110] characterized intra-laminar fracture in plain weave fabric reinforced polymer composites under mixed mode load. From the micrographs of fractured surface of specimen the effect of mixity on the failure mechanism and crack path is established. Finite element analysis is performed using effective elastic properties of the composite material obtained from meso-scopic analysis.

2.4 Thermal and thermo-mechanical characterization of polymer composites

The exponential growth of polymer applications has led to development of several new techniques for polymer characterization. No single technique has proved more useful than thermal analysis. This method delivers the information unobtainable by other means and has been used in many areas of basic and applied research, production and quality control [111]. The various techniques include dynamic mechanical analysis, thermo-gravimetric analysis and thermal conductivity analysis. Dynamic mechanical analysis (DMA) is a versatile technique that complements the information provided by the more traditional thermal analysis techniques such as differential scanning calorimetry (DSC), thermo-gravimetric

analysis (TGA), and thermal mechanical analysis (TMA). The performance parameters of the DMA are generally storage modulus, loss modulus and damping factor [112].

Dynamic mechanical analysis is an necessary and effective tool for determining viscoelastic properties of crystalline polymer and composite materials related to primary relaxations and other valuable parameters, such as crosslinking density [113], dynamic fragility [114], dynamic/complex viscosity, storage/loss compliance, creep compliance/stress–relaxation modulus and the non-Arrhenius variation of relation times with temperature [115]. The storage modulus or dynamic modulus typically related to the Young's modulus. It often associated with stiffness of a material and determine how stiff or flimsy a sample. It is regarded as a material tendency/ability to store energy applied to it for future purpose. Loss modulus or dynamic loss modulus, is a viscous response of the materials and regarded as materials tendency to dissipate energy applied to it [116]. Tan delta is expressed as a dimensionless number and regarded as the mechanical damping factor defined as the ratio of loss and storage modulus [117].

The degree of homogeneity of hybrid composites can be determined with Cole-Cole plot. The homogeneous composites show perfect semicircle in Cole-Cole plot. Furthermore, the interface adhesion characteristics of fiber and matrix can be evaluated using two parameters namely, adhesion efficiency factor (A) and reinforcement effectiveness coefficient (C). The lower value of A show better adhesion efficiency and higher value of C show less effectiveness of reinforcement [118]. Dynamic mechanical analysis (DMA) has proven a valuable tool for studying the structure of polymers and composites [119, 120]. Study of the glass transition by DMA involves measuring loss and storage modulus of the material in a given oscillation frequency from room temperature to above the glass transition temperature (Tg). During curing of a thermoset polymer, the number of crosslinks increases, consequently, reducing mobility of the molecular segments and increasing Tg of the material [121]. Once the temperature of the material exceeds the curing temperature, freezing of the reactive groups occurs, preventing further reactions [122]. Post-curing of the polymer also modifies loss and storage modulus, and its Tg, that can be used to verify completeness of the curing reaction.

The exhaustive study was conducted on influence of surface modification of fiber on the thermal and thermo-mechanical performance of natural fiber reinforced polymer composites [112, 116, 118, 123-129]. Positive alteration in the thermo-mechanical performance was observed with various surface modification treatments irrespective of type of fiber used. Ray et al. [123, 124] observed increase in storage modulus with the increase in

the jute fibre loading in the composites due to the reinforcement imparted by the fibres that allowed greater stress transfer at the interface. However, for all composites the storage modulus decreased with the increase in the temperature. Incorporation of the jute fibres in the resin matrix restricted the mobility of the polymer molecules at the interface and increased the Tg of the composites. The high damping parameter (tanδ) of the unreinforced resin was due to the deformation of the resin molecules in-between the cross-links on application of stress that was drastically reduced on incorporation of the untreated fibres in the composites. The storage modulus E' of the composites at 30°C was comparable with the flexural modulus. Shanmugam and Thiruchitrambalam [125] found that the storage modulus (E') of hybrid composites was less at higher temperature, but it increased on increasing the jute fiber content. Similarly, the loss modulus (E") was observed to increase on increase in the jute content due to effective stress transfer. Both storage modulus (E') and loss modulus were observed to be high for higher content of jute fiber reinforced composites. The value of Tg obtained from the loss modulus curve (E") is less than Tg from Tanδ curve. Tg shifting towards right in the graph indicates the evidence for good interfacial adhesion.

Sreenivasan et al. [126] revealed that the increasing wt% of natural fiber in polymer composites can increase the strength of the matrix. Nevertheless, it does not reflect this fact beyond 40 wt% of fiber loading. Accordingly, the 20, 30 and 40 wt% of fiber loading shows the higher value than the 10 and 50 wt% of fiber loading. The highest value of storage modulus was observed for 30 wt% of fiber loading and it ensures that the better interfacial bonding between fiber and matrix. As expected the lower wt.% as well as the higher wt.% of fiber loading shows the lowest storage modulus. Kumar et al. [127] fabricated two sets of composites with reinforcement of untreated and treated coconut sheath fiber in epoxy matrix using conventional hand lay-up method. The value of storage modulus improved from 2.3 GPa to 3.9 GPa at room temperature for untreated and treated coconut sheath fiber epoxy composites. However treatment of fiber results in decreased viscous response of coconut sheath fiber epoxy composites. The char yield of untreated fiber epoxy composite was higher than composite reinforced with treated one. It indicated the less amount of lignin present in the treated fiber epoxy composite than untreated composite.

Mohanty et al. [128] summarized experimental studies on vicso-elastic performance of jute fiber reinforced polymer composites. Effect of fiber loading and coupling agent on storage modulus, loss modulus and damping factor was investigated. The storage was improved with jute fiber reinforcement and the value was further improved with fiber treatment. The damping factor graph presented a strong influence of fibre content and

coupling agent on the relaxation process of polymer. TGA thermograms displayed an increase in the thermal stability of polymer matrix with fibre reinforcement and surface treatment. George et al. [129] prepared jute yarn reinforced polymer composites using technique called commingling method. The dynamic analysis of this commingled composites were studied for factors like fiber content and chemical treatment. The storage and loss modulus increased with fibre content where as damping factor decreased. Composites reinforced with treated jute fiber showed much higher storage and loss modulus values at all temperatures compared to untreated one. The glass transition temperature showed a marginal increasing tendency with fibre content and chemical treatments. Jawaid et al. [116] investigated dynamic mechanical performance of hybrid epoxy composite reinforced with jute and oil palm fibers. The hybrid composites were fabricated with varying ratio and stacking sequence of jute and oil palm fibers. The performance was also evaluated with Cole-Cole plot. The curves for Cole-Cole plot were in the form of imperfect semicircle which showed hetroginity of composite system

Baheti et al. [130] illustrated that all the properties of glass epoxy composites were greatly affected by operating temperature and weight fraction of fly ash. It was observed that the storage modulus of the activated fly ash filled composites improved over the entire temperature span as compared to unfilled composites. The reason for this was increased interface due to incorporation of fly ash which results in increased grafting of epoxy chains over fly ash particles. Similarly, Kaundal et al. [131] characterized series of two different unfilled and SiC filled glass epoxy composites using DMA. Improvement in storage modulus was observed up to 30 wt.% of glass fiber loading and for 10 wt.% of filler content. Glass transition temperature shifted towards higher side with incorporation of both the type of reinforcements. The addition of SiC particulate filler in glass epoxy composites enhanced the damping performance. Kumar et al. [132, 133] correlated the thermo-mechanical performance with erosion behavior of fiber reinforced polymer composites. Higher storage modulus was recorded for 30 wt.% of CFRP while in case of (G+C)FRP higher value was observed for 40 wt.%. Glass transition temperature was observed higher for higher fiber loading. Imperfect circles in Cole-Cole plot of the fiber reinforced vinyl ester resin composites was observed, which demonstrated heterogeneity of the system.

Stark [134] and Stark et al. [135-136] studied dynamic analysis study of commercially available prepeg epoxy material with carbon fiber. The performance was observed for varying heating rate and frequency. With increasing temperature, all three mechanical characteristic values storage modulus, loss modulus and damping factor were decreased.

Thereby, the influence of the frequency, which was quite pronounced at the beginning, was ever more reduced. Landro and Lorenzi [137] presented comparison between dynamic mechanical behavior of polypropylene-glass and polypropylene-natural fiber composites. Results were demonstrated superior performance of glass fiber compared to natural fiber reinforced polymer composites. Ornaghi et al. [138] evaluated performance of glass/sisal hybrid polyester composites focusing on dynamic mechanical analysis. Hybrid composites with different fiber loadings and different volume ratios between glass and sisal were studied. The effect of the fiber length was also been investigated. By DMA, an increase in the storage and loss modulus was found, as well as a shift to higher values for higher glass loading and overall fiber volume was also observed. It was also noticed an increase in the efficiency of the filler and the calculated activation energy for the relaxation process in the glass transition region.

Mandal and Alam [139] fabricated glass/bamboo reinforced polyester hybrid composites with replacing glass fibers gradually by bamboo fibers. With increase in bamboo fiber the storage modulus gradually decreased. Loss modulus was also found to decrease with loading while the damping property was found to increase marginally. Cole–Cole analysis was made to understand the phase behavior of the composite samples. Kumaresan et al. [140] studied dynamic mechanical performance of silicon carbide filled carbon epoxy composites using DMA. Results reported significant improvement in glass transition temperature of 10 wt% silicon carbide filled polymer composite compared to unfilled one. This improvement was due to interface modification of silicon carbide filled carbon epoxy composite. Hassan et al. [141] studied unreinforced and glass fiber reinforced polyamide composites for thermal and thermo-mechanical properties subjected to dry and wet conditions. TGA results showed 2% and 5% moisture absorbed by samples subjected to humid and wet conditions respectively. With absorption of moisture there were no significant change in melting temperature and crystallization temperature. DMA results showed that materials ability to dissipate energy as internal energy increased with moisture absorption. Ray [142] developed polymer matrix composites filled with fly ash up to 50 wt.% for high damping behavior. Unsaturated polyester resin matrix was modified with SBR latex particles in three proportions. Presence of latex particles significantly improved damping properties.

Thermal degradation of polymer and composite structures is a complex phenomenon and a great deal of research is performed on this subject [143-148]. The thermal degradation of a composite covers a wide field of important processes such as the development of heat resistant, thermal stabilization, and the characterization of high-temperature composites for

aircraft and aerospace usage [145]. Generally, the thermal degradation of a polymeric composite follows more than one mechanism, the existence of various concurrent chemical reactions accompanied by other physical phenomena such as evaporation, melting and ablation introduce further complication for the modeling of the degradation kinetics [146, 147]. Thermo-gravimetric analysis or thermal-gravim analysis (TGA) is a method of thermal degradation analysis in which changes in physical and chemical properties of materials are measured as a function of increasing temperature (with constant heating rate), or as a function of time (with constant temperature and/or constant mass loss) [150]. The Thermo-gravimetric analysis results indicated that the thermal stability of the high performance fibers can be characterized with the typical degradation temperatures. The results from thermo-gravimetric analysis may be presented by mass versus temperature (or time) curve, rate of mass loss versus temperature curve [151]. Ferreira et al. [152] studied the thermal degradation of an E-glass fibre reinforced unsaturated polyester composite using TGA. The char yield form glass fiber polyester composite is much higher than neat polyester. This was the indicated higher thermal stability of glass fiber. Rapid thermal degradation was observed between 300 to 400°C. Early start of degradation of composite filled with glass fiber was also observed due to early mobility of polymeric chains at the interface of fiber and polymer.

2.5 Erosive wear behavior of polymer composite

Erosion is the loss of material that due to repeated impact of small, solid particles. Influence of solid particle erosion was studied for different factors such as particle properties, impact parameters, particle concentration and material temperature [153]. Lee [154] described the necessity of wear resistant property glass fiber reinforced polymer composites for wind turbine blades. Work evaluated corrosion and wear resistance of various surface modifications of glass epoxy composites.

Ruff and wiederhorn [155] presented a review on single and multiple particle impact erosion of metals and ceramics. Report also presented the significant parameters for erodent particles and material characteristics. Humphrey [156] reported more comprehensive review of fundamentals of fluid mechanics relevant to solid particle erosion. Discussion on experimental techniques and fundamental considerations relevant to motion of solid particle were also included. In the year of 1995 Finnie [157] reviewed the influencing parameters and dominating mechanics during solid particle erosion of metals and ceramic materials. Experimental investigations were carried out with principal objective to evaluate erosion rate in flow passages and its relation with the other parameters involved in the process. Soderberg

et al. [158, 159] and Hutchings [160, 161] reported the advantages and disadvantages of such experiments. The experimental study by McLaury et al. [162] correlated the erosion rate of elbows and straight pipes with penetration rate and flow velocity for different elbow diameter. Megn and Ludema [163] approached the modelling concept in relation with erosion by providing information about the available wear models and prediction equations. The author concluded that no universal equation predicting erosion was exists.

The erosion rate and behavior of material for different levels of considered factors were observed [61, 62, 164-168]. Patnaik et al. [8] presented exhaustive review in the field of solid particle erosion properties of polymer composites. Review included processes and modes during erosion, prediction models for erosion process, implementation of DOE and statistical techniques etc. Zhang et al. [169, 170] strongly emphasized need of sustainable surface of wind turbine blades against rain erosion. This study included the fabrication of water jet erosion test rig to simulate the rain erosion in the laboratory. In this direction the use of discrete water jets, where so-called jet slugs was impacted on the surface of sample. Investigations had mapped the influence of water jet slug velocity and impact frequency. In this series of papers experiments were conducted on flat and curved samples too. Authors concluded that substrate curvature does not influence erosion rate. Therefore, flat panels, which are easier to handle during practical preparations, can be used.

Barkoula et al. [5] studied solid particle erosion response of epoxy composites reinforced with glass fiber and epoxy compatible glass fiber at impact velocity of 70 m/sec. Composites showed a linear increase of weight loss with impact angle from the beginning of the experiments. The maximum weight loss was found at 90 impact angle which illustrated brittle nature of composite. The composites with EP-compatible GF presented a much higher erosion resistance compared to the EP-incompatible GF reinforced composites. Biswas et al. [166] studied solid particle erosion properties of SiC filled glass polyester composites subjected to impact of silica sand with velocity of 43 to 65 m.sec. The maximum erosion was observed at 45^0 impingement angle for unfilled and at 60^0 for SiC filled composite, which shows semi-ductile behavior. Composite filled with 20 wt% SiC shows better erosion characteristic compared to all other composites. Erosion rate gradually increased with erodent velocity owing to higher kinetic energy of erodent particles. Taguchi approach was implemented for determining optimum values of control parameters. The experimental results were found in close agreement with FE (ANSYS) results. Similarly, Patnaik et al. [171] assessed the solid particle erosion behavior of alumina filled glass polyester composites for impact of silica sand particles with velocity of 32 to58 m/sec. The maximum erosion was

noticed at 60^0 impingement angle which indicate semi-ductile erosion behavior of composite. Microstructure showed that due to erosion matrix covering the fiber is chipped off and forms the crater showing the fiber body. Taguchi technique was used to determine local optimum value and Genetic Algorithm technique is used to determine global optimum parameters.

Harsha et al. [172] characterized glass and carbon fiber reinforced polymer composites subjected to solid particle erosion environment. The erosion rates of these composites were evaluated at different impingement angles and impact velocities. Unreinforced polymer and 20 wt.% glass fiber reinforced polymer composites exhibited maximum erosion rate at 30° impingement angle. However, other composites exhibited maximum erosion rate at 60° impingement angle. The moderate correlation was observed between erosion rate and mechanical properties of corresponding composite. Patnaik and tejyan [173] fabricated and investigated needle punched viscose fiber nonwoven mat reinforced polymer composites subjected to solid particle erosion. The control parameters affecting erosion studied were impact velocity, impact angle, fiber loading, and erodent size. Taguchi design of experiment approach and statistical technique analysis of variance were implemented to evaluate interdependence of control parameters.

Bagci and Imrek [12, 13] and Bagci [174] evaluated solid particle erosion characteristics of particulate filled fiber reinforced polymer composites. The filler materials used were boric acid, alumina, and silicon carbide in to glass fiber reinforced epoxy composites. The Taguchi design of experiment was successfully implemented to consider the process parameter like impact velocity, angle of attack, filler material, erodent size and fiber direction. Significant increase in erosion rate was observed with increase in impact velocity compared to variation in other parameters. Developed composite material with incorporation of boric acid with filler content of 30 wt.%, resulted in to decrease in erosion rate. This was attributed to formation of strong bond between filler material and epoxy resin. From the signal to noise ratios calculated for each set of experiment the ranking of different process parameters was done. The ranking obtained was also confirmed with help of analysis of variance method. The scanning electron microscope images were analyzed for stages and mechanism of erosion.

Biswas and Satapathy [175] and Rout and Satapathy [176] utilized industrial (red mud) and environmental (rice husk) waste as filler material to improve erosion resistance of glass fiber reinforced epoxy composites respectively. The steady state experiments were conducted to observe erosion behavior of these red mud filled glass epoxy composites and results were compared with predicted value by developed mathematical model. Significant

control factor and their interaction influencing the wear rate was identified using Taguchi approach. Filler content was found to have substantial influence in evaluating material loss. A comparison between unfilled and rice husk filled glass epoxy composites was presented. Optimal parameter setting in order to obtain minimum erosion rate was determined from Taguchi analysis. The filler (rice husk) content has second rank in the influencing parameters on minimization of erosion rate. The experimental results are in good agreement with values obtained from mathematical model and artificial neural network model.

Bijwe and Rattan [177] fabricated three polymer composites reinforced with carbon fabric with three weave pattern viz. plain, twill and satin by impregnation technique followed by compression moulding. These composites were characterized for adhesive, fretting, abrasive and erosive wear. Role of weave varied with wear mode but no weave performed best or worst in all wear modes. Rattan and Bijwe [10, 178] in their work illustrated fabrication and erosive wear characterization of carbon fabric reinforced thermoplastic composites. Study was conducted at varying attack velocity and angle. Due to reinforcement of carbon fabric the erosion resistance of composites deteriorated irrespective of angle of attack. In-spite of not very ductile polymer composites showed maximum erosion at impingement angle of 30º. Effect of weave pattern and fabrication technique on erosion performance of carbon fiber reinforced polymer composites was studied. Plain weave composites exhibited slightly better erosion wear resistance compared to twill and satin weave. Also SEM micrographs were critically analyzed to understand wear mechanism.

Plenty of past studies [17, 18, 18,179 – 184] are available on slurry jet erosion of metals and ceramics. But there is scarcity of literature on slurry jet erosion of polymeric materials. Hawthorne et al. [185] evaluated performance of composite material under impact of both dry particle jet and slurry jet condition at angle of impingement 20º and 90º. The slurry jet experiments were conducted with 200µm alumina particles impacting at 15 m/sec velocity and flow rate of 18 lit/min. However, dry jet erosion tests were conducted with 50 µm alumina particles impacting at 84 m/sec and feed rate of 2 gm/min. Dry jet erosion rate reported was three times more than slurry jet erosion rate. Micro-structural integrity and hardness of composites significantly affected the erosion resistance in all tests. Fang et al. [186] constructed slurry jet erosion test rig and series of slurry jet erosion tests were conducted using silica sand as erodent material. The various parameters such as impact angle, sand concentration and erosion time were studied. The brittleness property (function of hardness and stress intensity factor) was more convenient to explain erosion behavior of material.

Joshi at el. [187] presented study of slurry erosion behavior of glass epoxy composites filled with 5, 10 and 15wt.% alumina particles. The effect of variation of slurry concentration, contact angle and speed were considered for determination of erosion rate. Tests were conducted in accordance with Taguchi design of experiment for obtaining results in systematic manner. Analysis of variance was used to study contribution of individual parameter and regression equation was developed to predict the response. Contact angle of 60° exhibited highest erosion rate. Frosell et al. [188] tested relation between slurry particle concentration and erosion rate of thermoplastic polymer subjected to impact of jet. The results showed that slurry erosion rate was dependent on the slurry concentration and test duration. Two distinct erosion profiles (i.e. U and W) correlated with changes in erosion rate over the test duration.

Corsini et al. [189] demonstrated that when the blade erosion reaches the critical limit, the degradation of aerodynamic performance begins gradually. A numerical study was presented on determination of leading edge erosion patterns in an induced draft fan. The computational fluid dynamics codes were used to calculate particle trajectory. The numerical study clarifies the influence of flow structure, initial blade geometry particle size and concentration on erosion pattern. Wang and Yang [190] established new universal finite element model for erosive wear. The model incorporated two exchangeable material sub models for ductile and brittle materials respectively. The influence of impact angle, impact velocity and particle penetration were also discussed using developed model. The model was also able to calculate the erosion with different particle sizes and shapes. Liu et al. [191] developed criteria to generate solid particle erosion prediction in environment of dry gas and gas mists using computation fluid dynamics. The developed model predicted penetration rate and maximum erosion position. Initially the model was validated with set of 94 experimental tests conducted from the past study.

Hadavi et al. [192, 193] recorded the impact, rebound and fracture of erodent particle using numerical method in series of papers. In first part of paper, a novel method was developed to generate the CAD representation of the actual erodent particle geometry. The observations from numerical and experimental results revealed that the rebound erodent velocity was predicted in well agreement. Also the geometries of particle fragments matched well in terms of average circular diameter and roundness. Overall, the particle fragmentation was reasonably predicted using generated model. The second part of papers further verified the model developed for different process parameters such as; velocity, angle of attack and particle size on characteristics of erosion process. Increase in both velocity and angle of

attack resulted in more fragmentation of particle. However, with a particular kinetic energy, the numerical model predicted that smaller particles were most prone to fracture. The ratio of rebound and impacting velocity did not depend much on velocity at a given angle. The greater understanding of particle fragmentation provided by this study may have important applications in terms of assessing interference between incoming and rebound particles.

Vieira et al. [194] presented a comprehensive approach in modelling and computational fluid dynamics to determine erosion of material surface by sand particles entered in air. The predicted erosion values were compared with data available in past studies. The comparison exhibited good agreement in the values. Four correlations for erosion from literature were also studied and validated in simulations. Gnanavelu et al. [195] and Wang et al. [196] developed simulation model using computational fluid dynamics for prediction of slurry erosion behavior and erosion profile. The accuracy of this method was assessed by prediction of wear from further jet impingement tests under different flow velocities to that used to build the map and subsequently assessing against experiments. A good correlation between predicted and measured wear was observed. In general, the erosion profile generated under impact of jet of slurry resulted in 'W' shape.

2.6 Utilization of granite waste powder in various applications

The waste generated during industrial production of granite in recent times has observed harsh growth. These waste generated in different forms raised environmental issues related to disposal. Transportation of granite waste to recycling plants is also not economical. Granite powder is generated during cutting and grinding process of stone and when this powder gets mixed with water formed slurry waste. This results in generation of large amount of waste material. Nearly, 65% of the total production of granite is converted in to waste material in different forms. Due to restrictions imposed by government, the mining industries try to find gainful utilization of stone waste. Mostly, the prominent area of utilization of this granite waste powder is in construction industries such as; filler material for road construction, for manufacturing of bricks/tiles, soil stabilization and aggregate for concrete manufacturing. In addition to listed applications, fabrication and modification of thermo-set resin composites is also has potential for use of granite powder [197].

Rout et al. [198] and Rout and Satapathy [199] fabricated granite powder glass fiber reinforced polymer composites and characterized for mechanical and solid particle erosion performance. Granit powder is incorporated in to polymer composites up to 20 % by weight. The mechanical properties such as hardness tensile modulus and impact energy were

improved with addition of granite filler. However, negative hybridizing effect of granite powder was observed on tensile and flexural strength of composites. Improvement in solid particle erosion resistance was also reported. Filho and Neto [200] assessed performance of epoxy composite beams filled with granite under mechanical vibrations. Kareem [201] characterized properties of epoxy composites such as the thermal conductivity, thermal diffusivity, porosity and density as a function of weight fraction of granite. Ramakrishna and Rai [202] and Kareem [203] evaluated modification of the mechanical properties such as tensile, flexural, compressive strengths and impact strength with increase in filler content. Baskaran et al. [204] investigated thermal and thermo-mechanical analysis of polymer composite modified with granite as filler material. Thermo-gravimetric analysis illustrated higher thermal stability of composite material with incorporation of granite powder. Dynamic mechanical analysis showed improvement in storage modulus and glass transition temperature of composites filled with granite powder. Ramakrishna et al. [205] utilized granite powder particulate filler in epoxy composites in order to modify impact and compression strength. Comparative analysis for the properties demonstrated better performance of granite filled epoxy composites compared to unfilled composite.

In Civil Engineering and construction industries much study was conducted on utilization of granite waste. Singh et al. [206-208] presented exhaustive experimental study related to utilization of granite powder as replacement of fine aggregates in concrete. Concrete mixes were prepared with varying proportion of granite waste and river sand and performance of concrete blocks was assessed with characteristics such as strength, durability and workability. Performance of concrete blocks was assessed subjected to adverse exposure conditions such as acid attack, carbonization, sulphate attack, chloride penetration and elevated temperature. The results showed that 25 to 40 wt.% of river sand can be replaced by granite cutting waste. Torres et al. [209-211] studied the utilization of granite sludge waste in industrial porcelain tiles, ceramic floor tiles and roof tiles. The experimental results and their theoretical interpretation showed that suitable incorporation of granite sludge can result in porcelain tiles with superior properties, in terms of water absorption and bending strength. Sludge incorporation had negligible effect on density, shrinkage and plasticity during all stages of tile-production process, anticipating no modifications in the industrial production line. Granite sludge had a high content of total fluxing oxides that favor the maturation of the ceramic body at lower sintering temperatures. The results obtained concluded about the possibility of producing roof tiles incorporating 10 wt.% of granite wastes having excellent

properties (water absorption <6%, lower plastic deformation index, and bending strength values of about 14MPa and 38MPa for the green and sintered products, respectively).

2.7 Implementation of design of experiment (DOE) and optimization technique

Wear processes in composites are complex phenomena involving a number of operating variables and it is essential to understand how the wear characteristics of the composites are affected by different operating conditions [212-216]. Traditional experimental design required huge number of experimental runs to analyze the results. Hence, limitations on selection of operating conditions and their levels is always a major concern while doing research. The operating parameters were generally selected from past studies in the relevant area. But past studies are incompetent to provide the optimal testing parameters for the situation under investigation. A methodology for designing experiments was proposed by Ronald Fisher, in his innovative books: The *Arrangement of Field Experiments (1926)* and *The Design of Experiments (1935)*. Much of his pioneering work dealt with agricultural applications of statistical methods. In order to investigate effect of each factor on the performance variable, full factorial design may be beneficial. But factorial design has limitations on levels for each factor as number of experiments increases exponentially with increase in number of levels. If number of levels for factor is high the fractional design may be implemented in which some of the possible combinations are omitted.

Taguchi and Konishi [217] suggested the use of orthogonal arrays and Taguchi [218] devised an experiment design that applied signal-to-noise ratio with orthogonal arrays to the robust design of products and processes. In this procedure, the effect of a factor is measured by average results and therefore, the experimental results can be reproducible. Phadke [219], Wu and Moore [220] and others [221, 222] have subsequently applied the Taguchi method to design the products and process parameters. Erosion wear behavior of material includes effect of number of factors such as impingement angle, erodent velocity, erodent size, composition of material etc. The experiment was conducted using Taguchi orthogonal array of experiment design and significance of each factor was determined by using techniques like ANOVA, Genetic Algorithm, and Artificial Neural Network [62, 164-168, 171, 223, 224].

Development of new material generally encompasses series of composition which has to undergone different characterization methods according to end use. At the end of completion of all the experiments researches would deal with a matrix containing all developed alternatives along with obtained values of different tests. In order to obtain best alternative considering optimum performance against various attributes, use multi criteria

decision making (MDCM) technique is decisive. Amine et al. [225] emphasized on implementation of MCDM method when innovative concepts were introduced. Comparative analysis of six different MCDM techniques viz; weighed sum, weighted product, Kim & Lin, compromise programming, TOPSIS, and ELECTRE I, were studied for consistency of results, easy of understanding and adaption of decision type. The results illustrated that TOPSIS is the most consistent MCDM method for study under investigation.

2.8 The knowledge in earlier investigation

The exhaustive study of literature reveals that following knowledge gaps exist and need to be addressed in a systematic manner:

❖ Though much work has been reported on materials and manufacturing method of wind turbine blade, less has been reported comparative analysis unfilled and particulate filled natural and synthetic fiber reinforced polymer composite.

❖ Reports were available on use of conventional particulate filler materials in polymer composites but utilization of stone dust waste as particulate filler material for modifying material properties is scarily available.

❖ Much of research is available on solid particle erosion of polymer matrix composites but there is scarcity of literature on slurry erosion of fiber reinforced polymer composite in environment of jet containing sand particles along with water.

❖ It is hard to found past studies on numerical prediction of mechanical and erosion performance of polymer matrix composite together by use of simulation software.

❖ Mechanical and erosion performance of polymer matrix composite for wind turbine blade includes many performance defining criteria and use of statistical techniques to rank different classes of composites is fare. Though necessary to rank the different composite using multi criteria decision making method like technique for ordered of preference by similarity to ideal solution is rarely reported.

2.9 Objectives of this research work

It is thus clear that the effect of granite powder as filler material on mechanical and erosion wear performance for polymer matrix composite reinforced with natural and synthetic fiber has still remained a less studied area. It is felt that, a further study in this respect is needed particularly on the inclusion of granite powder both in view of the scientific understanding and commercial importance. Hence, the present work is undertaken to investigate

mechanical, thermo-mechanical, thermal and erosion wear characteristics of epoxy based hybrid composites. The objectives of the work are outlines as follows:

1. Fabrication of series of unfilled and granite powder filled fiber reinforced polymer composite materials.

2. To study the physical, mechanical and fracture characteristics of these particulate filled fiber reinforced polymer composites and also implementation of finite element simulation technique to predict the mechanical performance of wind turbine blade.

3. To characterize the thermo-mechanical and thermal conductivity of the unfilled and particulate filled fiber reinforced polymer composites.

4. To determine the slurry and dry erosion wear characteristics of the proposed polymeric composites in different operating conditions and at the end, Taguchi design of experiment technique is applied to calculate the experimental wear analysis of these composites.

5. Finally, Technique for order of preference by similarity to ideal solution (TOPSIS) method is followed to obtain best composite combination for wind turbine blade application by taking physical, mechanical and wear results in experimentally.

Chapter Summary

This chapter has provided

❖ A review of research works on various aspects of issues and challenges reported for fiber reinforced polymer composites for wind turbine blade.

❖ The knowledge gap in earlier investigations

❖ The objectives of the present work

The next chapter describes the materials and methods used for the fabrication of the Composites. Chapter also provides in-detail geometry, apparatus and procedure for physical, mechanical characterisation, thermal analysis, thermo-mechanical analysis and the erosive wear experimental planning using Taguchi method.

*****

<div align="right">

Chapter 3

MATERIALS AND METHODS

</div>

This chapter describes the raw materials and processing techniques used to fabricate the composites under this investigation. It includes the details of geometry, configuration and operating conditions as specified by standards under which mechanical, thermo-mechanical and thermal characterization has done. Chapter also explains the apparatus and test conditions for erosion wear analysis in both slurry jet and solid particle environment. The methodology for assessment of effect of different operating conditions on erosion wear is illustrated by Taguchi design of experiment (DOE) and analysis of variance (ANOVA). Finally, considering the mechanical and erosion wear properties ranking of composites under investigation has done applying multi criteria decision method.

3.1 Materials

3.1.1 Matrix Material

Matrix materials are of different types like metals, ceramics and polymers. The polymer matrices are most commonly used owing to its properties such as light weight, easy of fabricating complex shapes and ability to process with variety of reinforcements. Polymer matrices can be of two types: thermoplast and thermosets. The most commonly used thermosets are epoxy, polyester, vinylester and phenolics. Epoxy resin is the matrix material in the present investigation. Epoxy is a category of polymers which contain the epoxide functional group in their main chain. Epoxy resin can attach things together to itself, creating a strong bond. Epoxy resins are the most economical and widely used resin systems, especially in the FRP products for various applications. Epoxy resins can be formulated to obtain a wide range of properties ranging from soft and ductile to hard and brittle. Their advantages include low viscosity, low cost, and fast cure time. The properties of epoxy resin are [226]

1. Good adhesion to other material.
2. Good chemical and environmental resistance.
3. Good mechanical properties.
4. Good electrical insulating properties.
5. Low molecular weight of epoxy in liquid state gives them exceptionally high molecular mobility during processing. This property allows the liquid epoxy to quickly and thoroughly wet surfaces.
6. No byproduct during curing results in low shrinkage during hardening.

Due to several advantages over other thermoset polymer mentioned above epoxy (LY556) is used as matrix material for study. Its common name is Bishphenol-A-Diglycidyl-Ether. The hardener used with the epoxy has the designation HY-951. The epoxy resin and hardener are supplied by Huntsman Advanced Materials (India) Private Limited.

3.1.2 Fiber Material

In the proposed work, woven glass fibers, carbon fiber and jute fiber will be used as the reinforcing material in the composites under investigation.

Glass fiber: Glass is the most common fiber used in polymer matrix composites. Its advantages include its high strength, low cost, high chemical resistance and good insulating properties. The main types are E-glass (also called "fiber glass") and S-glass. E-glass fiber has an elastic modulus of 72.5 GPa and possess a density of 2.59 gm/cc.

Table 3.1 Properties of raw materials used

Property	Epoxy [59]	Glass fiber [227]	Carbon fiber [228]	Jute fiber [59]
Density, gm/cc	1.1	2.59	1.81	1.3
Ultimate tensile strength, MPa	--	521	4137	--
Elastic Modulus, GPa	3.42	72.5	242	55
Elongation at break, %	--	4.8	1.8	--

Carbon fiber: Carbon atoms are bonded together in crystals that are more or less aligned parallel to the long axis of the fiber to produce carbon fiber and this crystal alignment gives the fiber high strength-to-volume ratio. The amount of carbon percentage is 95% in carbon fiber; hence it has excellent mechanical properties. The properties of carbon fibers, such as high stiffness, high tensile strength, low weight, high chemical resistance, high temperature tolerance and low thermal expansion, make them very popular in aerospace, civil engineering, military, and motorsports, along with other competition structural applications. The sized glass fibers and carbon fibers are supplied by Hindoostan Technical Fabric Limited, Mumbai (India).

Jute Fiber: Jute is a long, soft, shiny vegetable fiber, collected from local market. The fibers are washed with normal water to remove dirt present on it and air dried at 25-30°C for 24 hrs. Then, fibers are immersed for 1 hr in solution of 5 wt.% NaOH with distilled water. After,

treated fibers are washed with distilled water to remove excess NaOH solution. Then, fibers are dried at 70ºC for 8 hrs and followed by vacuum (700-760 mm of Hg) dried at 60 ºC for 2 hrs. etc. The properties of raw materials are indicated in Table 3.1.

3.1.3 Particulate Material: granite powder

Granite is an igneous rock, with feldspar, quartz and mica as major components. Granite rejects produced in the cutting process of igneous stones are becoming a worrying factor for industry owners and environmentalists. After quarrying from the mines for every 20 mm thick slate of granite, 5 mm granite is converted in to fine powder. The granite powder produced from cutting and processing units show non-plastic behavior which results in comparable hardness with conventional ceramic filler material. Granite has silicone oxide as large fraction of total weight which increases hardness of granite as compared to marble dust [229]. The filler material used in present study is granite powder (density- 2.62gm/cm^3) collected from granite mines in the Jalore district, Rajasthan (India). The granite powder is sieved to obtain the particles between 80 to 100 µm. The chemical composition of granite powder is given in the Table 3.2

Table 3.2 Chemical compositions of Granite powder

Constituent	SiO$_2$	Al$_2$O$_3$	Fe$_2$O$_3$	LOI
%	71.59	15.03	5.96	5

3.2 Composite designation

As the literature review illustrated that the material used for wind turbine blade manufacturing based on the capacity of wind mill. The polymer composite materials used for wind turbine blade manufacturing are reinforced with synthetic fibers (such as carbon and glass fiber) for small to large wind mill and natural fibers for micro and mini wind mills. The composites under this investigation for this study are designated as shown in Table 3.3 to table 3.5

3.3 Composite fabrication

Fiber reinforced epoxy resin composites have been fabricated by conventional hand-lay-up techniques in five different weight proportions (i.e 10 wt.%, 20 wt.%, 30 wt.%, 40 wt.% and 50 wt.%) as mentioned in Table 3.6 to 3.8. After that three different weight percentages of mining waste like granite powder (8 wt.%, 16 wt.% and 24 wt.%) filled fiber reinforced epoxy composites are fabricated by keeping 40 wt.% fiber loading constant subsequently in all the particulate filled composites.

Table 3.3 Composition of glass fiber reinforced composite

Designation	Composition
EG10	Epoxy + 10 wt% glass fiber
EG20	Epoxy + 20 wt% glass fiber
EG30	Epoxy + 30 wt% glass fiber
EG40	Epoxy + 40 wt% glass fiber
EG50	Epoxy + 50 wt% glass fiber
EGG8	Epoxy + 40 wt% glass fiber + 8 wt% granite powder
EGG16	Epoxy + 40 wt% glass fiber + 16 wt% granite powder
EGG24	Epoxy + 40 wt% glass fiber + 24 wt% granite powder

Table 3.4 Composition of carbon fiber reinforced composite

Designation	Composition
EC10	Epoxy + 10 wt% carbon fiber
EC20	Epoxy + 20 wt% carbon fiber
EC30	Epoxy + 30 wt% carbon fiber
EC40	Epoxy + 40 wt% carbon fiber
EC50	Epoxy + 50 wt% carbon fiber
ECG8	Epoxy + 40 wt% carbon fiber + 8 wt% granite powder
ECG16	Epoxy + 40 wt% carbon fiber + 16 wt% granite powder
ECG24	Epoxy + 40 wt% carbon fiber + 24 wt% granite powder

Table 3.5 Composition of jute fiber reinforced composite

	Composition
EJ10	Epoxy + 10 wt% jute fiber
EJ20	Epoxy + 20 wt% jute fiber
EJ30	Epoxy + 30 wt% jute fiber
EJ40	Epoxy + 40 wt% jute fiber
EJ50	Epoxy + 50 wt% jute fiber
EJG8	Epoxy + 40 wt% jute fiber + 8 wt% granite powder
EJG16	Epoxy + 40 wt% jute fiber + 16 wt% granite powder
EJG24	Epoxy + 40 wt% jute fiber + 24 wt% granite powder

In the present study, granite powder is thoroughly dispersed in the matrix material using Digital Sonicator (Q-700-200, Qsonica, Newton, USA)) for homogeneity concerned. The low temperature curing epoxy resin and corresponding hardener are blended in a ratio of

10: 1 by weight as recommended by supplier and available literature. The mixing is done meticulously before the jute-fiber mats are reinforced in the matrix body.

Fiber mats are cut in the dimension of 400mm × 400mm and the wooden mould of 410 ×410×40 mm^3 is used for fabrication of the composites under investigation. The composite slabs are fabricated by conventional hand lay-up method followed by light compression molding technique. Easy release of composite from mould after curing is assured by applying releasing agent (Silicon spray). For granite powder filled epoxy composites care is taken to ensure a uniform sample since solid particles have a tendency to clump and tangle together when mixed. The curing of composites is takes place under a load of 25 kg for 24 hrs before removed from the mould. Then, these composite slabs are post-cured in the air for another 24 hrs after removed out of the mould. For testing, specimens of size specified by respective standard are cut from the prepared composite slabs using diamond cutter. Uniformity and homogeneity of the composite is maintained with utmost care during fabrication of composite materials.

3.4 Physical and Mechanical characterization

3.4.1 Hardness

Hardness measurement is done using a Vicker hardness tester (Walter Uhl, Ablar, Germany) confirming to standard ASTM E384. A diamond indenter, in the form of a right pyramid with a square base and an angle 136° between opposite faces, is forced into the material under a specified load. The two diagonals X and Y of the indentation left on the surface of the material after removal of the load are measured and their arithmetic mean L is calculated and Vickers hardness number is calculated using the following equation.

$$H_v = 0.1889 \ \frac{F}{L^2} \qquad\qquad\qquad 3.1$$

where,

$$L = \frac{X+Y}{2} \qquad\qquad\qquad 3.2$$

where, F is the applied load (N), L is the arithmetic mean of diagonals of square impression (mm), X is the horizontal length (mm) and Y is the vertical length (mm) of square impression.

3.4.2 Density and void fraction

The theoretical density of composite materials in terms of weight fraction can easily be obtained as for the following equations given by Agarwal and Broutman [230].

$$\rho_{ct} = \frac{1}{W_f/\rho_f + W_m/\rho_m} \hspace{4cm} 3.3$$

where, W and ρ represent the weight fraction and density respectively. The suffix *f, m* and *ct* stand for the fiber, matrix and the composite materials respectively.

The composites under this investigation consists of three components namely matrix, fiber and particulate filler. Hence, the modified form of the expression for the density of the composite can be written as

$$\rho_{ct} = \frac{1}{W_f/\rho_f + W_m/\rho_m + W_p/\rho_p} \hspace{3cm} 3.4$$

Where, the suffix 'p' indicates the particulate filler materials.

The actual density (ρ_{ce}) of the composite, however, can be determined experimentally by Archimedes' Principle. The volume fraction of voids (V_v) in the composites is calculated using the following equation:

$$V_v = \frac{(\rho_{ct} + \rho_{ce})}{\rho_{ct}} \hspace{4cm} 3.5$$

3.4.3 Tensile strength and tensile modulus

The tensile test for fiber reinforced polymer composite is generally performed on flat specimens. The dimension of the specimen is 250 mm ×25 mm × (2.5 - 5) mm according to standard test method for tensile properties of fiber reinforced polymer composites ASTM D3039. Thickness varies from 2.5 mm to 5mm, because for unfilled fiber reinforced epoxy composite the fiber loading taken in this present investigation are 10 wt.%20 wt.%, 30 wt.%, 40 wt.% and 50 wt.%.

In case of stone dust filled fiber reinforced epoxy composites the length and width is same as the unfilled composites, whereas the thickness will be 4mm for all the particulate filled composites. During the test a uniaxial load is applied through both the ends of the specimen at a crosshead speed of 2mm/min. The tensile test is performed in the universal testing machine and results are analyzed to calculate the tensile strength of composite samples. The pictorial view of universal testing machine is shown in Figure 3.1.

3.4.4 Flexural and Inter-Laminar Shear Strength

The short beam shear tests are performed on the composite samples at room temperature to evaluate the flexural strength and inter-laminar shear strength (ILSS). It is a 3- point bend test, which generally promotes failure by inter-laminar shear.

Figure 3.1 Universal Testing Machine

The SBS test is conducted as per ASTM standard **(D2344)** using the universal testing machine same as used for tensile testing. The configuration and loading arrangement for short beam strength test is shown in Figure 3.2. The dimension of the specimen is 40 mm ×10 mm × (2.5 - 5) mm and test is conducted at crosshead speed of 1mm/min. The flexural strength and flexural modulus of specimen is calculated using eqs. 3.6 and 3.7 [72] respectively. The inter-laminar shear strength (ILSS) is determined using following eq. 3.8 [231].

$$F\,S = \frac{3PL}{2bt^2} \qquad\qquad\qquad 3.6$$

$$F\,M = \frac{L^3m}{4bt^3} \qquad\qquad\qquad 3.7$$

$$ILSS = \frac{3P}{4bt} \qquad\qquad\qquad 3.8$$

where, P – maximum applied load, L – support span, m – slope of tangent, b – width of specimen, t – thickness of specimen.
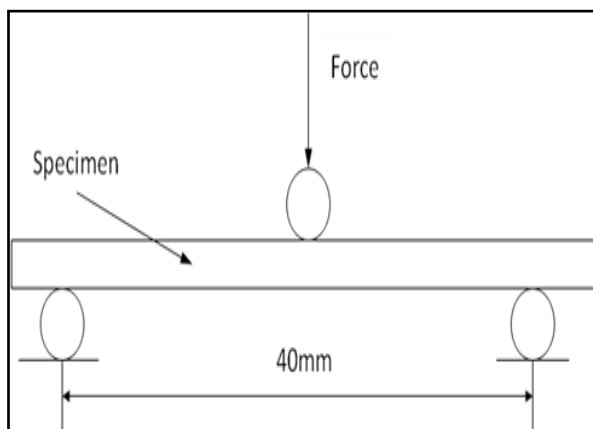
a   b

Figure 3.2 Configuration for flexural test

3.4.5 Impact strength

Impact test of unfilled and granite powder filled epoxy composites are conducted on pendulum type impact testing machine as per ASTM D256 (see Figure 3.3). The standard size of specimen for ASTM D256 is 63.5mm × 12.7mm × (2.5 – 5) mm with 'V' notch at the centre of length. In this test method the notch produces a stress concentration that increases the probability of a brittle, rather than a ductile, fracture. The specimen is held as a vertical cantilever beam and is broken by a single swing of the pendulum. The line of initial contact is at a fixed distance from the specimen clamp and from the centerline of the notch and on the same face as the notch.
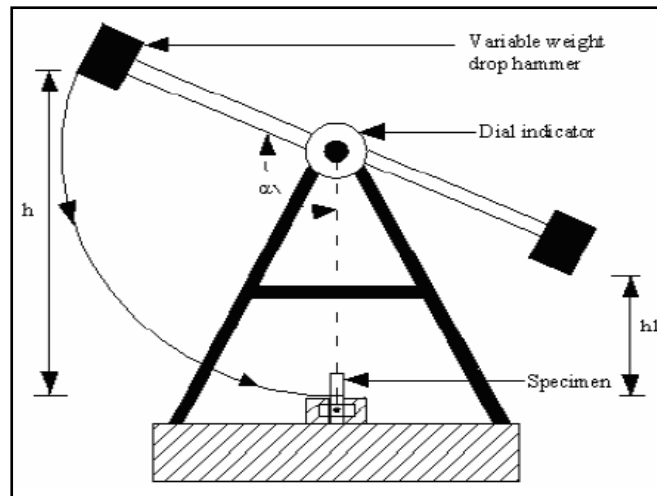
Figure 3.3 Schematic of apparatus for impact tester

3.4.6 Fracture toughness analysis

Fracture toughness (K_{IC}) is evaluated in crack opening mode (mode-I) using Universal testing machine same as used for tensile testing in single end notch bend (SENB) test configuration confirming to ASTM D5045. The test is conducted on specimen of 40 mm×10mm×(2.5 - 5) mm at cross head speed of 1 mm/min with different ratio of crack length to height of specimen (a/W) as 0.1, 0.3 and 0.5 respectively (see Figure 3.4a). The fracture toughness is calculated using eqs. 3.9 and 3.10 [ASTM D5045]. Figure 3.4b illustrates the pictorial view of specimen simply supported on rollers. All the mechanical tests are conducted on three specimens to get replicas and mean value of the result is reported.

$$K_{IC} = \frac{F}{B.W^{1/2}}.f\left(\frac{a}{W}\right) \qquad \text{with } 0 < \frac{a}{W} < 1 \qquad\qquad 3.9$$

$$f\left(\frac{a}{W}\right) = 6\left(\frac{a}{W}\right)^{1/2} \left\{ \frac{\left[1.99 - \frac{a}{W}\left(1 - \frac{a}{W}\right)\left(2.15 - 3.93\frac{a}{W} + 2.7\left(\frac{a}{W}\right)^2\right)\right]}{\left(1 + 2\frac{a}{W}\right)\left(1 - \frac{a}{W}\right)^{3/2}} \right\} \qquad 3.10$$

where, F – maximum force; B – width of the specimen; a – crack length; W – height of the specimen.

a   b
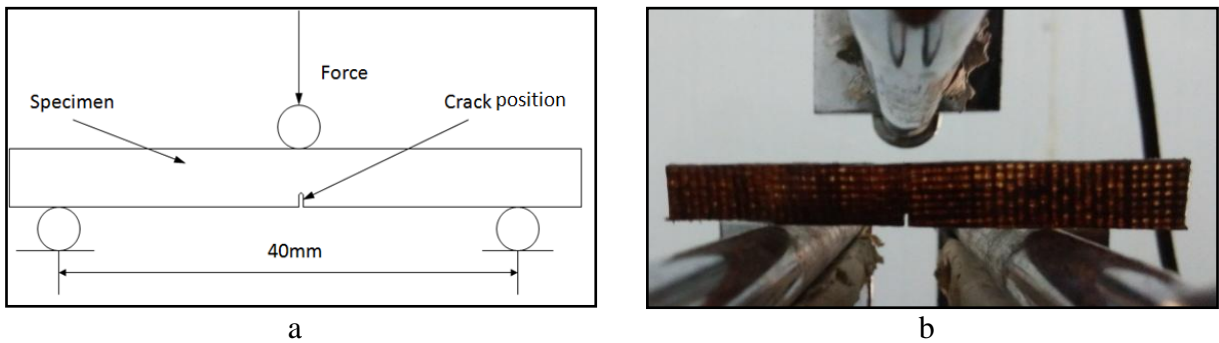
Figure 3.4 Configuration for fracture toughness test in mode I
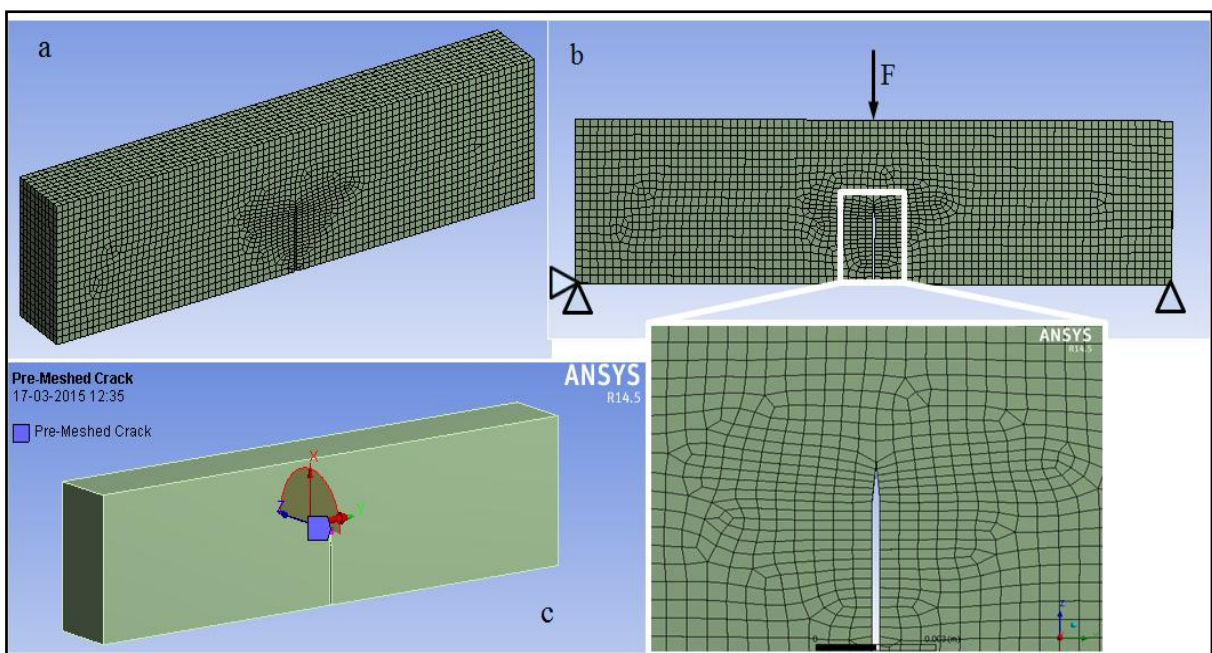
Figure 3.5 Finite element model for fracture test a) 3D model b) boundary condition and mesh at crack c) position of pre-meshed crack

Finally, ANSYS finite element code is used for numerical computations of fracture toughness of the unfilled and particulate filled polymer composites. Crack propagation and crack arrest can be predicted using finite element codes [232]. The three-dimensional finite element model of 3P- bend test is generated according to geometry of specimen in order to predict the stress intensity factor range during Mode I fracture test (see Figure 3.5a). The unfilled and granite powder filled glass epoxy composite model is treated as homogeneous isotropic material. The mesh density is generated using adaptive smart size to mesh menu. The finite element model of the proposed composite is formed with 83658 nodes and 18550 elements respectively. The finite element mesh and boundary conditions used in the analysis are shown in Figure 3.5b. The force 'F' is applied till the stress value at the environ of crack

tip reached to the ultimate tensile stress of concerned composite material. The nodes on the crack edge are assigned as pre-meshed crack as shown in Figure 3.5c. The stress intensity factor is calculated along the crack edge using interaction integral method [233].

3.5 Thermal and thermo-mechanical analysis

3.5.1 Dynamic Mechanical Analysis (DMA)

Thermo-mechanical properties of composite are obtained by performing dynamic mechanical analysis (DMA). The unfilled and granite powder filled glass epoxy composite are subjected to DMA in three point bending mode using dynamic mechanical analyzer (Perkin Elmer 8000, Waltham, Massachusetts, USA) confirming to ASTM D4065. The test configuration for DMA is shown in Figure 3.6a with specimen size of 25 mm×12 mm ×(2.5 − 5) mm. DMA is conducted in atmospheric environment at a fixed frequency of 1 Hz, with heating rate of $2°$C/min and for temperature range of 25 to $140°$C. Furthermore, the bonding characteristics of unfilled and granite powder filled fiber reinforced epoxy composite is evaluated using two parameters viz; adhesion efficiency factor (A) and reinforcement effectiveness coefficient (C) using eqs.3.11 and 3.12 [118],

$$A = \frac{1}{1 - W_f} \frac{\tan\delta_c}{\tan\delta_p} - 1 \qquad\qquad 3.11$$

$$C = \frac{\left(\frac{E'_g}{E'_r}\right) \text{ composite}}{\left(\frac{E'_g}{E'_r}\right) \text{ resin}} \qquad\qquad 3.12$$

where, W_f is the fiber weight fraction, $\tan\delta_c$ and $\tan\delta_p$ are the damping factor of the composite and polymer matrix respectively at a given temperature and E'_g and E'_r are the storage modulus values in the glassy (at $30°$C) and rubbery (at $140°$C) regions, respectively. The degree of homogeneity of polymeric composite material may be determined by Cole–Cole plot. Cole–Cole plot represents the relationship between the loss modulus (E″) and the storage modulus (E′). These plots study the structural changes that occurred in polymers after inclusion of reinforcement [234]. The pictorial view of dynamic mechanical analyzer is shown in Figure 3.6b.

3.5.2 Thermo-Gravimetric Analysis (TGA)

Thermo-gravimetric analysis (TGA) is a method to determine the loss of weight in a material with respect to increase in temperature under a controlled atmosphere and also determine the thermal stability of material. In general, the thermal analysis for the material is carried out in order to evaluate the chemical, physical and structural changes are occurring in a material,

under an imposed change in temperature. TGA is conducted using thermo-gravimetric analyzer (Perkin Elmer STA 6000, Waltham, Massachusetts, USA) (see Figure 3.7) to determine the mass loss of composite with the increase in temperature range from 30 to 500°C confirming to ASTM E1131. Thermo-gravimetric analysis is carried out on 10 – 20 mg of composite sample at a heating rate of 20 °C/min. The samples are subjected to heating in TGA in presence of high purity nitrogen under a constant flow rate 20 ml/min.

a   b
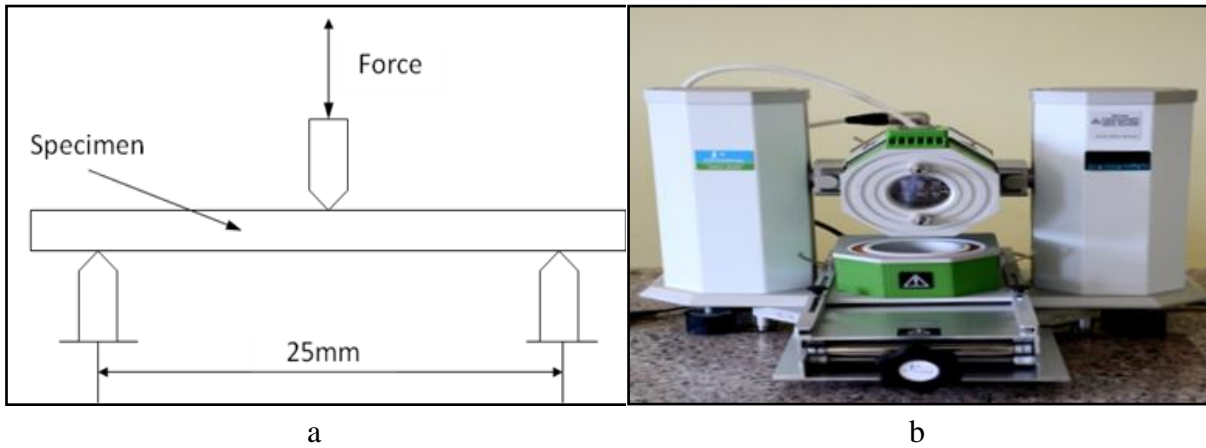
Figure 3.6 DMA in 3P bend mode a) Geometric configuration, b) pictorial view of apparatus

Figure 3.7 Pictorial view of TGA

a   b
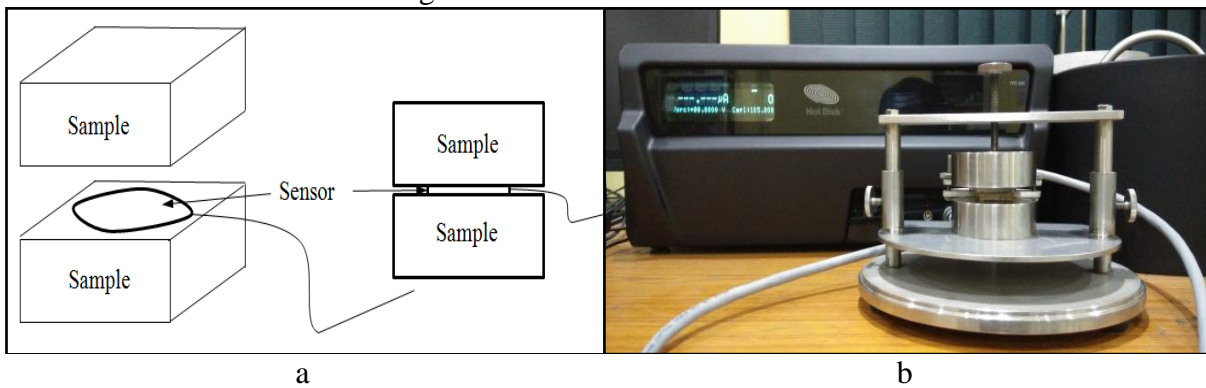
 Figure 3.8 Configuration for measurement of thermal conductivity of composite a) schematic diagram b) actual set up of Hot Disk TPS 500

3.5.3 Thermal conductivity

Thermal conductivity of composites is measured by hot disk method using thermal constant analyzer (Hot Disk TPS 500, Gothenburg, Sweden) according to ISO 22007-2. In order to match the instrument the samples are prepared in size of 25 mm×25 mm surface area with at least 2 mm thickness. When performing measurement, a plane Hot Disk sensor is placed between two pieces of samples. The thermal conductivity is measured by flow a known electrical power through the samples and recording increase in temperature as function of time. The test configuration and the pictorial view of the conducting setup are shown in Figure 3.8a and 3.8b respectively.

Table 3.6 Thermal conductivity of different constituent

Material	Epoxy [235]	Glass fiber	Jute fiber [237]	Carbon fiber [238]	Granite powder [239]
Thermal Conductivity (W/m-K)	0.154	1.3	0.04	7.81	2.68

The thermal conductivity of polymeric material can be predicted by numerical technique using finite element codes [235]. The thermal conductivity analysis is carried out for the conductive heat transfer through the composite body using the 2D finite element program ANSYS R14.5. The 2D geometrical model is generated using ANSYS design modeler. In the finite element analysis parameters of all materials are assumed to be isotropic, homogenous and temperature independent. The thermal conductivities of epoxy, glass fiber, jute fiber, carbon fiber and granite filler is given in the Table 3.6. The applied boundary conditions on the geometric model are shown in Figure 3.9. Two opposite sides are assumed to be perfectly thermally insulated. From either of the two remaining sides, heat flux of 10 W/m^2 is applied whereas other side is made as convective boundary. The temperature difference along the thickness is recorded from the obtained temperatures contours. The number of nodes and element formed the finite element geometry varies from 4385 nodes and 1318 elements to 31827 nodes and 9436 elements for various composites. The experimental and numerical value of thermal conductivity is compared with theoretical models available viz; series, parallel and geometric mean model (GMM) [236].
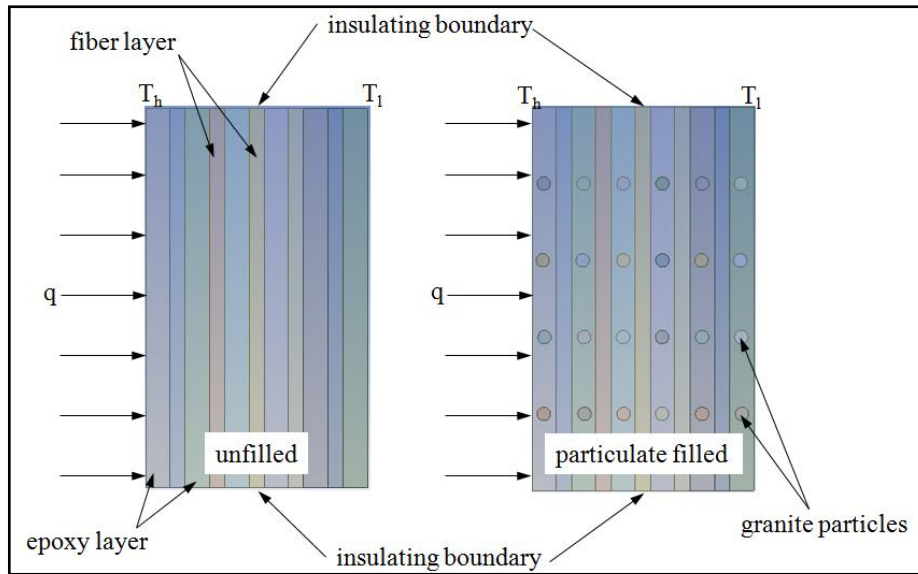
Figure 3.9 Finite element model boundary conditions for thermal conductivity

3.6 Erosion wear Analysis

3.6.1 Slurry erosion studies

Apparatus and test conditions for slurry jet erosion wear test. The slurry jet erosion wear test is carried out according to ASTM standard G-73 using slurry jet erosion tribometer (Ducom 411, Bangalore, India) as shown in shown in Figure 3.10a. The schematic diagram of slurry jet erosion tribometer is shown in Figure 3.10b. The test setup is consisting of the following units, one is mixing chamber where both the slurry as well the water is mixed together, a nozzle valve with internal diameter 3mm, a sample holding device (sample holder) and an angle plate where the sample can be kept in different angle along the slurry jet direction.
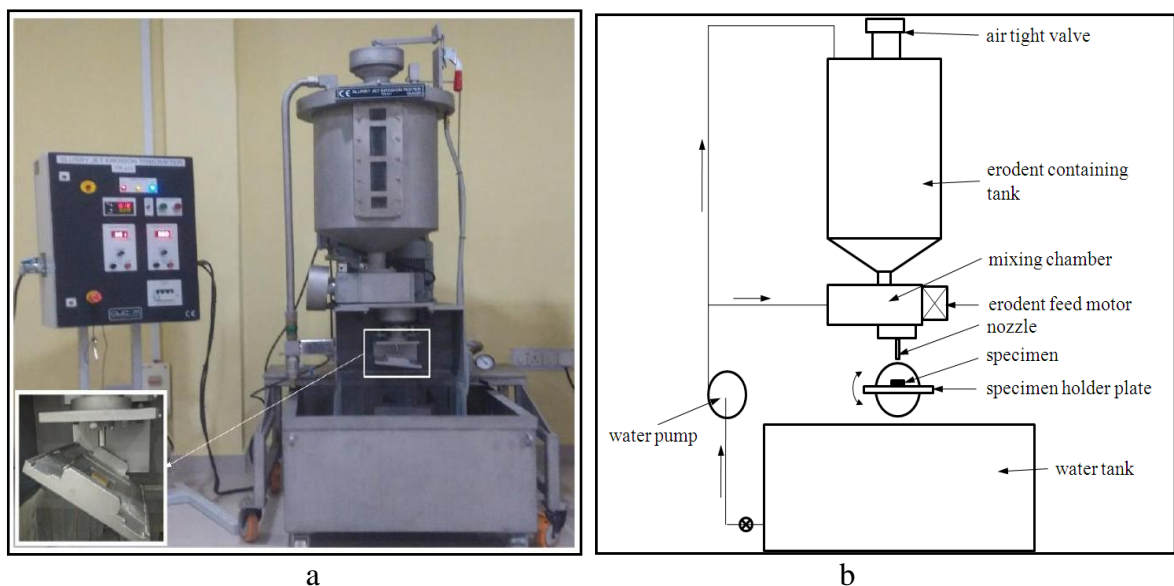
Figure 3.10 Slurry jet erosion tribometer a. Pictorial view-make DUCOM – TR411, b. Schematic diagram

The velocity of slurry flow ejected from the exit of nozzle is varying from 10 m/s to 40m/s. The stand-off distance between the sample surfaces to the nozzle tip is 50mm. The impingement angle is varies from 30° to 90° respectively in an interval of 15° and in each test the sample is wet-grounded by 700 grid abrasive papers, washed in clean water and finally after drying weighted using an analytical weighing balance with an accuracy of 0.01mg. After weighing of each sample before and after test the mass loss is calculated in terms slurry erosion rate. The same test is repeated three times to ensure the reproducibility of the results. The erodent material used in the present study is silica sand whose discharge is maintained constant for 160 g/min. The square samples of 25mm × 25mm are cut from the composite slab for slurry erosion wear test. The fixed parameters and control factors for slurry jet erosion test are depicted in Table 3.7. Finally, the eroded samples are analyzed by using scanning electron microscope (SEM) to know the wear damage mechanism in different magnifications.

Table 3.7 Parameters for slurry jet erosion test

Control Factor	Symbol	Fixed parameter	
Impact velocity	Factor A	Erodent	Silica sand
Fiber/Filler loading	Factor B	Erodent feed rate (gm/min)	160 gm/min
Impingement angle	Factor C	Carrier fluid	Water
Erodent size	Factor D	Test temperature	RT
		Nozzle diameter (mm)	3 mm

3.6.2 Solid particle erosion studies

Apparatus and test conditions for slurry jet erosion wear test.

The solid particle erosion tests are conducted using equipment (Ducom TR 471, Bangalore, India) containing facility to mix particles with compressed air and passed through nozzle confirming to ASTM D76. Pictorial view of equipment is shown in Figure 3.11a. The solid particles are fed from hopper and the mass flow rate is controlled by velocity of conveyor belt. The conveyor belt drops the particle in the stream of air and carried with the stream through nozzle of 1.5 mm diameter to hit the target material. The velocity of erodent ejected from the exit of nozzle is varying from 30 m/s to 75m/s. The stand-off distance between the sample surfaces to the nozzle tip is 10mm. The impingement angle is varies as 30°, 45°, 60°, 75° and 90° respectively. The erodent material used in the present study is silica sand whose discharge is maintained constant for 2g/min. The square samples of 25mm × 25mm are cut

from the composite slab for slurry erosion wear test. The fixed parameters and control factors for slurry jet erosion test are depicted in Table 3.8.

Table 3.8 Parameters for solid particle erosion test

Control Factor	Symbol	Fixed parameter	
Impact velocity	Factor A	Erodent	Silica sand
Fiber/Filler loading	Factor B	Erodent feed rate (gm/min)	2 gm/min
Impingement angle	Factor C	Carrier fluid	Air
Erodent size	Factor D	Nozzle diameter (mm)	1.5 mm
Environment temperature	Factor E		
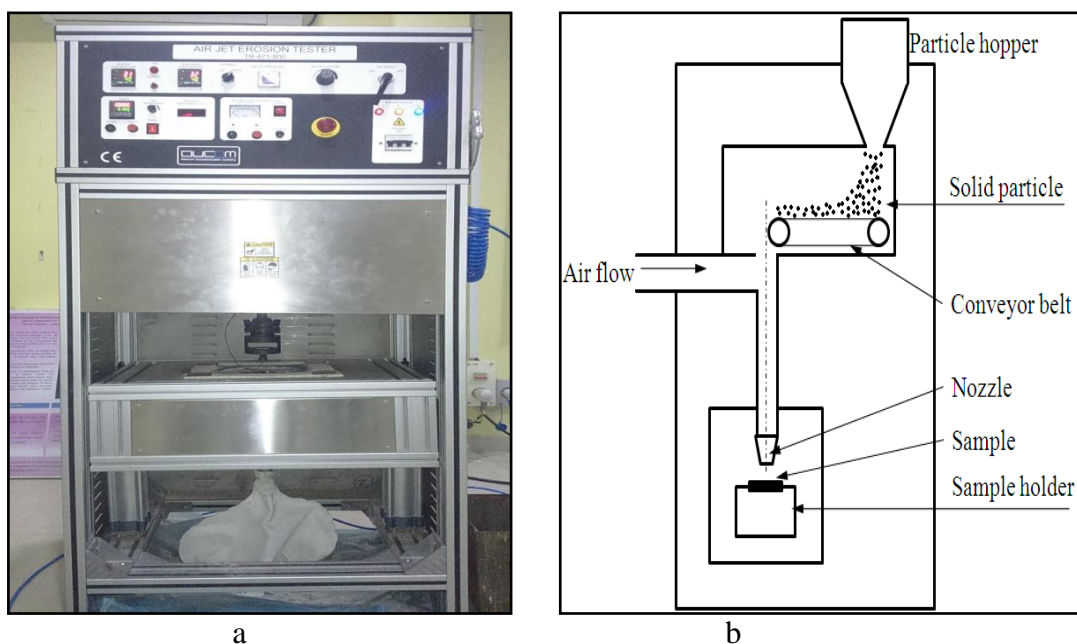
Figure 3.11 Solid particle erosion tribometer a. Pictorial view-make DUCOM – TR 471, b. Schematic diagram

3.6.3 Design of Experiments

Taguchi technique is a powerful tool for design of high quality systems based on orthogonal array experiments that provide much-reduced variance for the experiments with an optimum setting of process control parameters. It introduces an integrated approach that is simple and efficient to find the influence of process parameters on performance on the system with possible minimum number of experiments. From a scientific viewpoint, this is a tool for analyzing the sensitivity of output for the particular input parameter. The investigator needs to know the parameters involved, the range of these parameter, the levels assigned to each factor as well as a method to estimate and quantify the response of each factor. The design of experiments is a scientific approach to effectively plan and perform experiments, using

statistics. In such designs, the combination of each factor at every level is studied to determine the combination that would yield the best result [140]. Selection of control factors is an important stage of Taguchi applications and design of the factors and it is generally set by experimenter's experience. Erosion rate is governed by large number of control parameters such as impact velocity, impingement angle, fiber loading, filler content, erodent size, stand-off distance, erodent discharge rate, temperature etc [241, 242]. Of course it is necessary to explain that these factors are selected not only in order to reach best erosion wear resistant of composite material but also to optimize conditions for minimum erosion rate. Four combinations of control factors (levels) were selected for each of the studied factors. The selected control factors for slurry jet erosion and solid particle erosion along with their levels are presented in Table 3.9 and 3.10 respectively. In this study, L_{16} orthogonal array experiment design as shown in Table 3.11 is implemented to determine the influence of control parameter on erosion wear rate.

Taguchi's method uses a statistical measure of performance called signal-to-noise ratio (S/N), which is logarithmic function of desired output to serve as objective functions for optimization. The S/N ratio considers both the mean and the variability into account. The ratio of the mean (signal) to the standard deviation (noise) is defined as S/N ratio. Considering smaller is better characteristic, S/N ratio for minimum erosion rate can be calculated as logarithmic function of the loss function as shown below (eq. 3.13).

Lower is the better characteristic:

$$\frac{S}{N} = -10\log\frac{1}{n}\left(\sum_{i=1}^{n}(y_i^2)\right) \qquad\qquad 3.13$$

where, n is the number of observations, and y_i the observed data [219, 240]. "Lower is better" (LB) characteristic is suitable for minimizations of slurry erosion rate. The experimental results were analyzed using commercial software MINITAB, which is used in design of experiment applications.

Table 3.9 Levels of variables used in slurry jet erosion test

Control factor	Level				Unit
	I	**II**	**III**	**IV**	
A: Impact velocity	10	20	30	40	m/s
B: Fiber loading	10	20	30	40	wt.%
B: Filler content (granite powder)	0	8	16	24	wt.%
C: Impingement angle	30	45	60	75	Degree
D: Erodent size	100	175	250	325	μm

Table 3.10 Levels of variables used in solid particle erosion test

Control factor	Level				Unit
	I	**II**	**III**	**IV**	
A: Impact velocity	10	20	30	40	m/s
B: Fiber loading	10	20	30	40	wt.%
B: Filler content (granite powder)	0	8	16	24	wt.%
C: Impingement angle	30	45	60	75	Degree
D: Erodent size	50	100	150	200	μm
E: Environment temperature	25	35	45	55	℃

Table 3.11 Experimental design using L_{16} orthogonal array for erosion behavior analysis

$L_{16}(4^5)$ Expt. no.	**1** A (Impact velocity)	**2** B (Fiber/ filler content)	**3** C (Imping-ement angle)	**4** D (Erodent size)	**5** E (Temperature)*
1	1	1	1	1	1
2	1	2	2	2	2
3	1	3	3	3	3
4	1	4	4	4	4
5	2	1	2	3	4
6	2	2	1	4	3
7	2	3	4	1	2
8	2	4	3	2	1
9	3	1	3	4	2
10	3	2	4	3	1
11	3	3	1	2	4
12	3	4	2	1	3
13	4	1	4	2	3
14	4	2	3	1	4
15	4	3	2	4	1
16	4	4	1	3	2

* indicate dummy column in case of slurry jet erosion experiments

3.6.4 Numerical approach for slurry erosion behavior

Zhu et al. [20] and Bozzini et al. [21] utilized FLUENT code in the computation of erosion in multiphase flow in various geometries. In present article, erosion process of the test sample is numerically simulated under the multiphase flow of water/air and sand particles using commercially available CFD package, Fluent (ANSYS Inc.). The steady-state isothermal analysis is studied through following steps: (a) solving the continuous phase (water/air) flow; (ii) injecting the discrete phase (sand particle) at required velocity and flow rate; (iii) solving of the coupled flow and particle trajectories and (iv) tracking of the discrete phase. Details of numerical approaches are shown in the following subsections.

Computational models

The present investigation is performed by adopting 3-D mesh for the entire domain, an implicit method for the numerical solution of mass and momentum equations and a ReNormalizatio Group (RNG) $k - \varepsilon$ model for the turbulence. Multiphase flow is simulated using the Eulerian-Lagrangian approaches that involve the liquid water/dry air and sand particles. Simulation of a discrete phase in a Lagrangian frame of reference was assured by Discrete Phase Model (DPM). The fluid phase (water/air) is considered as a continuum phase, while the discrete phase is simulated by tracking the particles through the flow field. The RNG k-ε turbulent model is used to efficiently create the turbulence of the fluid flow in the region close to the wall, as well as in the region far from the wall. Erosion/accretion model is used to evaluate the erosion rate and erosion pattern on the sample surface. The model available in the FLUENT code for the calculation of the erosion rate is a simplified model taking into account the mass flow rate of the erodent particles, the surface area of the impacted erosion wall and function of impact angle. The erosion rate is determined by computational tool in terms of mass of material removed per unit area per unit time.

Geometry model

The geometry model of the domain including test samples and nozzle used in the simulation is generated according to the experimental condition using commercial ANSYS Geometric Modeling software. The 3D geometric model is discretized using adaptive mesh technique. Computational domain and geometry model details of test sample for impingement angle $90^{°}$ are shown in Figure 3.12. In agreement with FLUENT the geometrical entities are defines as inlet, outflow and erosion wall. The geometry can be modified to have specimen at impingement angle of 30°, 45°, 60° and 75° respectively. Discrete phase sand particles are approximated as spherical in shape. The sand particles are injected from nozzle (defined as inlet) with required velocity and flow rate. At inlet to the domain the boundary condition is applied as velocity inlet in FLUENT. The particle stream post impact on the erosion wall is defined as wall-jet with respect to the hitting direction on the wall. The exit of particles is assured by defining the outflow as pressure outlet.

3.7 Numerical analysis of wind turbine blade for static loading

The wind turbine blade consists of three parts such as root, mid span and tip section as shown in Figure 3.13. The shell of blade is of aerofoil section which is tapered and twisted from root to tip. The hub of the blade is cylindrical section which connects to the rotor of wind turbine [243]. The purpose of using numerical analysis in this work is to correlate the experimentally observed mechanical properties of test coupons with the static behavior of blade structure. In

present investigation, blade for wind turbine with capacity of 5 kW is under consideration. The aerofoil profile of NACA 4412 is generated using NACA coding and used throughout the length of blade from root to tip. The geometrical specifications of blade are, blade length= 2500 mm, root chord length= 330 mm, tip chord length= 130 mm, hub diameter= 67.5 mm, root to hub length= 300 mm respectively [14].
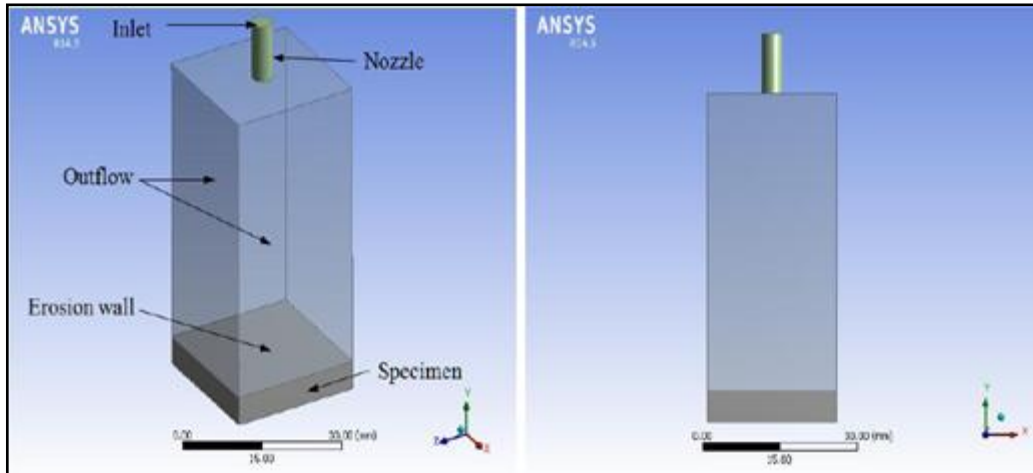
Figure 3.12 Computational domain and geometric model of test sample
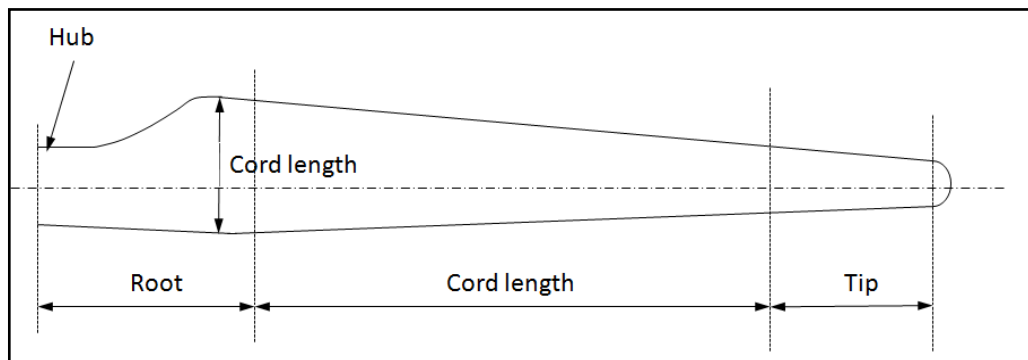
Figure 3.13 A typical blade plan and region classification
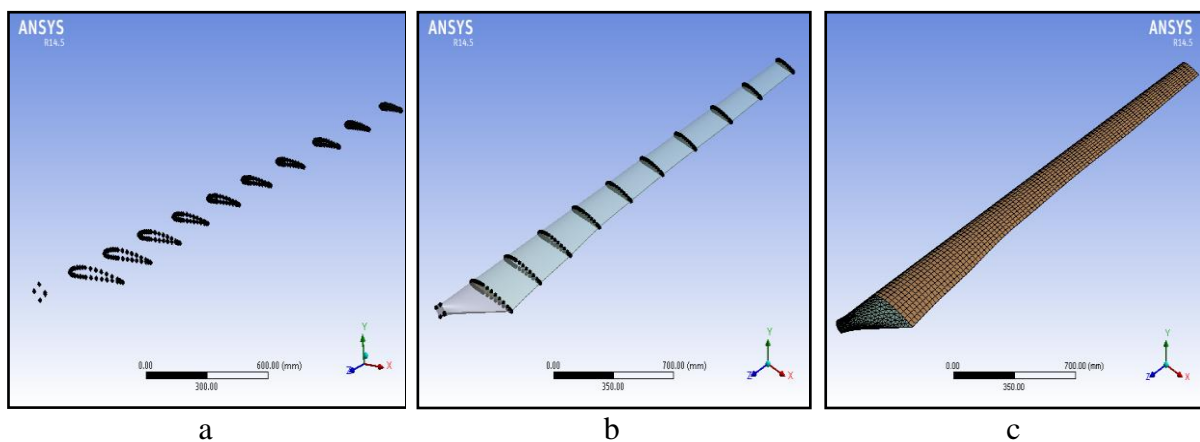
Figure 3.14 Stages of model generation and meshing a) profile points along the length, b) model generated from profile points, c) mesh generated for model

Profile points at ten sections along the length of the blade are calculated according to NACA 4412 profile. Profile points are generated and joined using ANSYS R14.5 design modeler and converted into surfaces. These surfaces are further lofted to generate solid geometrical model of blade. The complete blade is discretized into 78588 nodes and 41698 elements using adaptive meshing standard. The stages of model generation are shown in Figure 3.14. The material properties obtained from experimental results of test coupons are assigned to the geometric model as homogeneous isotropic. All the six degrees of freedom at the hub section of blade are constrained in this analysis. The composite blades are subjected to various combinations of loadings including aerodynamic loads, axial force and centrifugal force. The response of blade is recorded for wind speed of 10 m/s specifying the total force of 512 N acting on the blade for flap-wise bending [14].

3.8 Optimization of physical, mechanical and erosion wear behavior of the composites using TOPSIS method

Reinforcement of strong fiber in epoxy resin resulted in composite material with higher specific mechanical properties but it may not lead to erosive wear resistant material alone. Along with fiber, addition of ceramic particulate fillers resulted in to improvement in erosion wear resistance but may have adverse effect on weight and mechanical performance of composite. At same time it is necessary to obtain best composite material with excellent mechanical properties as well as minimum erosion wear. Such difficulty involving much performance defining criterion (PDC) can be regarded as multi criteria decision method (MCDM). In present investigation the TOPSIS method is implemented to reach for best alternative. The Technique for Order of Preference by Similarity to Ideal Solution (TOPSIS) is a multi-criteria decision analysis method originally developed by Hwang and Yoon [244] in 1981 with further developments by Yoon [245] in 1987, and Hwang et al. [246] in 1993. It tries to reach the alternative nearer to positive ideal solution and away from negative ideal solution. The performance defining criterions are having different degree of influence on decision of best alternatives. These degree of influence i.e. weights can be calculated using entropy method. The designation of all composites involved in TOPSIS for ranking is mentioned in the Table 3.3 to 3.5. The step in TOPSIS method is described below.

1. **Selection of PDC**

The decision making is multi attributed task. While selecting best composite material many number of mechanical, physical and wear properties are involved. It is a crucial phase in TOPSIS to decide PDC from these many numbers of properties at specific conditions. The identified PDC for present investigation are shown in Table 3.12.

2. **Decision matrix**

The decision matrix is created after identifying number of alternatives (M) and performance defining criterion (N). The decision matrix is formulated in M × N order as,

$$D_{M \times N} = \begin{pmatrix} a_{11} & a_{12} & ... & a_{1N} \\ a_{21} & a_{22} & ... & a_{2N} \\ \vdots & \vdots & \vdots & \vdots \\ a_{M1} & a_{M2} & ... & a_{MN} \end{pmatrix}$$

3.14

Where, a_{ij} an element of the decision matrix, $D_{M \times N}$ represents the actual value of the ith alternative in term of jth PDC.

3. **Weights for each PDC using entropy method**

It is obvious to know the relative importance of each criterion. There are many methods to determine weights for each criterion, such as the weighted evaluation technique, the eigenvector method, the weighted least square method, the entropy method, the AHP method and so on. Here, the entropy method is implemented to derive the weights of the PDC in the present investigation. The weight for individual criterion is determined without direct involvement of decision maker. Entropy generally used as a criterion for measurement of represented disorder. It is based on the principle that a wide data distribution shows more disorder than a packed distribution. The weights for individual PDC is calculated by below mentioned procedure.

    a. The projection value (P_{ij}) is obtained by normalizing the decision matrix ($D_{M \times N}$).

$$P_{ij} = \frac{a_{ij}}{\sum_{i=1}^{M} a_{ij}}$$

3.15

    b. The entropy of jth criterion is calculated using eq. 3.16

$$E_j = -k \sum_{j=1}^{N} P_{ij} \ln(P_{ij})$$

3.16

       where, k is constant and obtained as $k = \frac{1}{\ln(M)}$

    c. Dispersion value (DP_j) of each criterion is measured. However, the dispersion value is represented the inherent contrast intensity of each criterion. For higher value of (DP_j) the criterion in the problem is important. The dispersion values are calculated as:

$$DP_j = 1 - E_j$$

3.17

    d. Finally, weights of all the PDC is calculated as;

$$W_j = \frac{DP_j}{\sum_{j=1}^{N} DP_j}$$

3.18

Table 3.12 Description of the different performance defining criterion (PDC)

Performance defining criterion	Description of individual PDC	Performance implications of different PDC
PDC 1	The experimental density of the composite, determined by simple water immersion technique. ct ρ	Lower is good
PDC 2	The void content in the composites is calculated using difference in measured and theoretical density	Lower is good
PDC 3	Hardness as a measure of resistance to indentation under loads was measured on a Rockwell hardness tester	Higher is good
PDC 4	The tensile strength of the composite is the maximum stress that a material can withstand while being stretched or pulled before necking and is determined by using Universal Testing Machine.	Higher is good
PDC 5	The Flexural strength of the composite is defined as a material's ability to resist deformation in bending under load and is determined by using Universal Testing Machine.	Higher is good
PDC 6	The Inter-laminar shear strength of the composite is defined as a material's ability to resist shear failure at the interface of fiber and resin and is determined by using Universal Testing Machine.	Higher is good
PDC 7	The experimental Impact strength of the composite is defined as; the amount of energy absorbed before fracture and is determined by using Impact Testing Machine.	Higher is good
PDC 8	Fracture toughness is measured at 0.5mm crack length	Higher is good
PDC 9	Slurry jet erosion rate of the composites from the surface when the erodent particles of 325 μm size, having 10 m/sec velocity strikes the surface at 60 degree from a stand of distance (S.O.D.) of 50 mm.	Lower is good
PDC 10	Slurry jet erosion rate of the composites from the surface when the erodent particles of 325 μm size, having 20 m/sec velocity strikes the surface at 60 degree from a stand of distance (S.O.D.) of 50 mm.	Lower is good
PDC 11	Slurry jet erosion rate of the composites from the surface when the erodent particles of 325 μm size, having 30 m/sec velocity strikes the surface at 60 degree from a stand of distance (S.O.D.) of 50 mm.	Lower is good
PDC 12	Slurry jet erosion rate of the composites from the surface when the erodent particles of 325 μm size, having 40 m/sec velocity strikes the surface at 60 degree from a stand of distance (S.O.D.) of 50 mm.	Lower is good
PDC 13	Slurry jet erosion rate of the composites from the surface when the erodent particles of 325 μm size, having 30 m/sec velocity strikes the surface at 30 degree from a stand of distance (S.O.D.) of 50 mm.	Lower is good
PDC 14	Slurry jet erosion rate of the composites from the surface when the erodent particles of 325 μm size,	Lower is good

	having 30 m/sec velocity strikes the surface at 45 degree from a stand of distance (S.O.D.) of 50 mm.	
PDC 15	Slurry jet erosion rate of the composites from the surface when the erodent particles of 325 μm size, having 30 m/sec velocity strikes the surface at 75 degree from a stand of distance (S.O.D.) of 50 mm.	Lower is good
PDC 16	Slurry jet erosion rate of the composites from the surface when the erodent particles of 325 μm size, having 30 m/sec velocity strikes the surface at 90 degree from a stand of distance (S.O.D.) of 50 mm.	Lower is good
PDC 17	Solid particle erosion rate of the composites from the surface when the erodent particles of 250 μm size, having 30 m/sec velocity strikes the surface at 60 degree from a stand of distance (S.O.D.) of 10 mm at 50˚C	Lower is good
PDC 18	Solid particle erosion rate of the composites from the surface when the erodent particles of 250 μm size, having 45 m/sec velocity strikes the surface at 60 degree from a stand of distance (S.O.D.) of 10 mm at 50˚C	Lower is good
PDC 19	Solid particle erosion rate of the composites from the surface when the erodent particles of 250 μm size, having 60 m/sec velocity strikes the surface at 60 degree from a stand of distance (S.O.D.) of 10 mm at 50˚C	Lower is good
PDC 20	Solid particle erosion rate of the composites from the surface when the erodent particles of 250 μm size, having 75 m/sec velocity strikes the surface at 60 degree from a stand of distance (S.O.D.) of 10 mm at 50˚C	Lower is good
PDC 21	Solid particle erosion rate of the composites from the surface when the erodent particles of 250 μm size, having 60 m/sec velocity strikes the surface at 30 degree from a stand of distance (S.O.D.) of 10 mm at 50˚C	Lower is good
PDC 22	Solid particle erosion rate of the composites from the surface when the erodent particles of 250 μm size, having 60 m/sec velocity strikes the surface at 45 degree from a stand of distance (S.O.D.) of 10 mm at 50˚C	Lower is good
PDC 23	Solid particle erosion rate of the composites from the surface when the erodent particles of 250 μm size, having 40 m/sec velocity strikes the surface at 75 degree from a stand of distance (S.O.D.) of 10 mm at 50˚C	Lower is good
PDC 24	Solid particle erosion rate of the composites from the surface when the erodent particles of 250 μm size, having 40 m/sec velocity strikes the surface at 90 degree from a stand of distance (S.O.D.) of 10 mm at 50˚C	Lower is good

4. The TOPSIS method

The ranking of all composition under present investigation is determined using TOPSIS by following steps;

a. The decision matrix ($D_{M \times N}$) is normalised as $R = [r_{ij}]$

$$r_{ij} = \frac{a_{ij}}{\left[\sum_{i=1}^{M}(a_{ij})^2\right]^{1/2}} \qquad\qquad 3.19$$

b. Weighted normalized matrix (V_{ij}) by multiplying the normalized matrix by its associated weight (W_j) calculated by entropy method.

$$V_{ij} = W_j \times r_{ij} \qquad\qquad 3.20$$

c. The positive ideal solution (A^+) and the negative ideal solution (A^-) are determined based on the weighted normalized ratings as shown:

$$A^+ = (V_1^+, V_2^+ \dots V_N^+), \text{and } A^- = (V_1^-, V_1^- \dots V_N^-) \qquad\qquad 3.21$$

where,

$$V_i^+ = \begin{cases} (\max_i V_{ij}), & \text{if j is benifit criteria} \\ (\min_i V_{ij}), & \text{if j is cost criteria} \end{cases} \text{ and}$$

$$V_i^+ = \begin{cases} (\min_i V_{ij}), & \text{if j is benifit criteria} \\ (\max_i V_i^+), & \text{if j is cost criteria} \end{cases} \text{ for } j = 1, 2 \dots. N$$

d. The Euclidian distances between each of the alternatives and the positive ideal solution and the negative ideal solution are calculated as shown:

$$D_i^+ = \sqrt{\sum_{j=1}^{N}(V_i^+ - V_{ij})^2}, \qquad \text{and}$$

$$D_i^- = \sqrt{\sum_{j=1}^{N}(V_{ij} - V_i^-)^2}, \qquad \text{for } i = 1, 2 \dots. M \qquad\qquad 3.22$$

e. Finally, the overall preference or closeness index (CI) of the alternatives is calculated and then the alternatives are arranged in descending order according to their closeness index. The closeness index (CI) of the alternatives is calculated as:

$$CI_i = \frac{D_i^-}{D_i^+ + D_i^-}, \text{for } i = 1, 2 \dots. M \qquad\qquad 3.23$$

Chapter Summary

This chapter has provided:

- ❖ The descriptions of materials used in this study

- ❖ The details of composition and fabrication of the composites

- ❖ The physical, mechanical and thermal characterization of composites

- ❖ The description of erosion wear test and Taguchi experimental design approach

- ❖ Evaluation of optimal combination of physical, mechanical and erosion wear rate by TOPSIS method

The next chapter presents the physical and mechanical properties of the unfilled and granite powder filled fiber reinforced polymer composites.

*****

<div align="right">**Chapter 4**</div>

MECHANICAL CHARACTERIZATION OF THE COMPOSITES

The mechanical performance of composite material is always diverse from the performance of matrix and reinforcement materials. In the present investigation three dissimilar fibers with different mechanical properties are reinforced in epoxy matrix with granite powder as a new filler material is used in this research work. In the view of disparate properties of constituent material it is indispensable to characterize the developed composites for mechanical performance. This chapter presents the physical and mechanical properties of the unfilled and granite powder filled fiber (glass, jute and carbon) reinforced epoxy composites fabricated in present investigation. The interpretation of the results and the comparison among various composite samples are also presented. This chapter consists of three parts: first part describing physical and mechanical properties of unfilled and granite powder filled glass-epoxy composites (EG10-EG40 and EGG0-EGG24), second part describing physical and mechanical properties of unfilled and granite powder filled jute-epoxy composites and third part describing the physical and mechanical properties of unfilled and granite powder filled carbon-epoxy composites.

<div align="center">**Part-I**</div>

4.1 Physical, mechanical and fracture toughness analysis of unfilled and granite powder filled glass-epoxy composites

4.1.1 Density and void fraction

Polymeric materials are mostly acceptable for their excellent specific properties owing to low density. With the addition of fibers and particulate filler the density of fabricated composites are modified which in turn affect the specific properties. Formation of voids at the interface of matrix and reinforcement material is inevitable as composites that fabricated with manual hand lay-up method. Voids in the composites make them weak and cause the initiation of de-bonding early cracks during failure. The density and void fraction of unfilled and granite powder filled glass epoxy composite is shown in Table 4.1. The void fraction of unfilled glass epoxy composite is decreased from 7.71% to 3.17% with the increase in fiber loading from 10 to 50 wt.%. This shows close packing of fibers at higher weight fraction. However, the void fraction of granite powder filled glass epoxy composite is increased from 4.19 to 9.23% with the increase in granite powder content from 0 to 24 wt.%. The void fraction of composite is shown in an increasing in trend for the inclusion of filler particles [247]. It is clear from the results that any fiber reinforced polymer composites the void content is the

major factor which dominates the water absorption characteristics as the proposed material is specifically used for external environment applications i.e for wind turbine blade material. The formation of void in any polymeric composites depend on the number of reasons such as use of high viscosity resin in combination with closely packed fibers which are not completely mixed with the resin materials, improper arrangement of fiber layer in the matrix, uniform mixing of resin and hardener so that bubble may be formed during preparation of laminate structure respectively [248].

Table 4.1 Theoretical, experimental density and void fraction of composites

Composite	Theoretical density (g/cc)	Experimental density (g/cc)	Void fraction (%)
E + 10 wt.% GF	1.167	1.077	7.71
E + 20 wt.% GF	1.243	1.161	6.59
E + 30 wt.% GF	1.329	1.269	4.51
E + 40 wt.% GF	1.429	1.369	4.19
E + 50 wt.% GF	1.544	1.495	3.17
E + 40 wt.% GF + 0 wt.% GP	1.429	1.369	4.19
E + 40 wt.% GF + 8 wt.% GP	1.520	1.410	7.24
E + 40 wt.% GF + 16 wt.% GP	1.625	1.491	8.25
E + 40 wt.% GF + 24 wt.% GP	1.744	1.583	9.23

E – epoxy, GF – glass fiber, GP – granite powder

4.1.2 Hardness

The composite materials resist the indentation or penetration when the interface between matrix and reinforcement transfer the stress effectively when the load is applied on the composite surface. Hence, hardness of composite is a relative indication of effective stress transfer and closely packed structure. Figure 4.1 shows the hardness of composite increases with the increase in glass fiber as well as granite powder. This increased in hardness may be attributed to compressive force applied during hardness testing which compress the matrix and reinforcement both phases close to each other which results in the better stress transfer and resistance to indentation [249]. The hardness of unfilled composites reinforced with glass fiber from 10 wt.% to 50 wt.% in a step of 10 wt.% is 30, 34, 35, 37 and 38 Hv respectively. Similarly, with the addition of granite powder also, the hardness of composites are increased from 41, 44, and 47 Hv for addition of 8 wt.%, 16 wt.% and 24 wt.% granite powder respectively. Initially, with 20 wt.% glass fiber loading the hardness is increased by 13% as compared to composite with 10 wt.% fiber loading. Further, with the increase in fiber loading

from 30 wt.% to 50 wt.% the improvement in hardness of composite is not significant. However, with addition of granite filler significant improvement in hardness is observed i.e. 18.81%, 7.31% and 6.81% for addition of 8 wt.%, 16 wt.% and 24 wt.% granite powder respectively (see Figure 4.1).
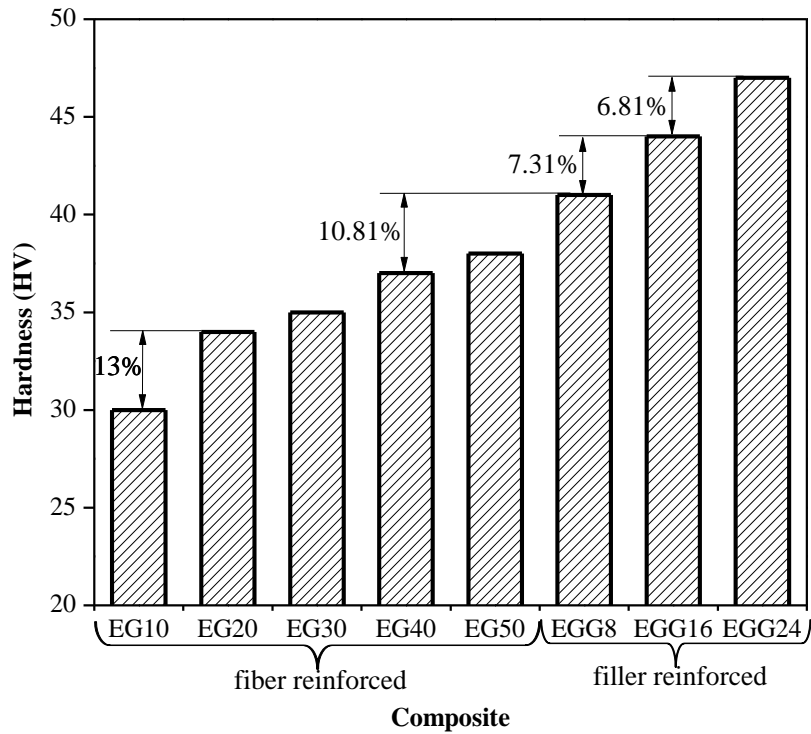
Figure 4.1 Effect of glass fiber loading and granite particulate content on hardness of composites

4.1.3 Tensile strength

The fibers are usually excellent in bearing the load when get stretched at their ends. When reinforced in different quantity with polymer resin to form fiber reinforced composite (FRP), the tensile properties get altered. The tensile properties may get further changed when particulate filler is incorporated. Gradual increase in tensile strength and modulus of composite with the increase in glass fiber loading is noticed (Figure 4.2). It clearly indicates that inclusion of glass fiber increases the load bearing capacity of composites. Similar, observations have also been recorded by Iba et al. [250] for glass fiber reinforced epoxy composite. However, the tensile properties are slightly improved initially for low granite particulate addition (i.e. 8 wt.%) and slowly decreased for higher amount (i.e. 16 and 24 wt.%) of granite powder addition (see Figure 4.2 and Table 4.2). It can be seen that the tensile properties have shown poor performance with the incorporation of granite powder

particulates in the matrix material. Past studies [251, 252] revealed that normally reinforcement in the composite resist the deformation of the matrix polymer reducing the tensile strain. Hence, even if the tensile strength decreases with filler addition the tensile modulus of the composite is expected to increase. But this is possibly not occurring in the present case also with the presence of higher weight fraction of granite powder and reduction in both tensile strength and modulus is recorded in spite of the reinforcement of long glass fibers.
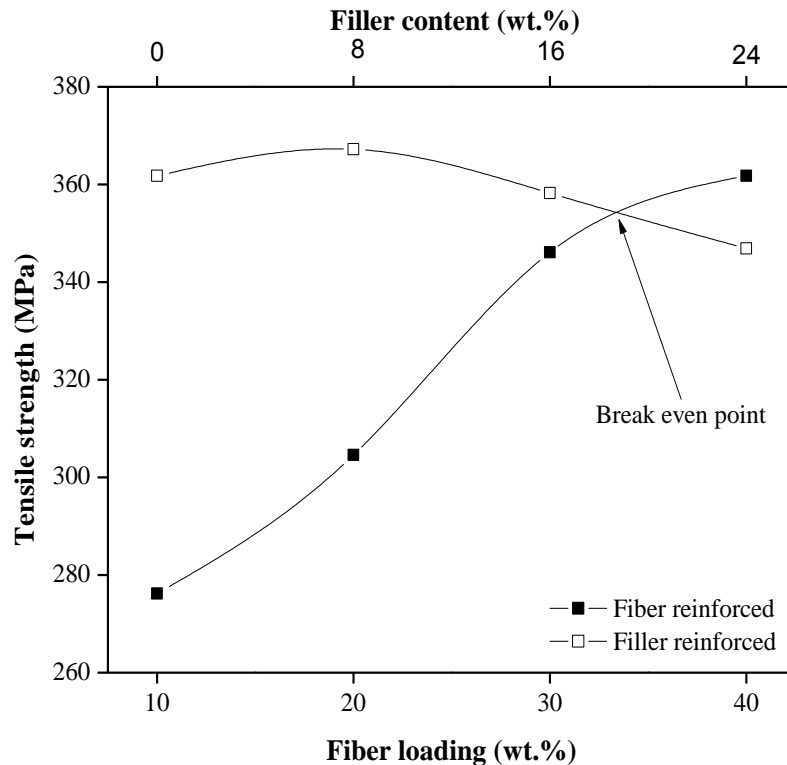
Figure 4.2 Effect of glass fiber loading and granite powder content on tensile strength

The drastic improvement in the tensile strength for the increase in fiber loading from 10 wt.% to 40 wt.% is observed. Further, addition of 50 wt.% glass fiber has insignificant improvement on the tensile strength. This improvement in the tensile strength may be attributed to higher tensile strength of fiber than epoxy matrix and better stress transfer form fiber to epoxy matrix without failure. Maximum improvement of 13.62% (from 304.6 MPa to 346.1 MPa) is recorded for increase in fiber loading from 20 wt.% to 30 wt.% whereas, least improvement of 0.14% (from 361.8 MPa to 362.3 MPa) is observed with the increase in fiber loading from 40 wt.% to 50 wt.% (see Table 4.2). More fiber-fiber interaction due to insufficient wetting by matrix material at higher fiber loading may be the reason for this insignificant improvement. Unfilled composite with 33 wt.% glass fiber and filled composite

with 19 wt.% granite powder shows same tensile strength (see break-even point in Figure 4.2). The values of tensile modulus for all the composites are shown in Table 4.2 and observed to be almost similar behavior like tensile strength. In fiber reinforced epoxy composites the tensile modulus goes on increasing with the increase in fiber loading up to 50wt.%. Whereas, particulate filled glass fiber reinforced epoxy composites the tensile modulus shows reverse trend.

4.1.4 Flexural strength

The flexural strength of laminated composites is evaluated by short beam strength in 3 point bending mode. Opposite surfaces are subjected to reverse nature of stresses. Flexural strength of unfilled and granite powder filled glass fiber reinforced epoxy composite is indicated in Figure 4.3. From Figure 4.3, can be concluded that the reinforcement of glass fiber has significant effect on flexural strength whereas, addition of granite particle has marginal effect on the flexural properties of composite. Similar, results were also observed by Abdulmajeed et al. [253] for unfilled and barium silicate filled unidirectional glass fiber reinforced polymer composite. Initially, with the increase in glass fiber loading from 10 wt.% to 20 wt.% the flexural strength of the composite is increased from 189.38 MPa to 206.56 MPa i.e. this increment in flexural strength is 10.66%. Further, reinforcement of 30 wt.% glass fiber significantly increased the flexural strength of composite to 294.38 MPa, which accounts to 42.52% increment as compared to composite with reinforcement of 20 wt.% glass fiber. The increment of 8.81% is observed (i.e. from 294.38 MPa to 320.31 MPa) for increase in fiber loading form 30 wt.% to 40 wt.% (see Figure 4.3). Further, increase of glass fiber beyond 40 wt.% has negligible positive effect on the flexural strength. This may be quantify as minor improvement in flexural strength from 320.31 MPa to 325.63 MPa (1.66%) for increase of glass fiber loading from 40 wt.% to 50 wt.% (see Table 4.2). From the obtained results it may be concluded that the reinforcement of 40 wt.% of glass fiber is reasonable in a view to achieve better flexural strength.

The granite filler content has marginal effect on the flexural properties of composite but with the increase in granite powder up to 8 wt.% the flexural strength is improved from 320.31 MPa to 327 MPa respectively. However, on further incorporation of granite powder from 16 wt.% to 24 wt.% results in decreasing in flexural strength from 309.06 MPa to 300.31 MPa respectively. The breakeven point with respect to flexural strength is found to be 32 wt.% of glass fiber or 18 wt.% of granite powder in the composite. As shown in Table 4.2, the flexural modulus of fiber reinforced epoxy composites is increased rapidly with the

increase in fiber loading. Whereas, flexural modulus improved for addition of granite powder content up to 16 wt.% and further addition of filler shows rapid decline in modulus.
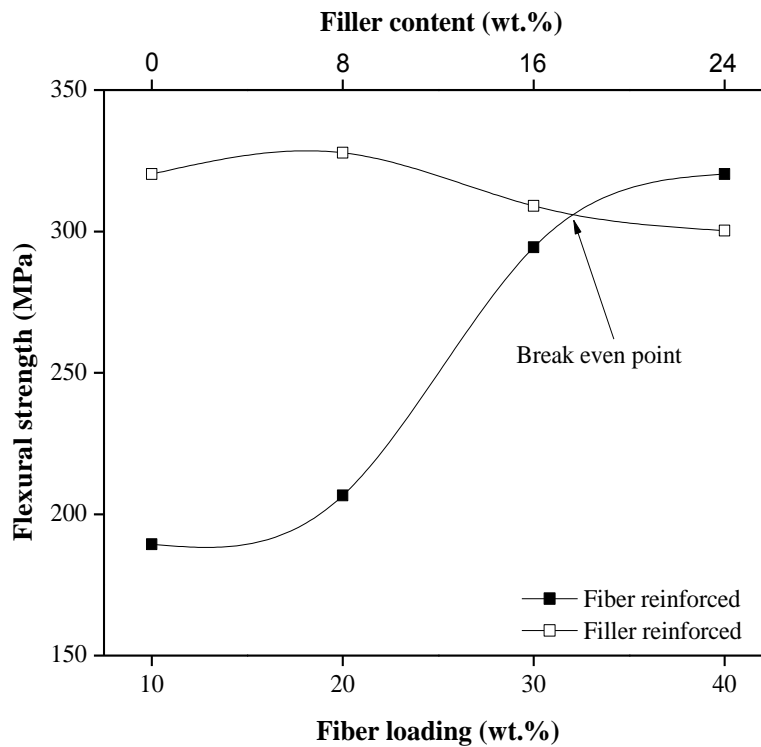
Figure 4.3 Effect of glass fiber loading and granite particulate content on flexural strength

4.1.5 Inter Laminar Shear Stress

The laminated composites are most prone towards delamination between the fiber matrix interfaces when shear stresses are applied [231]. Inter-laminar shear stress is an important matrix that dominated the mechanical property in the design of laminated composite. In general, stress transfer from fiber to matrix takes place through interface for which fiber/matrix interfacial strength is crucial and directly affects the strength of a composite to a great extent [254]. Inter laminar shear strength is improved from 9.47 MPa to 16.02 MPa with the increase in fiber loading from 10 wt.% to 50 wt.% (Figure 4.4). The highest improvement in the inter laminar shear strength from 10.33 MPa to 14.72 MPa (i.e 42.5%) is found for increase in fiber loading from 20 wt.% to 30 wt.%, this may be attributed to reduction in the void content for 30 wt.% glass epoxy composite. Addition of granite powder has insignificant effect on inter laminar shear strength of composite (see Figure 4.4). The values for inter laminar shear strength are reported as 16.39 MPa, 15.45 MPa and 15.02 MPa for incorporation of granite powder of 8 wt.%, 16 wt.% and 24 wt.% respectively (see Figure 4.4). Patnaik et al. [231] reported similar results for fly-ash, alumina and silicon carbide filled glass polyester composite.
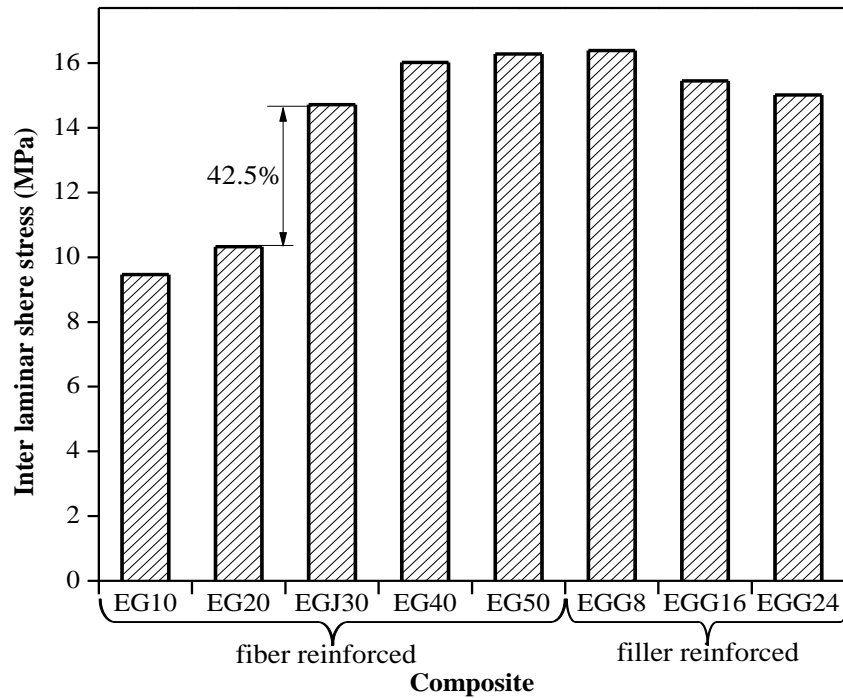
Figure 4.4 Effect of glass fiber loading and granite particulate content on inter laminar shear strength

4.1.6 Impact Strength

Impact strength is most widely specified mechanical property for polymeric material as they fail early under sudden applied loading. For glass fiber reinforced polymer composites the fracture mechanism under sudden loading shows fiber pullout which involves energy dissipation. This dissipated energy increases with increase in fiber loading which results in improvement in impact energy [255]. Further, the impact energy of composite is increased with addition of filler content as shown in Figure 4.5. This may be due to energy absorbed by filler particles present along the plane of fracture before debonding from matrix. The impact energy of unfilled and granite powder filled composite is shown in Figure 4.5. The rate of increase in impact strength is slightly higher in case of fiber loading than filler addition (shown in Fig. 12 by lines with slope of 0.37 and 0.3 respectively). The values of mechanical properties are collectively displayed in the Table 4.2. The values reported mean ± standard deviation.

4.1.7 Fracture toughness

Fracture toughness of a material is measured with the help of one of the parameter viz; the elastic energy release rate: G, the stress intensity factor: K, the J-integral, the crack-tip opening displacement (CTOD) and the crack-tip opening angle (CTOA). There are several

methods available for determining critical stress intensity factor (K_{IC}) viz, initial notch depth method, J-integral method, compliance technique, etc [80]. In present investigation, the stress intensity factor is evaluated using linear elastic fracture mechanics test according to ASTM D5045 for unfilled and granite powder filled FRP composite at crack length to width of specimen ratio (a/W) of 0.1, 0.3 and 0.5 respectively. The critical load is determined from the load–deflection curve. The variation of stress intensity factor of unfilled glass epoxy composites as function of a/W ratio is shown in Figure 4.6.
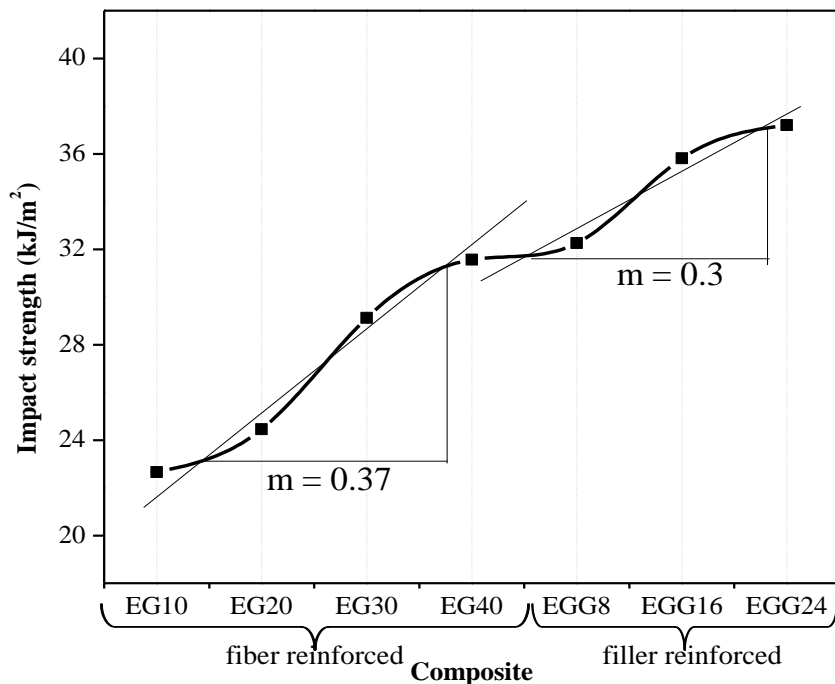
Figure 4.5 Effect of glass fiber loading and granite particulate content on impact strength

The experimental value of K_{IC} shows an increasing in trend with the increase in glass fiber loading which is indication of increase in ability of material to resist fracture strength. This may be caused due to extrinsic toughening mechanism which comes into action behind the crack tip after propagation of crack. Though the crack is propagated through the matrix the fibers acts as a bridge between the two separating fractured surfaces and results in resistance for further opening of crack. One more reason for toughening is formation of smaller cracks in the material around the main crack which relieve the stress at the crack tip and increases materials compliance. The rapid increase in the experimental value of K_{IC} is observed for initial reinforcement of glass fiber up to 40 wt.% and beyond this addition of glass fiber results in insignificant increase in values (Figure 4.6).

Table 4.2 Mechanical properties of unfilled and granite powder filled glass epoxy composite

Composite	Tensile strength (MPa)	Tensile modulus (GPa)	Flexural strength (MPa)	Flexural modulus (GPa)	ILSS (MPa)	Hardness (Hv)	Impact strength (kJ/m^2)
EG10	276.2 ± 20.84	3.84 ± 0.28	189.39 ± 12.69	2.58 ± 0.19	9.47 ± 1.1	30 ± 2	22.65 ± 2.25
EG20	304.6 ± 26.41	5.99 ± 0.31	206.56 ± 4.26	3.10 ± 0.31	10.33 ± 1	34 ± 1	24.45 ± 1.44
EG30	346.1 ± 51.49	7.37 ± 0.71	294.38 ± 32.42	4.06 ± 0.25	14.72 ± 1.8	35 ± 1	29.12 ± 1.81
EG40/EGG0	361.8 ± 5.69	8.24 ± 0. 68	320.31 ± 25.64	6.56 ± 0.64	16.02 ± 3.2	37 ± 1	31.56 ± 1.65
EG50	362.3 ± 11.58	8.37 ± 0.45	325.63 ± 17.75	7.52 ± 0.32	16.28 ± 1.5	38 ± 2	33.11 ± 2.32
EGG8	367.2 ± 27.6	8.57 ± 0.63	327.81 ± 6.4	6.89 ± 0.41	16.39 ± 1.6	41 ± 1	32.26 ± 2.15
EGG16	358.2 ± 34.56	8.09 ± 0.32	309.06 ± 18.05	7.35 ± 0.31	15.45 ± 2.6	44 ± 1	35.81 ± 1.62
EGG24	346.9 ± 9.5	7.92 ± 0.41	300.31 ± 22.2	5.46 ± 0.52	15.02 ± 2.6	47 ± 2	37.20 ± 1.8

For the a/W ratio of 0.5, the experimental value of K_{IC} increase to 4.5 MPa/m$^{1/2}$, 6.99 MPa/m$^{1/2}$, 10.99 MPa/m$^{1/2}$ and 11.50 MPa/m$^{1/2}$ for reinforcement of 20, 30, 40 and 50 wt.% of glass fiber respectively as compared to 2.98 MPa/m$^{1/2}$ for reinforcement of 10 wt.% glass fiber. The increase in stress intensity factor is 55%, 134%, 268% and 285% respectively for reinforcement of glass fiber. Significantly high modulus of glass fiber as compared to matrix material is responsible for the improvement in the fracture toughness. It is also observed that the effect of crack length on K_{IC} value is minor. Avci et al. [83] reported similar improvement in the fracture toughness with glass fiber loading in polyester resin and also reported approximately constant value of fracture toughness for varying a/W ratio.
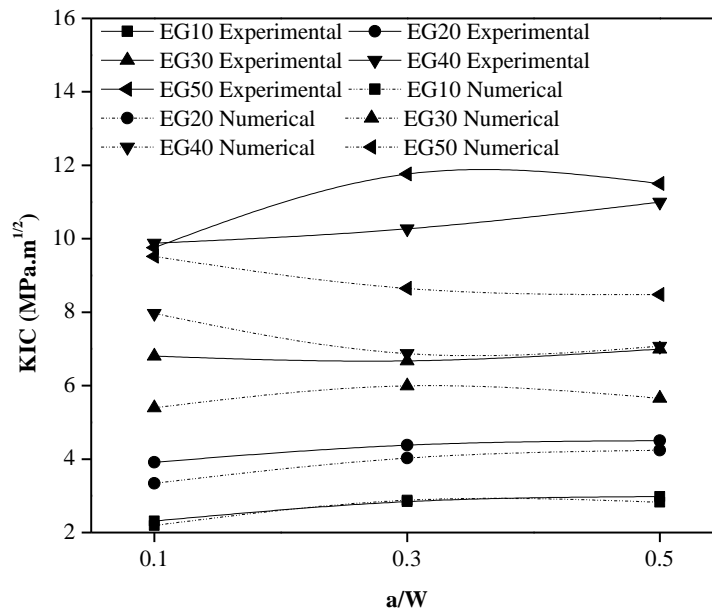
Figure 4.6 Variation of stress intensity factor of unfilled glass fiber reinforced epoxy composites

The fracture toughness of granite powder filled glass epoxy composite is exemplified in Figure 4.7 and revealed that the value of experimental value of K_{IC} increases for all the particulate filled glass epoxy composites as compared with virgin composite. This may be attributed to intrinsic toughening mechanisms due to presence of granite particles along the plane of crack propagation. This toughening processes act at the forefront of the crack tip to increase the material's toughness. This mechanism comes in to action in form of crack deflection and crack bifurcation due to presence of granite particles and crack meandering by void present in the composite materials. Highest improvement in experimental value of stress intensity factor is observed for composite with 16 wt.% granite powder at all the a/W ratios (Figure 4.7). Further addition of granite powder beyond 16 wt.% decreases the fracture

toughness of composite but its value is higher than that of virgin composite. At a/W ratio of 0.5 the improvement in stress intensity factor measured experimentally is 5.91%, 14.29% and 11.1% for addition of 8 wt.%, 16 wt.% and 24 wt.% granite powder as compared to unfilled composite. Yilmaz and Korkmaz [256] reported significant improvement in fracture toughness of PMMA by addition of wollastonite ($CaSiO_3$) up to 20 wt.%.
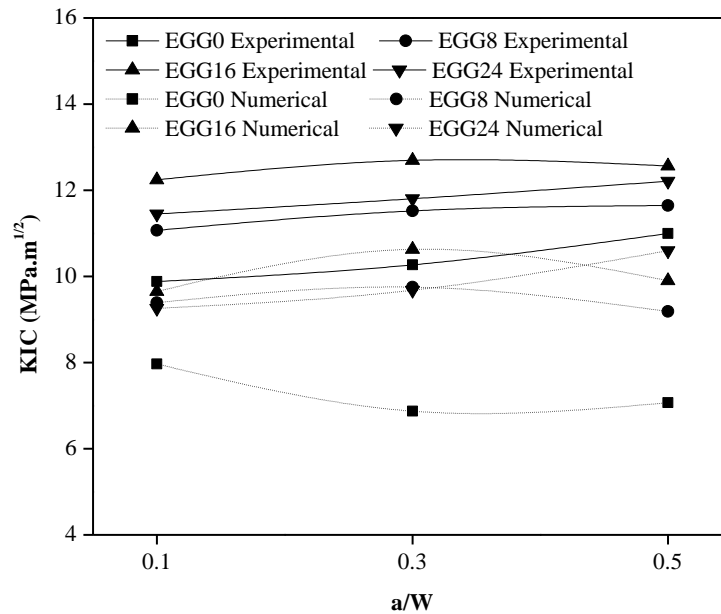
Figure 4.7 Variation of stress intensity factor of granite powder filled glass fiber reinforced epoxy composites

Figures 4.6 and 4.7 show the experimental values of K_{IC} overshoot with the numerical results both for unfilled and granite powder filled glass epoxy composites. For unfilled glass fiber epoxy composites the numerical results are in close agreement with experimental one. However, for granite powder filled composites the numerical values of fracture toughness are far lower that the experimental results. This may be due to modeling deficiency for intrinsic toughening mechanism in composites due to presence of granite powder on the path of crack front. For unfilled composite minimum variation in the value of K_{IC} is found at a/W = 0.3 for 10 wt.% glass fiber loading (1.41%). This variation of K_{IC} increases with the increase in fiber loading reached to 22.84% for composite with 50 wt.% glass fiber at a/W ratio is 0.5. Whereas, the minimum variation of about 13.18% is observed in case of 24 wt.% granite powder filled composite for a/W ratio 0.5 and the maximum variation is recorded for composite with 16 wt.% granite powder (21.18%).

(a)   (b)

(c)   (d)
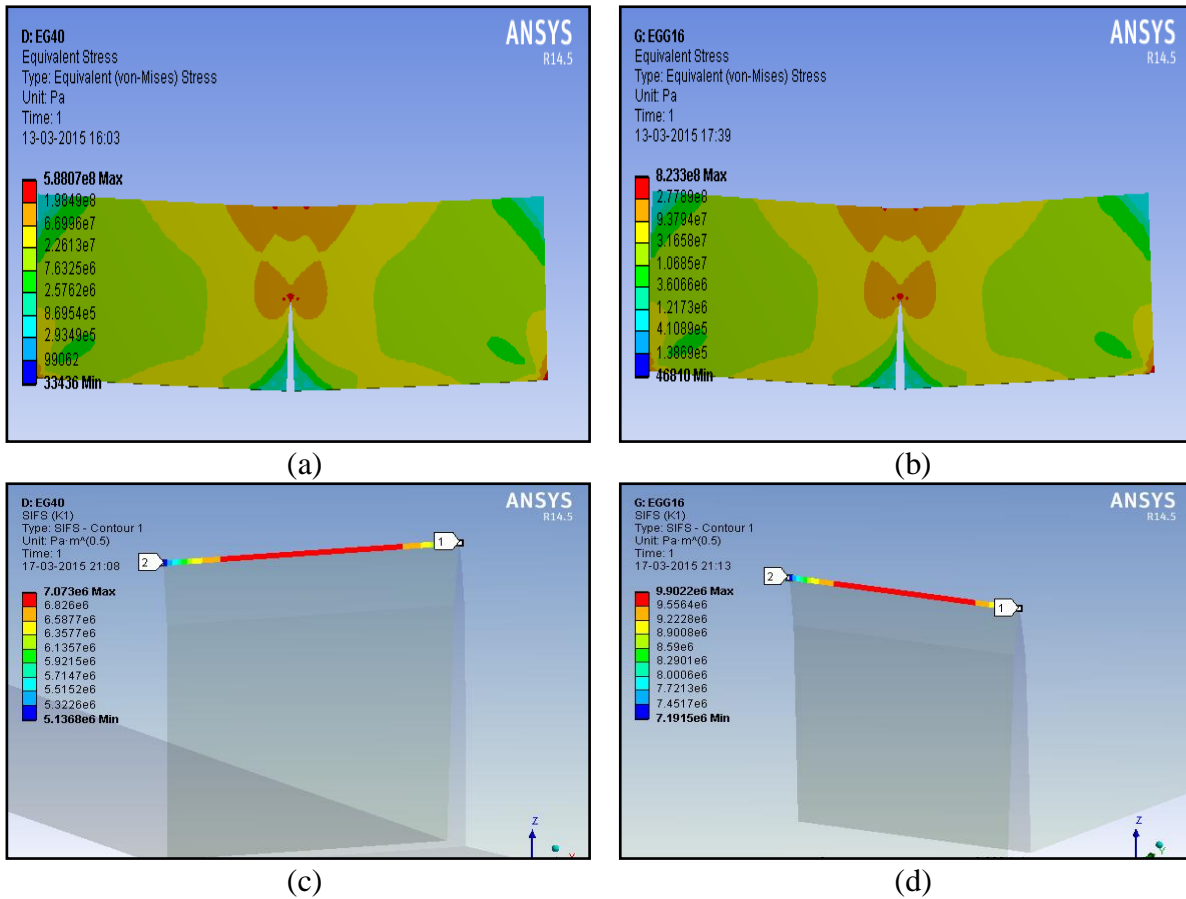
Figure 4.8 Numerical results for fracture analysis with a/W ratio of 0.5 a) von-Mises stress contour for EG40 b) von-Mises stress contour for EGG16 c) stress intensity factor along the crack front for EG40 d) stress intensity factor along the crack front for EGG8
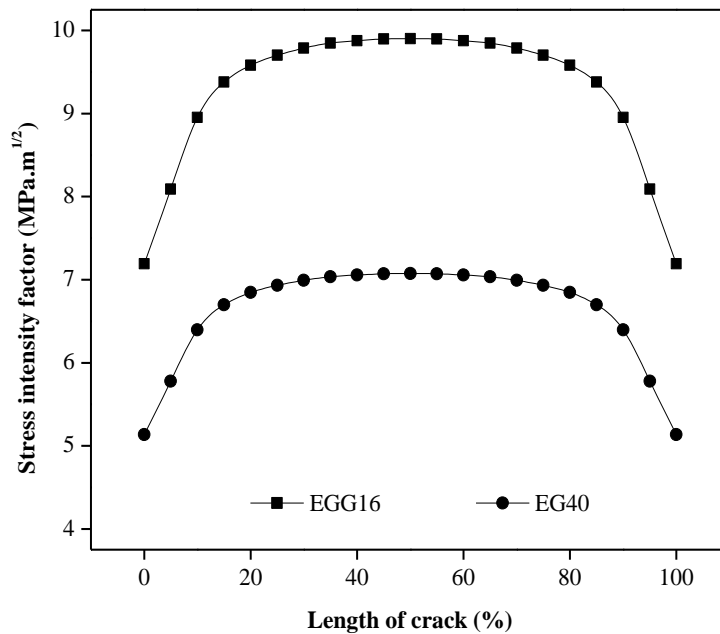
Figure 4.9 Numerical value of stress intensity factor along the length of crack front

Figures 4.8a and 4.8b show contour of von-Mises stress for a/W ratio of 0.5 for unfilled composite with 40 wt.% glass fiber loading and 16 wt.% granite powder filled glass epoxy composite respectively. Both the figures show development of kidney shaped stress contours at crack tip. Figures 4.8c and 4.8d show variation of stress intensity factor along the crack front. The maximum stress intensity factor at the crack tip is 7.07 MPa.m$^{1/2}$ and 9.90 MPa.m$^{1/2}$ for unfilled 40 wt.% glass fiber reinforced epoxy composite and 16 wt.% granite powder filled glass epoxy composite. The maximum stress intensity factor is at the centre of the length of crack front as shown in Figure 4.9.

4.1.8 Numerical analysis of wind turbine blade for static loading

Investigation of structural behavior of wind turbine blade has been traditionally accomplished using numerical model [257]. Figures 4.10a and 4.10b show the contours of von-Mises stresses developed in the blade during flap-wise bending for blade with unfilled 40 wt.% glass epoxy composite and 16 wt.% granite powder filled glass epoxy composite respectively. Interestingly it was found that there is no significant effect on variation of material due to stress developed in the blade. The maximum stress developed near the root section of the blade is 22.3 MPa in case of both the composites. Numerical value for stress generated is slightly at lower side than stress recorded at experimentally (i.e. 27 MPa) [14]. Figure 4.11a shows the flap-wise deflection of the blade at 10 sections along the length for unfilled 40 wt.% glass epoxy composite and the maximum deflection of 206.38 mm is observed at tip section (see Figure 4.11b). Figures 4.12a and 4.12b show the respective properties for 16 wt.% granite powder filled glass epoxy composite and the tip deflection is observed 210.21 mm for blade with 16 wt.% granite powder filled glass epoxy composite. The deflection at tip is in close agreement with experimental results (i.e 195 mm) [14].

Deflection of blade along the length for all the unfilled and granite powder filled glass epoxy composite is shown in Figure 4.13a and 4.13b. The deflection of blade gradually increased from hub towards tip of the blade and up to 0.5 m along the length of blade the deflection is negligible and having no effect on fiber loading. However, beyond 0.5 m length along the length of blade the deflection is influenced by glass fiber loading significantly. The maximum deflection at the tip is 442.6 mm (for 10 wt.% glass epoxy composite) and which is drastically reduce to 283.74 mm (for 20 wt.% glass epoxy) as shown in Figure 4.13a. Further, reduction in tip deflection is observed as 230.61 mm, 206.26 and 203.06 mm for blade with 30 wt.%, 40 wt.% and 50 % fiber loading respectively. Whereas, for granite powder filled glass epoxy composite the blade deflection is not much affected by granite powder addition as shown in Figure 4.13b. The tip deflection varies to

198.33 mm, 210.08 mm and 214.59 mm for granite powder filled composite as compared to tip deflection of 206.26 mm for blade with unfilled composites.

(a)   (b)
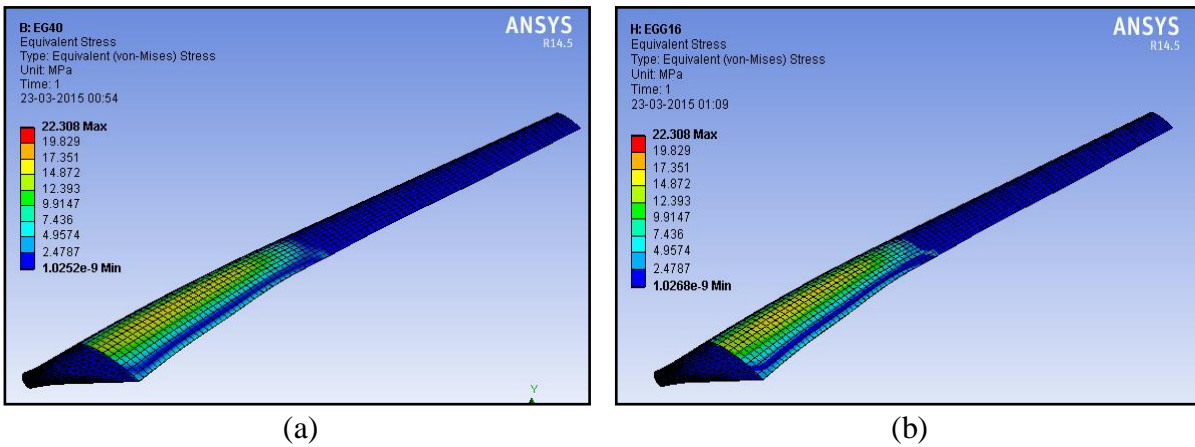
Figure 4.10 Stress contour plot for applied force a) unfilled composite with 40 wt.% of glass fiber b) 16 wt.% granite powder filled glass epoxy composite

(a)   (b)
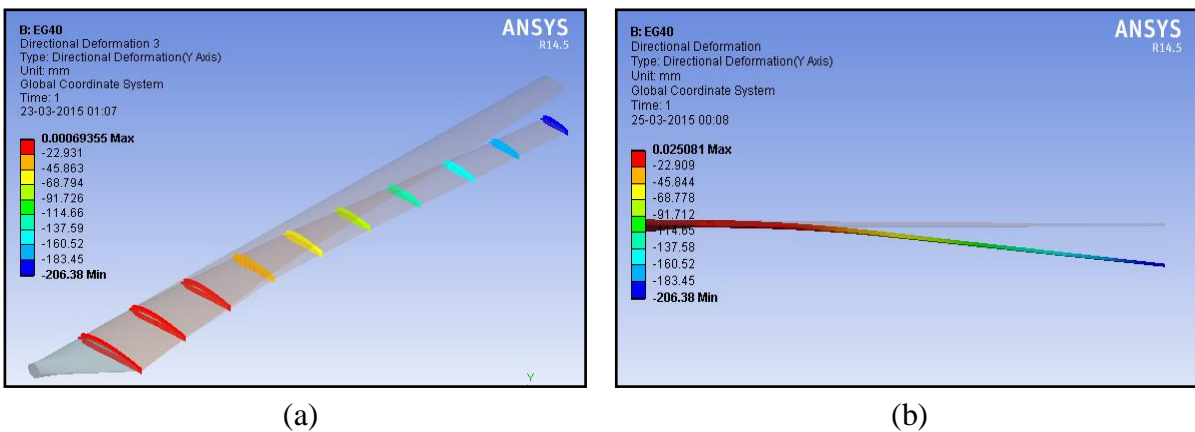
Figure 4.11 Flap-wise deflection of blade for unfilled 40wt.% glass epoxy composite a) at ten sections along the lengths of blade b) deflection from plane of rotaion

(a)   (b)
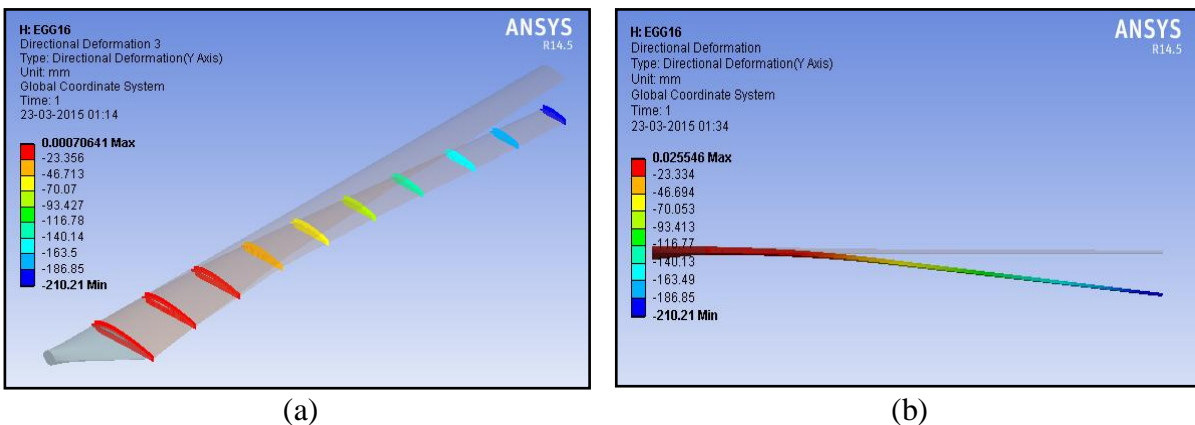
Figure 4.12 Flap-wise deflection of blade for 16 wt.% granite filled composite a) at ten sections along the lengths of blade b) deflection from plane of rotaion
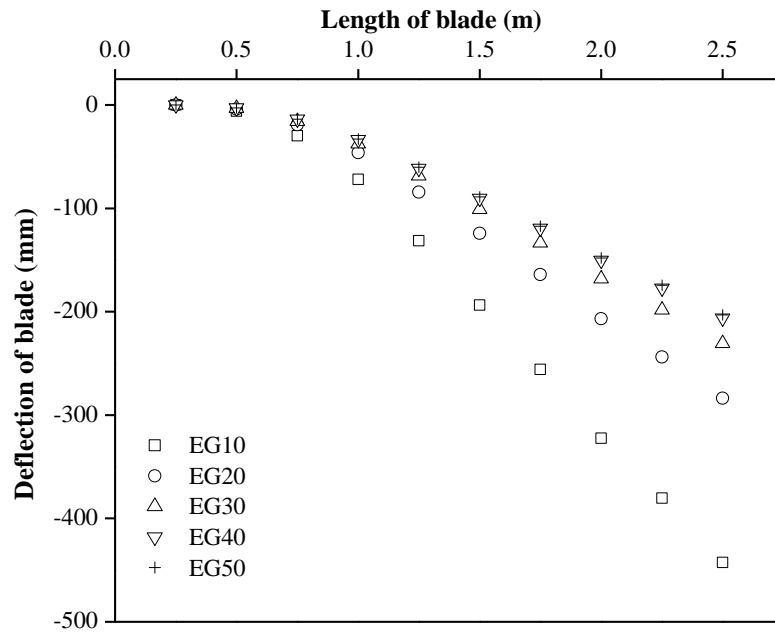
Length of blade (m)

Figure 4.13a Deflection along the length of blade for unfilled glass epoxy composite
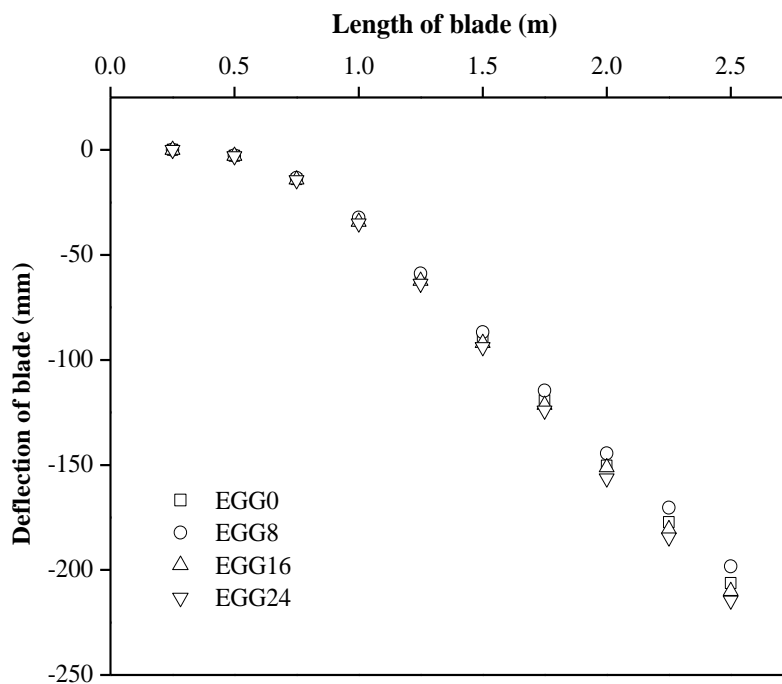
Length of blade (m)

Figure 4.13b Deflection along the length of blade for granite powder filled glass epoxy composite

Part-II

4.2 Physical, mechanical and fracture toughness analysis of unfilled and granite powder filled jute-epoxy composites

4.2.1 Density and void fraction

The presence of void content is strongly influence the mechanical and physical properties of fiber reinforced polymer composites. Air or other volatile matters exist in the composite during impregnation of reinforcement into the matrix or during manufacturing of composites [258, 259]. The theoretical and experimentally measured densities along with the corresponding volume fraction of voids for unfilled and granite powder filled jute epoxy composite are presented in Table 4.3. It is clearly seen that with the increase in jute fiber loading from 10 wt.% to 30 wt.%, there is a decrease in the void fraction from 6.37% to 2.96% respectively. This may be due to better fiber matrix interface bonding of the composites owing to proper wetting. However, with the increase in jute fiber loading from 30 wt.% to 50 wt.% the void content slightly increases from 2.96% to 3.07%. The main cause for the increase in void content may be incomplete wetting out of the fibers by the matrix would lead to the formation of voids in the composites [260].

Table 4.3 Measured and theoretical density of the composites

Composite	Measured density (g/cc)	Theoretical density (g/cc)	Volume of void fraction (%)
10 wt.% jute fiber	1.046	1.117	6.37
20 wt.% jute fiber	1.086	1.135	4.31
30 wt.% jute fiber	1.119	1.153	2.96
40 wt.% jute fiber	1.137	1.172	2.99
50 wt.% jute fiber	1.155	1.192	3.07
40 wt.% jute fiber + 8wt.% granite powder	1.177	1.233	4.55
40 wt.% jute fiber + 16wt.% granite powder	1.201	1.301	7.67
40 wt.% jute fiber + 24wt.% granite powder	1.243	1.376	9.68

For addition of 8 wt.%, 16 wt.% and 24 wt.% of granite powder in the composite increased the presence of void content hastily to 4.55%, 7.67% and 9.68% respectively compared to 2.99% for unfilled composite. This may be the result of entrapped air at the filler-matrix interface during mixing. Similar, results were also reported by Satapathy et al. [59] for SiC filled jute epoxy composite with the addition of hard ceramic particulates in a matrix material the void content gradually increases., i.e. increases in void content to 4.68%

and 5.22% for 10 and 20 wt.%   SiC content respectively as compared to void content 1.28% for unfilled composite. However, in all the composites the volume fractions of voids are reasonably small (< 10%). The quantitative information of void content is desirable for estimation of the quality of the composites. It is comprehensible that a good quality composite should have fewer voids. However, the presence of void is inevitable in composite fabricated particularly through hand-lay-up route.

4.2.2 Hardness

The hardness values of the unfilled filled composites show improvement in the hardness with the increase in fiber loading although the increment is not significant up to 30 wt.% jute fiber loading. Figure 4.14 shows the hardness of all the series of composites with variation of fiber loading and granite powder. It is found that at higher fiber loading the hardness value is improved. For reinforcement of jute fiber from 10 wt.% to 50 wt.% the hardness value is increased from 29 Hv to 37 Hv. This may be due to decrease in formation of air bubbles and voids in the composites which causes lesser in-homogeneity of composites.
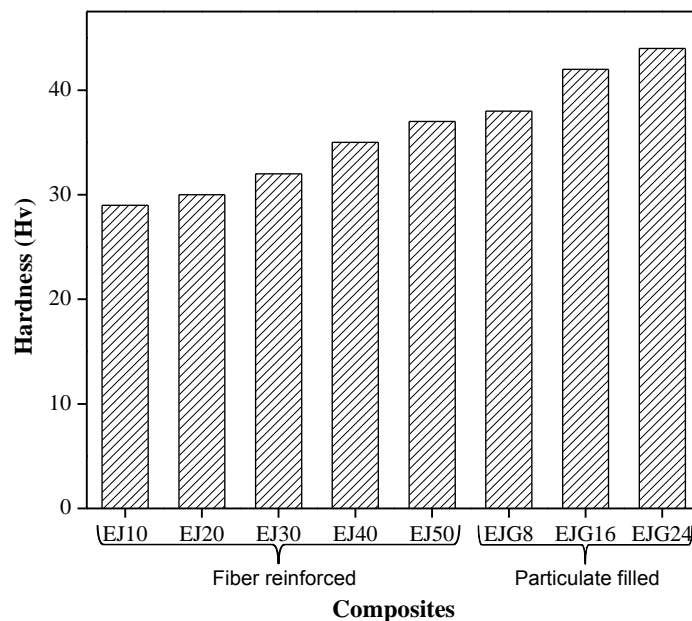
Figure 4.14 Hardness of unfilled and granite powder filled jute epoxy composite

It is also evident that the hardness value of granite powder filled jute epoxy composites is higher than unfilled jute epoxy composites. In particulate filled composite the particles distributed closer to each other as particulate content increases and hence, more strongly resists the penetration of composite. Reinforcement of granite powder in 8 wt.%, 16 wt.% and 24 wt.% result in improvement in hardness as 38 Hv, 42 Hv and 44 Hv respectively

compared to 35 Hv for unfilled composite. In general the hardness of composite is increased with the increase in reinforcement content irrespective of filler content and fiber loading in the polymer composites. This may be attributed to compressive force applied during hardness testing which press the matrix and reinforcement together which result in effective transfer of load and decrease in indentation. Mahapatra and Patnaik [11] also reported increase in hardness to 43 and 47 Hv for addition of 10 and 20 wt.% of silicon carbide filler in polymer composite respectively as compared to 39 Hv for unfilled fiber reinforced polymer composite.

4.2.3 Tensile and flexural strength

Tensile and flexural properties of jute epoxy composites with and without filler content are shown in Figures 4.15 and 4.16 respectively. Tensile strength increases with the increase in fiber loading from 28.33 MPa at 10 wt.% jute fiber to 34.26 MPa at 50 wt.% jute fiber (see Table 4.4). Jute fiber has relative higher tensile strength and modulus than epoxy matrix due to which jute fibers will initially carry the load and is transferred to epoxy matrix without the failure of matrix material, inducing better stress transfer. One more factor that has attributed for increase in tensile strength of fiber reinforced composites is due to alkali treatment of jute fiber. Generally, alkali treatment modifies the surface of jute fiber and promote fiber matrix interlocking which leads to better stress transfer between the matrix and jute fiber [261].
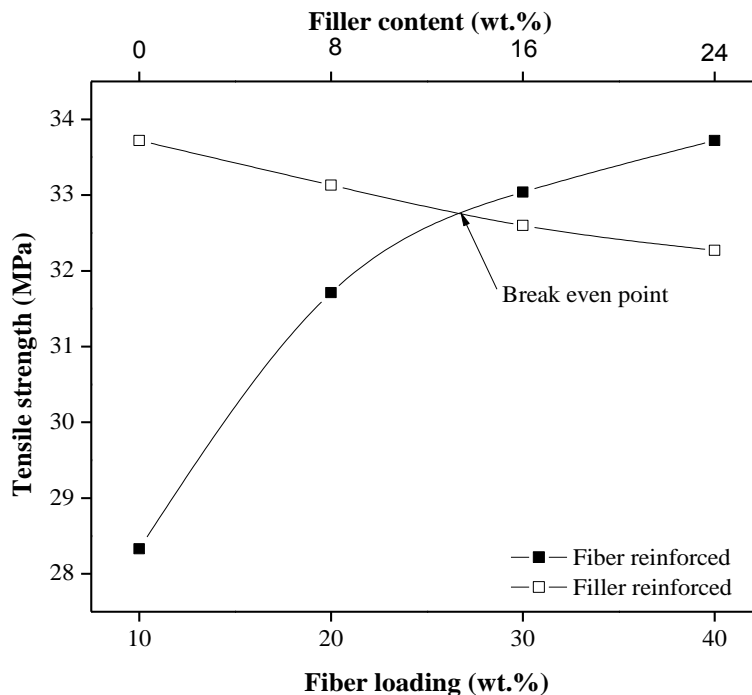
Figure 4.15 Effect of jute fiber and granite filler content on tensile strength

Composite reinforced with 50 wt.% of jute fiber exhibits maximum flexural strength which is 97.8 MPa (see Table 4.4). It is observed that flexural strength increases with the increase in jute fiber loading in the composite. The increase in flexural properties is due to presence of high modulus alkali treated jute fiber. Alkali treatment improved interfacial adhesion has reduced de-bonding of fiber from the matrix with improvement in properties of the composites [262]. The variations in tensile and flexural modulus of composites are illustrated in Table 4.4. It may be concluded that for any type of reinforcement initially the value of modulus is found to be increased (i.e up to 40 wt.% of jute fiber for unfilled composite and 16 wt.% granite powder for filled composite). Further, addition of reinforcement does not have significant improvement in modulus as per present analysis.
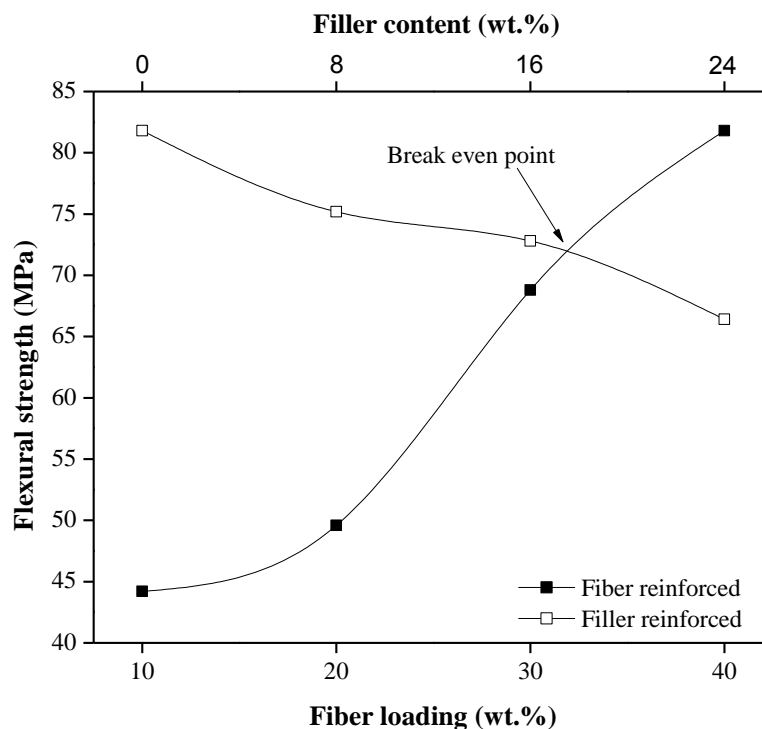
Figure 4.16 Effect of jute fiber and granite filler content on flexural strength

However, reinforcement of granite particulates in to the composite results in reduction in tensile and flexural strength of composite compared to unfilled composite. The tensile and flexural strength of composite with 40 wt.% jute fiber (consider as unfilled i.e 0 wt.% granite filled) is 33.72 MPa and 81.8 MPa respectively. The values are dropped to 33.13 MPa, 32.6 MPa and 32.27 MPa for tensile strength and 75.2 MPa, 72.8 MPa and 66.4 MPa for flexural strength with reinforcement of 8, 16 and 24 wt.% of granite powder respectively in the composites. There can be two reasons for reduction in the strength of polymeric composites. One may be the interface bonding between the filler particles and the matrix material that

may not be able to transfer the tensile stress which results in initiation of crack inside the matrix body; the other is that the corner points of the irregular shaped particulates result in stress concentration in the matrix. These two factors are responsible for reducing the tensile strength of the composites significantly. Figures 4.15 and 4.16 show that reinforcement of fiber has positive effect and incorporation of filler has negative effect on tensile and flexural strength. In order to determine extent of the granite powder addition in to jute epoxy composite without much compromise in properties the break even analysis is done. Results revealed the break even filler loading of 14 wt.% to 17 wt.% which shows equivalent results for 27 wt.% to 32 wt.% of jute fiber reinforcement.

4.2.4 Inter Laminar Shear Stress

Inter laminar shear stress (ILSS) is indication of ability of laminated composite material to sustain the shear stress developed along the plane of interface of matrix and fibers. Poor and weak interface in laminated composites show lower value for ILSS and vice versa. Figure 4.17 illustrated the ILSS for unfilled and granite powder filled jute epoxy composites. The change in ILSS shows trend similar with flexural strength. Initially, for increase in jute fiber loading from 10 wt.% to 20wt.% the value of ILSS is marginally improved from 2.76 MPa to 3.1 MPa (12.31% increase). However, for further addition of jute fiber from 20 to 30 wt.% significant improvement from 3.1 MPa to 4.3 MPa (38.7% increase) is observed.
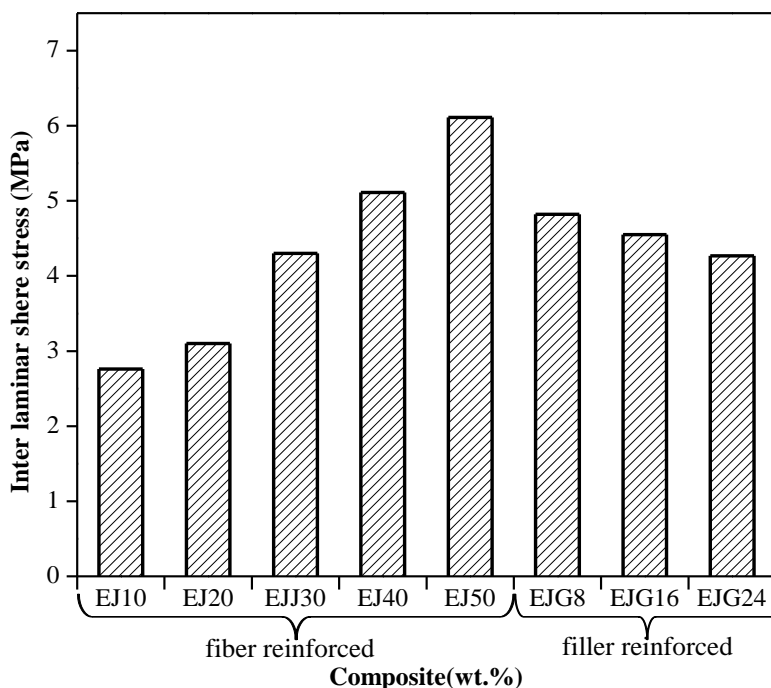
Figure 4.17 Effect of jute fiber loading and granite particulate content on inter laminar shear strength

The reason for this significant improvement is proper wetting of fibers which leads to increase in cross linking of polymeric chain at the interface. For further addition of jute fiber to 40 and 50 wt.% the values are improved to 5.11 MPa (18.83% increase) and 6.11 MPa (19.56% increase) respectively. The improvement of ILSS at higher fiber fraction is reduced due to fiber-fiber interaction which causes the area for initiation of de-lamination.

The granite powder filled jute epoxy composites shows marginal negative hybridizing effect on ILSS. The values are gradually drop off to 4.82 MPa, 4.55 MPa and 4.27 MPa for incorporation of 8, 16 and 24 wt.% granite powder respectively keeping jute fiber loading 40 wt.% constant. The addition of granite powder reduces the epoxy resin which reduces the proper wetting of fiber and increases the fiber-fiber contact. In tensile loading, both the layers of fibers may get stretched by equal quantity but in case of bending, either of the layers is stretched lower than other and cause early failure of composite in bending compared with tension with increase in filler content.

4.2.5 Impact strength

The impact strength of composites is increased with the reinforcement of either fiber and/or particulate filler. The impact failure of a composite occurs by factors like matrix fracture, fiber/matrix de-bonding and fiber pullout. However, when the applied load transferred by shear to fibers may exceed the fiber strength and then ultimately fiber fracture occurs. The fractured fibers may be pullout of the matrix, which involves energy dissipation as per observed literature [263].
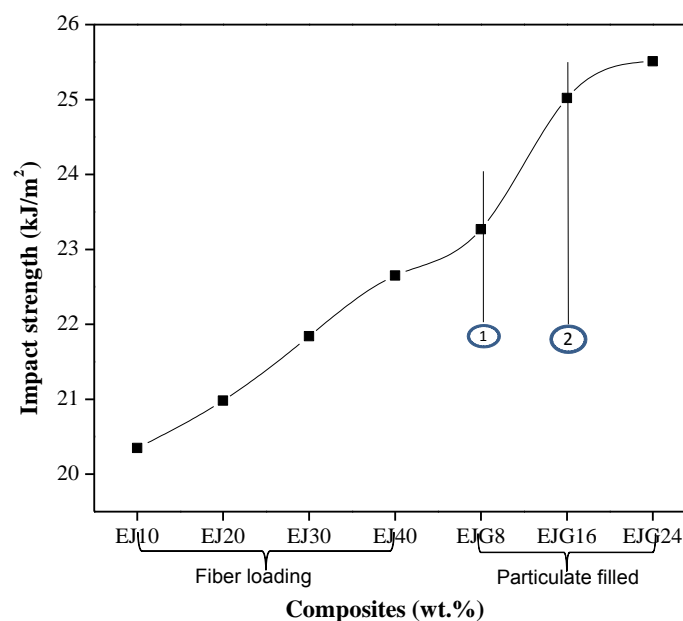
Figure 4.18 Variation in impact energy of unfilled and granite powder filled jute epoxy composite

Figure 4.18 illustrated the variation in impact strength Under sudden loading the amount of energy absorbed increases from 20.35 kJ/m^2 to 23.87 kJ/m^2 for variation of fiber loading fro 10 wt.% to 50 wt.% (see Table 4.4).The particulate addition in composite makes the fiber reinforced composite more toughened. This is due to improper matrix-particulates bonding which results in poor interfacial support. As impact energy for unfilled 40 wt.% jute fiber reinforced composite is 22.65 kJ/m^2 and for addition of 8 wt.% of granite powder in to 40 wt.% jute fiber reinforced epoxy composite is increased to 23.27 kJ/m^2. This increase in the impact strength of composite with incorporation of 8 wt.% of granite powder is 2.74% as compared with virgin composite. The significant improvement from 23.27 kJ/m^2 (indicated as point 1 in Figure 4.18) to 25.02 kJ/m^2 (indicated as point 2 in Figure 4.18) is observed for increase in filler content from 8 wt.% to 16 wt.% respectively.

4.2.6 Fracture toughness

Figure 4.19a and 4.19b illustrate the values of stress intensity factor measured by experimentally and predicted by using numerical method for unfilled and granite powder filled jute epoxy composites. The variation of stress intensity factor of unfilled jute fiber reinforced epoxy composites as a function of ratio of crack length to width of specimen (a/W) is shown in Figure 4.19a. It is observed that the value of K_{IC} is increased with the increasing in jute fiber loading. The increase in the experimental value of K_{IC} is drastic for initial reinforcement of jute fiber up to 30 wt.% and on further addition of jute fiber results in marginal increase in strength. It is also observed that the effect of crack length on K_{IC} value is minor. For the a/W ratio of 0.5, the experimental value of K_{IC} increased to 4.19 MPa/m$^{1/2}$, 6.94 MPa/m$^{1/2}$, 7.79 MPa/m$^{1/2}$ and 8.74 MPa/m$^{1/2}$ for reinforcement of 20, 30, 40 and 50 wt.% of jute fiber respectively as compared to 2.13 MPa/m$^{1/2}$ for reinforcement of 10 wt.% jute fiber. The increase in stress intensity factor is in the order of 1.9, 2.9, 3.6 and 4.1 times respectively.

The increase in fracture toughness of composite may be attributed to higher Young's modulus of jute fiber compared to epoxy resin. Similar, observations were reported in the past studies for reinforcement of glass and jute fiber in polymer composites [83, 84]. The numerically predicted values of K_{IC} for the unfilled jute epoxy composites show similar trend in improvement but the experimental values are slightly at the higher side than predicted values (see Figure 4.19a). This may be due to inability to model the fiber bridge formation at crack in software. This fiber bridge formation in experimental measurement absorbs some energy before tensile failure of fiber.

Table 4.4 Mechanical properties of unfilled and granite powder filled jute epoxy composites

Composite	Tensile strength (MPa)	Tensile Modulus (MPa)	Flexural strength (MPa)	Flexural modulus (MPa)	ILSS (MPa)	Hardness (Hv)	Impact strength (kJ/m^2)
EJ10	28.33 ± 1.05	624.6 ± 32.5	44.2 ± 2.65	736.3 ± 45.8	2.76 ± 0.3	29 ± 1	20.35 ± 0.2
EJ20	31.71 ± 2.11	848.6 ± 51.6	49.6 ± 4.32	1024.8 ± 27.6	3.1 ± 0.8	30 ± 1	20.98 ± 0.24
EJ30	33.04 ± 0.46	1045.3 ± 37.9	68.8 ± 4.49	1290.6 ± 24.1	4.3 ± 0.5	32 ± 2	21.84 ± 0.05
EJ40/EJG0	33.72 ± 1.73	1228.4 ± 84.6	81.8 ± 6.78	1258.3 ± 54.6	5.11 ± 0.8	35 ± 1	22.65 ± 1.10
EJ50	34.26 ± 2.59	1178.5 ± 108.5	97.8 ± 5.25	1013.3 ± 17.9	6.11 ± 0.2	37 ± 2	23.87 ± 1.36
EJG8	33.13 ± 1.15	1287.8 ± 21.5	75.2 ± 3.56	1397.5 ± 38.2	4.82 ± 0.2	38 ± 2	23.27 ± 0.56
EJG16	32.60 ± 0.51	1355.7 ± 52.4	72.8 ± 3.91	1450.6 ± 27.1	4.55 ± 0.3	42 ± 1	25.02 ± 1.89
EJG24	32.27 ± 0.84	1121.3 ± 32.8	66.4 ± 2.85	1045.3 ± 62.5	4.27 ± 0.5	44 ± 1	25.51 ± 1.52

The data represents mean ± standard deviation.
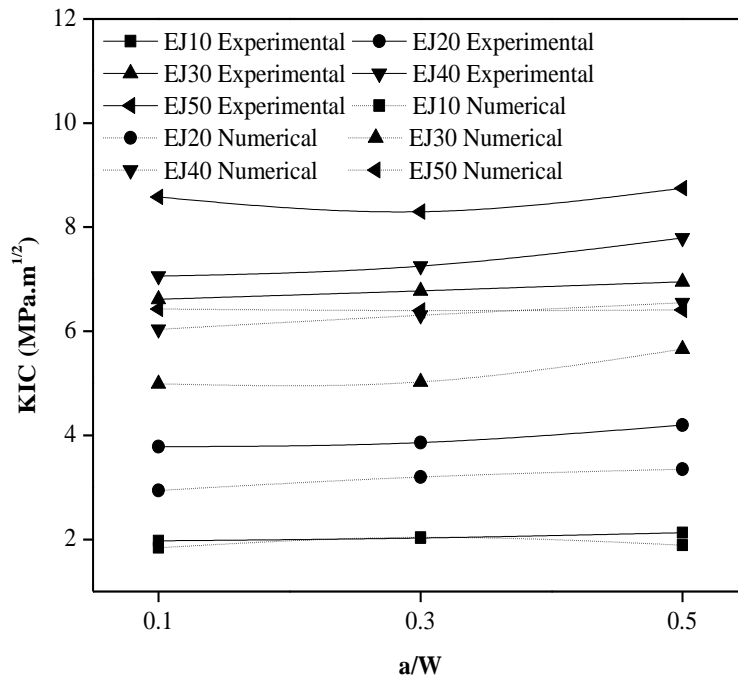
Figure 4.19a Stress intensity factor of unfilled jute-epoxy composite
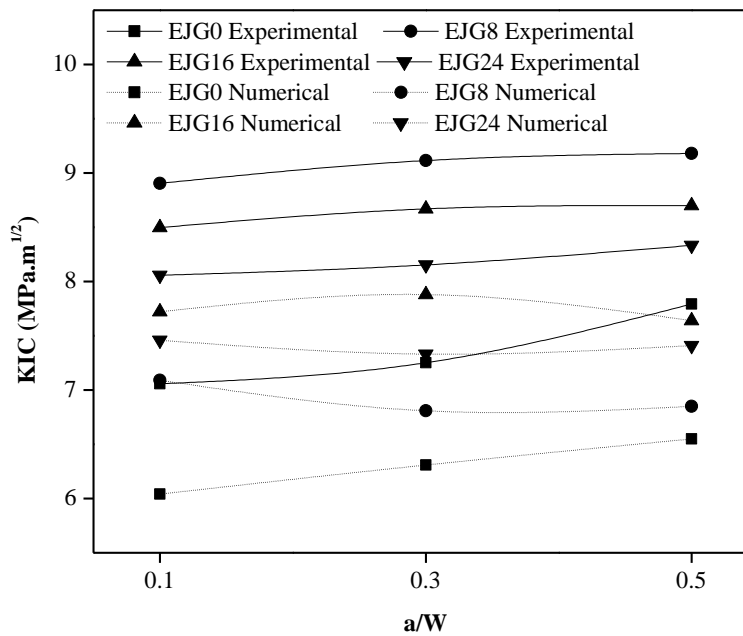
Figure 4.19b Stress intensity factor of granite powder filled jute-epoxy composite

Figure 4.20a shows the stress contour developed in the specimen for unfilled 40 wt.% jute epoxy composite with crack length to width ratio of 0.5, when subjected to fracture test

in mode I and corresponding value for K_{IC} along the length of crack is shown in the Figure 4.21c. The fracture toughness of granite powder filled composite is illustrated in Figure 4.19b and reported that the value of K_{IC} increases almost all the particulate filled jute epoxy composites. But the effect of increase in experimental value of K_{IC} is marginal in case of 16 wt.% and 24 wt.% of granite powder filled jute epoxy composites compared to virgin composite. It is observed that the composite shows tough response for all the weight percentage of granite powder addition compared to virgin composite. The reason for improvement in toughness may be the crack gets arrested by the granite particle which present along the plane of propagation of crack. Highest improvement in the experimental value of K_{IC} is observed for 8 wt.% granite powder filled jute epoxy composite and for 16 and 24 wt.% addition of granite powder the value is in the lower side but above value of virgin composite.

(a)   (b)

(c)   (d)
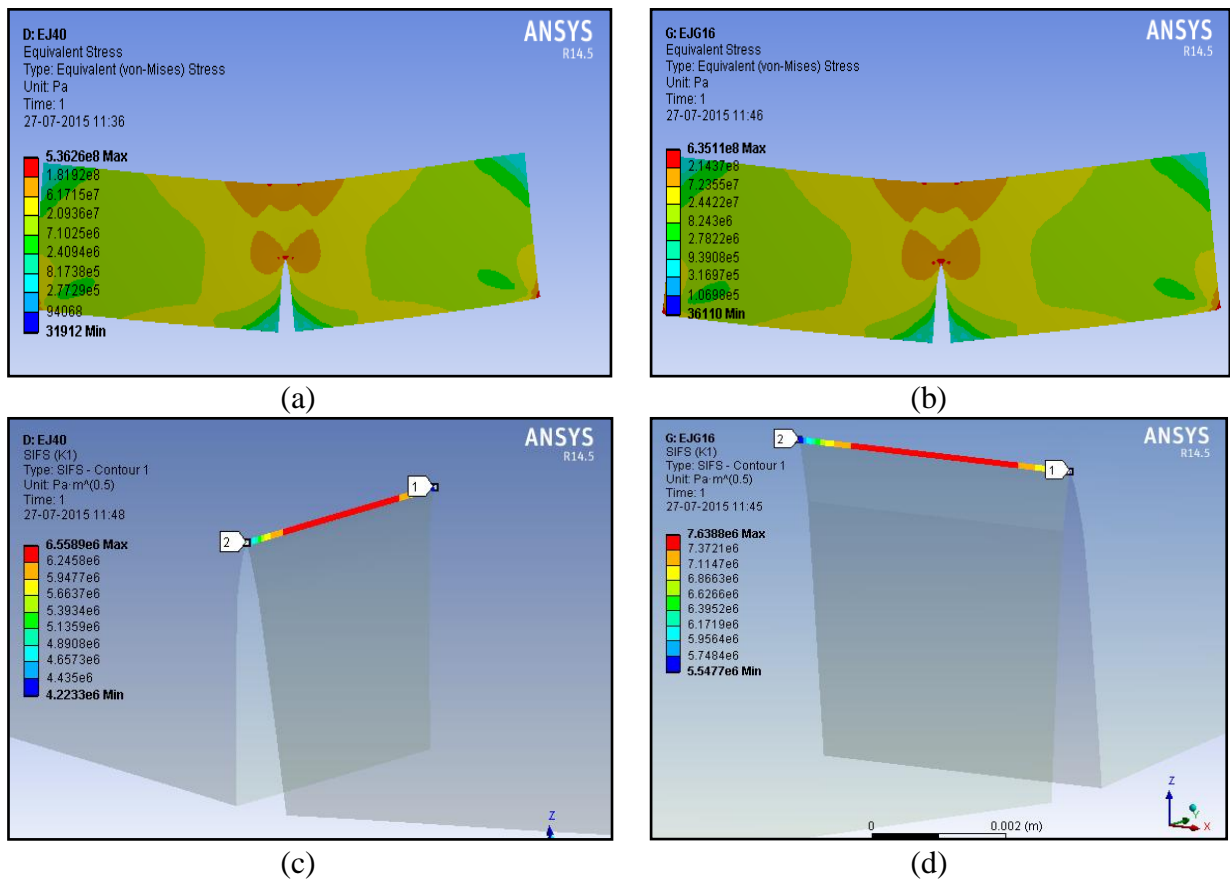
Figure 4.20 Numerical results for fracture analysis with a/W ratio of 0.5 a) von-Mises stress contour for EJ40 b) von-Mises stress contour for EJG16 c) stress intensity factor along the crack front for EJ40 d) stress intensity factor along the crack front for EJG8

Form both, experimental and numerical result it is evident that the effect of ratio of crack length to width of specimen is marginal on the value of K_{IC}. Figure 4.19b shows that the numerically predicted value for granite powder filled jute epoxy composites is higher compared to unfilled jute composite. The highest value is reported for 16 wt.% granite

powder filled jute epoxy composites as compared to virgin and other filled composites. For all the granite powder filled composites the numerically predicted values of K_{IC} are lower than the one determined from experimental method. The stress contour developed in the specimen of 16 wt.% granite powder filled jute epoxy composite (with a/W ratio of 0.5) subjected to fracture test in mode I is shown in Figure 4.20b. The stress intensity factor along the crack length for same composite specimen is shown in Figure 4.20d. Along the crack length the predicted value of K_{IC} varies and the value is decreased at the end of crack whereas, the highest value is observed at the half of the crack length (see Figure 4.21).
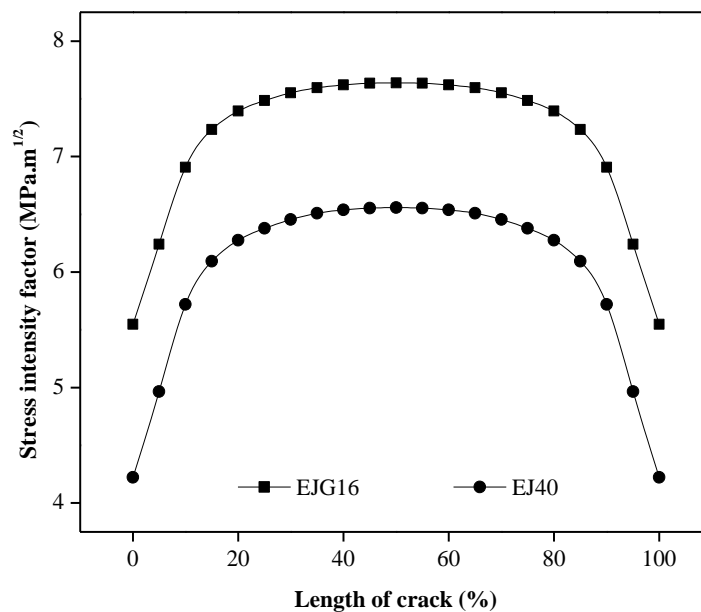
Figure 4.21 Numerical value of stress intensity factor along the length of crack front

4.2.7 Numerical analysis of wind turbine blade for static loading

Figure 4.22a and 4.22b show the stress contour developed in the wind turbine blade structure for unfilled 40 wt.% jute epoxy composite and 16 wt.% granite powder filled jute epoxy composite respectively. It is recorded that the value of maximum stress developed is 20.83 MPa in both the composites. Whereas, the tip deflection for granite powder filled jute epoxy composite is at lower side compared to tip deflection of virgin composite. The tip deflection of wind turbine blade for unfilled 40 wt.% jute epoxy composite is 1.385 m (see Figure 4.23a and 4.23b) and for 16 wt.% granite powder filled jute epoxy composite is 1.246 m (see Figure 4.24a and 4.24b). This is evident from the observed values of stress and tip deflection is addition of granite powder made the jute fiber reinforced composite stiff compared to unfilled one.

(a)   (b)
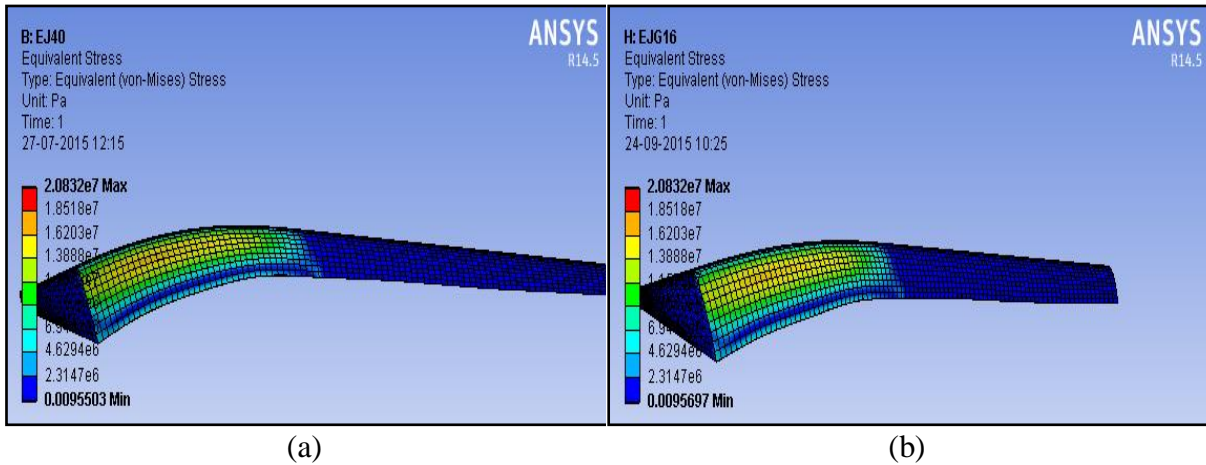
Figure 4.22 Stress contour plot for applied force a) unfilled composite with 40 wt.% of jute fiber b) 16 wt.% granite powder filled jute epoxy composite

(a)   (b)
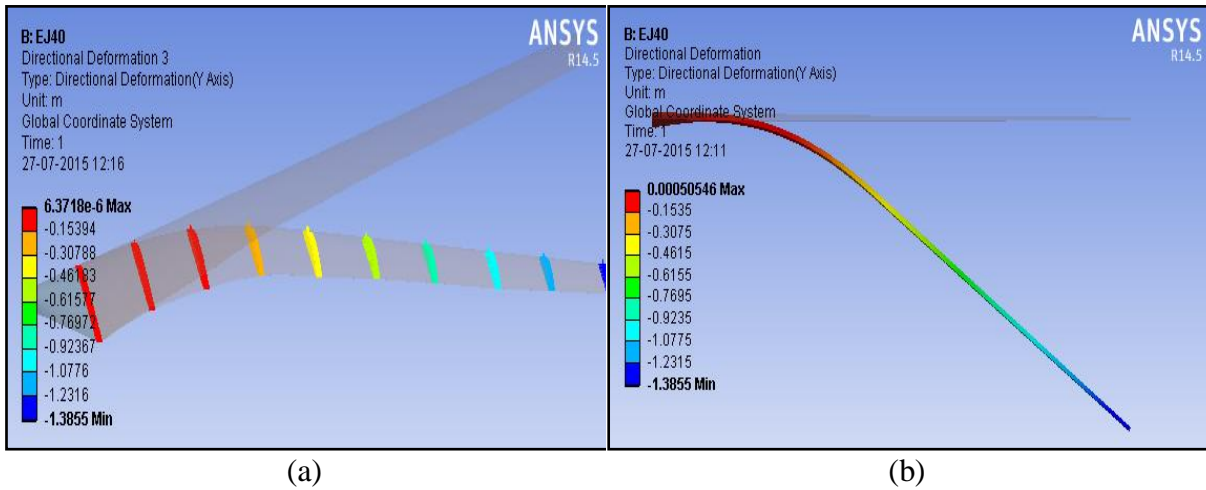
Figure 4.23 Flap-wise deflection of blade for unfilled 40wt.% jute epoxy composite a) at ten sections along the lengths of blade b) deflection from plane of rotaion

(a)   (b)
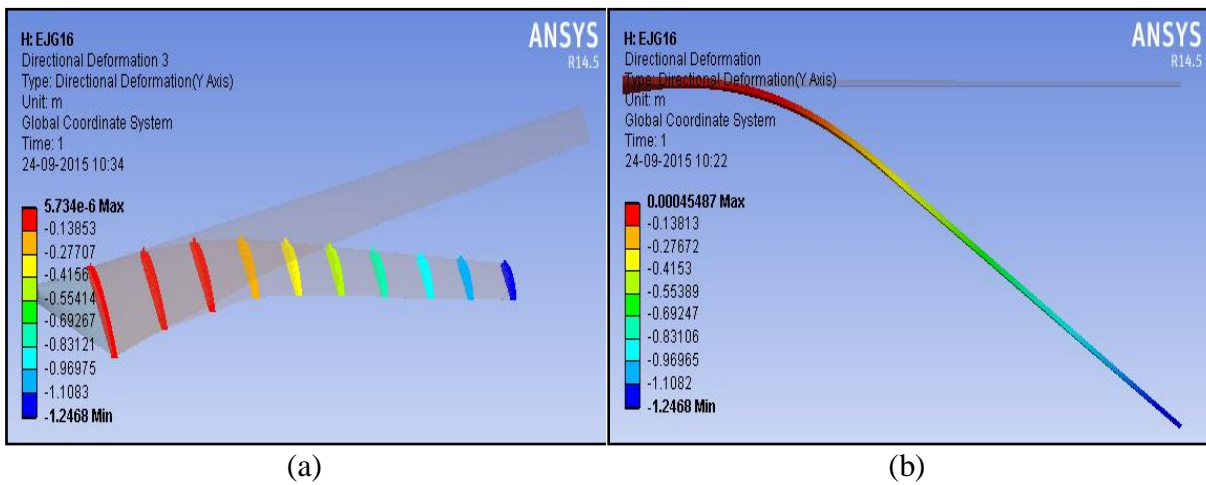
Figure 4.24 Flap-wise deflection of blade for 16 wt.% granite filled composite a) at ten sections along the lengths of blade b) deflection from plane of rotaion
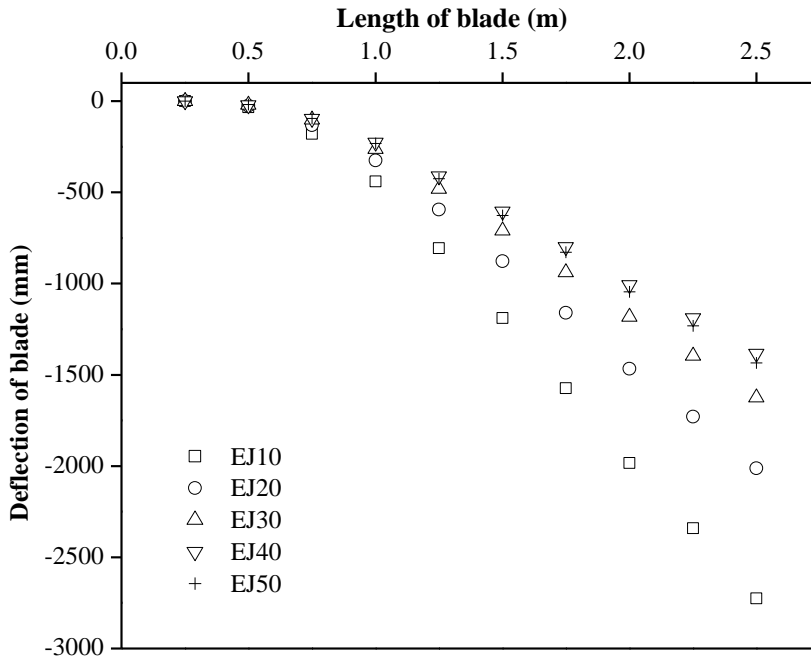
Figure 4.25a Deflection along the length of blade for unfilled jute epoxy composite
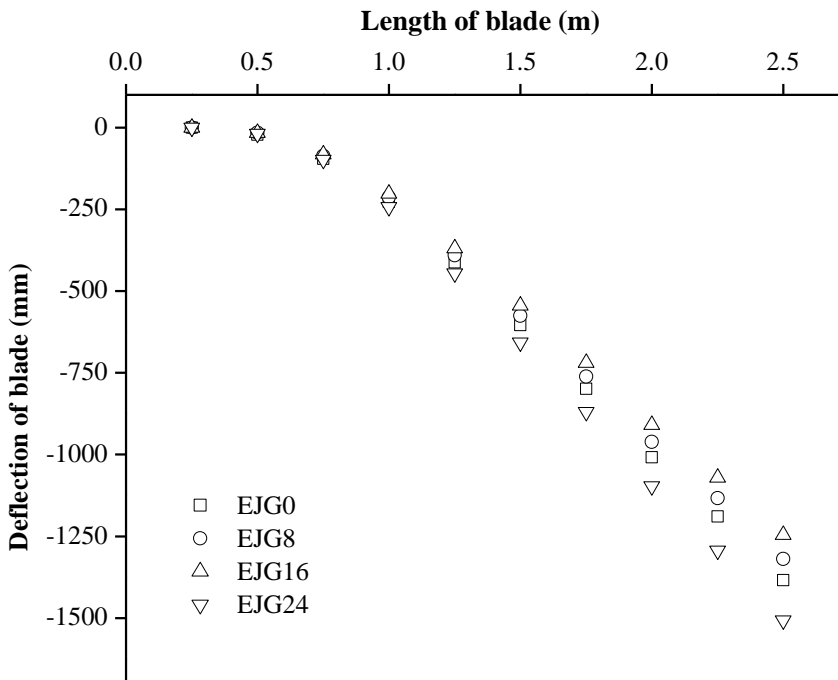
Figure 4.25b Deflection along the length of blade for granite powder filled jute epoxy composite

The deflection is observed for all the unfilled and granite powder filled jute epoxy composites is much higher than the deflection observed for the unfilled and granite powder

filled glass epoxy composites. The deflection of blade along the length of blade is also recorded for all the composites at ten equidistance points as shown in Figure 4.23a and 4.24a respectively. The variation in deflection at ten equidistance points along the length of blade for unfilled and granite powder jute epoxy composites are shown in Figure 4.25a and 4.25b respectively. The addition of jute fiber up to 40 wt.% shows significant reduction in deflection of blade but for further addition of jute fiber content of 50 wt.% does not lead to any effect in deflection of blade. The maximum tip deflection of 2.75 m is noticed for unfilled composite reinforced with 10 wt.% jute fiber. The deflection of tip for blade is reduced to 2 m, 1.5 m, 1.25 m and 1.25m for addition of 20, 30, 40 and 50 wt.% jute fiber respectively. Whereas, for granite powder filled jute epoxy composite the descending order of maximum tip deflection as EJG16, EJG8, EJG0 and EJG24 respectively. The incorporation of both the type of reinforcement improves the mechanical performance of composites which results in resisting deflection of wind turbine blade.

Part-III

4.3 Physical, mechanical and fracture toughness analysis of unfilled and granite powder filled carbon-epoxy composites

4.3.1 Density and void fraction

Measurement of density and void content of polymer matrix composite gives thought about how the composite perform when subjected to mechanical tests [264]. Measurement of accurate void content is quite difficult irrespective of the technique used for measurement. However, the relative measurement of density and void content for series of composite specimens were reliable and practical to obtain [265] the appropriate results. The void fraction is calculated by using the measured and theoretical density of unfilled and granite powder filled carbon epoxy composites are depicted in Table 4.5. Increase in density of composite with reinforcement of carbon fiber and granite powder with higher density than epoxy matrix, is obvious and same has been reported in the present investigation. The addition of carbon fiber from 10 wt.% to 50 wt.% results in close packing of fiber and epoxy with fewer voids. For filler addition at lower side (8 wt.%) also shows decrease in voids compared to virgin composite but further addition of filler content marginally increased the voids in the hybrid composite. This may be due to formation of void spaces at the interface between fiber and filler.

Table 4.5 Measured and theoretical density of the composites

Composite	Measured density (g/cc)	Theoretical density (g/cc)	Volume of void fraction (%)
10 wt.% carbon fiber	1.064	1.145	7.03
20 wt.% carbon fiber	1.113	1.193	6.68
30 wt.% carbon fiber	1.21	1.245	2.83
40 wt.% carbon fiber	1.268	1.303	2.65
50 wt.% carbon fiber	1.333	1.366	2.38
40 wt.% carbon fiber + 8wt.% granite powder	1.345	1.378	2.42
40 wt.% carbon fiber + 16wt.% granite powder	1.402	1.464	4.20
40 wt.% carbon fiber + 24wt.% granite powder	1.461	1.56	6.33

4.3.2 Hardness

Reinforcement in polymer matrix generally resulted in improvement of hardness of composites and improvement in hardness due to particulate filler is higher than reinforcement of fiber [11, 227]. The results obtained for the effect of fiber and filler in epoxy composite is in agreement with above statement and illustrated in Figure 4.26. The improvement in hardness with the increase in reinforcement may be attributed to the close packing of reinforcement and matrix under compressive force applied during hardness testing. Close packing is resulted in better stress transfer at the reinforcement-matrix interface which resists penetration of indenter. In unfilled carbon epoxy composites the significant improvement in hardness is observed from 31 H_V to 36 H_V with the increase in carbon fiber loading from 20 wt.% to 30 wt.% respectively. For granite powder filled carbon epoxy composites the significant improvement in hardness (from 42 H_V to 46 H_V) is observed with the increase in filler content from 8 wt.% to 16 wt.% respectively. From Figure 4.26, it is evident that influence of fiber and filler are marginal on hardness value of composites beyond reinforcement of 40 wt.% of fiber and 16 wt.% of filler material. Higher content of reinforcement resulted in fiber-fiber and fiber-filler interaction which is main cause of weak interface. Hardness is the important property affecting the erosion wear behavior of composite materials.

4.3.3 Tensile strength

Reinforcement of high modulus fiber in polymer matrix is improved the tensile strength and the composites become stiffer in the fiber direction [266]. With the increase in fiber loading

the tensile load bearing capacity is increased and the elongation at break decreases which results in improvement in tensile strength and tensile modulus of carbon fiber reinforced epoxy composite (see Figure 4.27). For initial increase in fiber loading up to 20 wt.% the rate of improvement in tensile strength is slow. This may be due to the less amount of interfacial area which is unable to transfer stress at interface between fiber and matrix. Further, significant improvement in tensile strength is observed for 30 and 40 wt.% fiber loading. This showed the sufficient interfacial area between fiber and matrix which results in good stress transfer at interface. However, Table 4.6 showed that higher fiber loading of 50 wt.% does not lead to significant improvement in tensile strength of unfilled carbon epoxy composite because of insufficient wetting of fiber and increase in fiber-fiber interaction.
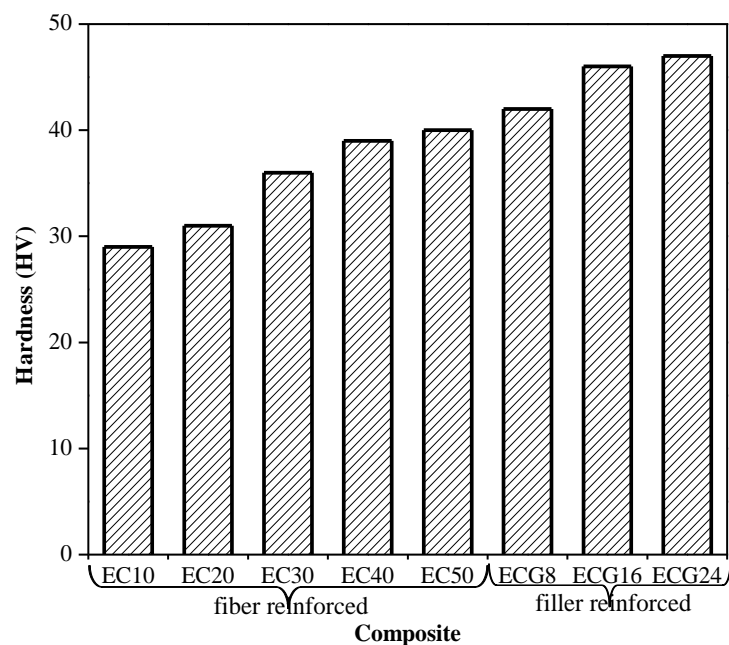
Figure 4.26 Effect of fiber and filler on hardness

Whereas, granite powder addition showed negative effect on tensile strength of particulate filled carbon epoxy composite as shown in Figure 4.27. Tensile strength of 8 wt.% granite powder filled carbon epoxy composite is slightly improved and further addition of granite powder results in marginal decrease in tensile strength. The decrease in tensile strength at higher filler content may be due to formation of stress concentration regions at the edges of granite particle and most prone to initiation of cracks. Variation in tensile modulus for unfilled and granite powder filled carbon epoxy composites are shown in Table 4.6. Reinforcement in polymeric resin resisted deformation of matrix material that reducing the strain. Hence, it is obvious to improve the tensile modulus of composite [252]. Accordingly,

the tensile modulus improved with reinforcement of carbon fiber in epoxy matrix but this is possibly does not happen in case of addition of granite powder and tensile modulus decreases with increase in granite powder in spite of reinforcement of long fibers. Increase in void content with addition of granite powder is may be the reason for decrease in tensile modulus. In the view of determining the optimum filler content with least compromise in tensile strength break-even point is determined as shown in Figure 4.27. Tensile strength of 21 wt.% granite powder filled carbon epoxy composite shows same value as one for 36 wt.% carbon fiber reinforced epoxy composite.
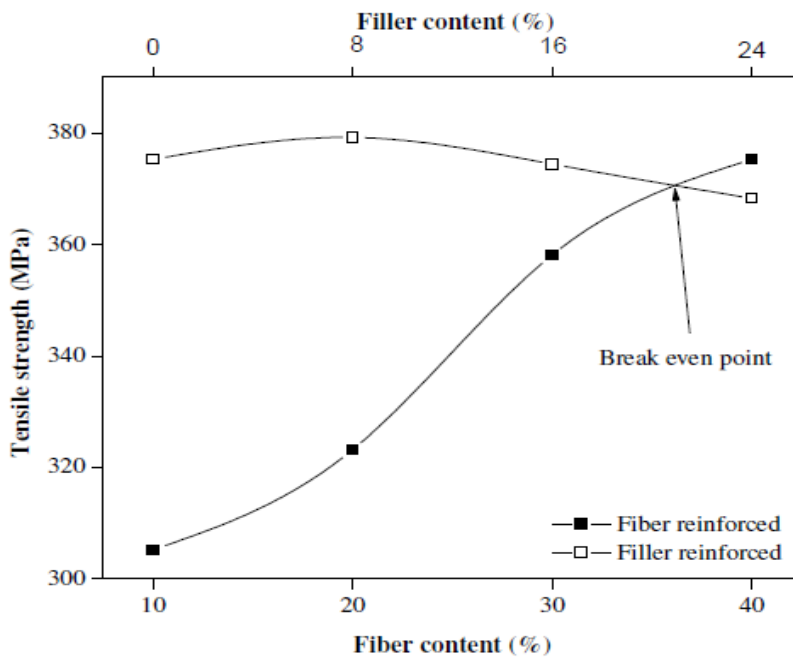
Figure 4.27 Effect of fiber and filler content on tensile strength

4.3.4 Flexural strength

Flexural strength is one of the important properties of the fiber reinforced polymer composite as they tend to fail in bending due to high lateral dimension to thickness ratio. Positive reinforcement effect of carbon fiber is observed on flexural strength of unfilled carbon epoxy composite as shown in Figure 4.28. Flexural strength of composite with 10 wt.% carbon fiber is 180.6 MPa which is improved to 212.8 MPa with the reinforcement of 20 wt.% carbon fiber (improvement 17.8%). Significant improvement of 40.6% is found for reinforcement of 30 wt.% carbon fiber from 212.8 MPa to 299.3 MPa respectively. Composite with carbon fiber loading from 40 wt.% showed flexural strength as 356.5 MPa which accounts to improvement of 19.1% compared the composite with 30 wt.% carbon fiber reinforcement. Similar, to tensile strength, increase in fiber loading to 50 wt.% does not lead to minor improvement in flexural strength (see Table 4.6). Flexural modulus of unfilled and granite

powder filled carbon epoxy composites are shown in Table 4.6. High strength fibers act as bridge between cracked surfaces and sustain more bending force with lower deformation [267]. Hence, flexural modulus of unfilled carbon epoxy composite is improved with the increase in fiber loading.
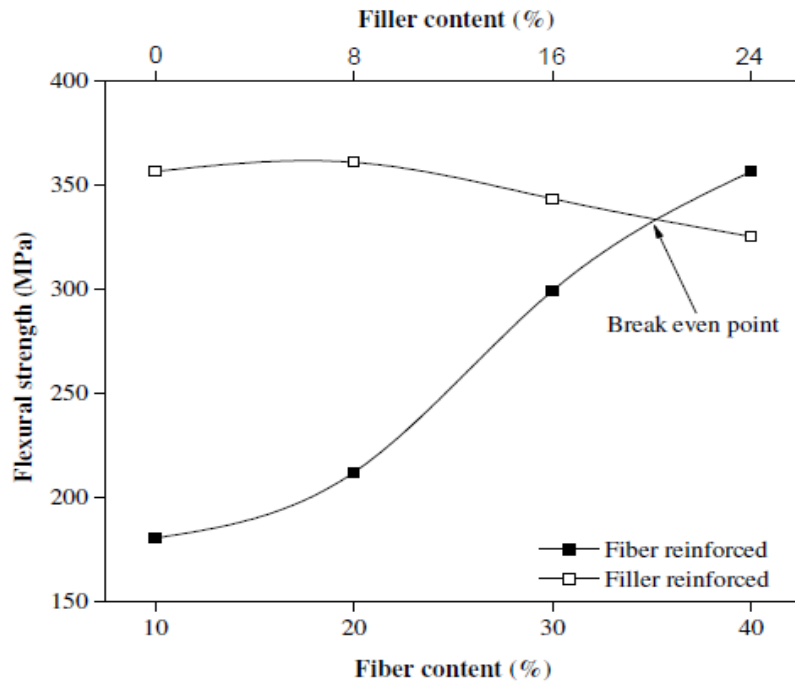
Figure 4.28 Effect of fiber and filled content on flexural strength

Effect of incorporation of granite powder in carbon epoxy composite is marginal. The flexural strength is improved from 356.5 MPa for unfilled composite to 360.9 MPa for 8 wt.% granite powder filled carbon epoxy composite. Further value slightly decreased to 343.4 MPa and 325.3 MPa for granite powder content of 16 and 24 wt.% respectively. Break-even analysis between unfilled and filled composites show that 20 wt.% granite powder filled carbon epoxy composite shows same flexural strength for 35 wt.% carbon fiber reinforced epoxy composite. Whereas, flexural modulus is decreased with increase in granite powder content in filled carbon epoxy composite. This may be due to early crack initiation at edges of granite particles in the fiber reinforced epoxy composites.

4.3.5 Inter-laminar shear strength

Composites laminate are most prone to failure by de-lamination between fiber layers when subjected to bending. Figure 4.29 shows the effect of fiber and/or filler content on inter-laminar shear strength (ILSS) of unfilled and granite powder filled carbon epoxy composites. ILSS increased with increase in fiber loading. Most significant improvement of 41% is found for increase in fiber loading from 20 wt.% to 30 wt.%. Further, increase in fiber loading from

30 wt.% to 40 wt.% resulted in improvement of ILSS by 19%. For 50 wt.% fiber loading the improvement is insignificant due to increase in fiber-fiber interaction because of improper wetting at higher weight fraction of fiber loading. Granite powder addition of 8 wt.% shows increase in ILSS to 18.04 MPa from 17.82 MPa for unfilled carbon epoxy composite. This improvement at lower filler content may be resulted of resistance of granite particles to debonding from matrix. However, the higher filler content generates region of stress concentration at edges of granite particle which resulted in decrease of ILSS of 16 wt.% and 24 wt.% granite powder filled carbon epoxy composites.
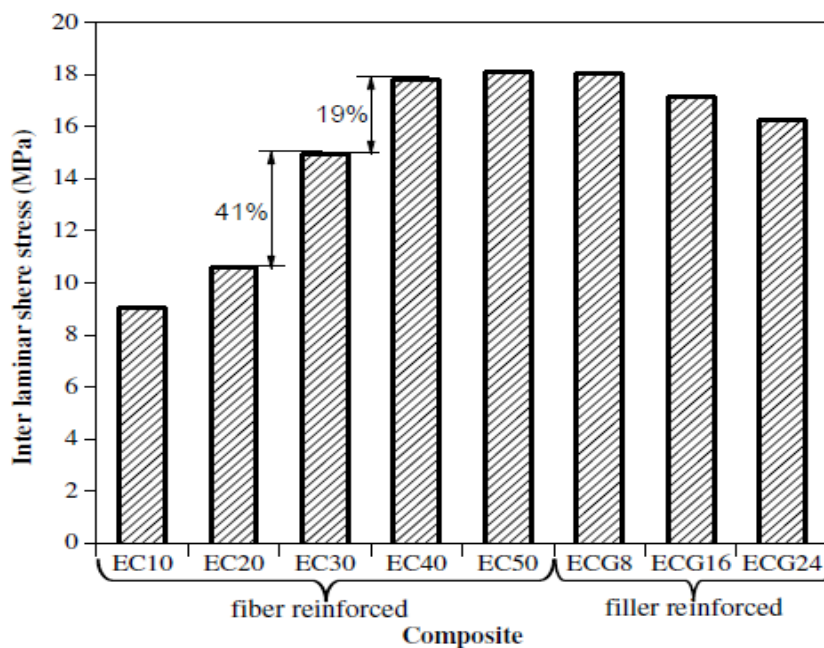
Figure 4.29 Effect of fiber and filled content on ILSS

4.3.6 Impact strength

Impact strength is determined in terms of energy absorbed before fracture by unit area under high strain rate loading in presence of notch. The Figure 4.30 shows impact strength of unfilled and granite powder filled carbon epoxy composites. It is clearly noticeable that the improvement in impact strength is quite large for fiber reinforced composite as compared to particulate filled composites. The increment in impact strength owing to reinforcement of fiber and filler is defined by lines with slope of 0.46 and 0.9 respectively. This may be due to higher amount of energy absorbed by fiber pull-out before fracture. Impact strength of 10 wt.% carbon fiber reinforced epoxy composite is 21.5 kJ/m^2 which improved to 23.6, 30.46 and 32.81 kJ/m^2 with fiber loading of 20, 30 and 40 kJ/m^2 respectively. Further addition 8, 16 and 24 wt.% of granite particles in composite shows linear improvement in impact strength to 33.47, 34.2 and 34.91 kJ/m^2 respectively. The mechanical properties of series of unfiled and granite powder filled carbon epoxy composites are illustrated in Table 4.6.
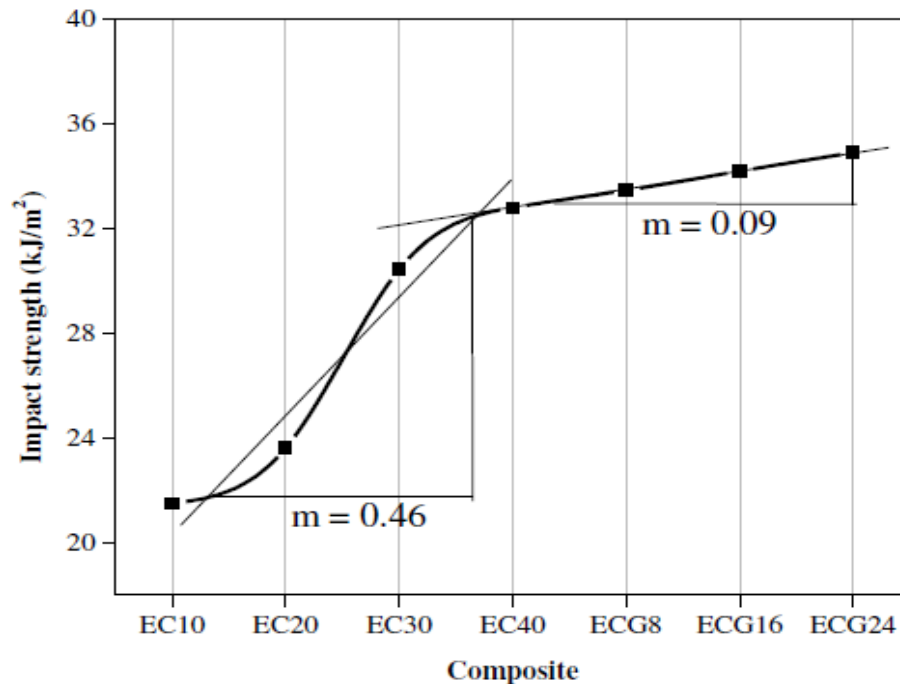
Figure 4.30 Effect of fiber and filled content on impact strength

4.3.7 Fracture toughness

Fracture toughness is usually used as a general term for measurement of material resistance to crack extension. The fracture toughness values may also serve as a basis in material characterization, performance evaluation, and quality assurance for typical engineering structures [80]. In present investigation the fracture toughness is evaluated by determining critical stress intensity factor (K_{IC}). Figures 4.31a and 4.31b illustrated both experimental and numerical value of K_{IC} for unfilled and granite powder filled carbon epoxy composite as a function of crack length to width ratio of specimen (a/W). It is clearly noticeable that the value of K_{IC} in both the unfilled and filled composites is not dependent on a/W ratio as it fairly remains constant for all three selected a/W ratio. Experimental value of K_{IC} for unfilled composite is improved significantly with the increase in fiber loading (see Figure 4.31a). The high strength fiber sustains higher load and crack initiated through matrix material, the fibers are still attached to crack surface that produce fiber-bridge in the crack wedge. The traction in the bridged fiber that increased the energy that required for further propagation of crack. This fiber bridge results in extrinsic toughening mechanism which played the major role behind the crack tip propagation. Extrinsic toughening is observed significant up to fiber loading of 40 wt.% and above this (i.e. for 50 wt.%) toughening is marginal. This may be due to improper wetting of fiber resulting in poor bonding between fiber and matrix interface. Thus, the traction force is decreased in bridged fiber though higher wt.% fibers are reinforced.

Table 4.6 Mechanical properties of unfilled and granite powder filled carbon epoxy composites

Composite	Tensile strength (MPa)	Tensile Modulus (MPa)	Flexural strength (MPa)	Flexural modulus (MPa)	ILSS (MPa)	Hardness (Hv)	Impact strength (kJ/m^2)
EC10	305.26 ± 15.25	3.89 ± 0.15	180.62 ± 7.2	2.39 ± 0.08	9.03 ± 0.7	29 ± 1	21.51 ± 2.13
EC20	323.21 ± 4.62	6.1 ± 0.23	212.18 ± 16.85	3.02 ± 0.09	10.6 ± 1.9	31 ± 1	23.63 ± 1.95
EC30	358.14 ± 23.85	7.67 ± 0.27	299.37 ± 17.21	4.20 ± 0.26	14.96 ± 1.42	36 ± 2	30.46 ± 1.22
EC40/ECG0	375.14 ± 17.56	8.78 ± 0.1	356.56 ± 28.66	7.04 ± 0.22	17.82 ± 1.26	39 ± 1	32.81 ± 3.05
EC50	378.4 ± 7.4	8.92 ± 0.08	361.875 ± 10.54	7.31 ± 0.29	18.09 ± 2.11	40 ± 1	33.02 ± 2.32
ECG8	379.41 ±13.65	8.7 ± 0.11	360.93 ± 18.74	7.10 ± 0.18	18.04 ± 1.36	42 ± 1	33.47 ± 1.65
ECG16	374.41 ± 22.78	8.52 ± 0.24	343.43 ± 15.78	6.93 ± 0.21	17.17 ± 1.91	46 ± 2	34.2 ± 2.44
ECG24	368.28 ± 7.12	8.39 ± 0.18	325.31 ± 24.2	6.27 ± 0.34	16.26 ± 2.15	47 ± 1	34.91 ± 1.27

The data represents mean ± standard deviation.

Granite powder addition up to 16 wt.% depicted positive effect on value of K_{IC} as shown in Figure 4.31b. The significant improvement in value of K_{IC} for addition of 8 and 16 wt.% of granite powder is reported because of intrinsic toughening mechanism. The granite particles present on the path of crack propagation bifurcate or deviate the crack which became cause for energy conservation. Further, addition of granite powder from 16wt.% to 24 wt.% that significantly decreased the value of K_{IC} but still the value is on higher side than unfilled composite for all the three a/W ratio. The numerical value of K_{IC} for unfilled and granite powder filled carbon epoxy composite is showing similar improvement with reinforcement of carbon fiber and granite powder. The value is determined numerically which shows lower value than one evaluated in experimentally because of deficiency of modeling extrinsic and intrinsic toughening of composite material due to reinforcement of fiber and filler respectively.

Minimum variation for value of K_{IC} by experimental and numerical method are recorded as 0.23 MPa.m$^{1/2}$ for unfilled 10 wt.% carbon epoxy composite for a/W ratio of 0.1. Whereas, maximum variation of 5.43 MPa.m$^{1/2}$ is recorded for 16 wt.% granite powder filled carbon epoxy composite at a/W ratio of 0.5. For unfilled carbon epoxy composites the numerical values of K_{IC} are in agreement with experimental values but in case of granite powder filled carbon epoxy composites the numerical values are slightly lower than the experimental values due to absence of extrinsic as well as intrinsic toughening mechanism during modeling the geometry.
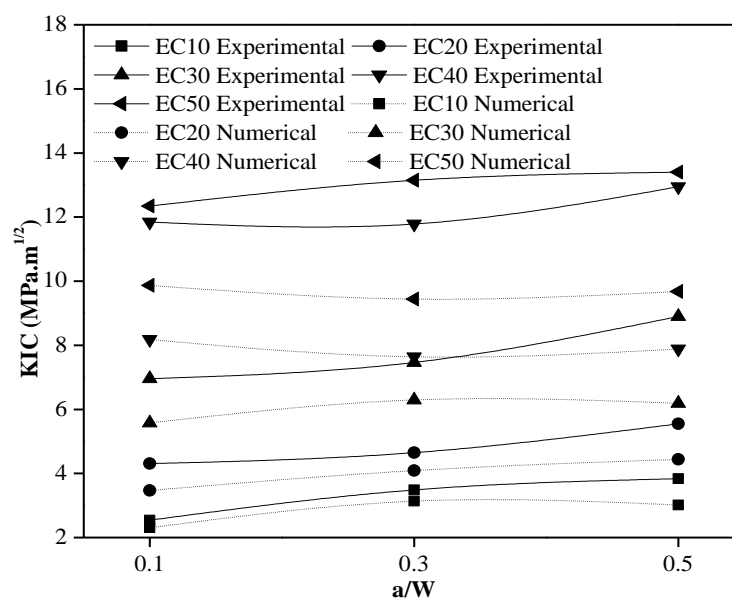
Figure 4.31a Fracture toughness of unfilled carbon epoxy composites
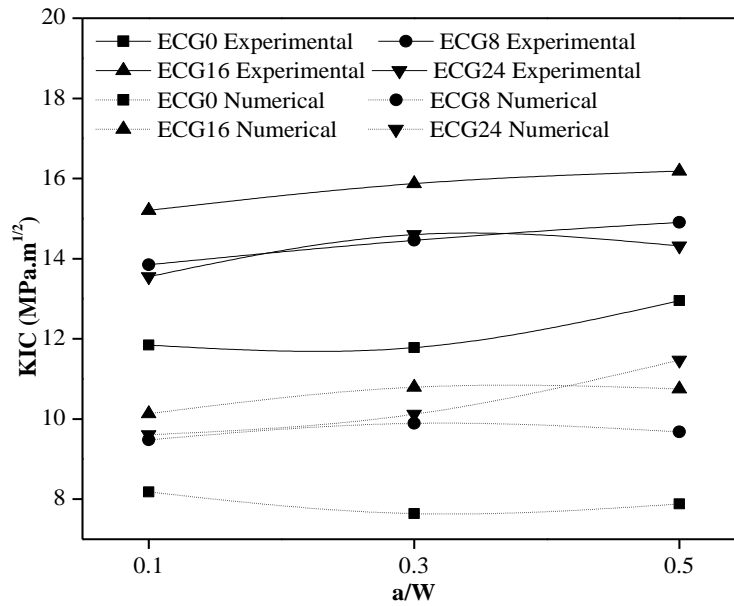
Figure 4.31b Fracture toughness of granite powder filled carbon epoxy composites
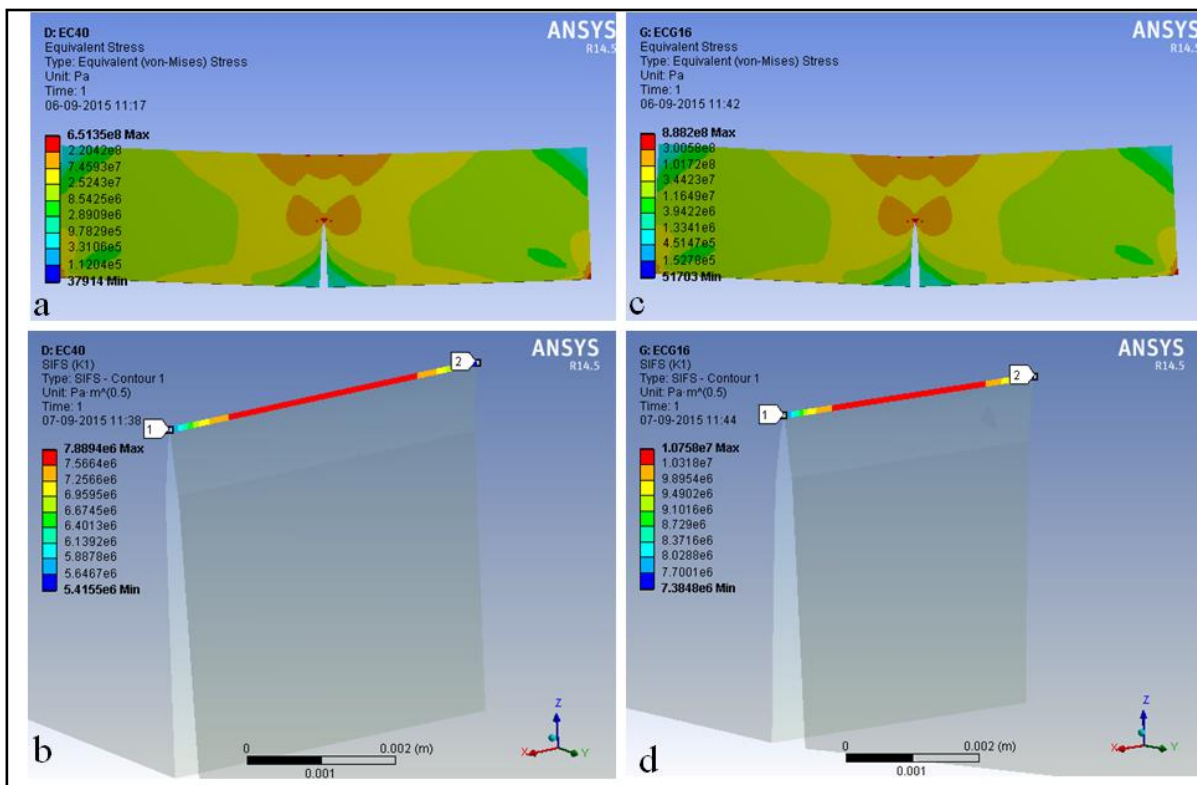
Figure 4.32 Numerical results for fracture analysis: (a) von-Mises stress contour for EC40, (b) von-Mises stress contour for ECG16, (c) stress intensity factor along the crack front for EC40, and (d) stress intensity factor along the crack front for ECG16.
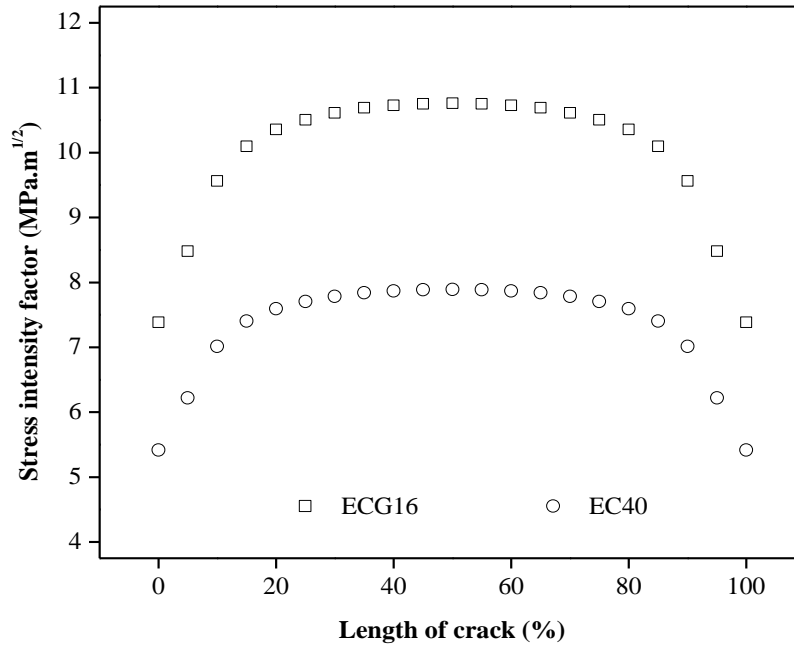
Figure 4.33 Numerical value of stress intensity factor along the length of crack front

Figure 4.32 shows the representative results for K_{IC} as obtained through numerical method. Figure 4.32a shows the stress contour developed in unfilled composite reinforced with 40 wt.% of carbon fiber at a/W ratio of 0.5. The stress developed in the environs of the crack is above the ultimate strength of particular composite. The value of K_{IC} along the crack length for 40 wt.% carbon epoxy composite is shown in Figure 4.32b. It is observed that the value is higher at the centre along the crack length and towards the end the value is lower. The corresponding data is represented in Figures 4.32c and 4.32d for 16 wt.% granite powder filled carbon epoxy composite. Similar, to unfilled composites, the observations are reported for stress contour shape and value of K_{IC} along the crack length for filled composites also. The maximum value of K_{IC} is determined numerically as 7.88 MPa.m$^{1/2}$ and 10.75 MPa.m$^{1/2}$ respectively for unfilled 40 wt.% carbon epoxy composite and 16 wt.% granite powder filled carbon epoxy composite. The predicted value for stress intensity factor along the crack length for composite designation EC40 and ECG16 is illustrated in Figure 4.33. The value is lower at 20% length of crack length on both sides and at the centre region highest value is observed.

4.3.8 Numerical analysis of blade

Deflection of blade computed from numerical analysis by using ANSYS R 14.5 for unfilled 40 wt.% carbon epoxy composite is shown in Figure 4.34. The deflection of blade is gradually increased from root to the tip of blade as shown in Figure 4.34a. The deflection of

blade up to 0.5m of length is negligible and maximum deflection of 193.21 mm is observed at the tip of the blade. The deformation of blade in the plane of rotation is shown in Figure 4.34b. Figures 4.35a and 4.35b show the corresponding values for 24 wt.% granite powder filled carbon epoxy composite. Similar to unfilled composite the 24 wt.% granite powder filled composite shows negligible deflection up to 0.5m length of blade and maximum deflection is observed at the tip of the blade. The deflection is recorded at tip section of the blade is 202.19 mm. For addition of 24 wt.% of granite powder which increased the tip deflection slightly by 8.98 mm and this increase in deflection is negligible as compared to length of blade (i.e. 2500mm) The observed deflection at the tip section of the blade is compared with experimental results as reported by Rajadurai et al. [14] (i.e. 195 mm).
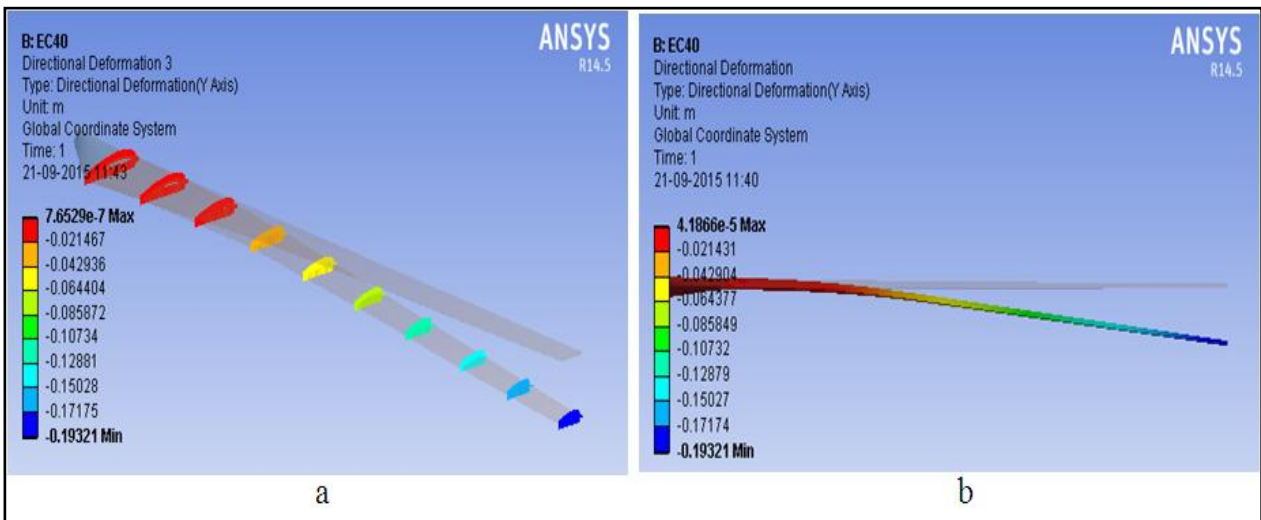
Figure 4.34 Flap-wise deflection of blade for unfilled 40 wt% carbon epoxy composite: (a) at 10 sections along the lengths of blade, and (b) deflection in the plane of rotation.
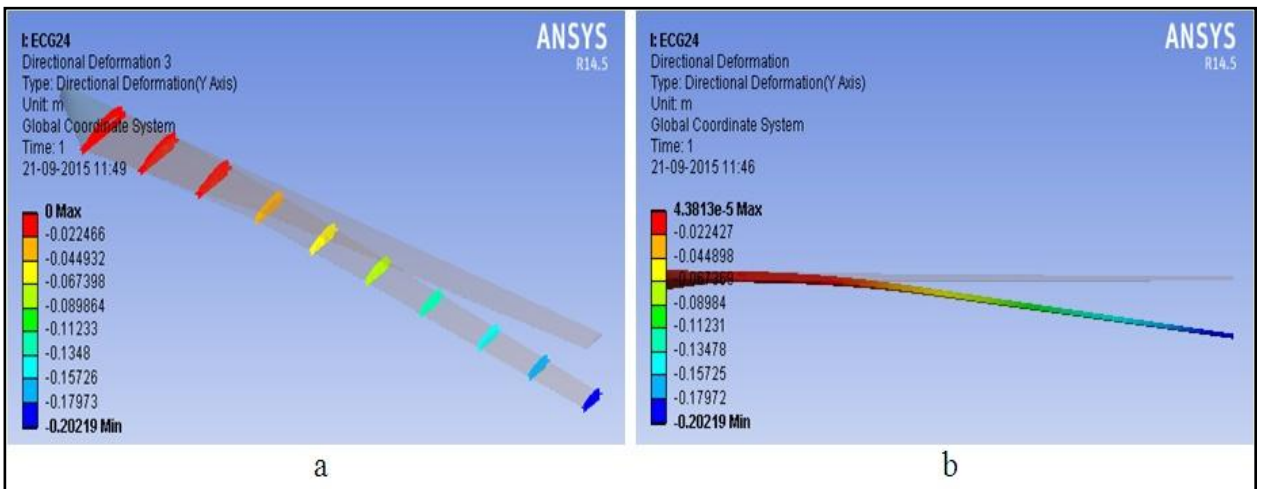
Figure 4.35 Flap-wise deflection of blade for 16 wt% granite filled carbon epoxy composite: (a) at 10 sections along the lengths of blade, and (b) deflection in the plane of rotation.
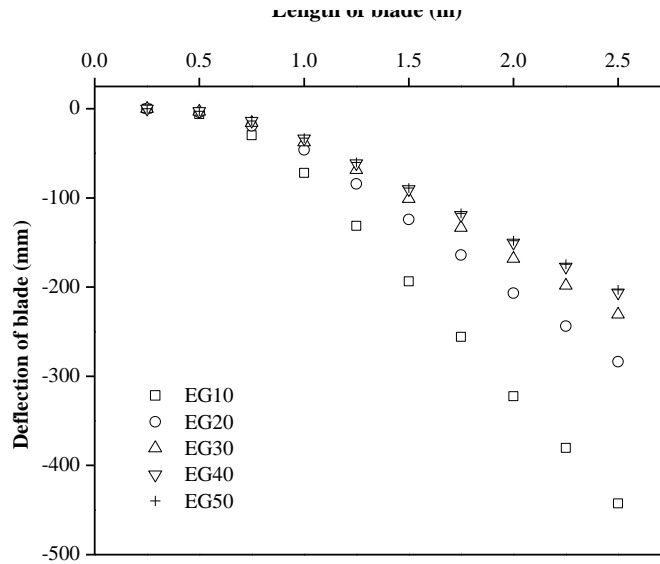
a
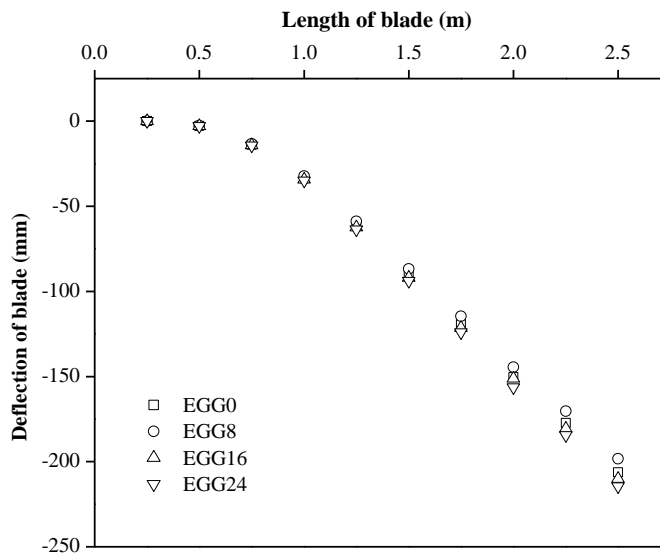
b

Figure 4.36 (a) Deflection along the length of blade for unfilled carbon-epoxy composite (b) Deflection along the length of blade for granite powder filled carbon-epoxy composite.

Figures 4.36a and 4.36b illustrate the deflection along the length of blade for unfilled and granite powder filled carbon epoxy composites respectively. Maximum deflection at tip of blade is recorded as 435.77mm for 10 wt.% carbon epoxy composite. The tip deflection is drastically decreased to 277.89mm with the reinforcement of 20 wt.% carbon fiber. Further, addition of carbon fiber to 30 wt.% and 40 wt.% resisted the tip deflection to 221.01mm and

193.07mm respectively. However, for 50 wt.% carbon fiber reinforcement no significant decreased in tip deflection is observed (see Figure 4.36a). Figure 4.36b shows that the deflection of blade is not much affected for varying the content of granite powder in composites. The tip deflection is recorded as 194.84mm, 198.96mm and 202.4 mm for incorporation of 8 wt.%, 16 wt.% and 24 wt.% granite powder as compared to 193.07 mm for unfilled carbon epoxy composite respectively.

Chapter Summary

This chapter has provided:

- ❖ The relative effects of type and content of different fibers on various physical and mechanical properties of polymer composites

- ❖ The mechanical and physical characterization of the granite powder filled fiber reinforced polymer composites.

- ❖ An attempt to validate the experimental value of fracture toughness with numerically predicted value using analysis software.

The next chapter presents the thermal and thermo-mechanical analysis of unfilled and granite powder filled fiber reinforced polymer composites.

*****

THERMAL AND THERMO-MECHANICAL ANALYSIS OF COMPOSITES

Thermal characterization of polymeric materials is a critical issue when composite is specifically used in above ambient temperature environment. A concise evaluation of the application of thermal analysis in polymer science and engineering is intended. It is important for the researchers to be certain to take advantage of the wide range of knowledge that can be gained by using multiple modes of thermal analysis. No single instrument is capable of entirely characterizing a material for thermal properties; therefore, the knowledge gained from multiple modes of thermal analysis must be presented in order to provide the most accurate description of the sample. Using additional methods for thermal analysis the material made the analysis multi-faceted. This chapter describes dynamic mechanical analysis, thermo-gravimetric analysis and thermal conductivity analysis of unfilled and granite powder filled fiber reinforced epoxy composites. Further, the results obtained from dynamic mechanical analysis are extracted to determine the bonding characteristics of reinforcement. Comparative study of thermal conductivity as measured in experimentally and then predicted through theoretical model. Finally, 2D finite element method is also discussed in this chapter.

Part-I

5.1 Thermal and thermo-mechanical analysis of unfilled and granite powder filled glass-epoxy composites

5.1.1 Dynamic Mechanical Analysis

Dynamic Mechanical Analysis (DMA) is conducted to observe the variation in the storage modulus (E'), loss modulus (E'') and damping factor (tan δ) as a function of temperature to characterize the thermal response of composite under cyclic mechanical stresses. Figures 5.1a and 5.1b show the effect of temperature on the storage modulus (E′) of the unfilled and granite powder filled glass epoxy composites. Below glass transition temperature (T_g) the values for E' of the composites are found to be spacious to each other for unfilled and filled composites which shows greater contribution of glass fiber and granite filler towards the stiffness of the composites at low temperature. The composite filled with 24 wt.% granite powder is exceptional which shows negative hybridizing effect on storage modulus. The reason may be increased filler-fiber and/or filler-filler interaction which diminishes effective stress transfer between reinforcement and matrix material which causes the decrease in the value of E′ [132]. Decreasing trend of E′ value is observed with increase in temperature,

however no change is observed in E′ above 90°C. In rubbery region (after transition phase) the E′ remains slightly higher for higher fiber loading or filler content which indicate the effect of both fiber and/or filler reinforcement at higher temperatures i.e above T_g as shown in Figures 5.1a and 5.1b.
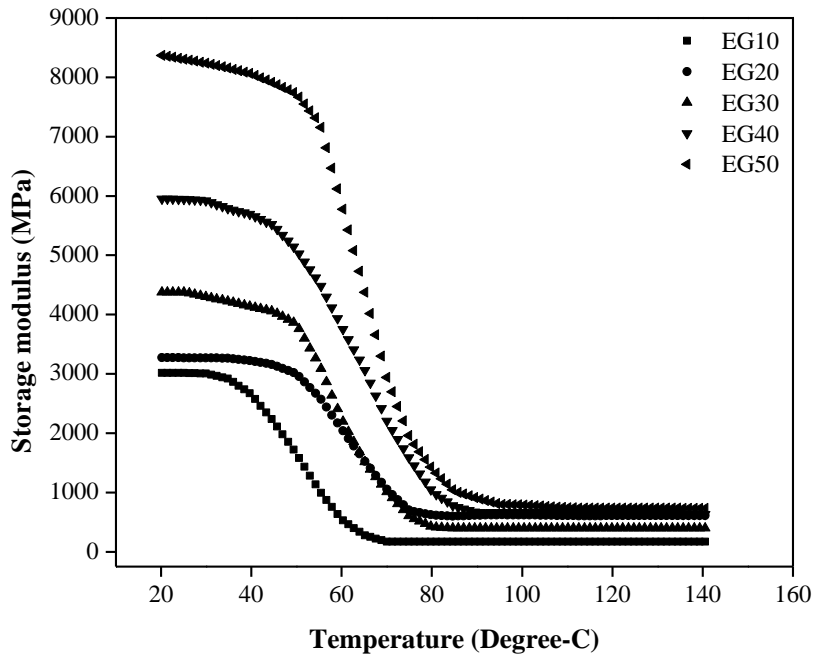
Figure 5.1a Variation of storage modulus of unfilled glass epoxy composite
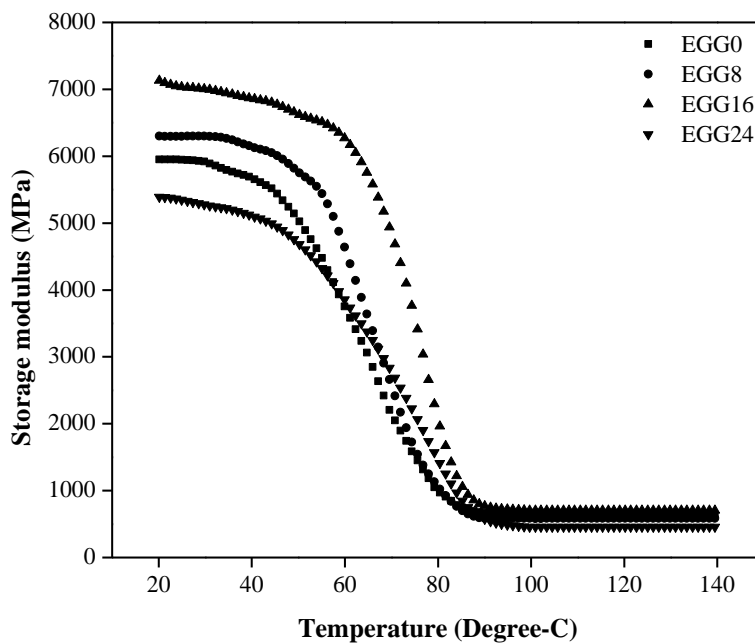
Figure 5.1b Variation of storage modulus of granite powder filled glass epoxy composite

In this research work, as observed from the above graphs both the unfilled and granite powder filled glass epoxy composites are showing significant role in glassy, glassy to rubbery and in rubbery region of composites. However, inclusion of 50 wt.% glass fiber results in steadily increase in E′ value up to 8.37 GPa from 3.01 GPa for 10 wt.% glass fiber epoxy composite (Figure 5.1a). Addition of 8 wt.% and 16 wt.% of granite powder causes to improve the E′ value to 6.99 GPa and 7.13 GPa respectively as compared with 5.95 GPa for unfilled composite (Figure 5.1b). However, by the incorporation of 24 wt.% granite powder drastically reduces the E′ value to 5.39 GPa.

The energy dissipation capability or loss modulus (E″) of the material has theoretical correspondence to the toughness of the composite. The variation of E″ under cyclic stresses as a function of increasing in temperature for unfilled and granite powder filled glass epoxy composite is as shown in Figures 5.2a and 5.2b respectively. Loss modulus peak shifted towards higher temperature is observed from Figure 5.2a with respect to increase in fiber loading. This shifting may be caused because of the restriction in mobility of the polymeric chain at the fiber surface [132]. The loss modulus curve shows broadening and higher value of peak with the increase in fiber loading. The filled composites also show an increase in loss modulus peak and broadening of peak for 8 wt.% and 16 wt.% of granite powder content (Figure 5.2b). This broadening and increase in loss modulus peak is because of the transition relaxation process of polymeric chain or due to increase in rigidity of polymeric chain [268].
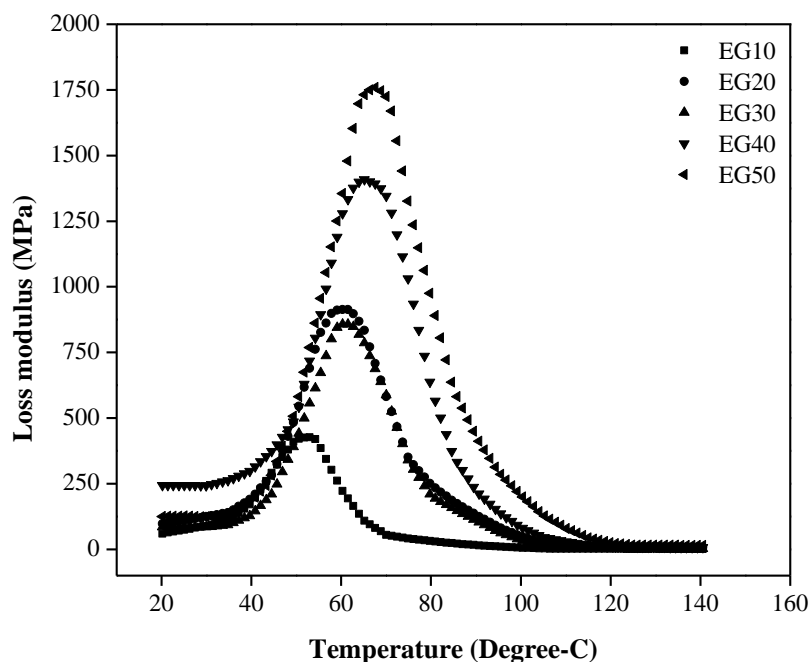
Figure 5.2a Variation of loss modulus of unfilled glass epoxy composite

The peak loss modulus for composite with 24 wt.% granite powder shows lower value as compared to virgin composite (Figure 5.2a). Temperature corresponding to the peak E" and peak Tan δ can be considered as T_g. However, temperature corresponding to peak loss modulus is more realistic value for T_g as compared to temperature corresponding to peak damping factor [269]. Table 5.1 shows the value of T_g corresponding to peal loss modulus for the unfilled and granite powder filled glass epoxy composite.
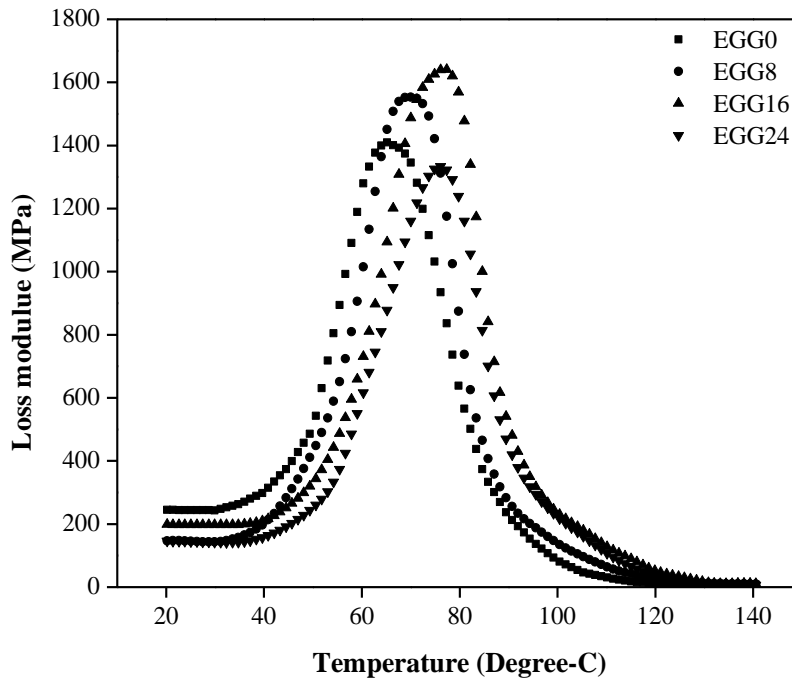
Figure 5.2b Variation of loss modulus of granite powder filled glass epoxy composite

The variation of damping factor (Tan δ) of unfilled and granite powder filled glass epoxy composite is shown in Figures 5.3a and 5.3b respectively. Damping property of composites is significantly affected by reinforcement/matrix interaction, void content as well as filler distribution and the type of fiber reinforcement [270]. The damping factor is found to be improved in the glassy-rubbery transition region for unfilled and granite powder filled composites. This may be due to increase in the mobility of polymeric chain within this temperature region, which results in more dissipation of energy at the interface of reinforcement. The height of the Tan δ peak has been observed maximum for the composite with a fiber loading of 50 wt.% indicating enhanced in damping performance which is followed by the composite with 40 wt.% of fiber loading (Figure 5.3a). Similarly, the value of peak damping factor decreased for lower weight fraction of fiber loading.
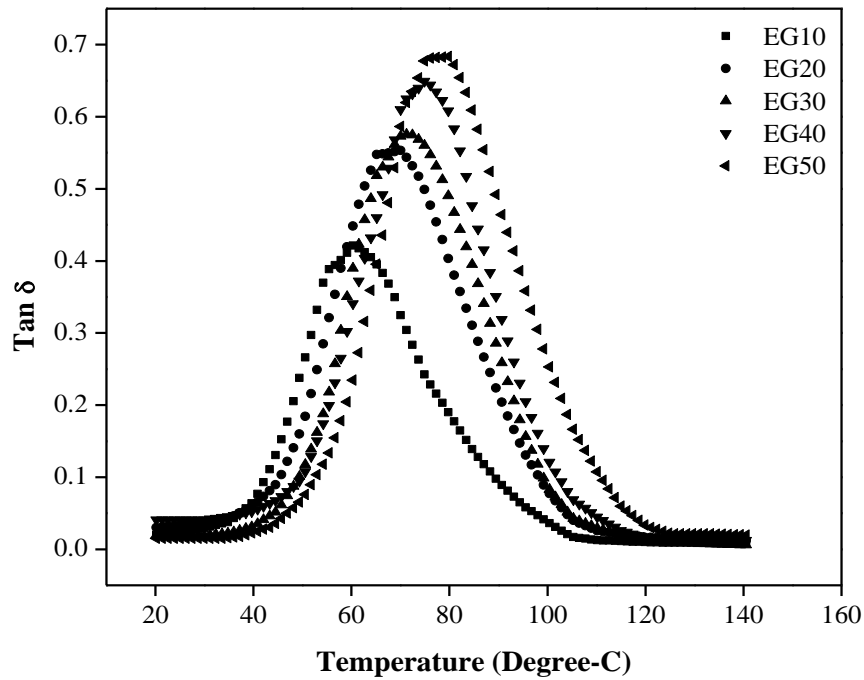
Figure 5.3a Variation of Tan δ of unfilled glass epoxy composite
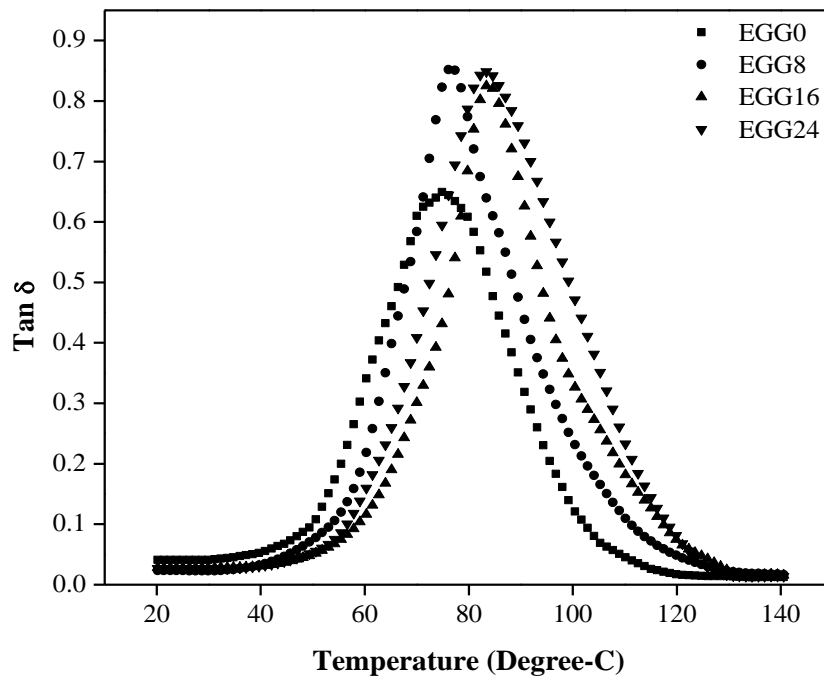
Figure 5.3b Variation of Tan δ of granite powder filled glass epoxy composite

The increase in damping factor at higher fiber loading (40 and 50 wt.%) may be due to poor interface (source for energy dissipation) between fiber and matrix. Incorporation of granite powder improved the damping factor of composite as compared to virgin composite

(Figure 5.3b). The peak damping factor for unfilled glass epoxy composite is 0.649 and it increased to 0.852, 0.824 and 0.849 for addition of 8 wt.%, 16 wt.% and 24 wt.% of granite powder respectively. This shows strong correlation between the damping factor with void content for granite powder filled glass epoxy composite. The temperature corresponding to peak damping factor shows positive shift (towards higher temperature) for both the types of reinforcement. The glass transition temperature corresponding to peak damping factor is shown in Table 5.1.

Table 5.1 Coefficient, peak height and glass transition temperature for unfilled and granite powder filled glass epoxy composites

Composite	Coefficient, C	[*]Adhesion efficiency factor, A	Glass transition temperature ($^\circ$C) T_g	
			from E''_{max}	from $\tan\delta_{max}$
EG10	0.804	-0.247	53.01	60.31
EG20	0.243	0.222	61.52	70.3
EG30	0.487	0.233	61.52	71.25
EG40/EGG0	0.420	0.565	65.17	74.89
EG50	0.507	0.959	67.60	79.76
EGG8	1.159	0.379	70.03	76.11
EGG16	1.067	0.398	77.32	83.40
EGG24	1.231	0.373	76.11	83.40

[*] calculated at T_g corresponding to peak loss modulus.

Table 5.1 shows the data (reinforcement effectiveness coefficient, adhesion efficiency factor and glass transition temperature) extracted from dynamic mechanical analysis of unfilled and granite powder filled glass epoxy composites. The effectiveness of reinforcement is inversely proportional to coefficient value (C) [271]. Results show better effectiveness of fiber as reinforcement than that of filler material. The adhesion efficiency (A) is calculated at T_g corresponding to peak loss modulus. Lower values of adhesion efficiency indicate stronger adhesion between the reinforcement and the matrix material [118]. Composite with 10 wt.% fiber shows strong adhesion (A= −0.247) between glass fiber and matrix material and it becomes poorer with the increase in fiber loading. For granite filled glass epoxy composite the adhesion efficiency is varied from 0.373 to 0.398, which shows better adhesion than unfilled composite with 40 and 50 wt.% of glass fiber. It was found that T_g value of composite is shifted to higher temperatures after incorporation of glass fiber as well as granite powder due to their higher thermal stability of reinforcement in comparison to epoxy resin.

Cole-Cole plot

The single relaxation peaks are not enough to describe the visco-elastic behaviour of the polymeric materials. Cole–Cole plot is used to examine the structural changes occurring in cross linked polymers after incorporation of reinforcement into polymeric matrices [269]. A Cole-Cole plot consists of constructing complex plane plot, in which E″ is plotted against E′. The behaviour of material is characterized by the Cole–Cole plots as reported to indicate the homogeneity of the system. Homogeneous polymeric systems are reported to show a perfect semi-circle diagram [272]. The Figures 5.4a and 5.4b show the Cole-Cole plots for unfilled and granite powder filled glass epoxy composites. The addition of fiber and filler content indicate the shape of Cole-Cole plot as imperfect semicircle. The imperfect circle indicates that there is heterogeneity in both the unfilled and granite powder filled glass epoxy composites.
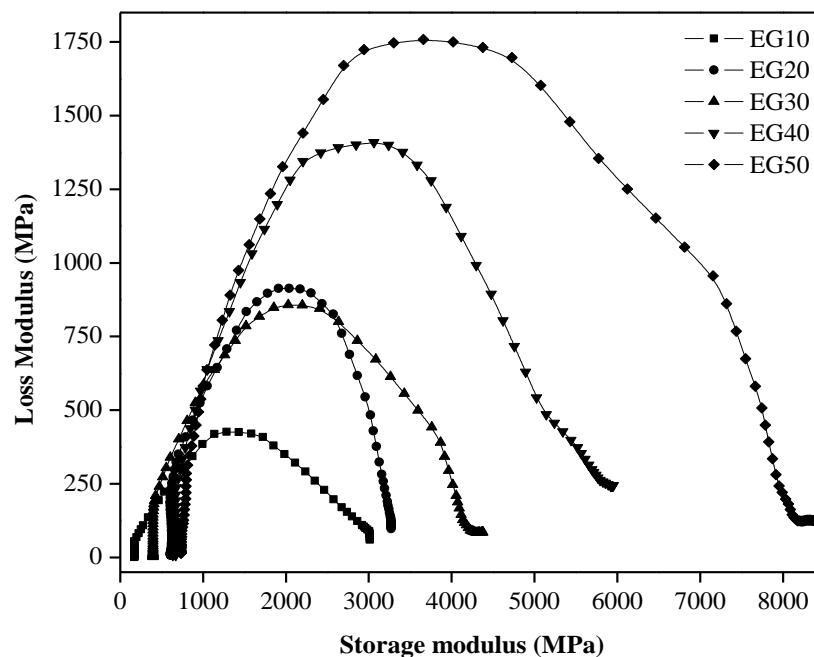
Figure 5.4a Cole-Cole plot for unfilled glass epoxy composites

5.1.2 Thermo-mechanical correlations to mechanical performance of composite

The storage modulus (E′) of unfilled and granite powder filled glass epoxy composites at 30ºC are comparable with the flexural modulus as shown in Figure 5.5. The storage modulus and flexural modulus are significantly improved with the incorporation of glass fiber in the matrix material. Inclusion of low wt.% (up to 16 wt.%) of granite powder is marginally improved both the properties however, further addition of granite powder decreases the

properties drastically. The minimum difference of 0.17 GPa in storage and flexural moduli are observed for unfilled 20 wt.% glass epoxy composite whereas, maximum difference of 0.71 GPa is recorded for unfilled 50 wt. % glass epoxy composite (Figure 5.5). Unfilled glass epoxy composites show higher value of storage modulus than flexural modulus, except to composite with 40 wt.% glass fiber loading which indicated better performance of fiber reinforced composites under cyclic stresses. Whereas, storage modulus value is lowered than the flexural modulus for granite powder filled glass epoxy composite. This may be due to the deboning of granite particle under cyclic stresses in the glass epoxy composites.
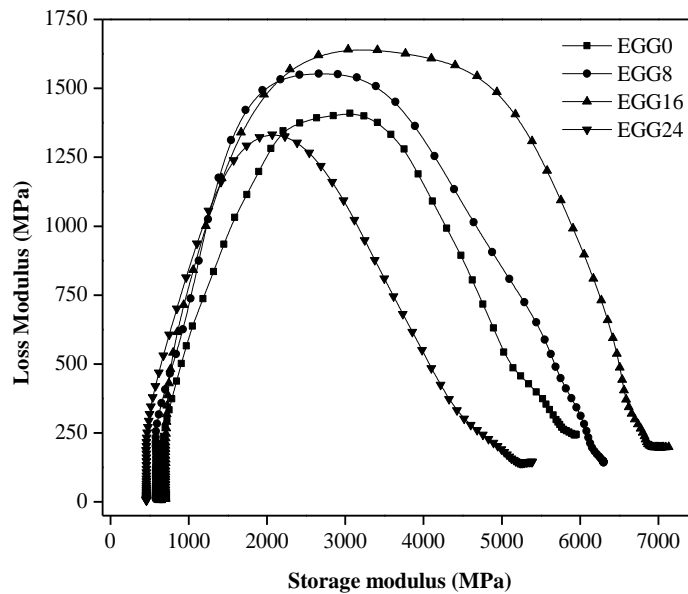
Figure 5.4b Cole-cole plot for granite powder filled glass epoxy composites
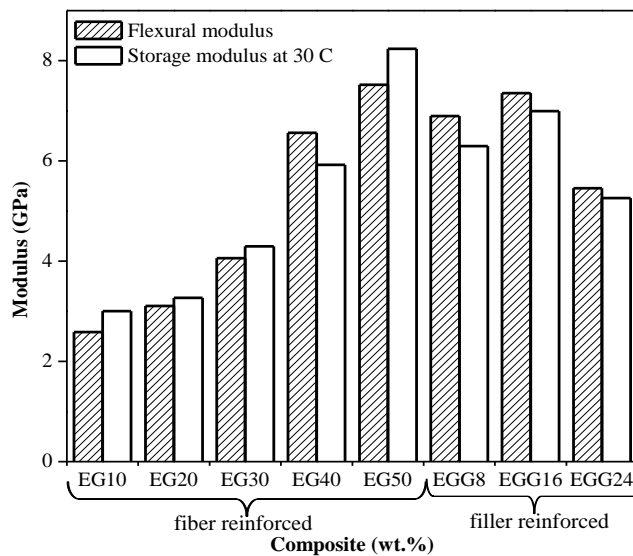
Figure 5.5 Comparison between flexural modulus and storage modulus at 30°C

5.1.3 Thermo-gravimetric analysis

Thermo-gravimetric analysis is performed to determine the thermal stability curve of composite material. The loss of percentage weight as function of increase in temperature is illustrated in Figures 5.6a for unfilled glass epoxy composites. It is observed that initial degradation of epoxy resin starts at temperature of 250ºC. Further, the degradation of composite reinforced with 10 wt.% of glass fiber is rapid compared to composite reinforced with higher wt.% of fiber. The thermal stability of composite is controlled by matrix material as well as reinforcement material [273]. The degradation curve is identical for all composites within the temperature range of 350 to 400ºC. In this region the complete degradation of epoxy takes place. Above this temperature the curves are spacious to each other owing to higher fraction of glass fiber content which is thermally stabled above 500ºC. Figure 5.6b illustrated the thermal stability curve for granite powder filled glass epoxy composites. Up to the temperature of 350ºC the curves are similar and above this temperature also the granite powder filled composites depicted no much variation in weight compared to virgin composite.
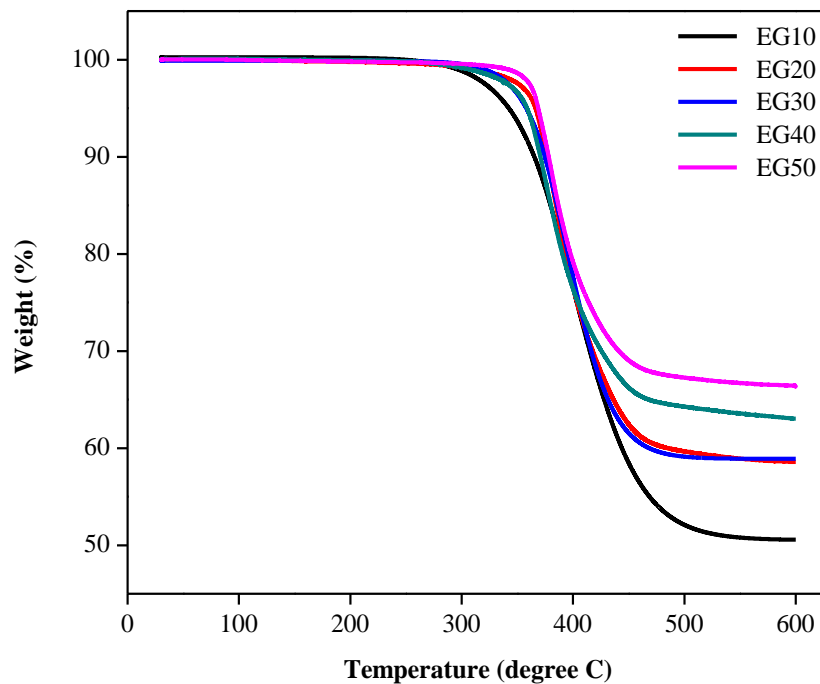
Figure 5.6a Thermal stability curves for unfilled glass epoxy composites
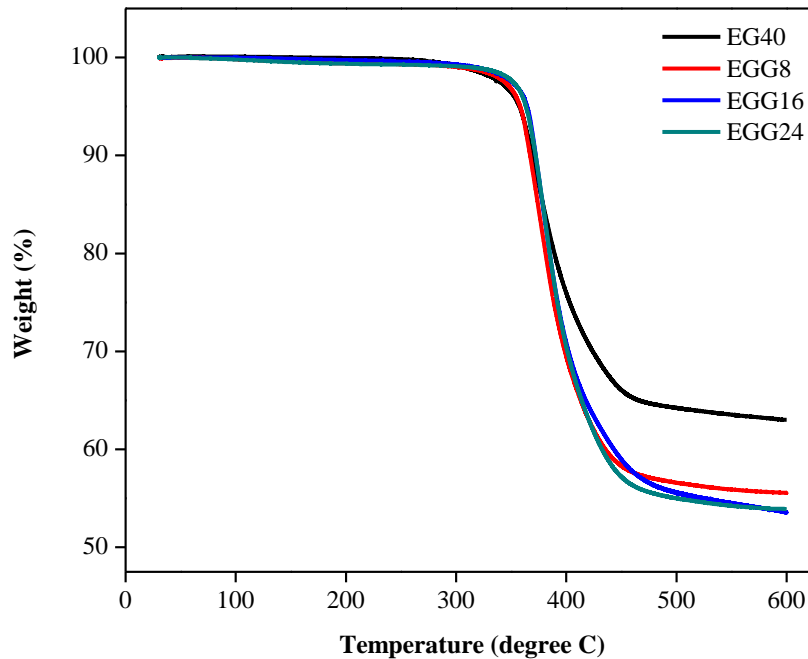
Figure 5.6b Thermal stability curves for granite powder filled glass epoxy composites

5.1.4 Thermal conductivity analysis

The effective thermal conductivity of unfilled and granite powder filled glass epoxy composite is predicted using numerical simulation technique and the theoretical model is compared with experimental results. The experimentally measured thermal conductivity through hot disk method for unfilled glass epoxy composites are 0.211, 0.265, 0.341, 0.48 and 0.523 W/m-K for fiber loading 10, 20, 30, 40 and 50 wt.% respectively. However, experimental values of thermal conductivity for incorporation of 8, 16 and 24 wt.% of granite powder are 0.612, 0.813 and 0.886 W/m-K respectively. The temperature profiles obtained from the finite element analysis for the unfilled and granite powder filled glass epoxy composites are illustrated in Figures 5.7a to 5.7d. The higher temperature variation between surface of application of heat flux and convective surface indicates lower thermal conductivity and vice versa. The predicted temperature variation in the unfilled composite with 10 wt.% glass fiber loading is 0.591°C as shown in Figure 5.7a. However, Figure 5.7 b shows the predicted variation in temperature of 0.265 °C for unfilled composite with 40 wt.% glass fiber loading. Figures 5.7c and d show the temperature contours for 8 wt.% and 16 wt.% granite powder filled epoxy composite respectively, which shows marginal improvement in the thermal conductivity with increase in granite powder content.
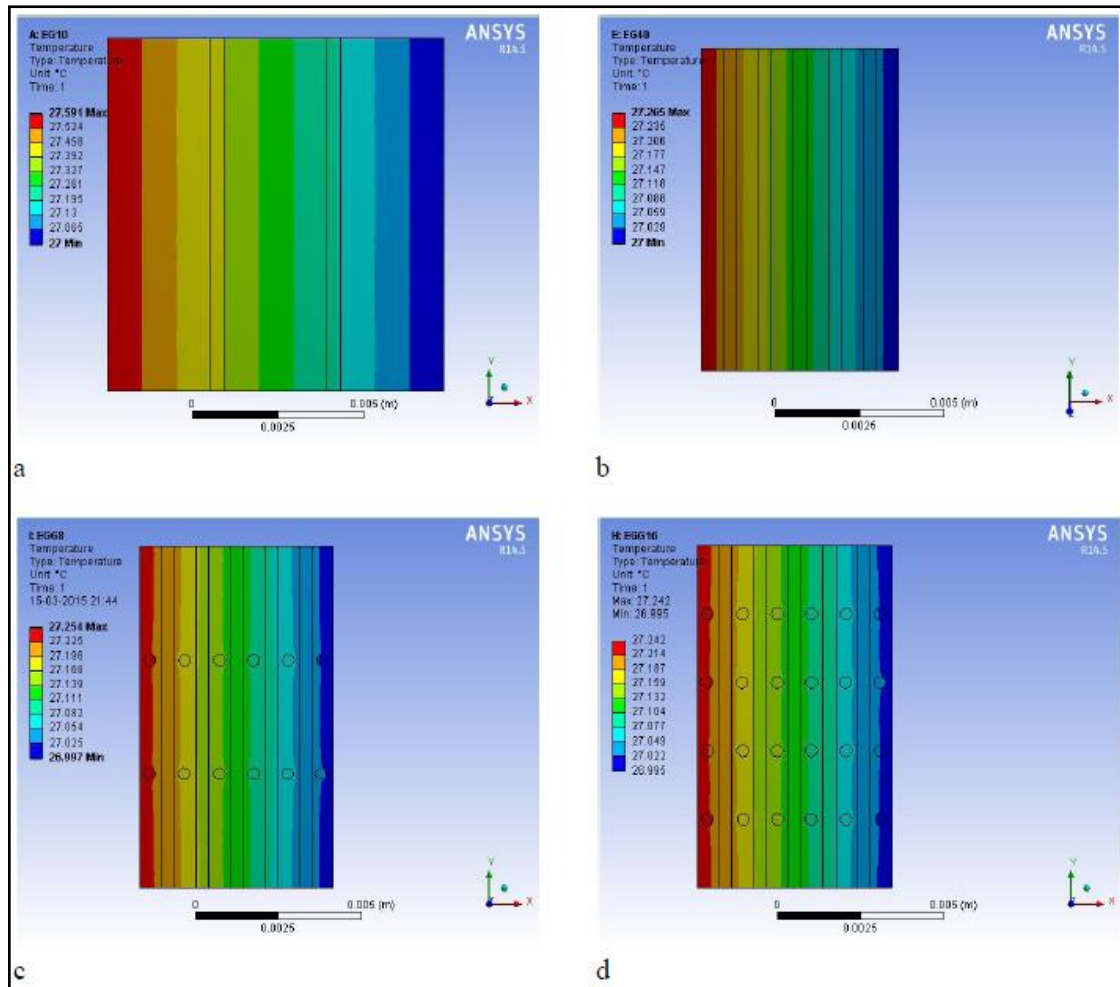
Figure 5.7 Temperature contour of composite with a) 10 wt.% glass fiber, b) 40 wt.% glass fiber, c) 40 wt.% glass fiber filled with 8 wt.% granite powder and d) 40 wt.% glass fiber filled with 16 wt.% granite powder
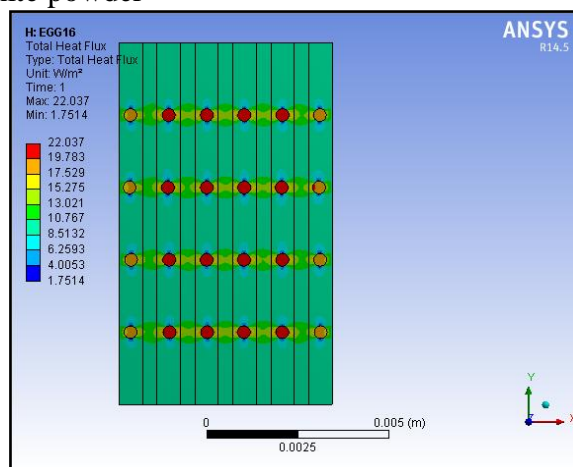
Figure 5.8 Thermal flux contours for 16 wt.% granite powder filled epoxy composite

From the contours it is clearly observed that the inclusion of fiber and filler material helps to improve the thermal conductivity of composite. Strip of thermal lines are less diverted at the fibers but significantly diverted at particulate fillers, as thermal conductivity of filler is higher than fiber and matrix material. In order to understand the heat conduction

process inside the composite, thermal flux contour of 16 wt.% granite powder filled glass epoxy composite is shown in Figure 5.8. It is observed that the heat tends to pass through the granite particles in composites which make it easier for heat conduction and it results in the improvement of effective thermal conductivity of composites [233].
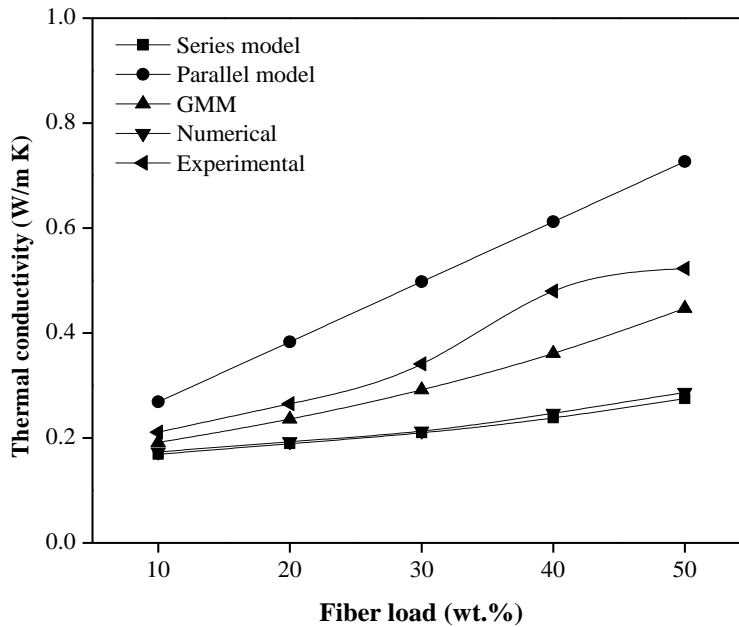
Figure 5.9a Variation in thermal conductivity of unfilled glass epoxy composite
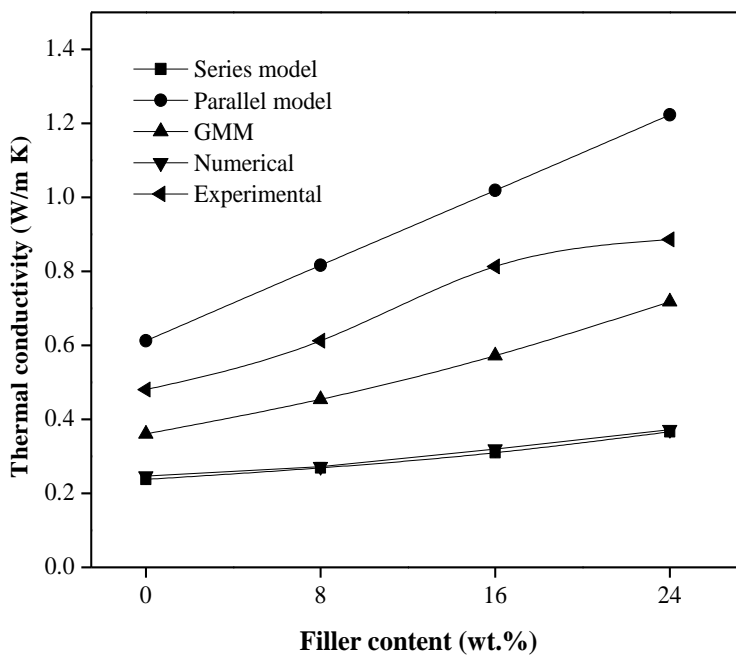
Figure 5.9b Variation in thermal conductivity of granite powder filled glass epoxy composite

Figures 5.9a and 5.9b compared the thermal conductivity of composites numerically, theoretically and experimentally as a function of fiber loading and filler content. It is observed that parallel model has upper bound of thermal conductivity and lower bound of thermal resistance and series model has lower bound of thermal conductivity and upper bound of thermal resistance. The numerical and experimental values of thermal conductivity are in moderate to good agreement with one obtained from theoretical models. The numerically predicted values are in closed agreement with series model whereas; experimental values are in moderate agreement with geometric mean model (GMM) model. The numerically predicted thermal conductivity of unfilled glass epoxy composite is 0.173, 0.193, 0.213, 0.247 and 0.287 W/m-K for different glass fiber loading (10, 20, 30, 40 and 50 wt.%) respectively. The error between experimental and numerically predicted values of thermal conductivity is increased as 18%, 27%, 37% and 48 % for unfilled composites (with glass fiber loading as 10, 20, 30 and 40 wt.%) and further the error slightly decreased to 45% for 50 wt.% glass epoxy composite. Similarly, for inclusion of granite powder of 8, 16 and 24 wt.% on the glass epoxy composites the numerically predicted thermal conductivity is, 0.272, 0.272 and 0.372 W/m-K compared to composite with 0 wt.% granite powder filled (0.247 W/m-K) composite. The error for experimentally and numerically predicted values of thermal conductivity are 55, 60, and 58% for addition of 8, 16 and 24 wt.% granite powder.

Part-II

5.2 Thermal and thermo-mechanical analysis of unfilled and granite powder filled jute-epoxy composites

5.2.1 Dynamic Mechanical Analysis (DMA)

Storage modulus (E') for unfilled /filled jute fiber reinforced composites

Dynamic mechanical analysis of unfilled and granite powder filled jute fiber reinforced epoxy composite is shown in Figures 5.10 to 5.12. The variation of E' is as a function of temperature for unfilled jute epoxy composites as shown in the Figure 5.10a. Value of E' is increased with the increase in jute fiber loading up to 30 wt. %. This may be due to greater stress transfer at the interface of fiber and matrix zone [123]. For further increase in fiber reinforcement there may be improper interfacial bonding which results in reduction in value of E'. Past study reported that value of E' is reduced with the increase in fiber layers [274] in the composites.

Figure 5.10a is clearly illustrate three distinct regions I, II and III viz, glassy region (30 °C to 75 °C), glassy/rubbery transition region (75 °C to 105 °C) and rubbery or low

modulus region (above 105°C) respectively. Below the glass transition temperature (T_g), the value of E' decreases slowly with the increase in temperature. However, in the environs of T_g, sharp decline in the value of E' is observed which indicates occurrence of glassy/rubbery transition stage. Above T_g, the value of E' is much lower than that at room temperature showing molecular mobility in composite. This behavior occurs due to increase in molecular mobility in polymer chain above T_g which results in weakening of fiber-matrix interfacial bond [275]. In the working temperature of 25 to 50 °C the lowest decreased in the value of E' is reported from this research is 98% in case of 40 wt.% jute fiber reinforced composite. Similarly, highest reduction in E' is 94% for 10 wt.% jute fiber reinforced epoxy composite.
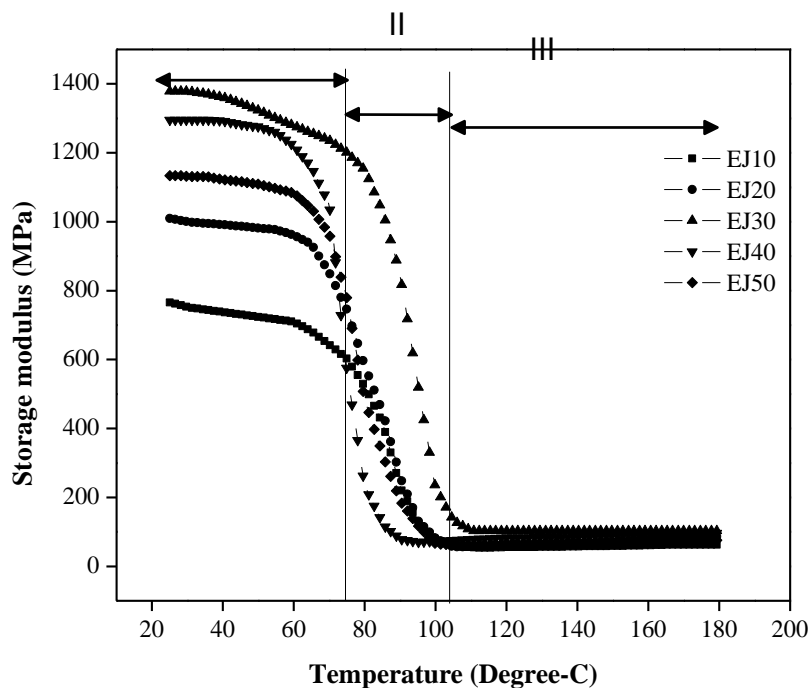
Figure 5.10a Variation of storage modulus of unfilled jute epoxy composite

The coefficients C for different composite are indicated in Table 5.2. Lower the value of C higher the efficiency of the reinforcement. The value of C is maximum for 50 wt.% jute fiber reinforcement and minimum for 20 wt.% jute fiber reinforcement. Figure 5.10b shows the storage modulus of granite powder filled jute fiber reinforced epoxy composites. The incorporation of 8 wt.% and 16 wt.% of filler content in the virgin composite leads to increase in storage modulus however, on further increase in filler content to 24 wt.% the storage modulus decreases drastically. At room temperature the value of E' is increased by 6% and 11% with addition of 8 wt.% and 16 wt.% granite powder and further addition of 24 wt.% granite powder in the composite that decreases the value of E' by 18% of its value to the

virgin composite. In the working temperature range from 25°C to 50°C the reduction in storage modulus are 95%, 97%, 99% and 97% for virgin composite, 8 wt.%, 16 wt.% and 24 wt.% granite powder reinforced composites respectively.
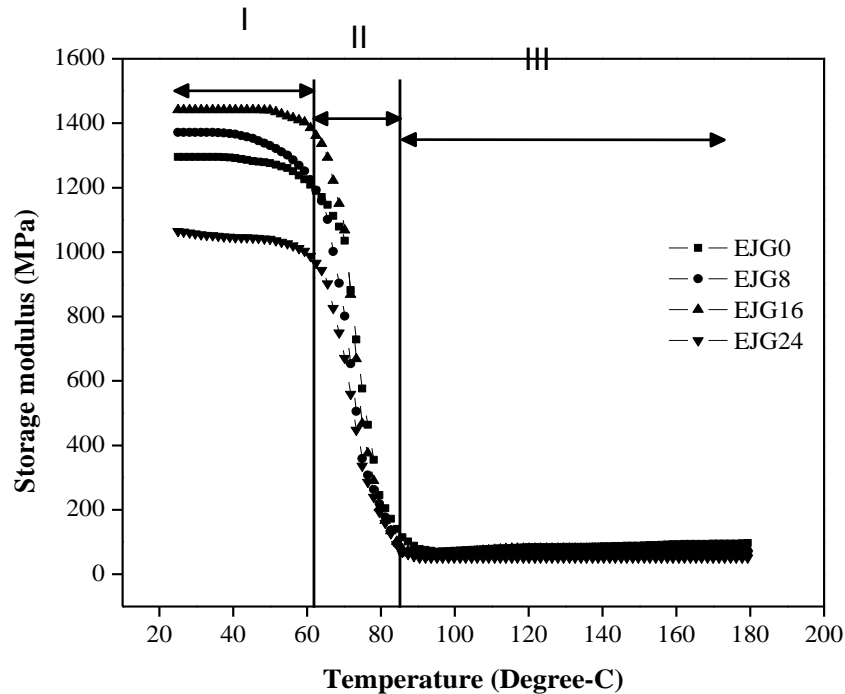
Figure 5.10b Variation of storage modulus of granite powder filled jute epoxy composite

Similar, to unfilled composite, particulate filled composites show glassy region – I (25 °C to 65 °C), glass transition region – II (65 °C to 85 °C) and rubbery region –III (above 85 °C). At room temperature the movement of chain segment is mostly frozen due to closely pack arrangement. As the temperature increases, the components of polymeric material become more mobile and lose their close packing arrangement, leading to decrease of storage modulus in the glass transition region (65 °C to 85 °C). The decay in storage modulus with the increase in temperature for the composites at all wt.% of granite powder that remain almost same in the glass transition range. In rubbery region no significant change in storage modulus is observed.

Loss modulus (E'') for unfilled / filled jute fiber reinforced composites

Loss modulus (E'') is measured of energy dissipated as heat per cycle under deformation or it is viscous response of material. Figure 5.11a shows effect of temperature on loss modulus of unfilled jute fiber reinforced epoxy composite. It can be observed that the value of E'' is increased and then decreased with the increase in temperature irrespective of percentage of fiber reinforcement. Effect of fiber loading on value of E'' is found more influencing in the

vicinity of T_g. The E'' value in transition region is significantly higher for composites, which may be resulted of increase in internal friction that enhances the dissipation of energy [269]. Below T_g the value of E'' is found minimum for 10 wt.% of jute fiber reinforcement (11 MPa) and maximum for 30 wt.% jute fiber reinforcement (34 MPa). It is also observed from Figure 5.11a that the curve broadens for increase in jute fiber reinforcement from 10 wt.% to 30 wt.%. This broadening is attributed to difference in state of matrix surrounding the fiber and rest of the matrix which ultimately reduces the molecular mobility [125]. From this study, it is observed that composite with 30 wt.% jute fiber reinforced composite has maximum broadening as compared to other composites.
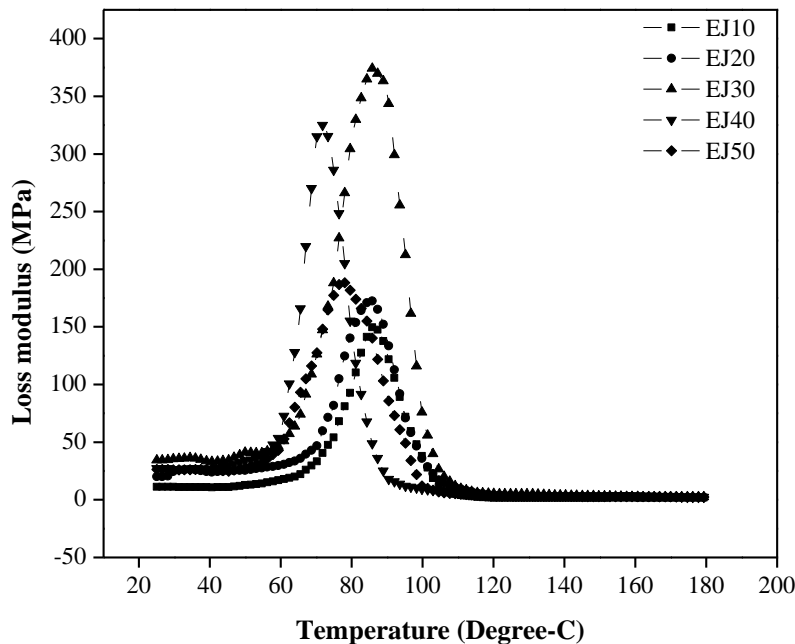
Figure 5.11a Variation of loss modulus of unfilled jute epoxy composite

The value of temperature corresponds to maximum E'' and maximum damping factor can be considered as T_g. It was reported that T_g values obtained from the E'' curve were more realistic as compared to those obtained from damping factor [269]. The T_g obtained from loss modulus for different wt.% of jute fiber reinforced composite is illustrated in Table 5.2. It can be concluded that T_g value found from E'' curve is lower than that from damping factor curves. The value of T_g initially remains unaffected with the increase in fiber loading up to 30 wt.%, further it shows marginal reduction in the value of T_g. Similarly, for granite powder filled jute fiber composites the variation of loss modulus as a function of temperature is shown in Figure 5.11b. Below T_g loss modulus of composite shows higher value for filled

composite than virgin and proportionally increased with increase in filler loading. At room temperature the loss modulus is increased by 15%, 125% and 277% for composite filled with 8 wt.%, 16 wt.% and 24 wt.% of granite powder respectively as compared to virgin composite. In the transition region negligible increase in the loss modulus is observed for addition of 8 wt.% and 16 wt.% of granite powder but, for 24 wt.% granite powder addition shows 1.6 times increase in loss modulus. This shows improvement in energy dissipation ability of the composite with reinforcement of filler loading [276].
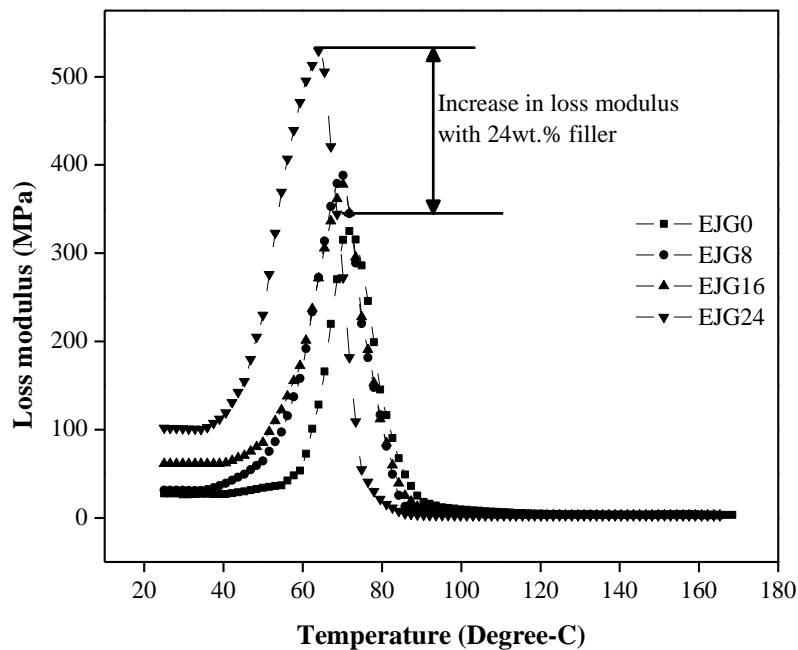
Figure 5.11b Variation of loss modulus of granite powder filled jute epoxy composite

The loss modulus curve broadens in the environs of T_g with increase in filler content. There is no significant difference as observed in loss modulus of composites in the rubbery region. The value of T_g from E" peak for composites is shown in the Table 5.2. The value of T_g is unaffected with the reinforcement of granite powder up to 16 wt.%, on further increase in the filler content dramatically decreases the T_g value. This may be due to close distribution of particulates at higher filler loading that increases the particulate-particulate and/or particulate-fiber interaction. Fiore et al. [277] reported similar results for glass transition temperature of arundo donax filled epoxy composite. The value of T_g for virgin and filled composite up to 16 wt.% filler is in the range of $71.76^{\circ}C$ to 70.20 °C. This means that the presence of the granite powder up to 16 wt.% does not reduce the mobility of the matrix

chains, due to the weak filler–matrix interfacial adhesion. For composite with 24 wt.% of granite powder the value of T_g drops to 63.97 °C.

Damping factor (Tan δ) for unfilled/filled jute fiber reinforced composites

Damping is the dissipation of energy in a material under cyclic load. Damping factor is a measured of how well a material can get rid of energy and is reported as the tangent of the phase angle. Conversely, it also provides information about how good a material can absorb energy [126]. The variation in the damping factor value, measured over the range of temperature is presented in the Figure 5.12a for unfilled jute epoxy composites. It is observed that, in transition region the damping factor increased with increase in temperature. It reached to maximum value and further in rubbery region it fall down. It is also observed for all composites the damping factor value below T_g is quite low due to polymeric chains are in frozen state in this temperature range. Peak values of damping curves are observed in the descending order for 40 wt.%, 10 wt.%, 20 wt.%, 50 wt.% and 30 wt.% of jute fiber reinforcement respectively. This may be attributed in the decreasing rate of energy loss in the composite during testing. This may also possible due to enhancement of storage modulus of composite which could limit the degree of freedom of polymeric network at atomic level. Nevertheless, it is only true up to 30 wt.% of jute fiber reinforcement. Beyond that the value of damping factor starts to increase, possibly because of weak interfacial bonding due to presence of more fiber to fiber contact [126].
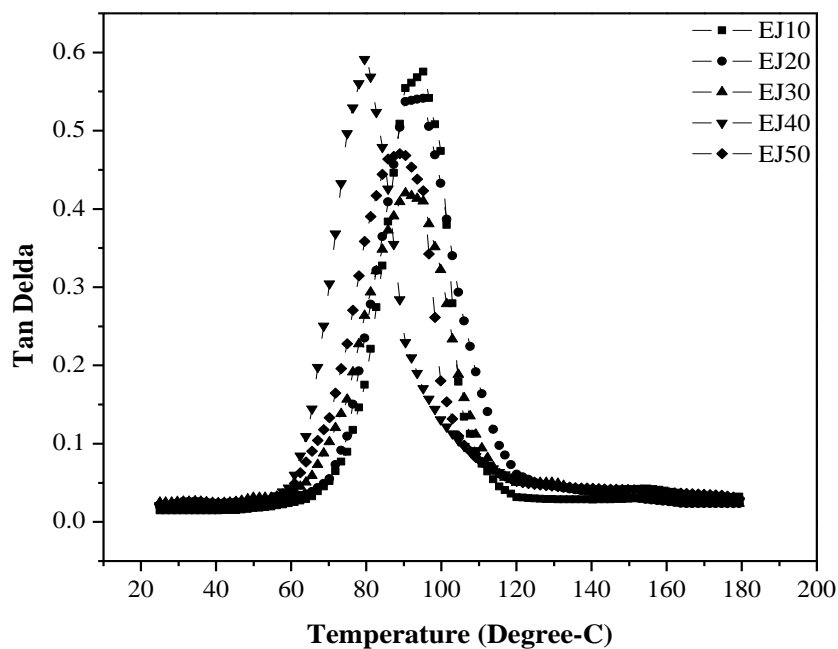
Figure 5.12a Variation of damping factor of unfilled jute epoxy composite
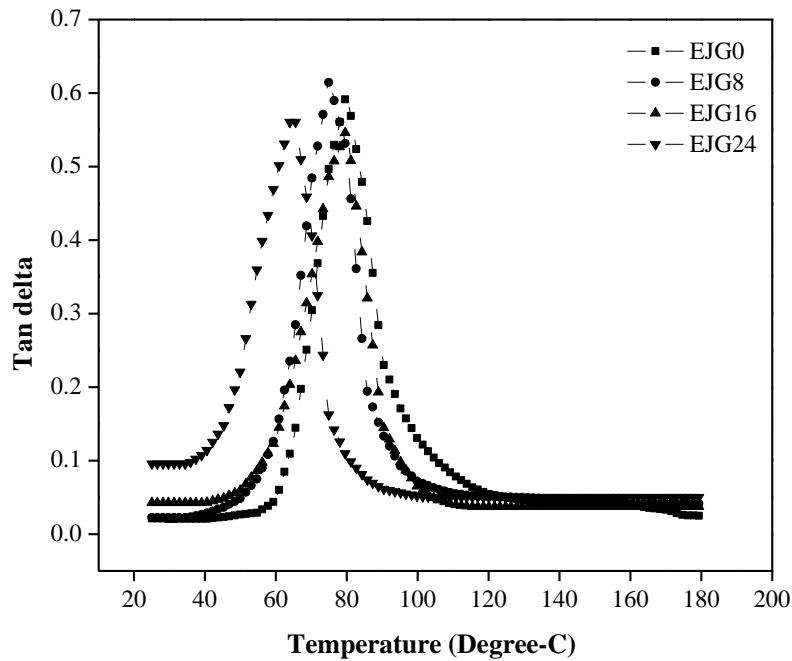
Figure 5.12b Variation of damping factor of granite powder filled jute epoxy composite

Highest value of damping factor is observed for 40 wt.% jute fiber reinforced composite at glass/rubbery transition region. The value of peak damping factor and T_g from damping factor curve are given in the Table 5.2. The value of T_g is found to be unaffected up to 30 wt.% of jute fiber reinforcement. Further addition of jute fiber loading results in decreasing the value of T_g due to decrease in fiber-matrix interfacial bonding and presence of fiber-fiber interaction. The trend in variations of T_g from damping factor curve is in good agreements with T_g as obtained from loss modulus curve.

The storage modulus and loss modulus are in phase with each other by angle δ. The ratio of loss modulus to storage modulus referred as damping factor (Tan δ). Figure 5.12b shows the variation in damping factor for granite powder filled jute composite as a function of temperature. It is observed that peak value of damping factor negligibly varies in the range of 0.55 to 0.61 for all the composites. For 8 wt.% of granite powder loading peak damping value is 0.61 as compared to peak damping value 0.59 for virgin composite. Further for addition of granite powder of 16 wt.% and 24 wt.% the peak damping value reduced to 0.55 and 0.56 respectively. The damping value of all granite powder filled composites is comparably higher which shows marginal effect of particulate filler material on damping factor, thus confirming the presence of weak filler-matrix adhesion [277]. The glass transition temperature is obtained from damping curve as indicated in Table 5.2. The curve reveals that

addition of 8 wt.% to 16 wt.% of granite powder has marginal decreased in the T_g but for addition of 24 wt.% of granite powder that reduces the value of T_g to 63.97 °C from 79.56 °C for virgin composite.

Table 5.2 Coefficient, peak height and glass transition temperature of unfilled and granite filled jute epoxy composites

Composite	Coefficient, C	*Adhesion efficiency factor, A	Glass transition temperature ($^{\circ}$C) T_g	
			from E''_{max}	from $\tan\delta_{max}$
EJ10	0.5544	-0.13018	85.79	95.15
EJ20	0.5278	0.043546	85.79	95.15
EJ30	0.6042	0.086239	85.79	90.47
EJ40/EJG0	0.6058	0.253673	71.76	79.56
EJ50	0.6731	0.283796	78.00	88.91
EJG8	0.9238	0.429104	70.20	74.88
EJG16	0.8142	0.142641	70.20	79.56
EJG24	0.9380	1.002065	63.97	63.97

* calculated at T_g corresponding to peak loss modulus.

Cole-Cole plot

The degree of homogeneity of polymeric composite material may be determined by Cole-Cole plot. These plots study the structural changes that occurred in polymers after inclusion of reinforcement [234]. Cole–Cole plot represents the relationship between the loss modulus (E'') and the storage modulus (E'). According to Ferry [272] the plot between E'' and E' for homogeneous polymeric system will be perfect semicircle.

Cole-Cole plots for unfilled and granite powder filled jute fiber reinforced epoxy composites are shown in Figures 5.13a and 5.13b. These plots are drawn between loss modulus (E'') and storage modulus (E') for unfilled and particulate filled composites. Figure 5.13a shows the Cole-Cole plot for unfilled jute fiber reinforced epoxy composites and in this plot most of the curves show different layering patterns with imperfect semicircular shape. Therefore, the nature of the plot is observed to assess homogeneity of the system [234]. For unfilled jute fiber composite, with the increase in fiber loading decreases the degree of homogeneity except to 50 wt.% jute epoxy composite. However, with the addition of granite particulates in the original fiber reinforced epoxy composites the plot patterns are constrained by both the physical presence of the granite fillers and or jute fibers and there may be any possible change in chemical interaction between the phases. Figure 5.13b depicts that

composites became more heterogeneous with incorporation of granite powder. The composite with 24 wt.% granite powder shows hasty trend in plot which indicates highest degree of heterogeneity.
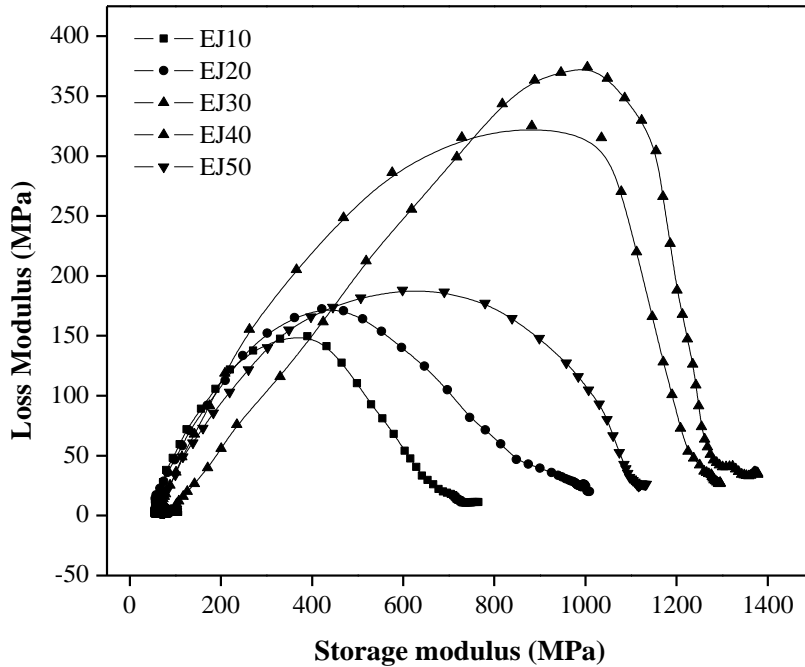
Figure 5.13a Cole-Cole plots of unfilled jute epoxy composite
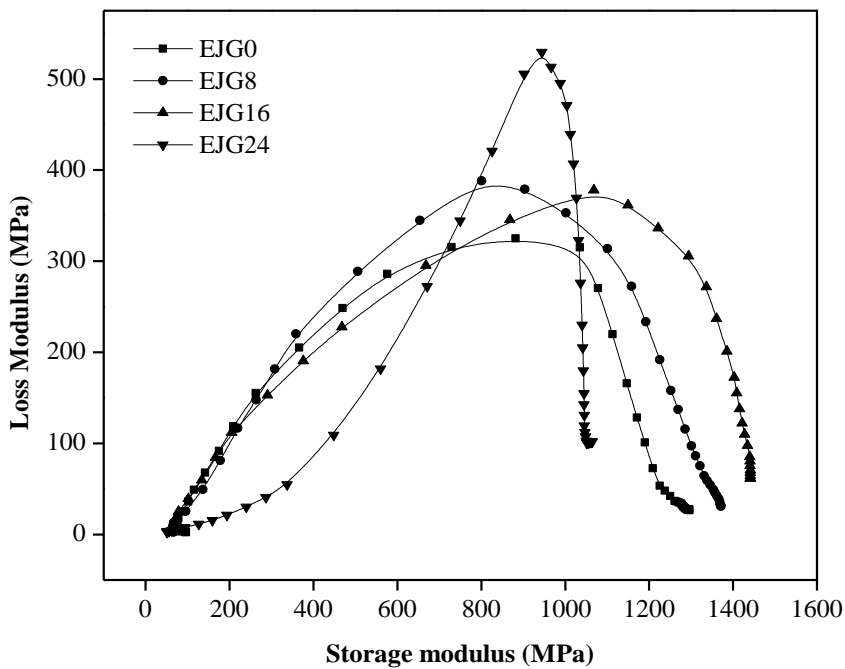
Figure 5.13b Cole-Cole plots of granite powder filled jute epoxy composite

5.2.2 Thermo-mechanical correlations to mechanical performance of composite

Being conducted in same configuration, the flexural modulus and storage modulus at room temperature showed good agreement with each other (see Figure 5.14). The value of storage modulus is higher than flexural modulus for unfilled jute epoxy composites except to unfilled composite with 20 wt.% jute fiber. This shows the better performance of composites to cyclic loading. The trend of improvement of both the moduli are identical with improvement up to 30 wt.% jute fiber loading and for higher fiber loading the values are decreased. In case of granite powder filled jute epoxy composites, much variation in the values of both moduli is not observed. Highest variation in flexural and storage modulus of 120 MPa is observed for unfilled 50 wt.% jute epoxy composite. Whereas, lowest variation of 9 MPa is observed for 16 wt.% granite powder filled jute epoxy composite.
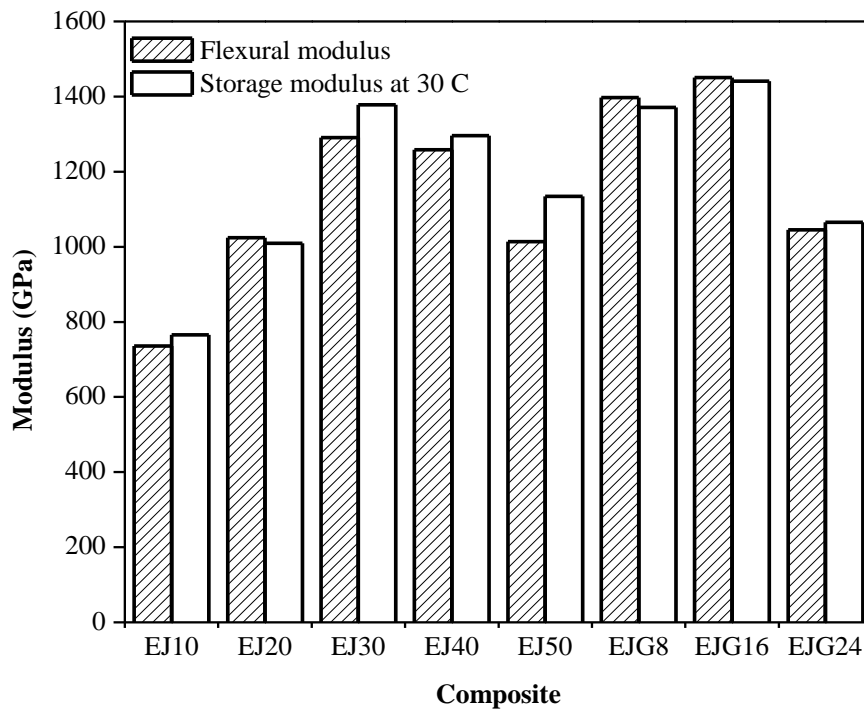
Figure 5.14 Correlation between flexural modulus and storage modulus

5.2.3 Thermo-Gravimetric Analysis

Thermo-gravimetric analysis (TGA) is a method to determine the loss of weight in a material with respect to increase in temperature under a controlled atmosphere and also determine the thermal stability and composition. In general, the thermal analysis for the material is carried out in order to evaluate the chemical, physical and structural changes are occurring in a material, under an imposed change in temperature. Figures 5.15a and 5.15b show the TGA

curves for different wt.% of jute fiber loading and granite powder content respectively. These curves are clearly depicts three distinct regions viz, thermally stable region-I, decomposition-II and thermal degradation-III. Most thermal degradation is observed in the temperature range of 300 to 500 ºC. In the initial stage (up to 100 ºC) of region-I the weight loss starts with evaporation of moisture content absorbed. In region-II weight loss occurred due to decomposition of lower molecular weight hemicelluloses followed by thermal degradation of cellulose and epoxy [127].
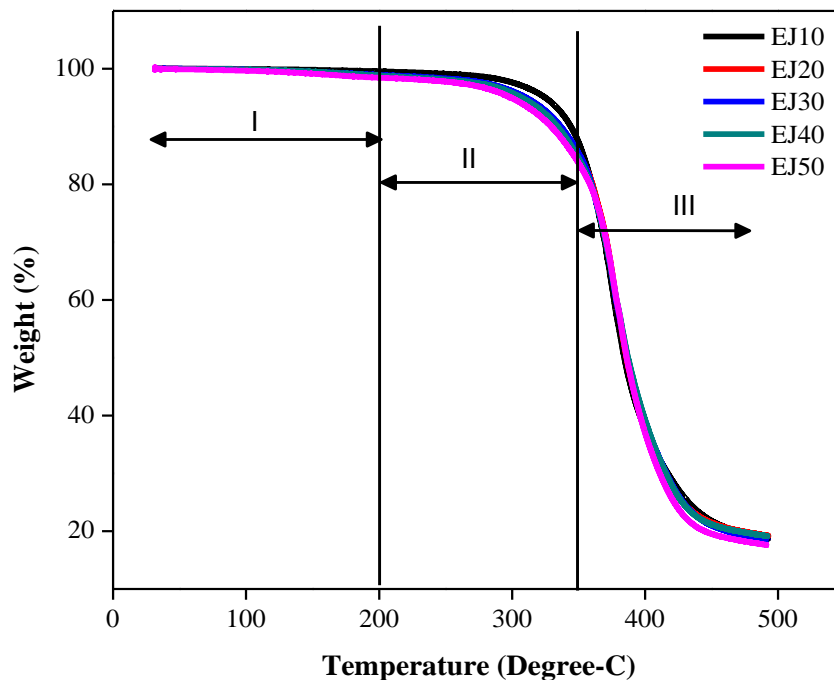
Figure 5.15a Variation of weight of unfilled jute-epoxy composite

There is not much significant difference in the degradation curve of unfilled jute fiber reinforced epoxy composite. Degradation starts slightly earlier as jute fiber loading increases, this may be due to start of decomposition of hemicelluloses and cellulose content in the natural fiber. More significant difference is observed in the degradation curve of granite powder filled composites and the weight loss for granite filled composite starts earlier but the rate of degradation is found to be lowered as compared to virgin composite. This may be attributed to higher thermal degradation temperature of granite powder. At temperature about 500°C all the composite exhaust thermally stable residue which is found in higher wt.% for higher filler content. Residual loading granite filled composite is in the order of 21%, 25% and 28% for filler loading of 8 wt.%, 16 wt.% and 24 wt.% respectively as compared to 18% for virgin composite.
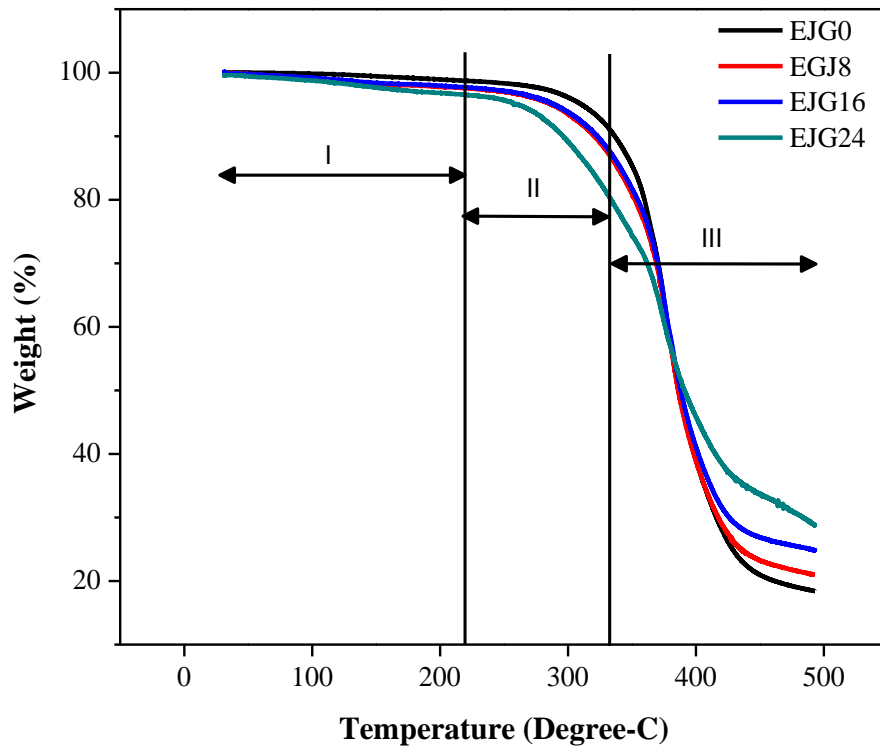
Figure 5.15b Variation of weight of granite powder filled jute-epoxy composite

5.2.4 Thermal conductivity Analysis

The thermal conductivity of composite is evaluated by three methods viz; numerical method using Ansys 14.5, experimental testing using Hot Disc method and also using theoretical models available. In numerical method the heat flux is applied at one edge of geometry and the temperature variation is observed at opposite edge. Maximum variation in temperature between both ends is an indication of lower thermal conductivity and vice versa. The observed temperature contours for different composites is illustrated in Figure 5.16. The temperature difference of 0.442ºC (Figure 5.16a) is observed for 10 wt.% jute fiber loading compared to 0.613ºC (Figure 5.16b) for 40wt.% jute fiber loading. It depicts the relative decrease in thermal conductivity with increase in fiber loading owing to reinforcement of lower thermally conductive jute fiber. However, temperature difference of 0.6ºC (Figure 5.16c) and 0.582ºC (Figure 5.16d) is observed for 8 wt.% and 16 wt.% granite powder addition in jute epoxy composites respectively. This shows improvement in the thermal conductivity of the composites with the incorporation of granite powder in different weight percentages.
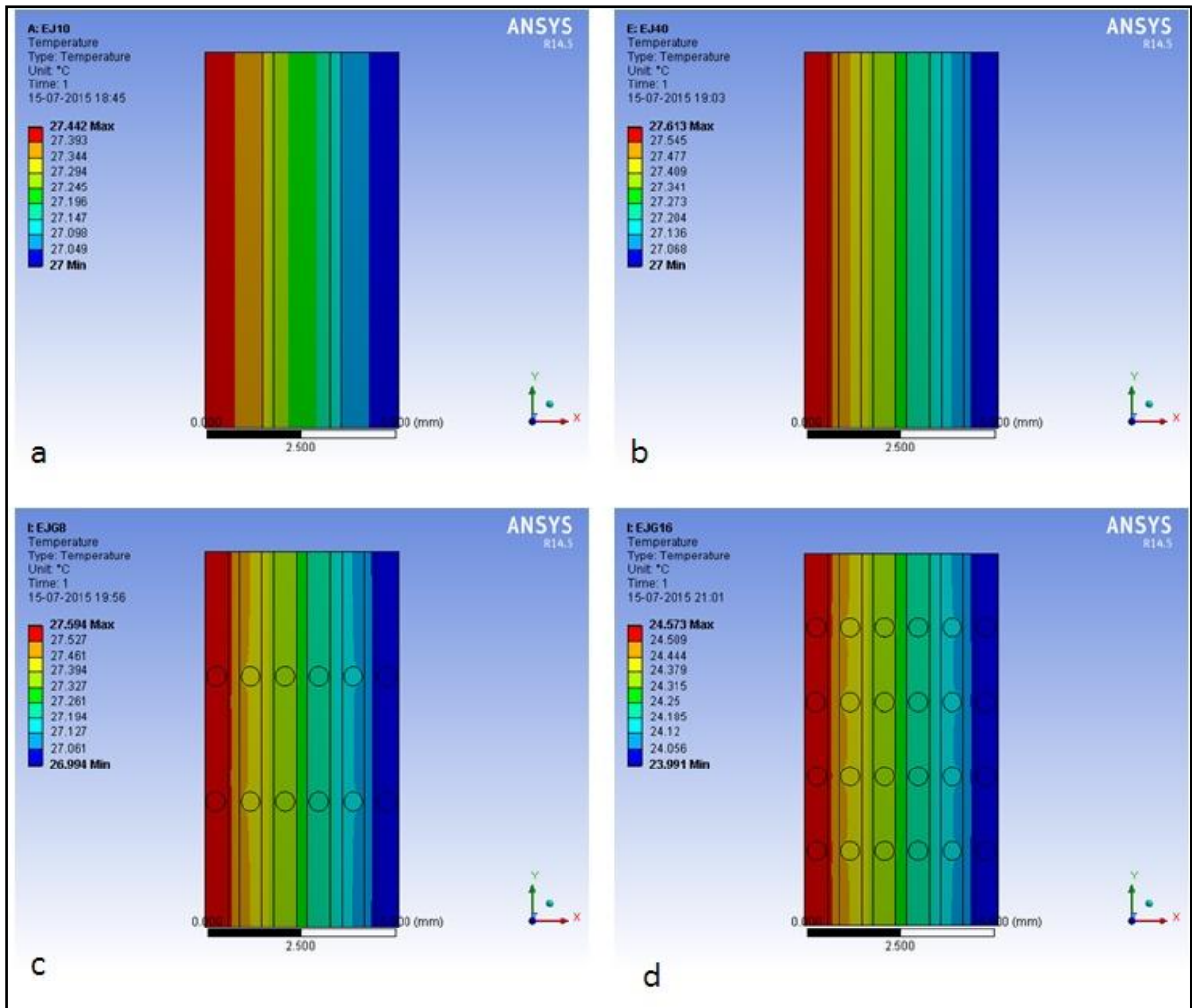
Figure 5.16 Temperature contour developed for flow of heat flux for (a) unfilled 10 wt.% jute epoxy composite, (b) unfilled 40 wt.% jute epoxy composite, (c) 8 wt.% granite powder filled jute epoxy composite and (d) 16 wt.% granite powder filled jute epoxy composite
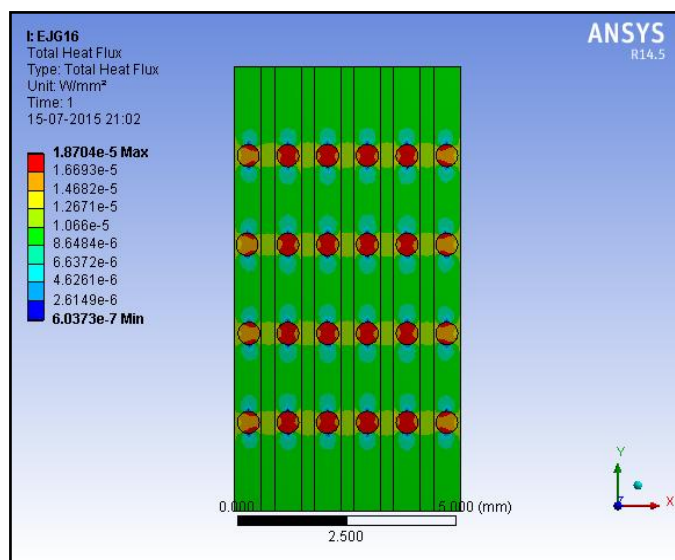
Figure 5.17 Heat flux generated in constituent material for 16 wt.% granite powder filled composite

Figure 5.17 shows the heat flux generated in the jute epoxy composite filled with 16 wt.% granite powder. The maximum heat energy transfer is through granite powder particles as compared to jute fiber and epoxy matrix. Thermal conductivity of the composites is evaluated by all the various modes showed linearly decrease in the value with the increase in jute fiber loading (see Figure 5.18a). The reinforcement of thermally insulating jute fiber in epoxy matrix is resulted in decrease in thermal conductivity of composite material. The values as estimated by various modes for unfilled jute epoxy composites are in good agreement with each other with marginal difference. The experimental values of thermal conductivity are 0.139, 0.125, 0.107, 0.096 and 0.081 W/m-K for reinforcement of 10, 20, 30, 40 and 50 wt.% jute fiber. These values are close to the values predicted by numerical method using Ansys finite element simulation technique.
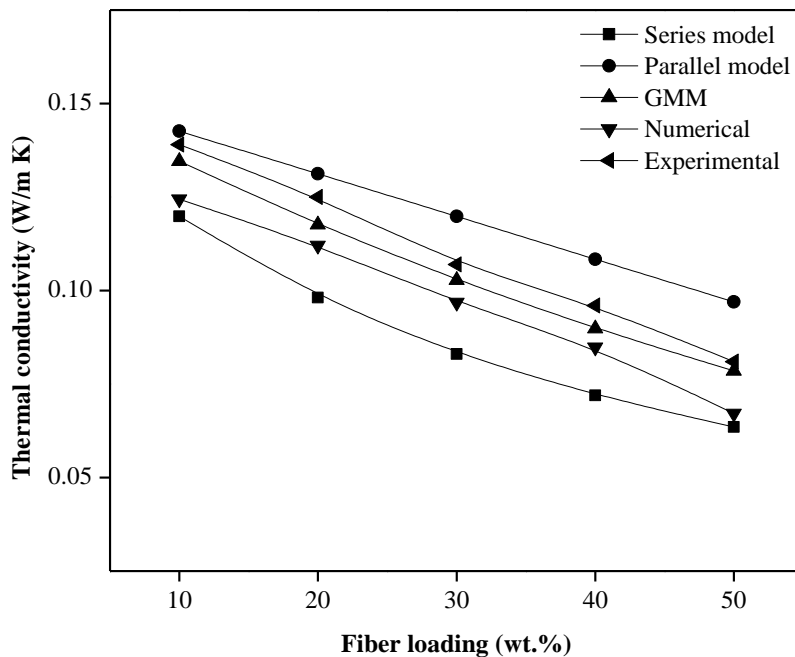
Figure 5.18a Comparison of thermal conductivity evaluated by different modes for unfilled jute epoxy composites

The values of thermal conductivity estimated by various modes as function of wt.% of filler content is depicted in Figure 5.18b. The value of thermal conductivity is observed to increase marginally with the increase in granite filler content except to the value estimated by parallel mode. The parallel mode indicated the drastic increase in thermal conductivity of the composite with addition of granite powder. Whereas, the values estimated by series, GMM, Numerical and experimental method are in close agreement. The experimental value of

thermal conductivity for incorporation of 8, 16 and 24 wt.% granite powder are 0.14, 0.16 and 0.2 w/m-K compared to 0.096 W/m-K for virgin jute epoxy composite.
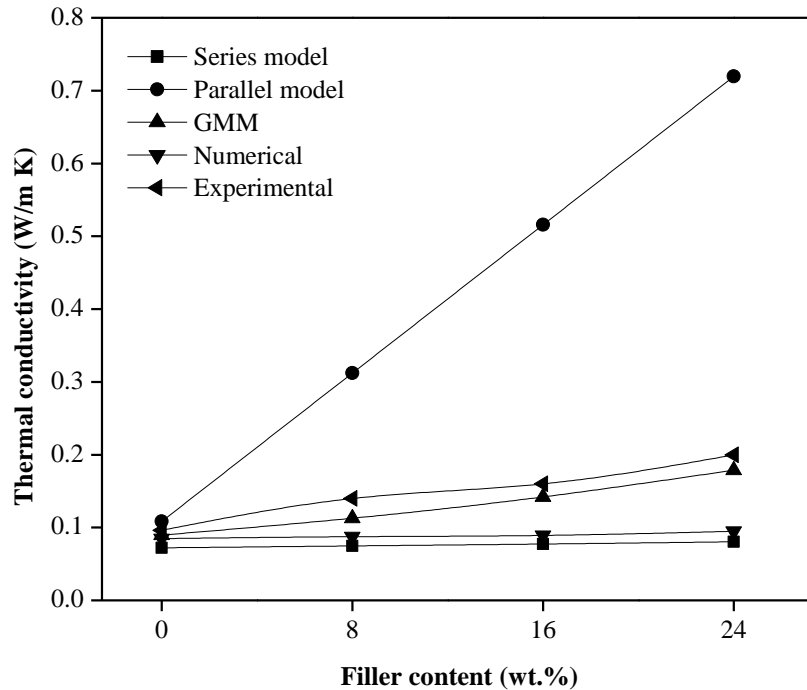
Figure 5.18b Comparison of thermal conductivity evaluated by different modes for granite powder filled jute epoxy composites

Part-III

5.3 Thermal and thermo-mechanical analysis of unfilled and granite powder filled carbon-epoxy composites

5.3.1 Dynamic Mechanical Analysis (DMA)

The storage modulus (E') of composite material shows the load bearing capacity and the value is comparable to the measured flexural modulus [278]. The variation of storage modulus of unfilled carbon epoxy composites as function of temperature is shown in Figure 5.19a. Behavior of composites is separated in three different regions viz; glassy stage-I (below 50°C), glass transition state-II (50 – 90°C) and rubbery state-III (above 90°C). In state I (below 50°C) the value of E' is spacious to each other which show the contribution of fiber reinforcement on stiffness of composite at lower temperature. Maximum improvement in value of E' is found with the increase in fiber loading from 30 to 40 wt.% (see Figure 5.19a), which is in agreement with improvement in flexural modulus of composite (see Table from chapter 4).
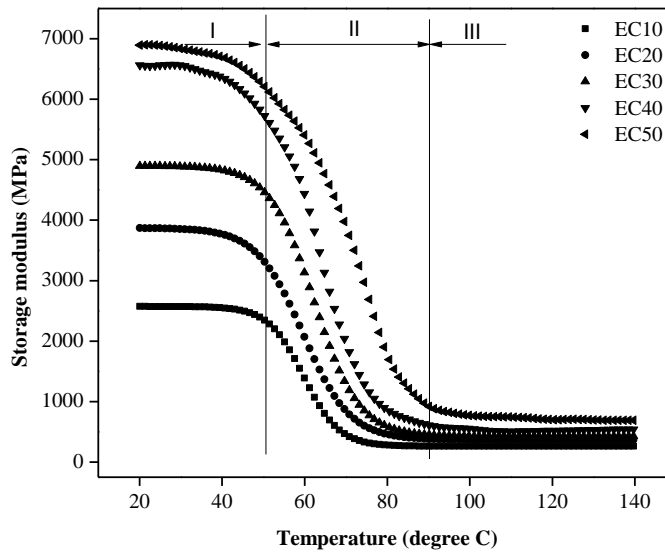
Figure 5.19a Storage modulus of unfilled carbon epoxy composites
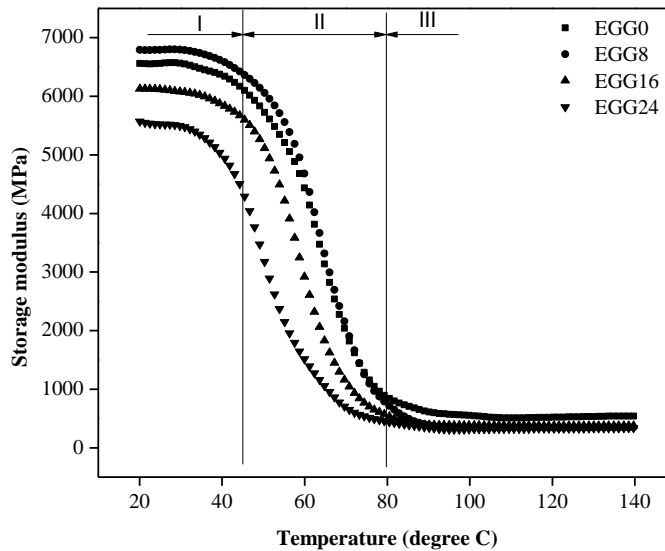
Figure 5.19 b Storage modulus of granite powder filled carbon epoxy composites

Within the range of normal environment temperature (25 – 50°C) the maximum reduction of value of E' up to 85% is recorded for 20 wt.% carbon fiber epoxy composite. Whereas, minimum reduction in value of E' is recorded up to 91% for 10 and 30 wt.% carbon fiber epoxy composite from 25 to 50°C. Above 50°C the value of E' is rapidly decreased as glass to rubbery transition state starts but above 90°C no variation in value of E' is recorded. In rubbery state also the value of E' is higher for higher fiber loading which again shows the

contribution of fiber to storage modulus. Figure 5.19b represented the variation in the value of E' for granite powder filled carbon epoxy composites with respect to temperature. Similar to unfilled composite the trend is divided in to three region viz; I- glassy state (below 45°C), II- transition state (45 to 80°C) and III- rubbery state (above 85°C).

In state-I the value of E' remains more or less constant with marginal reduction and the values are closer to each other as compared with unfilled composites (Figure 5.19a). This shows marginal contribution of granite filler content on value of E'. The value of E' for 8 wt.% granite content is slightly higher than unfilled composite whereas, further addition of granite powder by 16 and 24 wt.% decline the performance compared with unfilled composite. This is possibly due to filler-fiber and/or filler-filler interaction which weaken the stress transfer between matrix and reinforcement [132]. In state-II the rapid decline in the value of E' is recorded to possibly lowest value. Though the value of E' for 8 wt.% granite powder filled carbon epoxy composite is slightly higher as compared with unfilled composite in state-I, it decline to lower value in state-III. The reason for this may be at higher temperature the granite particle does not contribute to strength due to free movement along in the rubbery matrix whereas, the strength in this temperature region is due to fibers only.

The loss modulus (E'') signify viscous response or the energy dissipation ability of the material that has theoretical correspondence to the toughness of the material [133]. Figures 5.20a and 5.20b show the trend of loss modulus as function of temperature. The value of E'' is constant at lower side in lower temperature region (below 45°C) and it increases to its maximum but decreases to lower value in the transition region between glassy and rubbery state. Further, in rubbery state the E'' remain constant at its lowest value. In glassy region the composite is stiff and showing elastic response which results in minimum energy dissipation capacity in this region. In transition region between glassy and rubbery state the stiffness of composite is rapidly decline due to mobility in polymeric chain within matrix and hence, more amount of energy is dissipated within this region. Whereas, at higher temperature in rubbery region the polymeric chains are completely damaged therefore, in this region the composite does have neither stiffness nor energy dissipation capacity [132].

Figure 5.20a shows increase in peak value of E'' with increase in fiber loading which may be attributed to poor interface via enhanced chain mobility due to less cross linking density [138]. At higher fiber loading the poor interface is due to improper wetting of fiber in matrix. Addition of granite powder has opposite effect in peak value of E'' as compared to unfilled carbon epoxy composite (see Figure 5.20b). The value of peak E'' is reported lower for granite powder filled composite than unfilled composite. The temperature corresponding

to peak loss modulus and peak Tan δ are considered as glass transition temperature (T_g). However, the temperature values corresponding to peak loss modulus are more realistic values T_g [269]. The values of T_g for unfilled and granite powder filled carbon epoxy composites is shown in Table 5.3. The shift in value of T_g towards higher temperature shows the higher sustainability of polymeric chain for higher fraction of fiber loading [132]. Conversely, the decrease in value of T_g for addition of granite powder is reported because of start of early mobility of polymeric chain.
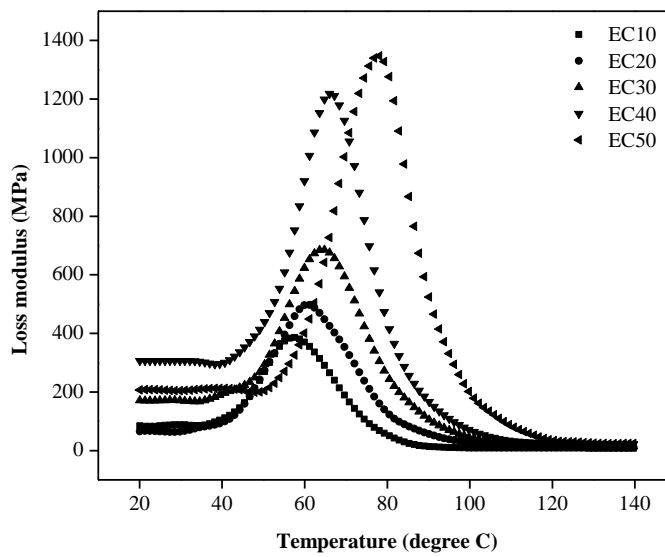
Figure 5.20a Loss modulus of unfilled carbon epoxy composites
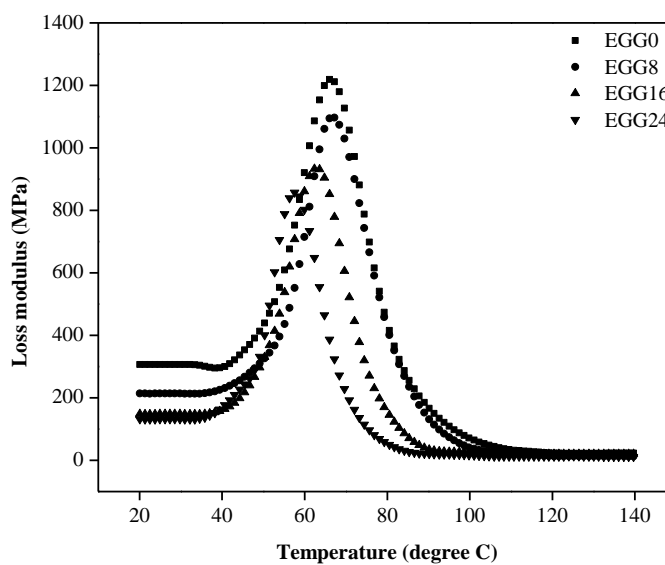
Figure 5.20b Loss modulus of granite powder filled carbon epoxy composites
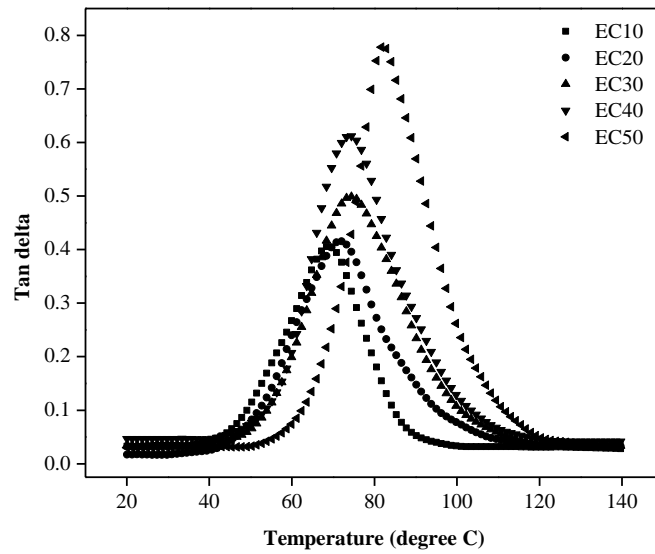
Figure 5.21a Tan δ of unfilled carbon epoxy composites
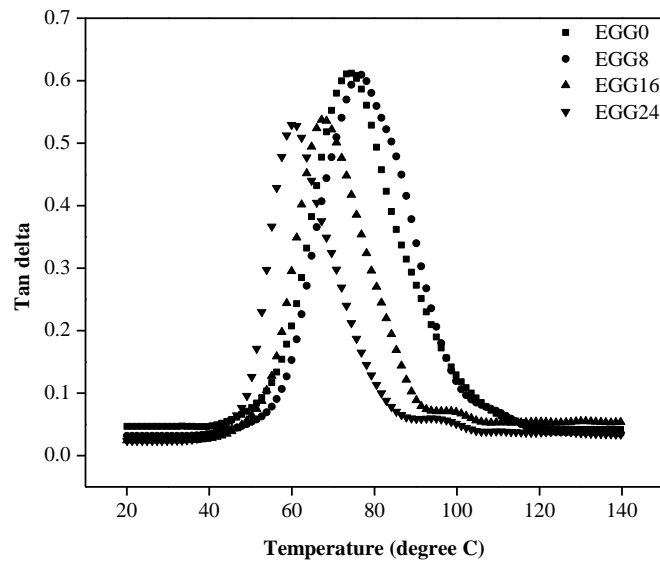
Figure 5.21b Tan δ of granite powder filled carbon epoxy composites

The damping factor or tan δ of the material gives the balance between the elastic phase and viscous phase in a polymeric structure. The fibers carry the maximum amount of stress and allow only small amount of it to strain the interface between fiber and matrix. Hence, stronger the interface between fiber and matrix signify less energy dissipation in the composite [128]. The tan δ peak is increased with increase in fiber loading that attributed to poor fiber matrix interface (see Figure 5.21a). For 50 wt.% fiber loading the proper wetting of fiber does not happen which increases fiber-fiber interaction resulted in to higher energy

dissipation. Figure 5.21b shows damping property of granite powder filled carbon epoxy composites. For lower fraction of granite powder addition in to carbon epoxy composite (8 wt.%) does not lead to decrease in peak damping factor which shows that the matrix-reinforcement interface properties are not much affected by incorporation of 8 wt.% of granite powder. However, for 16 and 24 wt.% granite powder addition in to carbon epoxy composite shows considerable decrease in peak damping factor. The value of T_g corresponding to peak damping factor are depicted in Table 5.3. The values of T_g corresponding to peak damping factor are higher than the value corresponding to peak loss modulus. Similar, observations were also reported in past study for unfilled and particulate filled glass epoxy composites [126].

Table 5.3 Coefficient, peak height and glass transition temperature of unfilled and granite powder filled carbon epoxy composites

Composite	Coefficient, C	*Adhesion efficiency factor, A	Glass transition temperature ($^\circ$C) T_g	
			from E''_{max}	from $\tan\delta_{max}$
EC10	0.445004	-0.48753	57.55	68.42
EC20	0.470669	-0.32653	61.17	72.05
EC30	0.513631	-0.06997	64.79	74.46
EC40/ECG0	0.53515	0.469388	66	74.46
EC50	0.405385	1.567347	78.08	81.71
ECG8	1.572067	0.024054	67.21	76.87
ECG16	1.341684	0.107804	62.38	67.21
ECG24	1.457101	0.455897	57.55	59.96

* calculated at T_g corresponding to peak loss modulus.

5.3.2 Correlation between mechanical and thermo-mechanical performance

The storage modulus of composite is comparable with the flexural modulus of the same composite [278]. Figure 5.22 shows the correlation between storage modulus (thermo-mechanical performance) at 30°C temperature with flexural modulus (mechanical performance) of unfilled and granite powder filled carbon epoxy composites. Both the properties are in increasing trend with the increase in fiber loading with most significant improvement for increase in fiber loading from 30 wt.% to 40 wt.% respectively. Higher storage modulus than flexural modulus up to 30 wt.% carbon fiber reinforced epoxy composite shows better performance of composite against cyclic stresses. This phenomenon is not seen for 40 and 50 wt.% carbon fiber epoxy composites. Granite powder addition has same negative hybridizing effect on mechanical as well as thermo-mechanical performance.

Highest closeness for storage modulus and flexural modulus of 0.17 GPa is observed for unfilled 10 wt.% carbon fiber epoxy composite and lowest closeness of 0.86 GPa is observed for 16 wt.% granite powder filled carbon epoxy composite.
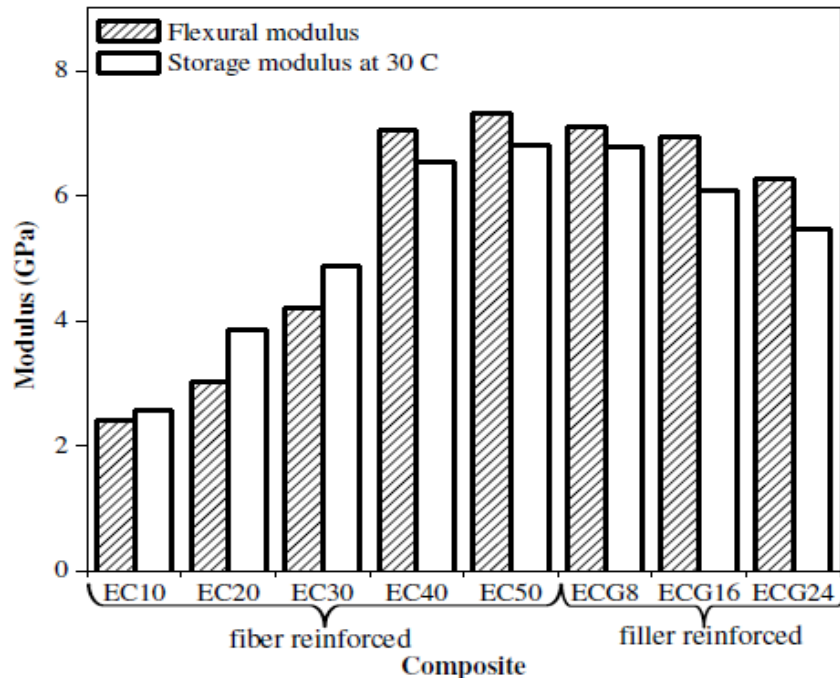
Figure 5.22 Storage modulus at 30°C and flexural modulus of composites

5.3.3 Thermo-Gravimetric Analysis (TGA)

Thermo-Gravimetric Analysis (TGA) is a method to evaluate the thermal degradation trend and thermal stability of composite under controlled atmosphere [236]. TGA curves for unfilled and granite powder filled carbon epoxy composites is shown in Figures 5.23a and 5.23b respectively. The composite materials are complete thermally degraded in temperature range of 30 to 500°C and beyond 500°C temperature negligible weight loss is observed. Both the unfilled and particulate filled composites are thermally stable below 300°C temperature and above 350°C rapid thermal degradation is started. Exploded view in Figure 5.23a shows early start of degradation for lower fiber loading of unfilled composite.

At 500°C the residue amount found more for higher fraction of fiber content due to thermal stability of carbon fiber at mentioned temperature. Figure 5.23b shows thermal weight loss of granite powder filled carbon epoxy composites as a function of temperature. Early degradation is observed (in exploded view) with increase in the granite powder content because of improper interface bonding between filler and matrix. At temperature of 500°C higher amount of residue with the increase in filler content is attributed to melting point of granite powder.
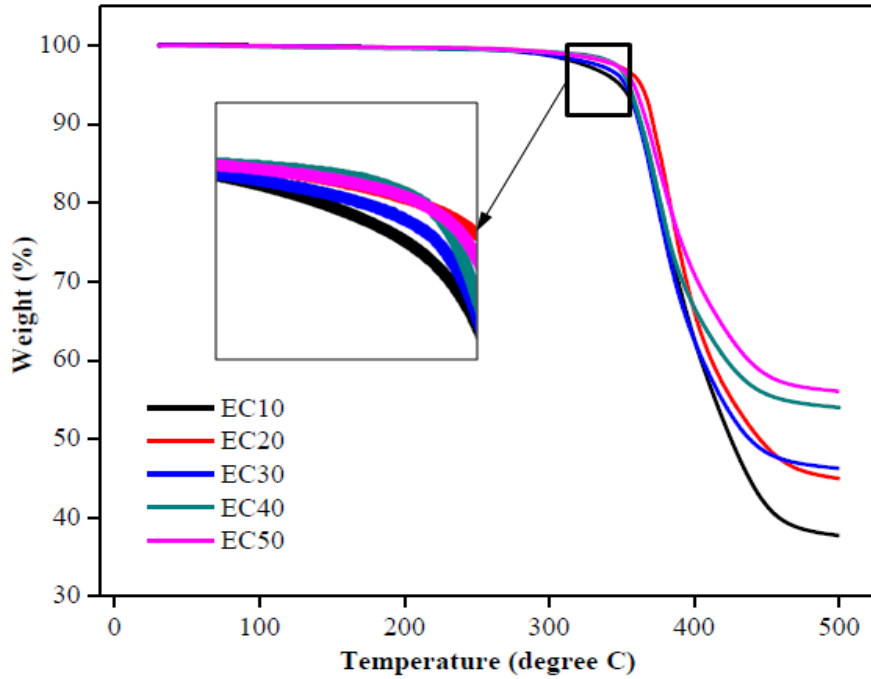
Figure 5.23a Variation of weight of unfilled carbon-epoxy composite
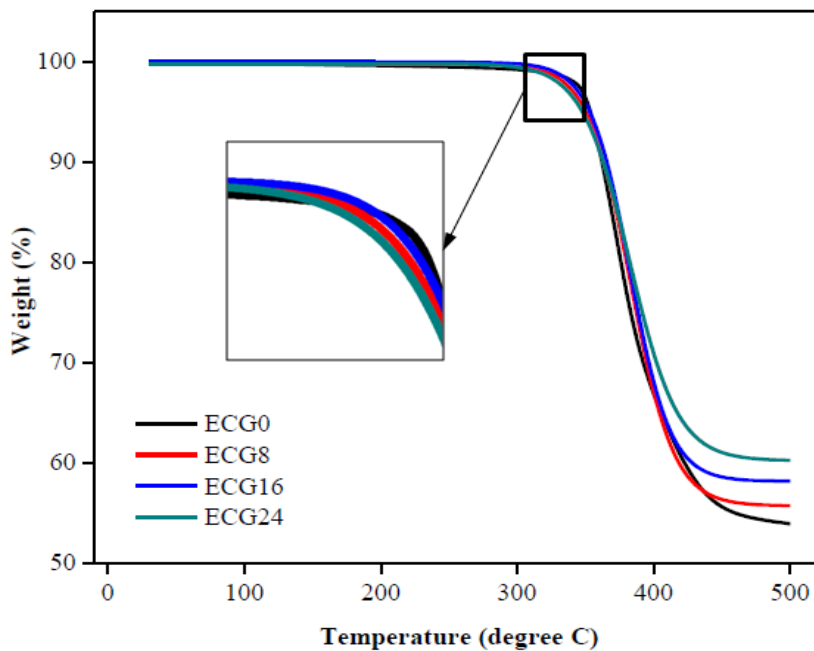
Figure 5.23b Variation of weight of granite powder filled carbon-epoxy composite

5.3.4 Thermal Conductivity analysis

Thermal conductivity of composite material is depending on the conductivity of matrix as well as reinforcement material. The value can be predicted using numerous theoretical models available. The series model and parallel model gives the lower bound value and upper bound value of thermal conductivity of composite. Figure 5.24a and 5.24b illustrated the thermal conductivity determine using different modes for unfilled and granite powder filled

carbon epoxy composites respectively. All the values fall between upper lower bound and upper bound values. Experimental value of unfilled carbon epoxy composite is increased with increase in fiber loading. This increase in thermal conductivity is attributed to higher thermal conductance of carbon fiber compared to epoxy resin. The value is increased from 0.205 W/m-K for unfilled 10 wt.% carbon epoxy composite to 0.291, 0.363, 0.543 and 0.608 W/m-K for unfilled 20, 30, 40 and 50 wt.% carbon epoxy composites respectively. In case of unfilled composites at lower wt.% of carbon fiber the values of thermal conductivity evaluated by different modes are close to each other except to value calculated by parallel mode and the difference in values is increased with increase in fiber loading.
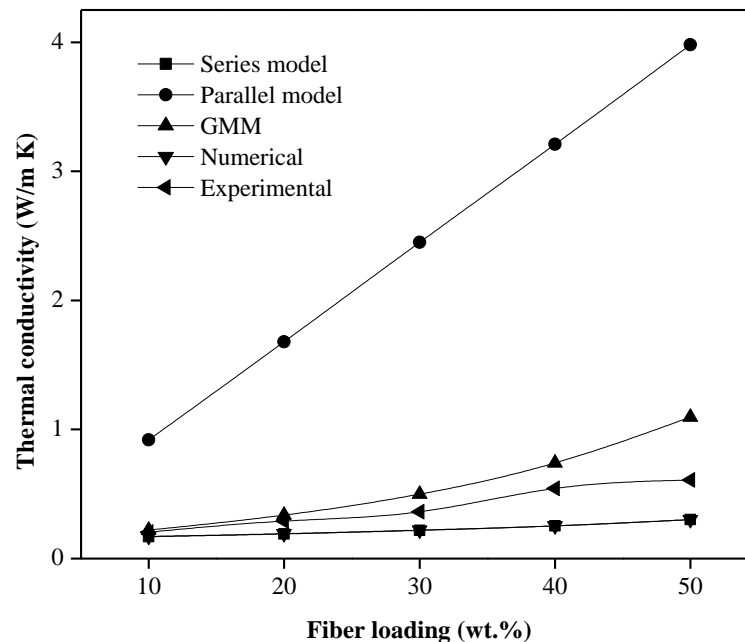
Figure 5.24a Variation in thermal conductivity of unfilled carbon epoxy composite

Incorporation of granite powder in carbon epoxy composites has marginal effect on the value of thermal conductivity evaluated by different modes (see Figure 5.26b). The numerical results are in close agreement with results obtained by series mode whereas; the experimental results are in marginal agreement with geometric mean model. Experimental thermal conductivity of unfilled composites are 0.732, 0.942 and 0.983W/m-K for incorporation of 8, 16 and 24 wt.% granite powder respectively. Granite powder filled carbon epoxy composites are also follows the limit by series model (lower bound value) and parallel model (upper bound value). The results show that reinforcement of thermally conductive

carbon fiber and granite powder does not lead to significant improvement in thermal conductivity of unfilled and granite powder filled carbon epoxy composites.
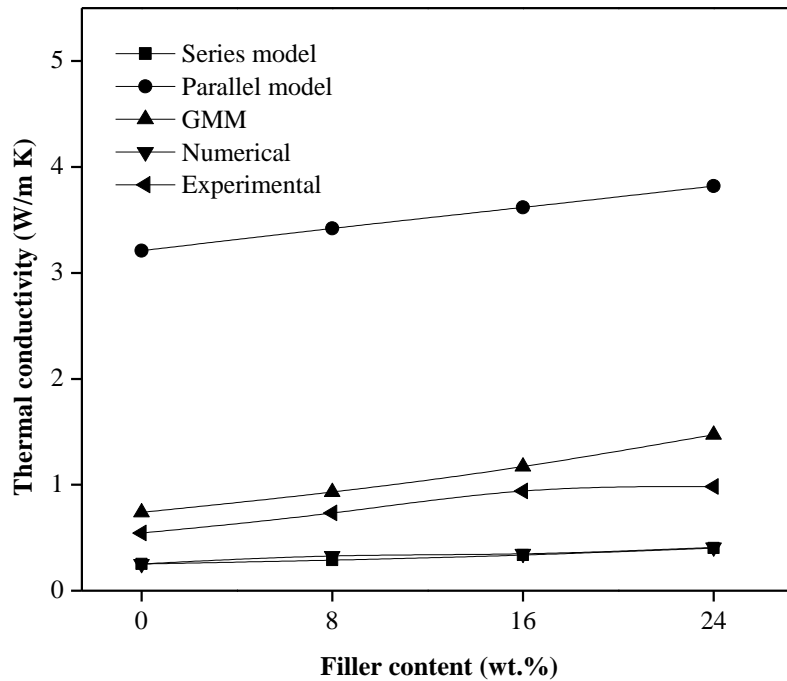
Figure 5.24b Variation in thermal conductivity of granite powder filled carbon epoxy composite

2D finite element model is used to determine the thermal conductivity of hybrid composite material. The evaluation is based on the temperature difference observed along the thickness of composite. The maximum temperature indicates lower thermal conductivity and vice versa. The temperature contour indicating difference along the thickness is illustrated in Figure 5.25. Temperature difference of 0.447 and 0.19ºC is observed for composite reinforced with 10 and 40 wt.% carbon fiber respectively (see Figure 5.25a and 5.25b). This is indication of improvement in thermal conductivity with higher fiber loading. Figure 5.25c and 5.25d depicted the temperature difference of 0.183 and 0.172ºC for incorporation of 8 and 16 wt.% granite powder in carbon epoxy composite respectively. Marginal variation in temperature cause slight variation in thermal conductivity. Thermal flux developed along the 2D geometry is different due to variation of thermal conductivity of epoxy resin and reinforcement. Thermal flux generated in 16 wt.% granite powder filled carbon epoxy composite is shown in Figure 5.26.
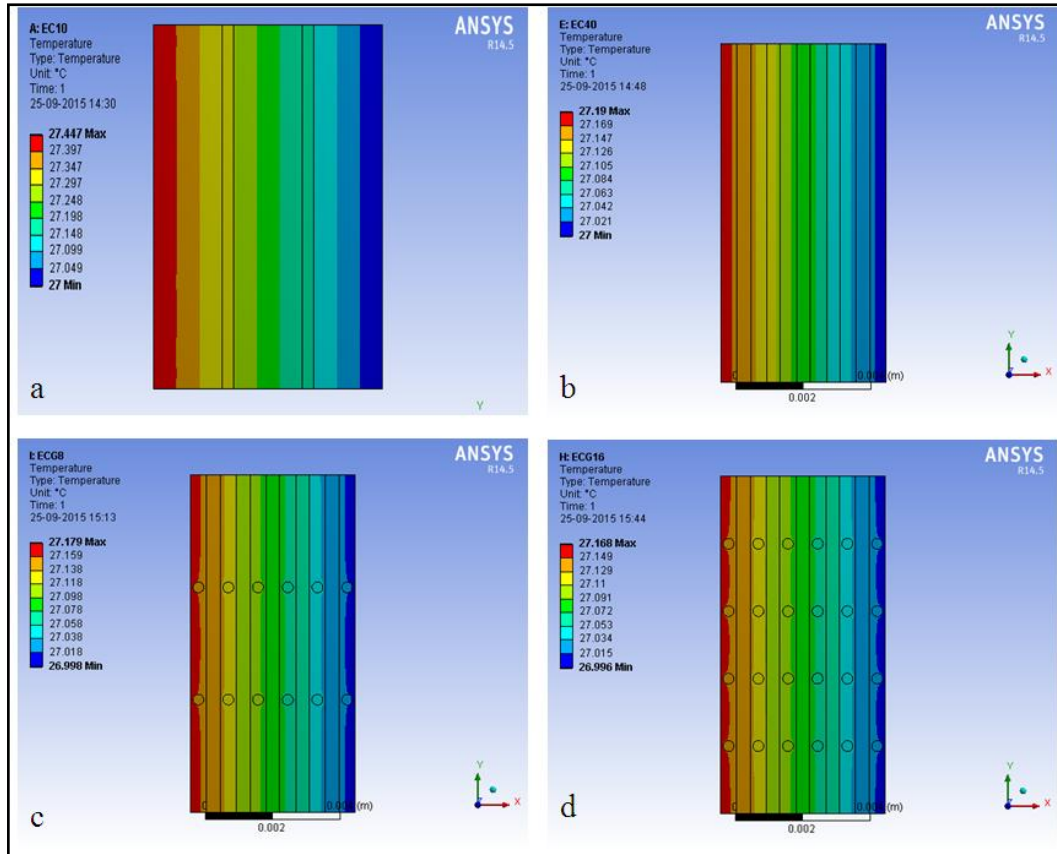
Figure 5.25 Temperature contours for (a) EC10, (b) EC40, (c) ECG8 and (d) ECG16
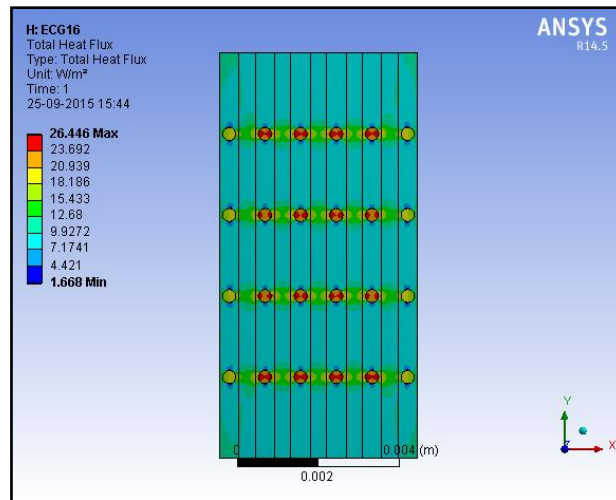
Figure 5.26 Thermal flux developed in 16 wt.% granite powder filled carbon epoxy composite

Chapter Summary

This chapter has provided:

❖ Dynamic mechanical analysis and thermo-gravimetric analysis of unfilled and granite powder filled fiber reinforced polymer composites.

❖ Reinforcement effectiveness and adhesion efficiency factor of unfilled and granite powder filled fiber reinforced polymer composites.

❖ The thermal conductivity measurement and their numerical validation using 2D finite element program.

The next chapter presents the erosion test in the environment of slurry jet and air jet impact for the composites under investigation, their statistical interpretation and optimization of all the properties by TOPSIS method.

<div align="center">*****</div>

<div align="right">

Chapter 6

</div>

<div align="center">

EROSION WEAR BEHAVIOR AND OPTIMIZATION OF COMPOSITES

</div>

Fiber reinforced polymer composites (FRP) are commonly used materials in automotives, marines, pulp pipelines and structural components like wind turbine blades. During running period the above mentioned applications are completely exposed to external environment from impact of heavy solid sand particles with wind, water droplets mixed with environmental dusts and or insects etc specifically in extreme climates like desert environment. This may leads to subsequent deterioration of materials and minimizes the life of the intended component. This chapter describes steady state experimental runs, by varying impact velocity and impingement angle conducted on unfilled and granite powder filled fiber reinforced epoxy composites. Further, design of experiment orthogonal array design is used to evaluate the degree of significance of individual factor on erosive wear rate in both the slurry and solid particle conditions. This chapter consists of three sections, section A describing the erosion behavior of composites that subjected to impact of slurry jet, section B describing solid particle erosion characteristics for the composites under investigation and section C describing the ranking of alternatives by using TOPSIS method.

Section A: Slurry erosion behavior

<div align="center">

Part-I

</div>

Slurry jet erosion wear analysis of unfilled and granite powder filled glass-epoxy composites

6.1 Steady state slurry jet erosion behavior

6.1.1 Influence of impingement angle on erosion rate

Hutching [279] observed that the jet erosion behavior is greatly affected by the conditions under which it takes place. By changing impingement angle, fiber loading, properties of erodent material the erosion can show brittle or ductile behavior. The peak erosion can be obtained at 30° and 90° impingement angles for ductile and brittle materials respectively but this grouping is not authoritative [5]. The erosion rate of unfilled and granite powder filled glass epoxy composites at impact velocity 30 m/s, stand-off distance 50 mm, erodent size 325 µm and sand flow rate 160 g/min for different impingement angles is illustrated in Figures 6.1a and 6.1b respectively. The peak erosion rate for unfilled composite with 10 and 20 wt.% glass fiber is at 60° impingement angle whereas, for further addition of 30, 40 and 50 wt.% glass fiber show peak erosion at 75° impingement angle (see Figure 6.1a). Addition of glass fiber in epoxy resin shifts the peak erosion rate from impingement angle 60° to 75°. It shows

transition of material from semi-ductile to brittle behavior due to reinforcement of glass fiber. The erosion rate of unfilled glass epoxy composites is reduced for reinforcement of glass fiber from 10 to 40 wt.% at all the impingement angles under consideration. This may be due to incorporation of brittle glass fiber in to epoxy resin which shifts peak erosion at higher impingement angle [280]. Further, reinforcement of 50 wt.% glass fiber results in increasing erosion rate at all impingement angle except to impingement angle of 30˚. The reason for this may be early exposure of glass fiber to impact of sand particles.
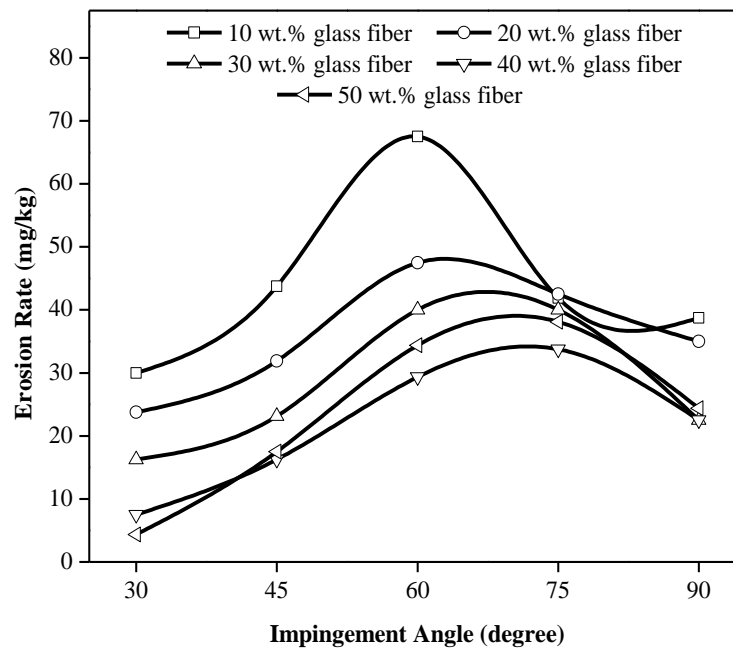
Figure 6.1a Influence of impingement angle on erosion rate of unfilled glass epoxy composite

Figure 6.1b shows erosion wear behavior of granite powder filled glass epoxy composite as function of impingement angle. Incorporation of granite powder has positive effect at all the impingement angle under study as far as erosion rate is concerned. Reduction in erosion rate is marginal for filled glass epoxy composite with 8 wt.% granite powder content but significant reduction is observed with addition of 16 wt.% granite powder in glass epoxy composite. Further, addition of 24 wt.% granite powder shows again only marginal positive effect on erosion rate. Uniformity and population density of granite powder may be the cause for this uneven positive effect on erosion rate. At 8 wt.% granite powder addition the granite powder distribution is uniform but population density is lower and for 24 wt.% of granite powder addition the population density is higher but it causes agglomeration. However, at 16 wt.% granite powder addition population density is moderate and uniformity

is good which results in higher positive effect on erosion rate. It is also observed that, at higher impingement angle the effect granite powder content is significant as compared to lower impingement angle. This shows that addition of granite powder helps to improve wear resistance against impacting particle at higher impingement angle than abrading at lower impingement angle.
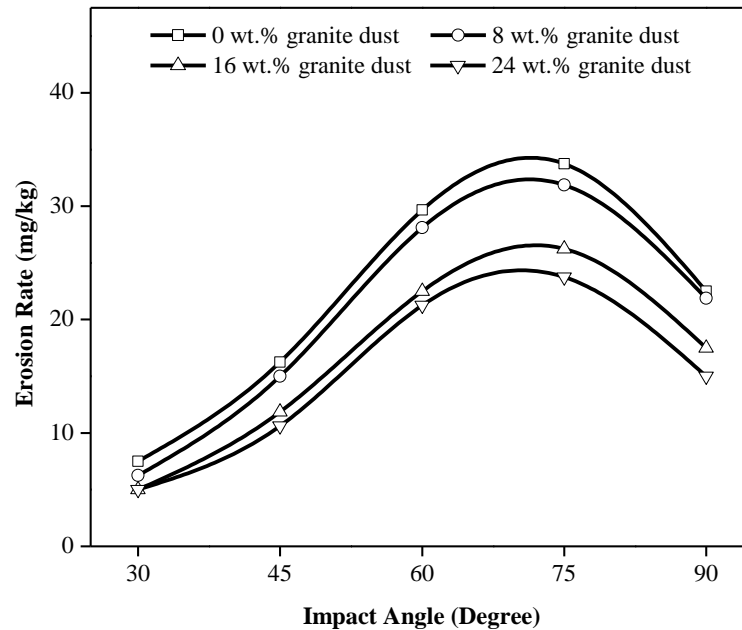
Figure 6.1b Influence of impingement angle on erosion rate of granite powder filled glass epoxy composite

6.1.2 Influence of impact velocity on erosion rate

The erosion rate of unfilled and granite powder filled glass epoxy composites at impingement angle 60˚, stand-off distance 50mm, erodent size 325 µm and sand flow rate 160 g/min for varying impact velocity from 10m/s to 40m/s is illustrated in Figures 6.2a and 6.2b respectively. The erosion rate is greatly affected by impact velocity and the effect of both the reinforcement is significant at higher impact velocity. The effect of reinforcement of glass fiber is negligible on erosion rate for impact velocity of 10 and 20 m/s as shown in Figure 6.2a (illustrated as phase I). Further increase in velocity from 20 m/s to 30 m/s start to increases the erosion rate for all the composition of unfilled glass epoxy composites (phase II). Rapid increase in erosion rate is observed for high velocity of 40 m/s (phase III). The rate of increase in erosion rate is higher for composite with lower wt.% of glass fiber reinforcement. Erosion rate at 40 m/s is reduced from 174.37 mg/kg to 153.75 mg/kg (i.e.

11%) for increase of glass fiber loading from 10 wt.% to 20 wt.%. Further at 30 wt.% erosion rate is reduced to 131.87 mg/kg (i.e reduced by 14%). Highest reduction from 131.87 to 85.62 mg/kg (i.e. 35%) is observed for increase in glass fiber loading from 30 wt.% to 40 wt.% (see Fig. 4a). However, the erosion rate for 50 wt.% glass fiber reinforced composite is slightly increased to 92.5 mg/kg.
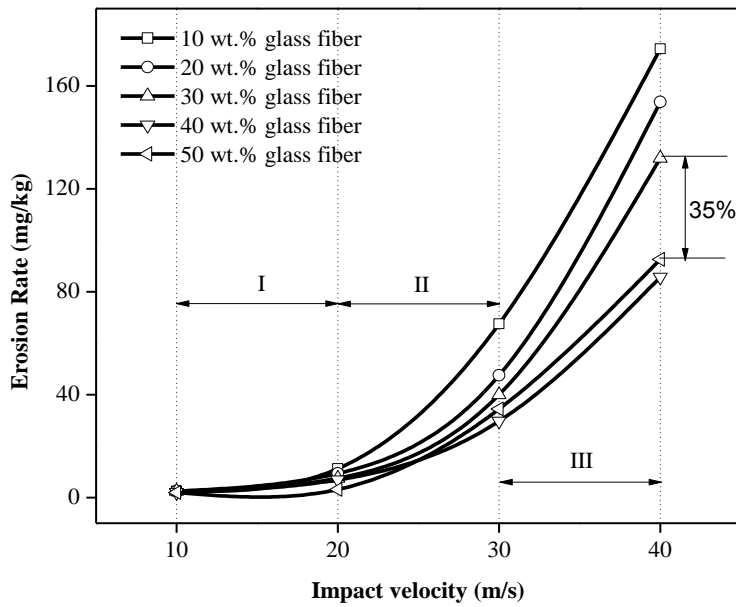
Figure 6.2a Influence of impact velocity on erosion rate of unfilled glass epoxy composite
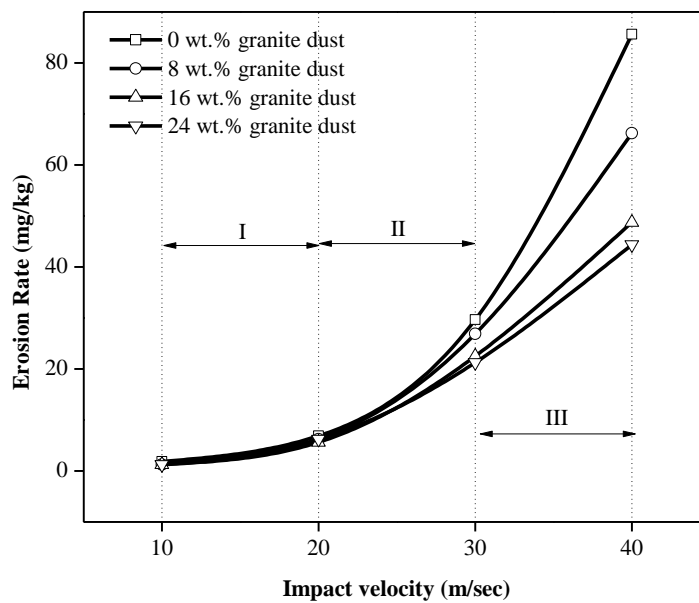
Figure 6.2b Influence of impact velocity on erosion rate of granite powder filled glass epoxy composite

Figure 6.2b shows that increase in erosion rate for all granite powder filled glass epoxy composites is fairly remains same for impact velocity of 10 and 20 m/s (phase I). The erosion rate is marginally reduced with increase in wt.% of granite powder at impact velocity of 30 m/s (phase II). At impact velocity 40 m/s incorporation of granite powder shows highest influence on erosion rate (phase III). Addition of granite filler in the 40 wt.% glass fiber reinforced epoxy composite positively decreases the slurry erosion rate and the effect is more significant at higher impact velocity. Higher hardness of granite powder with the presence of SiO_2 (i.e 71.59%) is may be the cause for reduction in erosion rate. Granite particles absorb kinetic energy of erodent material and trying to resist removal of particles from target material. At higher velocity of 40 m/s the reduction in erosion rate for 8 wt.% granite powder filled glass epoxy composite is reduced from 85.62 mg/kg to 66.25 mg/kg (i.e. 22%). Addition of 16 wt.% granite powder further reduces the erosion rate to 48.75 mg/kg (i.e. 26%). However, addition of 24 wt.% granite powder reduces erosion rate marginally to 44.37 mg/kg (i.e. 8%).

6.1.3 Erosion shape

In case of erosion occurred by jet of slurry consisting of sand particles with water, the static back pressure is generated on the sample with highest pressure at the centre point of impact (known as stagnation point). This back pressure reduces velocity and deflects the erodent particle path slightly away from the stagnation point and the restricted the material removal at the stagnation point. This causes uneven material removal from the test sample [18]. Hence, in addition to erosion rate, it is necessary to observe the eroded surface profile as erosion rate is not uniform along the eroded surface. At normal impact the representative cross section of 'W' shape of scar for eroded surface profile of granite powder filled glass epoxy composite at 40 m/s impact velocity is shown in Figure 6.3. All the different profiles are like round bowl with protruded island at the middle. Researchers were reported similar observations for profile of eroded surfaces in slurry erosive wear condition [281-283].

At normal impact (90° impingement angle) the shape of 'W' scar is symmetrical for all the different samples which show uniform distribution of sand particles in the flow. Minimum material removal is observed at centre of the scar and the reason for low material removal is high static back pressure which evolves as stagnation point at the centre of scar. The static back pressure imposed on the specimen surface is maximum at the centre of wear scar and gradually reduced from the centre to the outer region (Figure 6.4a). Figure 6.4b shows the sand particle trajectory before and after impact on the specimen for normal impact.

The particles are directed in all the direction after impact uniformly. Figure 6.5 shows the static back pressure generated on the samples at varying impingement angle
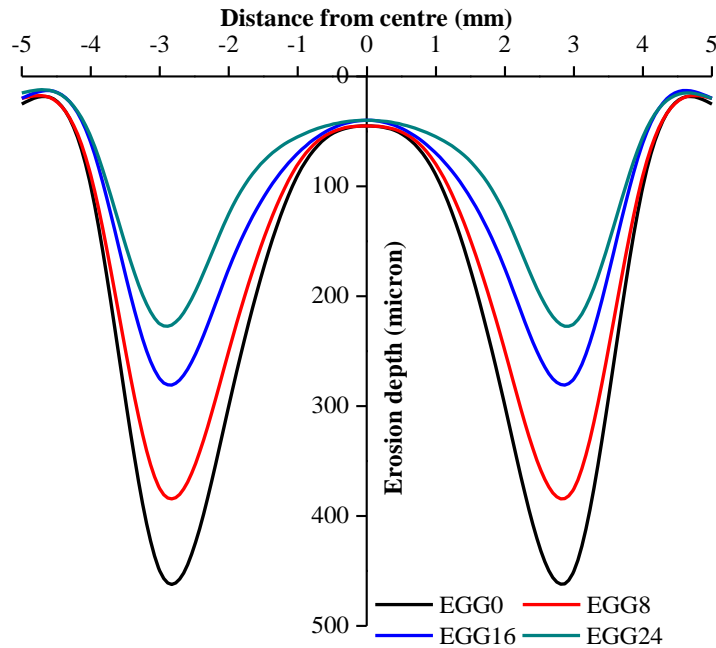
Figure 6.3 Effect of addition of granite on profile of eroded surface

(a)   (b)
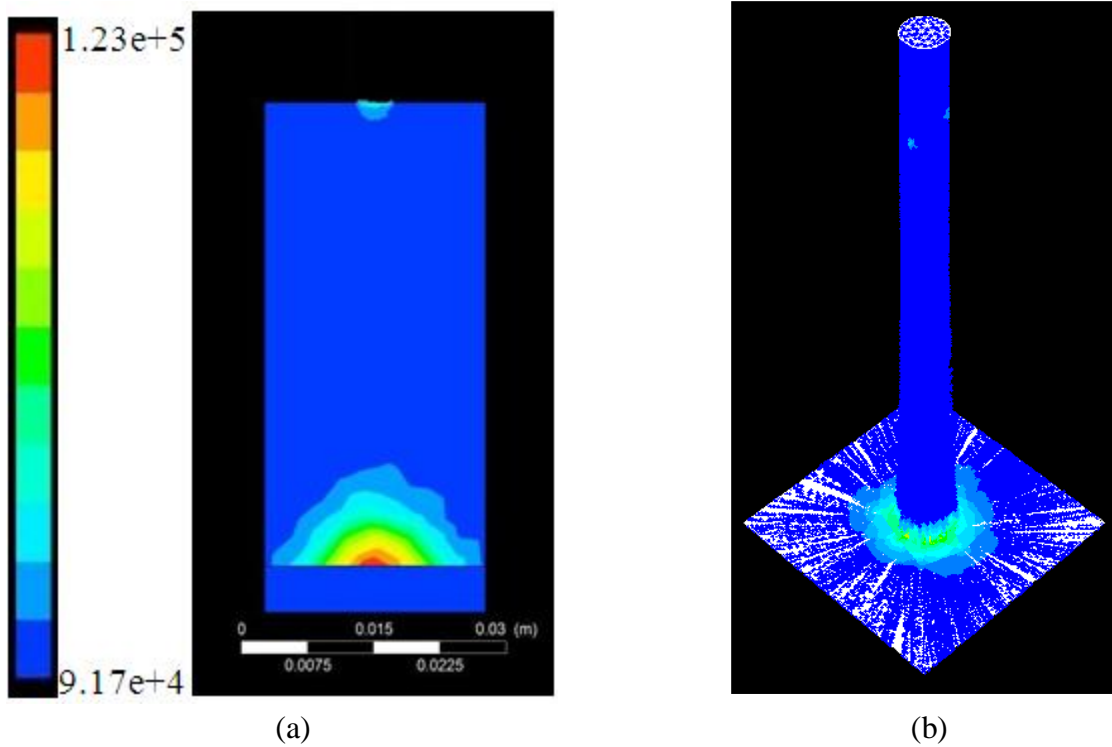
Figure 6.4 Simulation results of slurry erosion process for normal impact (a)Static back pressure on test specimen (b) particle trajectory on the specimen

30°   45°   60°   75°
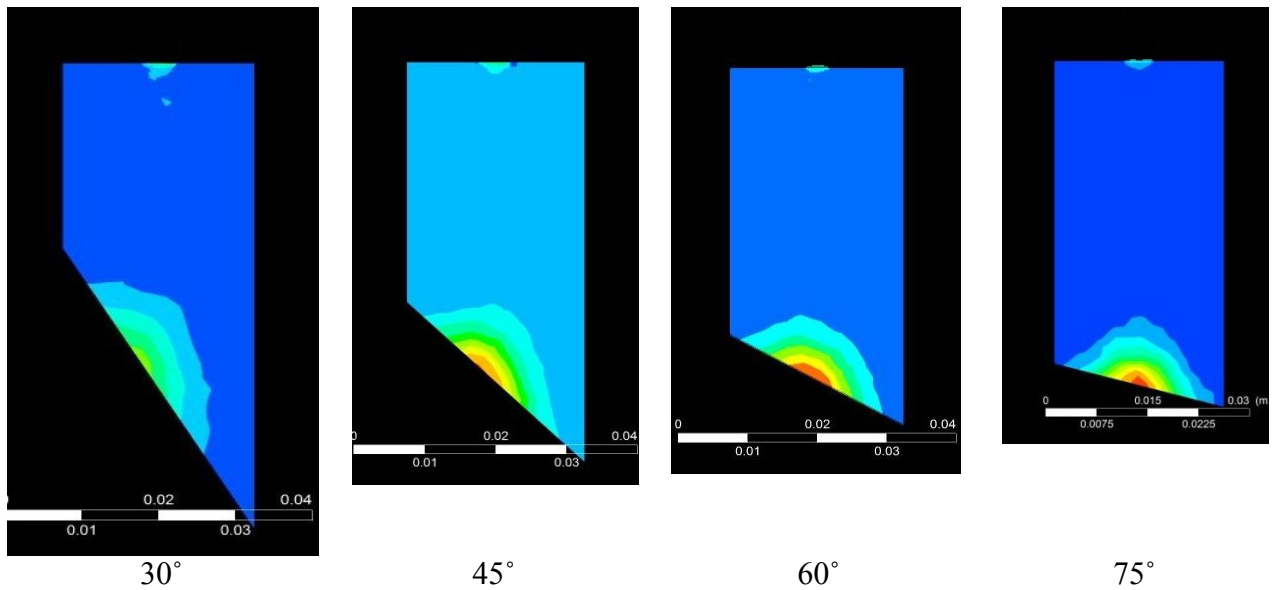
Figure 6.5 Static pressure on the sample surface at varying impact angles

6.1.4 Numerical analysis

Figures 6.6a to 6.6d show the simulation results using ANSYS Fluent for the unfilled and granite powder filled glass epoxy composite. Figures 6.6a(i) and 6.6a(ii) show contour of erosion rate and particle traces for jet impact velocity of 30 m/s at impingement angle 45° for 40 wt.% glass epoxy composite. The maximum erosion rate observed for this particular case is 2.16×10^{-5} kg/m^{2}sec. With increase in impingement angle from 45° to 60° for same composite the maximum erosion rate is increased to 2.81×10^{-5} kg/m^{2}sec (see Figures 6.6b(i) and 6.6b(ii)). The particle traces in the both case shows the sliding of sand particles after impact on the surface of specimen.
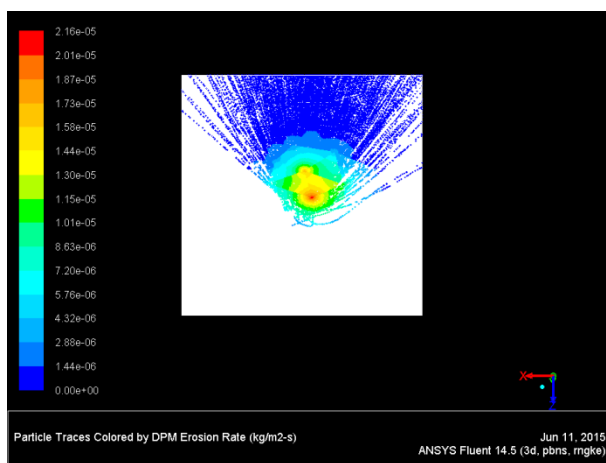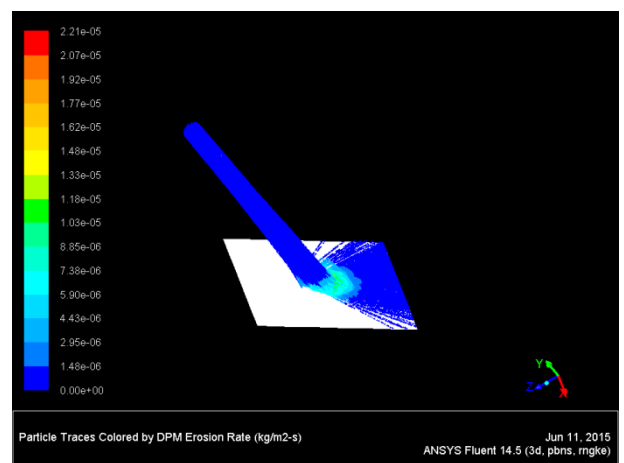
(i)   (ii)

Figure 6.6a Contour for erosion rate and particle traces for jet impact velocity of 30 m/sec at 45^0 impingement angle for 40 wt.% glass fiber-epoxy composite
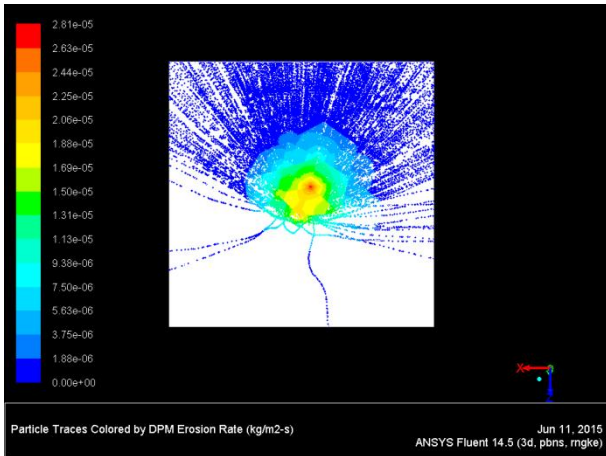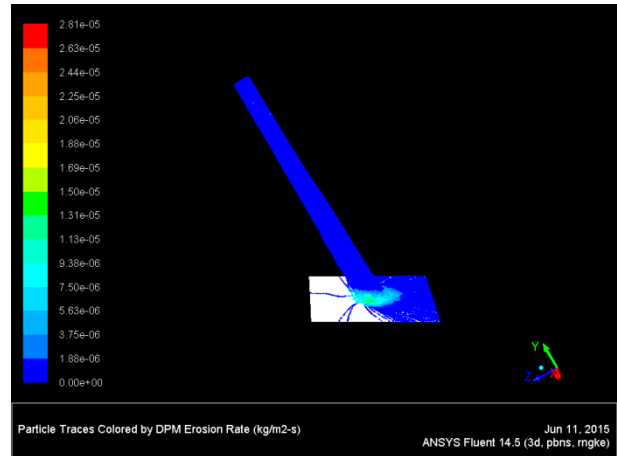
(i)   (ii)

Figure 6.6b Contour for erosion rate and particle traces for jet impact velocity of 30 m/sec at 60^0 impingement angle for 40 wt.% glass fiber-epoxy composite
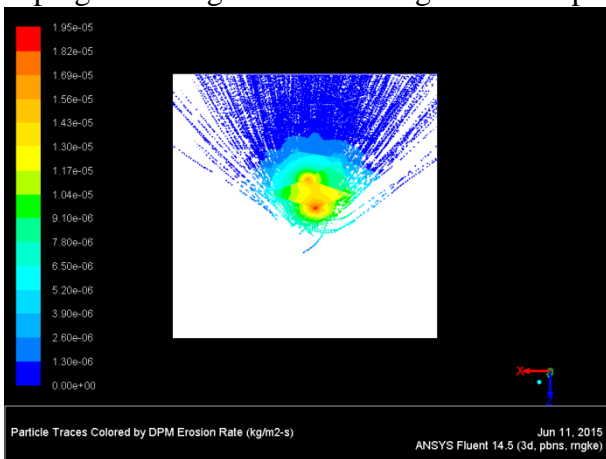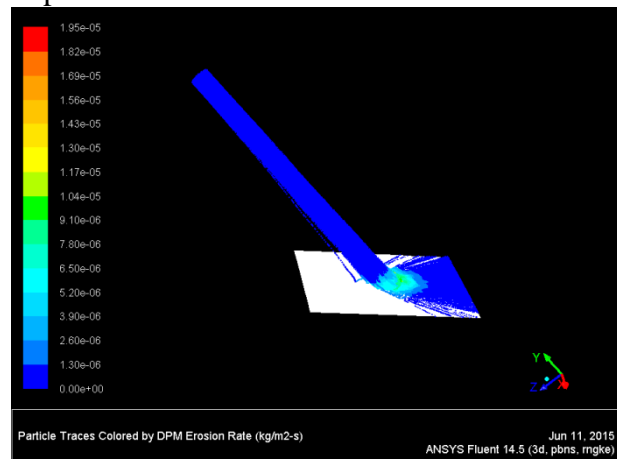
(i)   (ii)

Figure 6.6c Contour for erosion rate and particle traces for jet impact velocity of 30 m/sec at 45^0 impingement angle for 16 wt.% granite powder filled jute fiber-epoxy composite
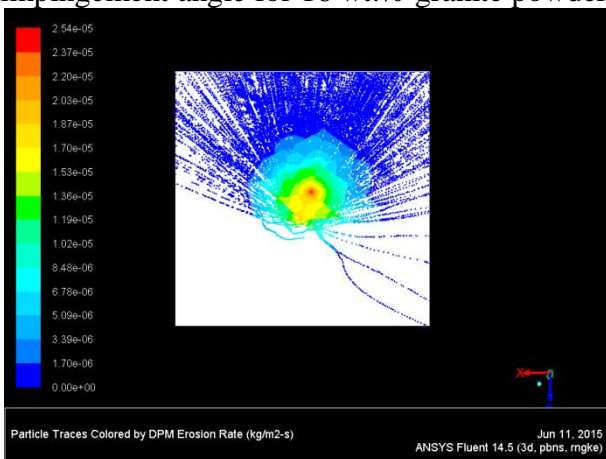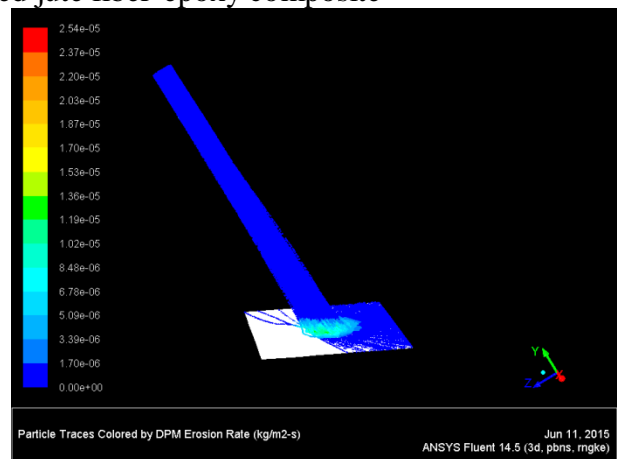
(i)   (iii)

Figure 6.6d Contour for erosion rate and particle traces for jet impact velocity of 30 m/sec at 60^0 impingement angle for 16 wt.% granite powder filled jute fiber-epoxy composite

At jet impingement angle 45˚ almost all particles are sliding in forward direction whereas, for 60˚ angle of jet impingement few particles are sliding in backward direction.

The amount of sand particles sliding in backward direction reduces with lowering the angle between slurry jet and surface of sample. Granite powder filled glass epoxy composites shows similar trend in increase in maximum erosion rate with increase in impingement angle from 45˚ to 60˚ (see Figures 6.6c and 6.6d). The maximum erosion rate for 16 wt.% granite powder filled glass epoxy composite at 45˚ impingement angle is 1.95×10^{-5} kg/m²sec whereas, for 60˚ impingement angle the maximum erosion rate is 2.54×10^{-5} kg/m²sec. From the particle traces it is clearly observed that eroded surface area is increasing for the lower impingement angle. This may be due to larger horizontal component of velocity which results in sliding of sand particle rather than impacting. Figure 6.4b shows shape of eroded surface as circle at normal impact of jet containing water and sand whereas, Figures 6.6a(ii), 6.6b(ii), 6.6c(ii) and 6.6d(ii) show the shape of eroded surface as ellipse for impact at other than normal to the surface of sample. The proposed CFD code is validated by comparing the trends of simulation results with experimental results for erosion rate.
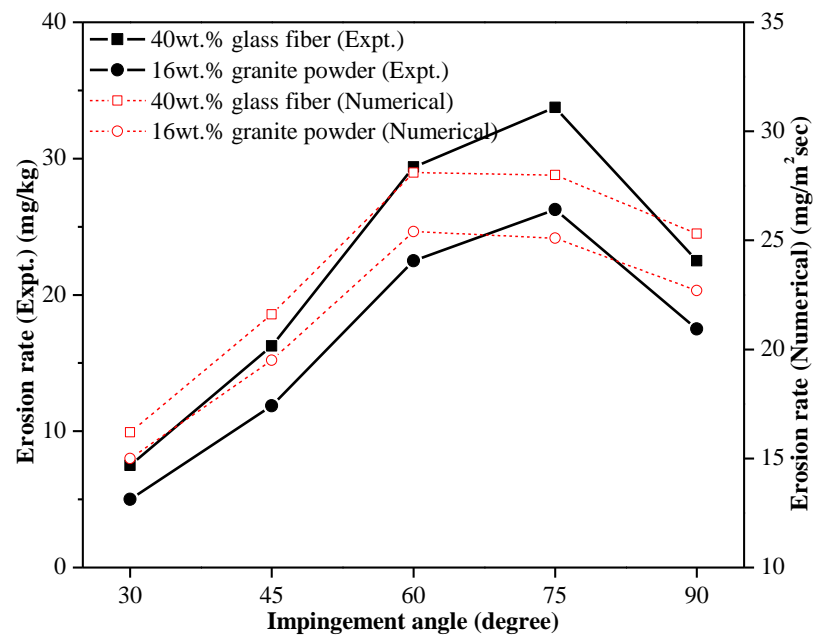
Figure 6.7 Validation of trend for experimental and simulation results for unfilled and granite powder filled glass epoxy composites

Figure 6.7 shows good agreement of simulation results and experimental results as far as trend is concerned. The experimental results shows the maximum erosion rate at 75˚ impingement angle whereas, simulation results shows maximum erosion rate at 60˚ impingement angle (see Figure 6.7). This difference may be due to approximations made

while simulating the erosion process using CFD code. Both the experimental as well as simulation results shows semi-ductile behaviour of composite material when subjected to high velocity impact of jet containing water and sand particles.

6.2 Taguchi experimental design and ANOVA

The experimental result and corresponding S/N ratios for erosion rate of unfilled and granite powder filled glass epoxy composite are shown in Table 6.1a and 6.1b respectively. Control parameters and their main effect on erosion rate for unfilled and granite powder filled glass epoxy composites are shown in Figures 6.8a and 6.8b respectively. The optimal control parameters and the best level of each control factor can be determined from main effect plots for S/N ratios. According to the response for S/N ratios for unfilled glass epoxy composite in Figure 6.8a, the minimum erosion rate is designated as factor A (Level 1, S/N = -3.443), factor B (Level 4, S/N = -13.494), factor C (Level 1, S/N = -17.568), and factor D (Level 3, S/N = -17.661).

From the main effect response for S/N ratios of granite powder filled glass epoxy composites as shown in Figure 6.8b, the optimum control parameter combinations for minimum erosion rate are accomplished with 10 m/s impact velocity (A1), 24 wt.% granite powder content (B4) and 175 μm erodent size. Analysis of control factors will give the additional important information about the influencing parameter. The highest difference of S/N ratio for control factors indicates the strongest influence on erosion rate. It can be seen from Table 6.2a and 6.2b that the strongest influencing parameter on erosion rate is impact velocity, followed by fiber/ filler content, impingement angle and erodent size in case of both unfilled and granite filled glass epoxy composite.

ANOVA was performed to understand the importance level of control factors for erosion rate in unfilled and granite powder filled glass epoxy composites. The ANOVA results for the erosion rate of unfilled and granite powder filled glass epoxy composite are shown in Table 6.3a and 6.3b. The last column of each table indicates significance of individual control factor on erosion rate. It is known that smaller is the p-value, greater is the significance of the factor corresponding to it [284]. From the analysis of variance for unfilled glass epoxy composite, it is concluded that impact velocity (p = 0.000) and fiber loading (p = 0.003) are the significant control parameters for erosion rate, whereas impingement angle (0.032) and erodent size (0.04) are least significant control parameter. Similarly, for granite filled glass epoxy composite, same rank is observed for significance of control parameters with p-value 0.002 for impact velocity, 0.009 for filler content, 0.219 for impingement angle and 0.263 for erodent size. Thus, the most effective control parameter after impact velocity is

fiber loading and filler content for unfilled and granite powder filled glass epoxy composite respectively.

Table 6.1a Experimental design using L_{16} orthogonal array (unfilled glass-epoxy composites)

Sl No	Impact velocity (A) (m/s)	Fiber loading (%) (B)	Impingement angle (C) (degree)	Erodent size (D) (μm)	Erosion rate (Er) (mg/kg)	S/N ratio (db)
1	10	10	30	100	2.50	-7.95
2	10	20	45	175	2.50	-7.95
3	10	30	60	250	1.25	-1.93
4	10	40	75	325	0.62	4.08
5	20	10	45	250	12.50	-21.93
6	20	20	30	325	6.87	-16.74
7	20	30	75	100	5.00	-13.97
8	20	40	60	175	8.12	-18.19
9	30	10	60	325	67.50	-36.58
10	30	20	75	250	19.38	-25.74
11	30	30	30	175	16.88	-24.54
12	30	40	45	100	8.75	-18.84
13	40	10	75	175	97.50	-39.78
14	40	20	60	100	56.88	-35.09
15	40	30	45	325	35.00	-30.88
16	40	40	30	250	11.25	-21.02

Table 6.1b Experimental design using L_{16} orthogonal array (granite powder filled glass-epoxy composites)

Sl No	Impact velocity (A) (m/s)	Filler content (B) (%)	Impingement angle (C) (degree)	Erodent size (D) (μm)	Erosion rate (Er) (mg/kg)	S/N ratio (db)
1	10	0	30	100	2.50	-7.95
2	10	8	45	175	1.88	-5.46
3	10	16	60	250	1.25	-1.93
4	10	24	75	325	0.62	4.08
5	20	0	45	250	10.00	-20.00
6	20	8	30	325	5.62	-15.00
7	20	16	75	100	4.38	-12.81
8	20	24	60	175	3.75	-11.48
9	30	0	60	325	29.69	-29.45
10	30	8	75	250	16.25	-24.21
11	30	16	30	175	13.13	-22.36
12	30	24	45	100	3.75	-11.48
13	40	0	75	175	76.87	-37.71
14	40	8	60	100	49.38	-33.87
15	40	16	45	325	21.88	-26.79
16	40	24	30	250	5.00	-13.97
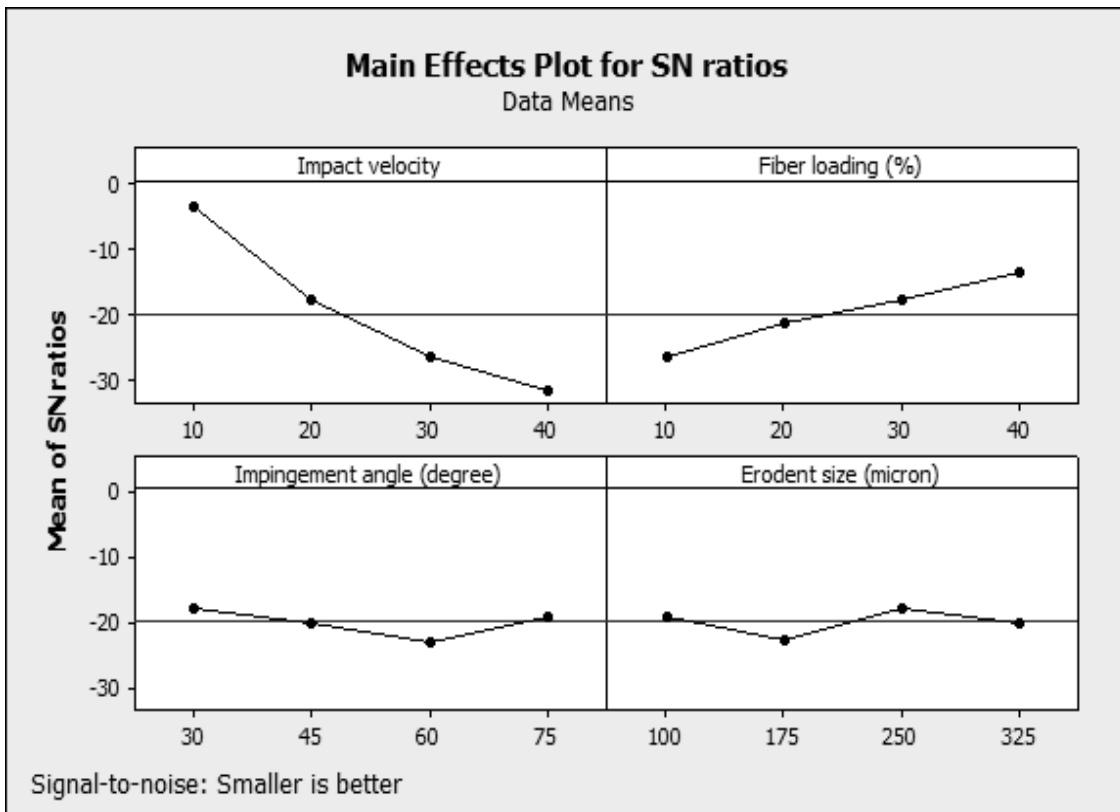
Figure 6.8a Effect of control parameters on average S/N ratio for unfilled glass epoxy composite
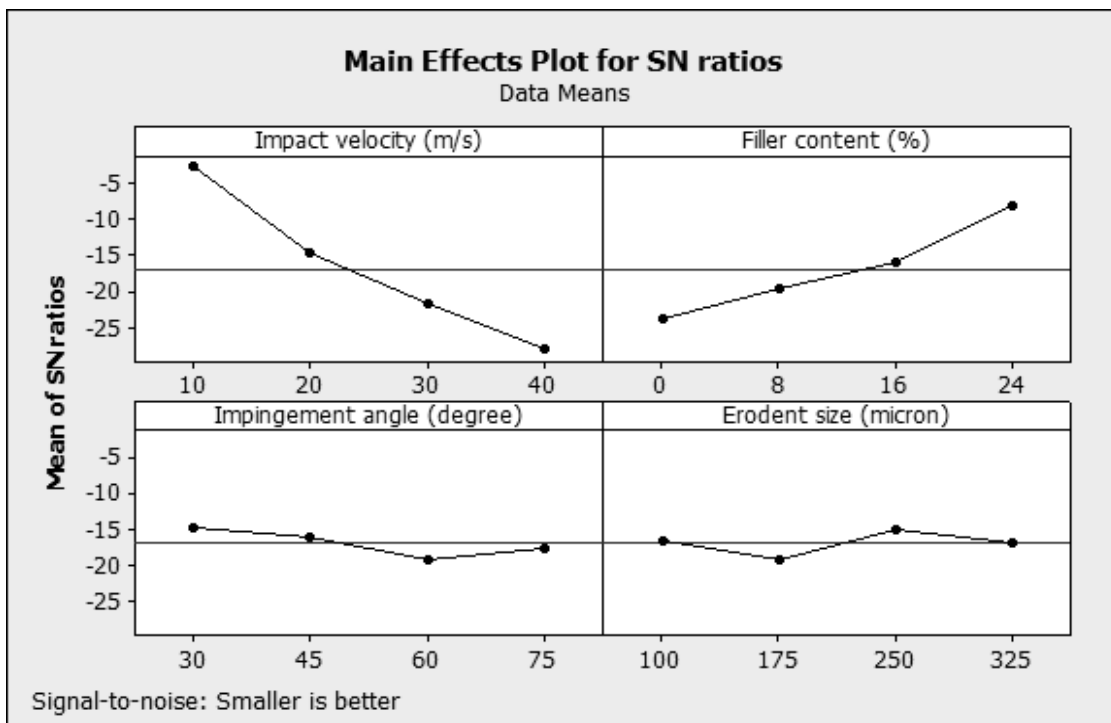
Figure 6.8b Effect of control parameters on average S/N ratio for granite powder glass epoxy composite

Table 6.2a Response table for S/N ratio (unfilled glass epoxy composite)

Level	Control factor			
	Impact velocity	Fiber loading	Impingement angle	Erodent size
1	-3.443	-26.566	-17.568	-18.969
2	-17.715	-21.387	-19.905	-22.620
3	-26.429	-17.836	-22.955	-17.661
4	-31.696	-13.494	-18.855	-20.033
Delta	28.252	13.071	5.387	4.959
Rank	1	2	3	4

Table 6.2b Response table for S/N ratio (granite powder filled glass epoxy composite)

Level	Control factor			
	Impact velocity	Filler content	Impingement angle	Erodent size
1	-2.819	-23.781	-14.826	-16.532
2	-14.826	-19.637	-15.935	-19.255
3	-21.878	-15.980	-19.185	-15.034
4	-28.091	-8.215	-17.667	-16.793
Delta	25.272	15.567	4.667	4.221
Rank	1	2	3	4

Table 6.3a Results of ANOVA for unfilled glass epoxy composite

Source	DF	Seq SS	Adj SS	Adj	F	P
A: Impact velocity	3	1829.35	1829.35	609.79	377.03	0.000
B: Fiber loading	3	367.65	367.65	122.55	75.77	0.003
C: Impingement angle	3	63.34	63.34	21.11	13.05	0.032
C: Erodent size	3	53.08	53.08	17.69	10.94	0.040
Error	3	4.85	4.85	1.617		
Total	15	2318.27				

Table 6.3b Results of ANOVA for granite powder filled glass epoxy composite

Source	DF	Seq SS	Adj SS	Adj	F	P
A: Impact velocity	3	1410.42	1410.42	470.14	85.90	0.002
B: Filler content	3	524.53	524.53	174.84	31.94	0.009
C: Impingement angle	3	44.18	44.18	14.727	2.69	0.219
C: Erodent size	3	36.70	36.70	12.232	2.23	0.263
Error	3	16.42	16.42	5.473		
Total	15	2032.25				

6.3 Surface morphology

The eroded surfaces of the composites are examined by scanning electron microscope (SEM) post erosion. The surface morphology and their change are very useful for the internal (reinforcement and matrix bonding) and external conditions (impingement angle and impact velocity) [279]. The wear mechanism for unfilled and granite powder filled glass epoxy composites in steady state condition by varying impingement angle and keeping other parameters constant is shown in Figure 6.9. From micrograph observations of eroded surfaces, it revealed that composites under consideration demonstrate several stages of the erosion and material removal process. Initially, there is local removal of matrix material from the impacted surface; which caused for exposure of the fibers to the direct impact of sand particles. Sand particle impact on fibers causes to break the fiber perpendicular to their length. Further, continuation of erosion by sand particles resulted in to damage of interface between fibers and matrix [241].

Figures 6.9a and 6.9b show microstructure of eroded surface for unfilled 40 wt.% glass epoxy composite at impact velocity 30 m/s, erodent discharge 160 gm/min, erodent size 325 μm, stand-off distance 50mm and nozzle diameter 3mm. During erosion process when hard sand particles impacted on the specimen the martial removal takes place due to transfer of impact energy to composite material (cutting) and/or sliding of erodent after impacting (abrading). As a function of impingement angle, parallel component of velocity is resulted in to abrasion and normal component of velocity is resulted in to cutting. From the Figure 6.9, general conclusion may be draw as at low impingement angle the dominant wear mechanism is observed as abrasion caused by sliding erodent material after impact and at higher impingement angle the material is removed by cutting.

Figure 6.9a shows removal of matrix material due to sliding of erodent particles on the specimen after impact. Due to low impingement angle 30° the erodent particles are forced to slide in same direction as shown in figure by direction arrow. The particles are not refracted in transverse direction which resulted in matrix retained un-eroded in the transverse direction. Relatively higher impingement angle (i.e. 60°) results in heavy removal of material in form of detachment and separation of fibers from matrix and further fiber fracture as shown in Figure 6.9b. Considerable fraction of kinetic energy is transferred to composite material which results in complete removal of fiber layer and leaving behind the cavities along the length of fiber in matrix material. At 75° impingement angle initially matrix material is removed by impacting sand particles and after removal of matrix layer the sand particles directly impact on the fiber which results in multiple fiber fracture as shown in

Figure 6.9c. Multiple fiber fracture shows severe material removal which is in support with peak erosion rate (see Figure 6.1a) of 40 wt.% glass epoxy composite at 75˚. Normal impact of sand particles on target material demonstrates fracture of fiber perpendicular to their length as shown in Figure 6.9d. Due to hard impact of sand particles fiber-fiber delamination is also observed.
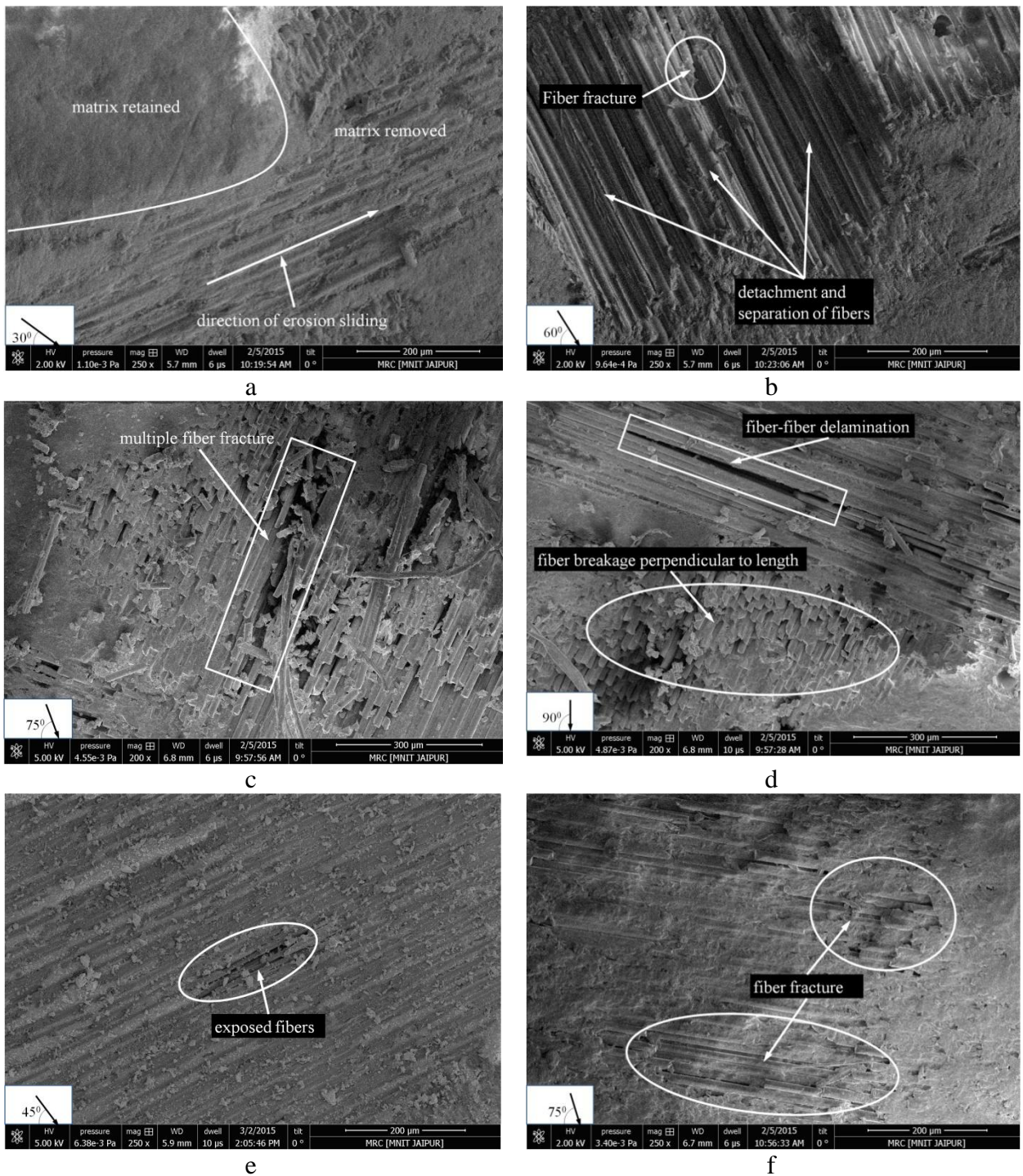
Figure 6.9 Scanning electron micrograph of unfilled and granite filled glass fiber-epoxy composites under steady state condition with varying impingement angle

In this work particulate filler is used in order to lower expenses, utilize waste and increase material strength. SEM views of eroded samples of granite powder filled glass epoxy composite are analyzed. The Figures 6.9e and 6.9f illustrates the eroded surface of 8 wt.% granite powder filled glass epoxy composites at varying impingement angle, while other control factors are kept constant (i.e. impact velocity 30 m/s, erodent discharge 160 gm/min, erodent size 325 µm, stand-off distance 50mm and nozzle diameter 3mm). Erosion of granite powder filled composite (i.e. 8 wt.%) at 45° impingement angle, resulting in damage of matrix material and exposure of fibers to environment which can be clearly seen in Figure 6.9e. The fibers are still held firmly in place by the matrix surrounding them. The traces of granite particles are also visible which prevents complete exposure of fibers. Due to presence of component of velocity parallel to the surface micro grooves are generated along the length of fiber. Figure 6.9f shows removal of matrix and exposure of more fibers to direct impact of sand particles. Fiber fracture is also observed perpendicular to length of fiber. Effect of granite particle to glass epoxy composite is clearly revealed by comparing micrographs in Figure 6.9c (unfilled 40 wt.% glass epoxy composite) and Figure 6.9f (8 wt.% granite powder filled glass epoxy composite). Inclusion of granite particle prevents severe exposure of fibers to direct impact of sand particles.

Figures 6.10a to 6.10d show surface morphology of unfilled and granite powder filled glass epoxy composites as observed from Taguchi experimental results (Tables 6.1a and 6.1b). Figure 6.10a shows, at low impingement angle (30°), for unfilled 20 wt.% glass epoxy composite at 20 m/s impact velocity the fibers are exposed due to removal of matrix material and the fiber fracture is also observed (see Table 6.1a, Expt. Run 6). Whereas, with increase in impact velocity at impingement angle 60°, for unfilled 20 wt.% glass epoxy composite at 40 m/s impact velocity fiber fracture at consecutive layers is also observed in Figure 6.10b (see Table 6.1a, Expt. Run 14). Eroded surface of 8 wt.% granite powder filled glass epoxy composite at 20 m/s impact velocity and 30° impingement angle is shown in Figure 6.10c (see Table 6.1b, Expt. Run 6). The micrograph shows resistance to removal of matrix material due to presence of granite powder. Minimum material removal from the surface is in agreement with experimental result for 30° impingement angle (see Figure 6.1b). With increase in velocity (40 m/s) and impingement angle (60°) resulted in higher normal component of velocity which is responsible for complete removal of granite powder and fiber fracture perpendicular to their length as shown in Figure 6.10d (see Table 6.1b, Expt. Run 14).

a (unfilled run 6)   b (unfilled run 14)

c (filled run 6)   d (filled run 14)
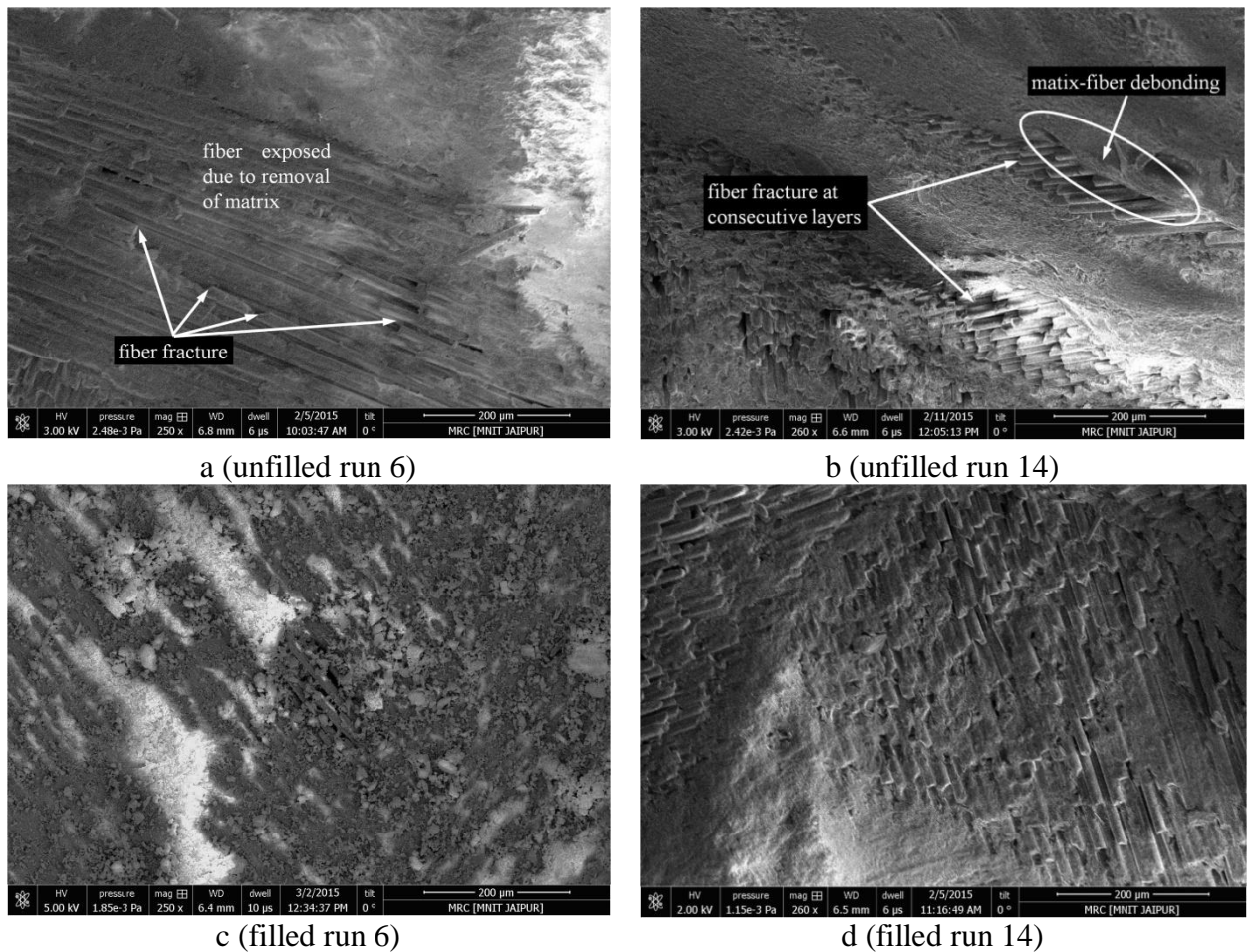
Figure 6.10 Scanning electron micrograph of unfilled and granite powder filled glass fiber-epoxy composites (Taguchi Design of Experiment)

Part-II

Slurry jet erosion wear analysis of unfilled and granite powder filled jute-epoxy composites

6.4 Steady state slurry erosion rate

6.4.1 Influence of impingement angle on slurry erosion rate

Slurry erosion rate of unfilled alkali treated jute epoxy composites in slurry jet environment for different impingement angle keeping other parameters constant (impact velocity: 30m/sec, stand-off distance: 50 mm and erodent size: 325μm and erodent temperature: RT) is illustrated in Figure 6.11a. It is observed that at $60^{°}$ impingement angle, all the unfilled jute epoxy composites show maximum erosion rate and the increasing order of erosion rate for jute fiber reinforced epoxy composites are as EJ40< EJ50<EJ30<EJ20<EJ10 respectively. Hutching [279] observed that the jet erosion behavior is greatly affected by the conditions under which it takes place. By changing impingement angle, fiber loading, properties of erodent material the erosion can show brittle or ductile behavior. The peak erosion can be

obtained at 30° and 90° impingement angle for ductile and brittle erosion respectively but this grouping is not authoritative [5].
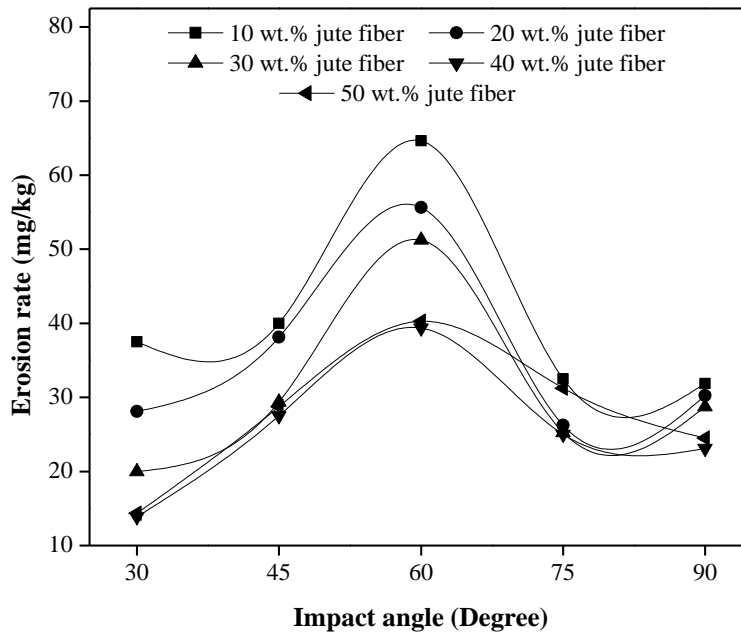
Figure 6.11a Variation of erosion rate with impingement angle for different wt.% fiber loading
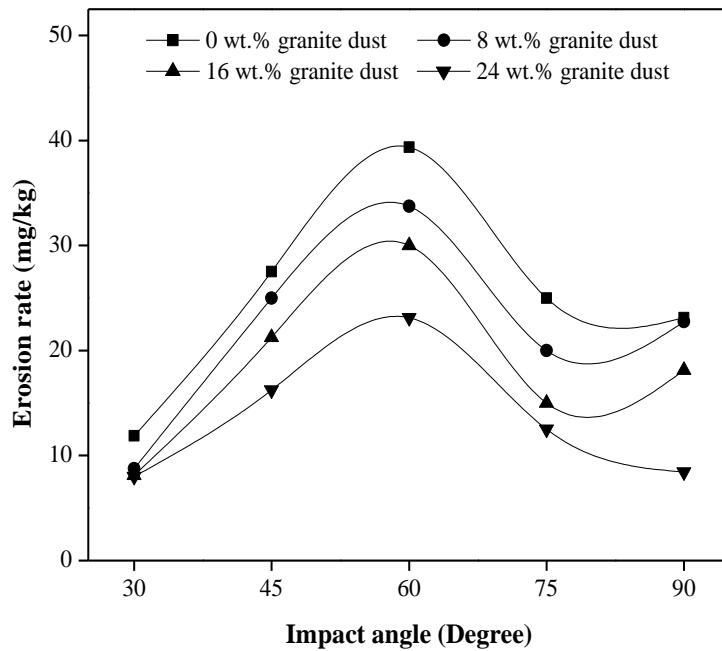
Figure 6.11b Variation of erosion rate with impingement angle for different wt.% filler content

Peak erosion rate at $60°$ depicts semi-ductile erosion behavior of composite. The peak erosion rate at $60°$ impingement angle for 50 wt.% jute fiber loading is increased marginally to 40.25 mg/kg. Similar trend is also reported by Gupta et al. [285] for natural fiber reinforced epoxy composite. This may be due to at higher content of fiber reinforcement the matrix is incapable to proper wetting of fiber which, results in improper bonding between fiber and matrix i.e. matrix does not cover the whole fiber [61]. Figure 6.11b shows the steady state slurry erosion rate of granite powder (0 wt.%, 8 wt.%, 16 wt.% and 24 wt.%) filled jute epoxy composites with varying impingement angle from $30°$ to $90°$ respectively at constant impact velocity = 30m/sec, stand-off distance = 50 mm and erodent size = 325μm and erodent temperature = RT.

Inclusion of granite powder in the jute epoxy composites the erosion resistance is improved as compared to the unfilled jute epoxy composites. However, particulate filled composites are also showing maximum erosion rate at $60°$ impingement angle like unfilled jute epoxy composites (see Figures 6.11a and 6.11b). At $60°$ impingement angle both erosion and abrasion plays an important role. The sand particles are slides on the surface of composite after impacting while dropping down. Thus removing the material due to impact energy (erosion) as well as sliding energy (abrasion). While at $30°$ impingement angle the kinetic energy of erodent particle is transferred to matrix material during sliding (abrasion) only, while at $90°$ impingement angle the kinetic energy is converted in to impact energy (erosion). The minimum value of erosion rate is observed at $90°$ impingement angle for composite filled with 24 wt.% of granite powder (see Figure 6.11b) in the alkali treated jute epoxy composite. The reduction in slurry erosion rate at $60°$ impingement angle for 8 wt.%, 16 wt.% and 24 wt.% granite powder filled composites are 13.77%, 23.80% and 41.27% respectively as compared to unfilled alkali treated jute epoxy composites. This reduction in erosion rate with increase in filler content may be due to addition of hard particulates which absorb impact as well as kinetic energy of erodent particles before getting eroded from the target material.

6.4.2 Influence of impact velocity on slurry erosion rate

Figures 6.12a and 6.12b illustrate slurry erosion rate of unfilled and granite filled alkali treated jute epoxy composites respectively as a function of impact velocity. Results are obtained by conducting tests by varying impact velocity from 10 m/s to 40 m/s keeping all other parameters constant (impingement angle = $60°$, velocity = 30 m/sec, stand-off distance = 50 mm and erodent size = 325 μm and erodent temperature = RT). The kinetic energy of erodent particle is responsible for removal of material form surface of composites. The

quadratic nature of curves in Figures 6.12a and 6.12b are in good agreement with the known fact that kinetic energy of erodent particle is proportional to square of impact velocity.

Initially at lower impact velocity i.e between 10 m/s to 20 m/s (phase-I) the slurry erosion rate is quite low and there is no significant variation in erosion rate with respect to fiber loading. As low erosion rate is attributed to restriction to erodent by water film on the composite to directly impact on target material. Further, with the increase in impact velocity from 20 m/s to 30 m/s the slurry erosion rate is significantly increased (phase-II). This may be due to at higher impact velocity the composite surface behaves plastic deformation and more amount of matrix material is removed initially. However, on further increase in impact velocity i.e above 30 m/s (phase-III) the slurry erosion rate increases rapidly that may be due to penetration of hard silica particles along with water films on the composite surface. However, the actual velocity of erodent particle impacting on the composite surface will be much lower than impact velocity of slurry that is due to particle rebound which shows shielding effect in case of slurry and fluid dynamic condition [286-288].

Figure 6.12a shows significant reduction in erosion rate with the increase in fiber loading from 10 wt.% to 40 wt.%. However, on further increase in fiber loading i.e up to 50 wt.% the slurry erosion rate observed to be marginal effect as far as reduction in erosion rate is concerned. The reduction in slurry erosion rate from 30 wt.% to 40 wt.% jute epoxy composites are 161 mg/kg to 100 mg/kg i.e 37% reduction as indicated zone A in Figure 6.12a. However, on further increase of jute fiber loading from 40 wt.% to 50 wt.% reduction in slurry erosion rate is observed from 100 mg/kg to 93 mg/kg (i.e 7% reduction). It may be due to improper interfacial bond between fiber and matrix material in case of 50 wt.% jute fiber loading. Hence, it may be concluded that for further analysis in any structural and or slurry erosion analysis 40 wt.% fiber loading is considered, as this much percentages of fiber loading with respective to epoxy resin shows minimum slurry erosion rate in slurry environment.

Similarly, Figure 6.12b shows granite powder filled alkali treated jute epoxy composites by varying impact velocity under steady state condition. Addition of granite filler in the jute epoxy composites (optimal combination: 40wt.% jute fiber + Epoxy) positively decrease the slurry erosion rate and the effect is more significant at higher impact velocity. This may be due to higher hardness of granite powder with the presence of SiO_2 (i.e 71.59%), this absorbs kinetic energy of erodent material and trying to resist removal of particles from target material. At higher impact velocity of 40m/s reduction in erosion rate is 32% for addition of granite powder from 0 to 8 wt.%, 25% reduction in erosion rate for addition

granite powder from 8 to 16 wt.% and 20% reduction in erosion rate for addition of granite powder from 16 to 24 wt.% (Figure 6.12b).
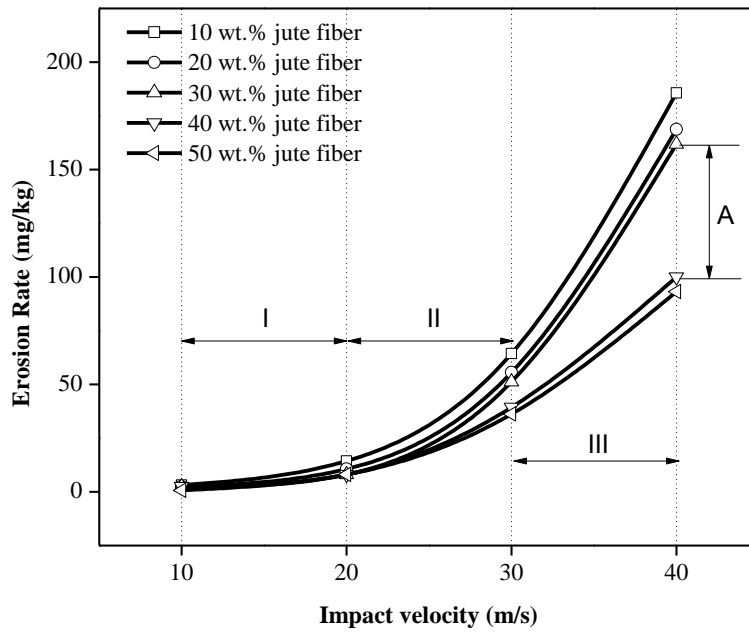
Figure 6.12a Influence of impact velocity on erosion rate different wt.% fiber loading
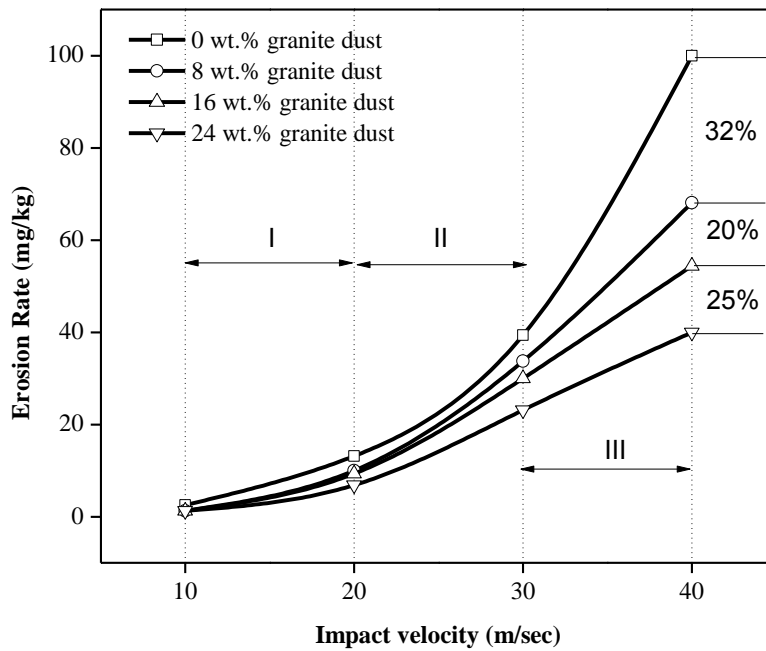
Figure 6.12b Influence of impact velocity on erosion rate different wt.% filler contiment

6.4.3 Slurry erosion profile

In addition to slurry erosion rate, it is necessary to observe the eroded surface profile as erosion rate is not uniform along the eroded surface. At normal impact the representative cross section of 'W' shape for eroded surface profile of unfilled 40 wt.% jute fiber reinforced epoxy composite at different velocity is shown in Figure 6.13 and it seems like round bowl with protruded island at the middle. Researchers were reported similar observations for profile of eroded surfaces in slurry erosive wear condition [281-283]. At normal impact the shape of 'W' scar is symmetrical for all the different velocities which show uniform distribution of sand particles in the flow. The minor material removal is observed at the centre scar and the reason for low material removal is high static pressure which evolves as stagnation point at the centre of scar. However, the shape of eroded surface profile for impingement angle other than 90° illustrates the shift of stagnation point towards the tilt of nozzle.
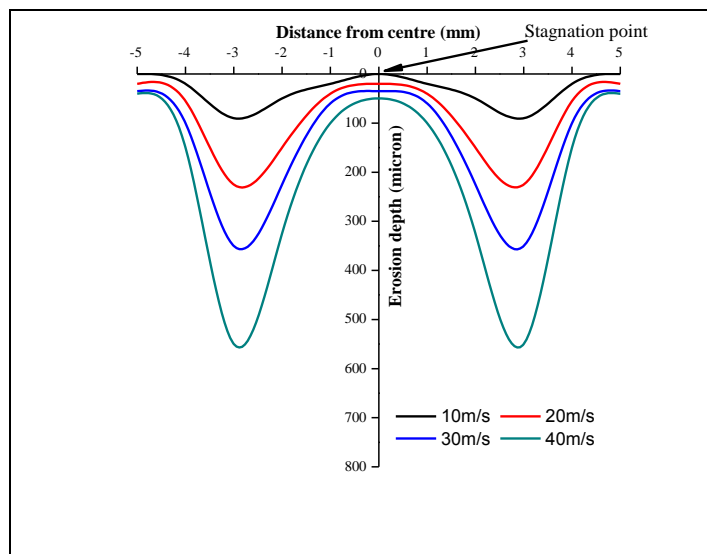
Figure 6.13 Profile of eroded surface with respect to different impact velocities

6.4.4 Numerical Analysis

Figures 6.14a – 6.14b show contours for erosion rate and particle traces for unfilled and granite filled jute fiber epoxy composite. Figure 6.14a(i) shows higher peak erosion rate for 60° impingement angle as compared to Figure 6.14b(i) for 45° impingement angle for unfilled composite with 40 wt.% jute fiber. The highest erosion rate for 40 wt.% alkali treated jute fiber epoxy composite for impact velocity of 30m/s reduces from 3.16×10^{-5} kg/m^{2}sec to 2.38×10^{-5} kg/m^{2}sec due to change in direction of flow field from 60° to 45°. Similar, trend for granite powder filled composites is also observed for impact angle of 60° and 45°. Figures

6.14c(i) and 6.14d(i) show decreasing in maximum erosion rate from 3.09×10^{-5} kg/m^{2}sec to 2.27×10^{-5} kg/m^{2}sec due to change in impingement angle from 60° to 45° for 16wt.% granite powder filled jute fiber epoxy composite. From the above analysis it is concluded that the peak erosion in both the simulated and experimental results are in close proximity as far as impingement angle is concerned. Figures 6.14a(ii) and 6.14b(ii) show the particle traces on the eroded surface of specimen for impingement angle of 60° and 45° respectively for unfilled composite reinforced with 40 wt.% of jute fiber. It is clearly illustrated that, in spite of reduction in peak erosion rate the eroded surface area is increased for lower impingement angle. This may be attributed sliding of erodent particles after impact on the surface of specimen for lower impingement angle. The Figures 6.14a(ii), 6.14b(ii), 6.14c(ii) and 6.14d(ii) depict the shape of eroded surface as an ellipse, whose major axis length is inversely proportional to angle of impingement.

(i)   (ii)
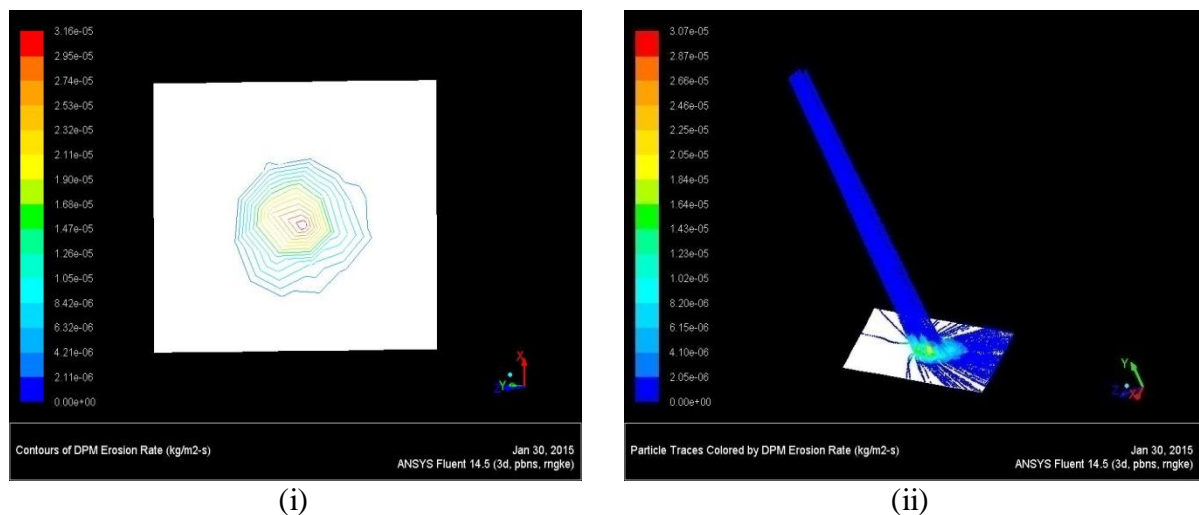
Figure 6.14a Contour for erosion rate and particle traces for jet impact velocity of 30 m/sec at 60^0 impingement angle for 40 wt.% jute fiber-epoxy composite

(i)   (ii)
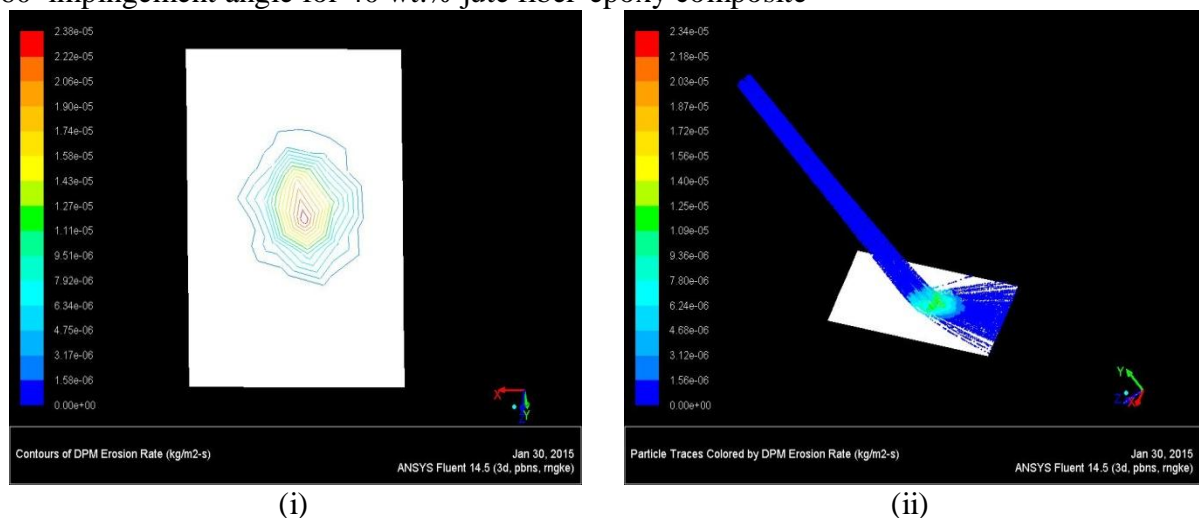
Figure 6.14b Contour for erosion rate and particle traces for jet impact velocity of 30 m/sec at 45^0 impingement angle for 40 wt.% jute fiber-epoxy composite
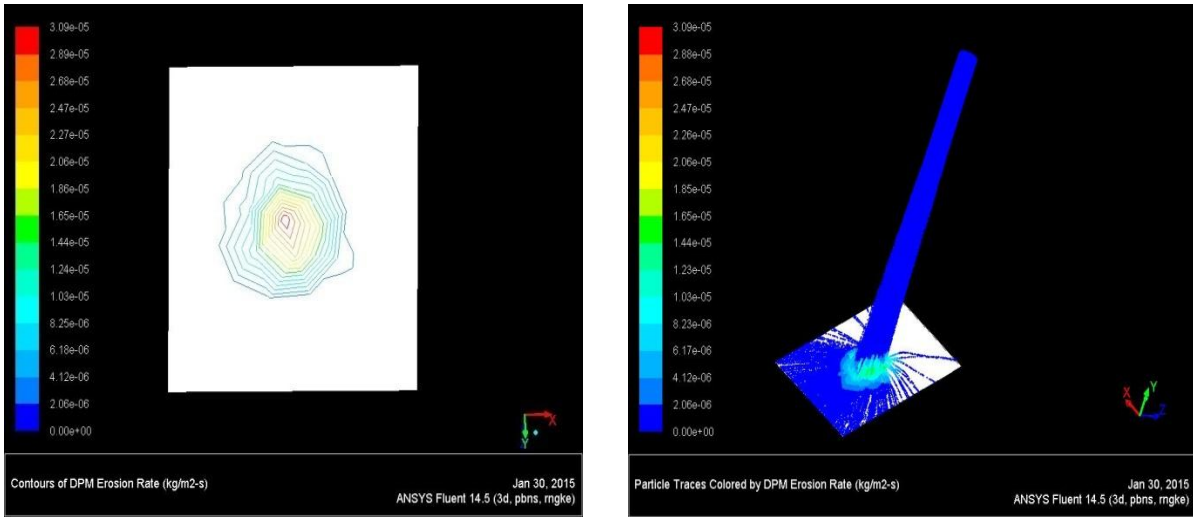
(i)   (ii)

Figure 6.14c Contour for erosion rate and particle traces for jet impact velocity of 30 m/sec at 60^0 impingement angle for 16 wt.% granite powder filled jute fiber-epoxy composite
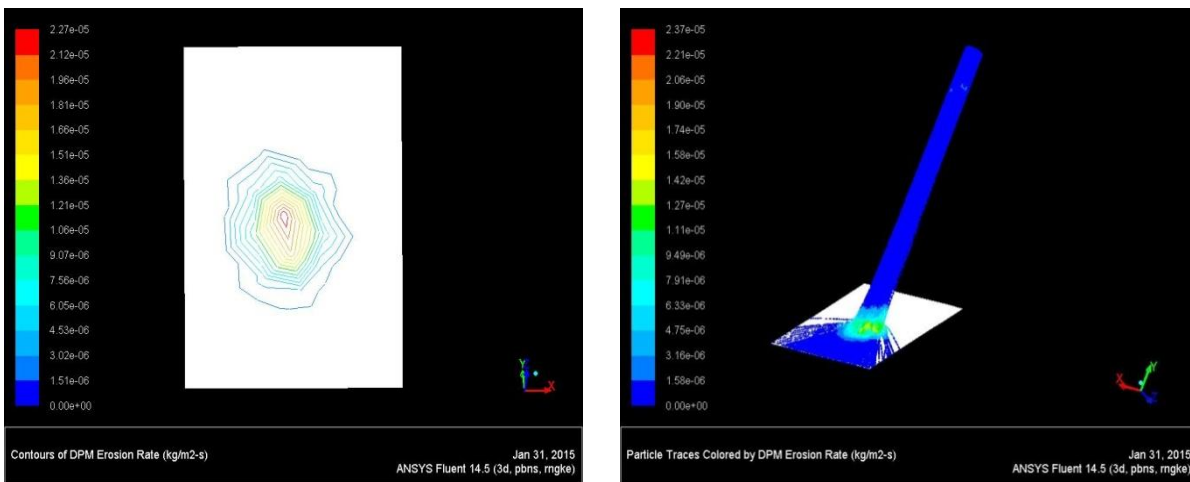
(i)   (ii)

Figure 6.14d Contour for erosion rate and particle traces for jet impact velocity of 30 m/sec at 45^0 impingement angle for 16 wt.% granite powder filled jute fiber-epoxy composite

The proposed CFD approach is validated by comparing obtained trend of experimental slurry erosion results with the numerical one for unfilled and granite powder filled alkali treated jute epoxy composites at constant impact velocity: 30 m/sec, erodent size: 325 μm, stand-off distance: 50 mm, erodent temperature: RT (see Figure 6.15). In both the experimental and numerical simulated results show the maximum slurry erosion rate around $60^{°}$ impingement angle irrespective of fiber/filler combination.
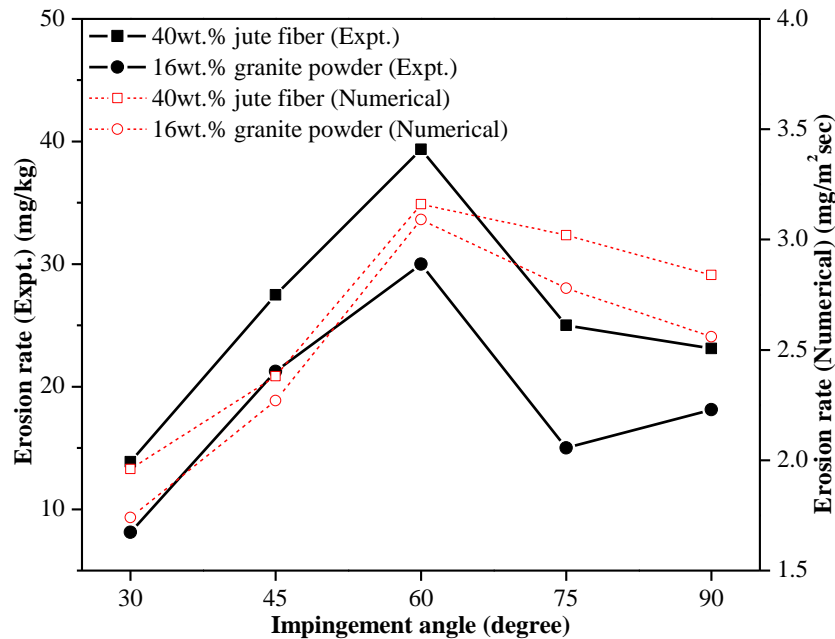
Figure 6.15 Numerical and experimental correlation for trend of erosion rate with impingement angle for unfilled and granite powder filled jute fiber composite

6.5 Taguchi design of experiment for unfilled and granite powder filled jute epoxy composites

Table 6.4a and 6.4b shows the slurry erosion rate of unfilled and particulate filled jute epoxy composites respectively under slurry erosive environment using Taguchi design of experiment principle (MINITAB-16). Each experiment is conducted for three times and average values of three replicas for erosion rate for unfilled and particulate filled jute epoxy composites are presented. The overall mean of S/N ratio for unfilled and granite filled jute epoxy composite is found to be -22.07 db and -22.36 db (decibel) respectively. Figures 6.16a and 6.16b show graphically the effect of all four control factors on slurry erosion rate. For unfilled jute-epoxy composite, the optimum factor combination is A1 (impact velocity of 10 m/s), B4 (fiber loading of 40 wt.%), C2 (impingement angle of 45$^{°}$) and D3 (erodent size of 250 µm). Analysis of S/N plots for granite filled jute–epoxy composite leads to conclusion that factor combination of A1 (impact velocity of 10 m/s), B4 (filler content of 24 wt.%), C4 (impingement angle of 75$^{°}$), D3 (erodent size of 250 µm) gives minimum erosion rate. It is clear from the Figures 6.16a and 6.16b that factor A (impact velocity) and factor B (fiber loading/filler content) are the most significant factor while factor C (impingement angle) and factor D (erodent size) have relatively less significant influence.

Table 6.4a Experimental design using L_{16} orthogonal array (unfilled jute-epoxy composites)

Sl. No.	Impact velocity (A) (m/s)	Fiber loading (B) (%)	Impingement angle(C) (degree)	Erodent size (D) (μm)	Erosion rate (Er) (mg/kg)	S/N ratio (db)
1	10	10	30	100	6.25	-15.91
2	10	20	45	175	0.62	4.08
3	10	30	60	250	1.25	-1.93
4	10	40	75	325	3.75	-11.48
5	20	10	45	275	14.38	-23.15
6	20	20	30	325	10.00	-20.00
7	20	30	75	100	7.50	-17.50
8	20	40	60	175	6.25	-15.91
9	30	10	60	325	64.38	-36.13
10	30	20	75	250	25.00	-27.95
11	30	30	30	175	29.37	-29.35
12	30	40	45	100	8.12	-18.19
13	40	10	75	175	115.00	-41.21
14	40	20	60	100	91.88	-39.26
15	40	30	45	325	51.87	-34.29
16	40	40	30	250	17.50	-24.86

Table 6.4b Experimental design using L_{16} orthogonal array (granite powder filled jute-epoxy composites)

Sl. No.	Impact velocity (A) (m/s)	Filler content (B) (%)	Impingement angle (C) (degree)	Erodent size (D) (μm)	Erosion rate (Er) (mg/kg)	S/N ratio (db)
1	10	0	30	100	10.63	-20.52
2	10	8	45	175	2.50	-7.95
3	10	16	60	250	1.25	-1.93
4	10	24	75	325	0.63	4.08
5	20	0	45	275	13.12	-22.36
6	20	8	30	325	15.00	-23.52
7	20	16	75	100	13.13	-22.36
8	20	24	60	175	13.75	-22.76
9	30	0	60	325	39.38	-31.90
10	30	8	75	250	26.25	-28.38
11	30	16	30	175	21.25	-26.54
12	30	24	45	100	16.25	-24.21
13	40	0	75	175	51.25	-34.19
14	40	8	60	100	48.75	-33.75
15	40	16	45	325	45.63	-33.18
16	40	24	30	250	25.62	-28.17

Although, S/N plots obtained from Taguchi analysis are indicators of the relative significance of various control factors, this can be confirmed after performing the analysis of variance (ANOVA).Significance of various factors can be determined by performing analysis of variance (ANOVA). ANOVA results for erosion rate of composites with different weight percentage of alkali treated jute fiber loading and granite powder content are presented in Tables 6.5a and 6.5b respectively. This analysis is undertaken for a level of confidence of significance of 95%. The last column of each table indicates significance of individual control factor on erosion rate. The ANOVA results for unfilled jute epoxy composites (Table 6.5a) shows that, the impact velocity (p = 0.027) and fiber loading (p = 0.251) have great significance on erosion rate and impingement angle (p = 0.565) and erodent size (p = 0.623) presents less significance on erosion rate. For granite filled jute epoxy composite similar trend of significance is observed from Table 6.5b. The factor impact velocity (p = 0.025) and filler content (p = 0.295) shows more significance and impingement angle (p = 0.750) and erodent size (p = 0.658) have less significance on erosion rate.

Table 6.5a ANOVA table for slurry erosion rate: unfilled jute epoxy composite

Source	DF*	Seq SS*	Adj SS*	Adj MS*	F*	P*
A: Impact velocity	3	1823.75	1823.75	607.92	14.67	0.027
B: Fiber loading	3	291.25	291.25	97.08	2.34	0.251
C: Impingement angle	3	101.37	101.37	33.79	0.82	0.565
D: Erodent size	3	83.84	83.84	27.98	0.68	0.623
Error	3	124.32	124.32	41.44		
Total	15	2424.62				

Table 6.5b ANOVA table for slurry erosion rate: granite powder filled jute epoxy composite

Source	DF*	Seq SS*	Adj SS*	Adj MS*	F*	P*
A: Impact velocity	3	1510.16	1510.16	503.39	15.59	0.025
B: Filler content	3	191.53	191.53	63.84	1.98	0.295
C: Impingement angle	3	41.13	41.13	13.71	0.42	0.750
D: Erodent size	3	58.11	58.11	19.37	0.60	0.658
Error	3	96.87	96.87	32.87		
Total	15	1897.81				
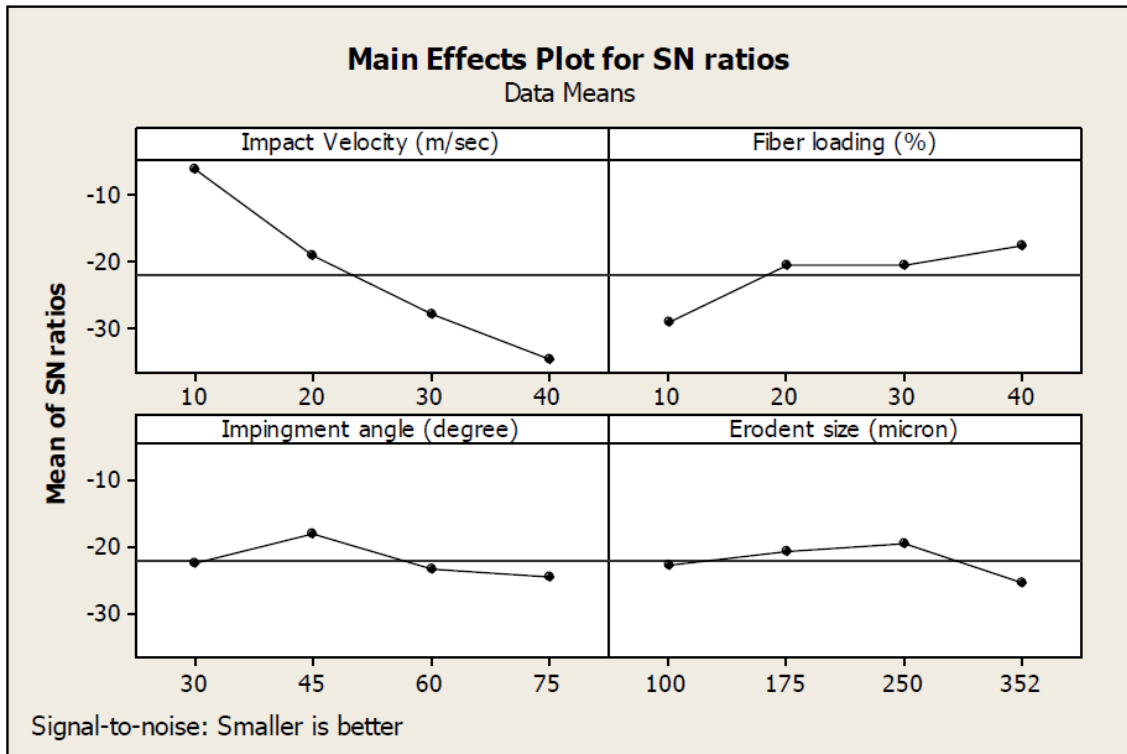
Figure 6.16a Effect of control factors on erosion rate unfilled jute epoxy composite
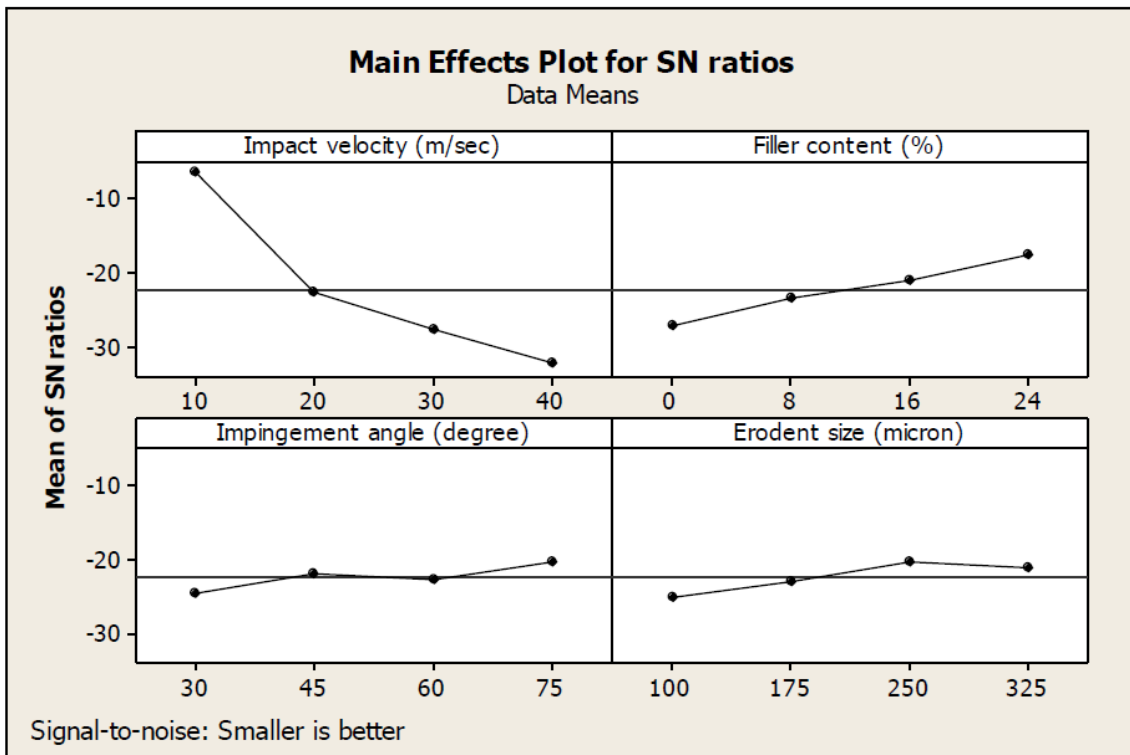
Figure 6.16b Effect of control factors on erosion rate of granite powder filled jute-epoxy composite

6.6 Surface morphology

The eroded surfaces of the composites are examined by scanning electron microscope pre and post erosion. The surface microstructure and their change are very informative with respect to the internal (reinforcement, filler and matrix bonding) and external conditions (impingement angle and impact velocity) [279]. The wear mechanism for variation of impingement angle in steady state condition is observed i.e by varying one input factor at a time keeping other factors remaining constant (impact velocity 30 m/s, erodent discharge 160 gm/min, erodent size 325 μm, stand-off distance 50mm and nozzle diameter 3mm) with respect to slurry erosion rate for jute fiber reinforced epoxy composite as shown in Figures 6.17a to 6.17f.

During erosion when hard solid sand particles impact on surface of composite, deformation is generated in forms of matrix micro-cracking, interlayer debonding, crater formation, particles debonding, micro plowing and fiber fracture. Purely un-eroded surface microstructure is shown in Figure 6.17a for comparison. Unworn surface shows comparably smooth structure along with presence of some voids due to air entrapped during fabrication by conventional hand lay-up method. At relatively low impingement angle (i.e. 30°) for 10 wt.% jute fiber loading and impact velocity of 30 m/s the fiber-matrix debonding is observed due to micro plowing along the sliding of erodent particle on the surface after impact as shown in Figure 6.17b.

The dominant wear mechanism at low impingement angle is observed as abrasion caused by sliding of erodent particle after impact on the target material. Micrograph clearly shows the direction of erosion due to sliding the erodent material. Figure 6.17c shows the eroded surface of 20wt.% jute fiber composite (impact velocity of 30 m/s, impingement angle of 45°) and is observed that matrix material is removed by continuous impact of mixture water jet and erodent particles. Also the longitudinal cracks are found in the direction of sliding of erodent material at lower impact velocity, which shows the wear caused by impact of erodent material as well as abrasion. However, Figure 6.17d depicts peak erosion at 60° impingement angle of 20 wt.% alkali treated jute epoxy composites and shows dominating wear mechanism that may be inter-layer debonding of fibers which results in heavy removal of matrix material. Fibers are exposed to direct impact of jet of erodent material causes fiber fracture. At higher impingement angle (75°) of slurry jet the surface morphology shows complete removal of matrix material (see Figure 6.17e). Scattering of fibers is indication of complete removal of matrix material for composite with 40 wt.% jute fiber loading. No wear track is observed on the surface as wear caused by impact of erodent material instead of erodent sliding at low impingement angle. When slurry jet impacts on the surface in the

normal direction the material is removed purely impact of erodent material. Initially the matrix material is removed and further impact of erodent results in fiber fracture and fiber scattering (Figure 6.17f) for 30 wt.% jute epoxy composite.

(a) Virgin en-eroded surface

(b) 10 wt.% jute fiber,30° impingement angle
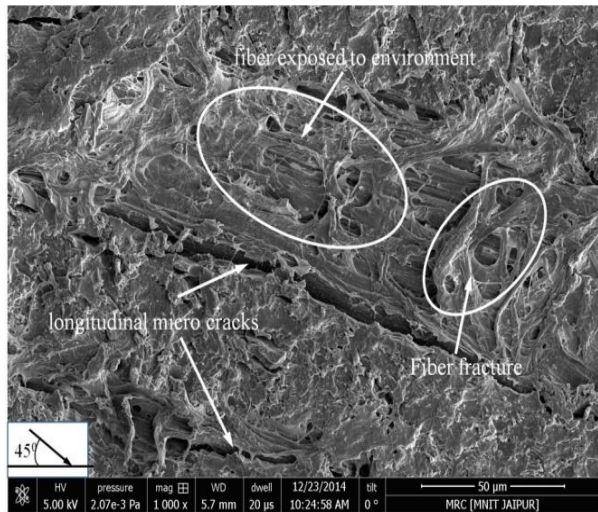
(c) 20 wt.% jute fiber, 45° impingement angle
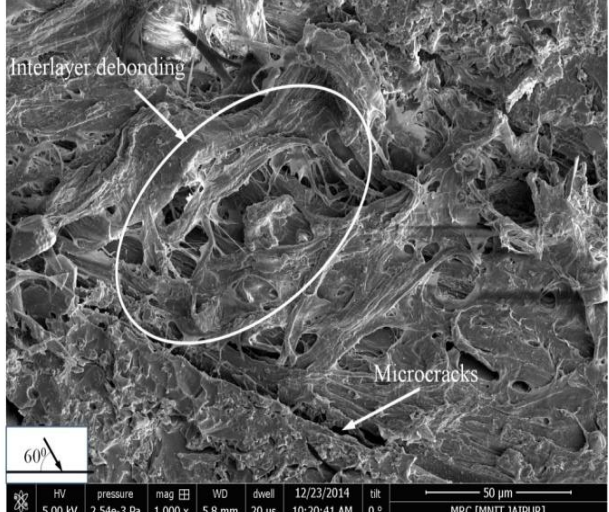
(d) 20 wt.% jute fiber, 60° impingement angle
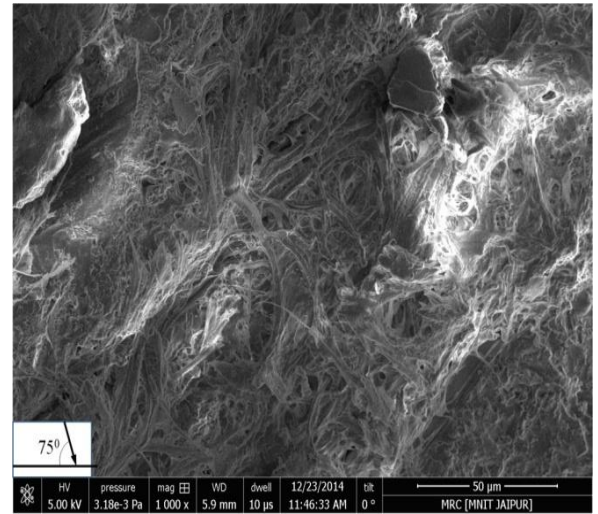
(e) 40 wt.% jute fiber, 75° impingement angle
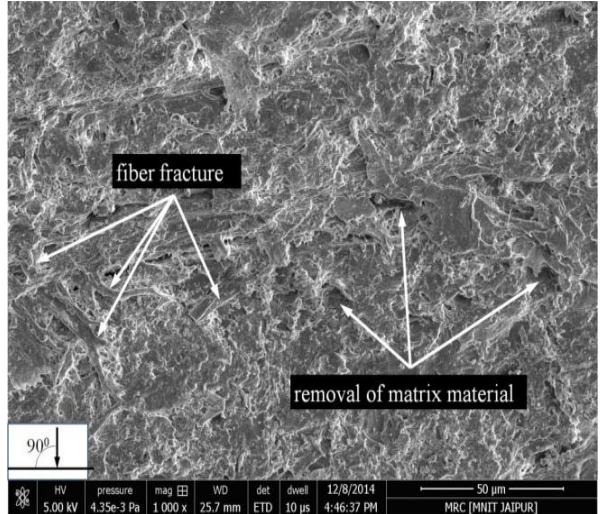
(f) 30 wt.% jute fiber, 90° impingement angle
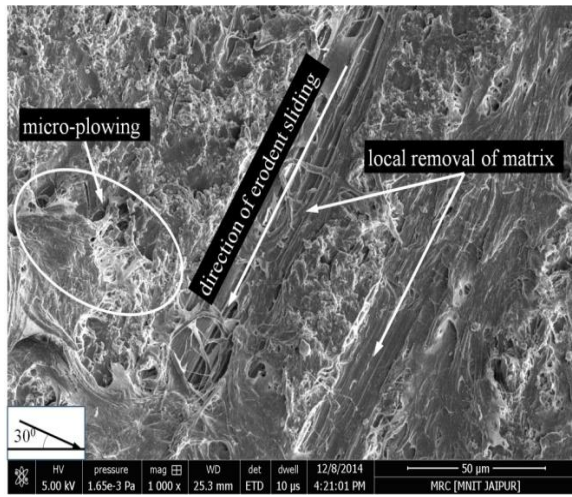
(g) 8 wt.% granite powder, 30º impingement angle
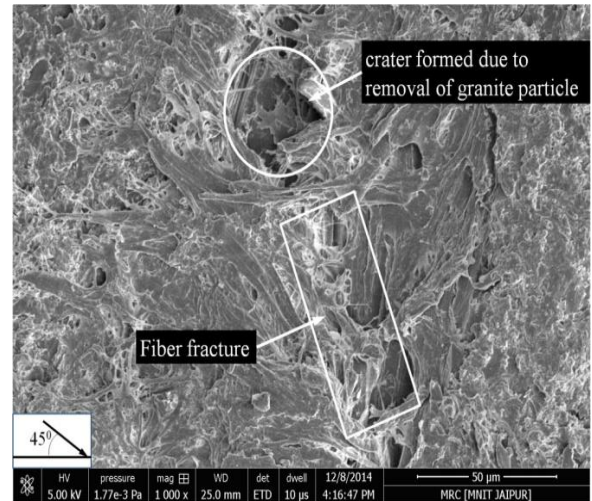
(h) 8 wt.% granite powder, 45º impingement angle
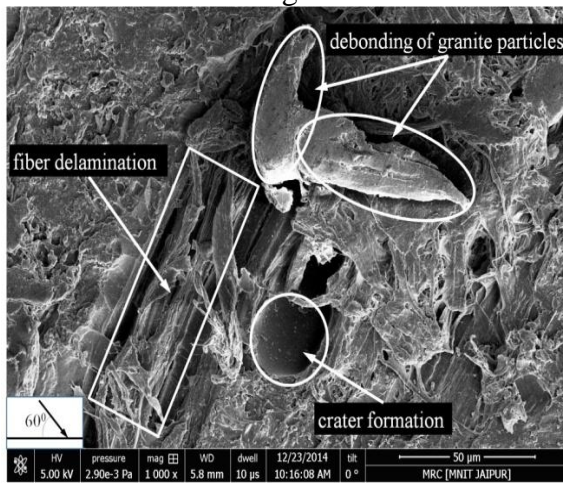
(i) 16 wt.% granite powder, 60º impingement angle
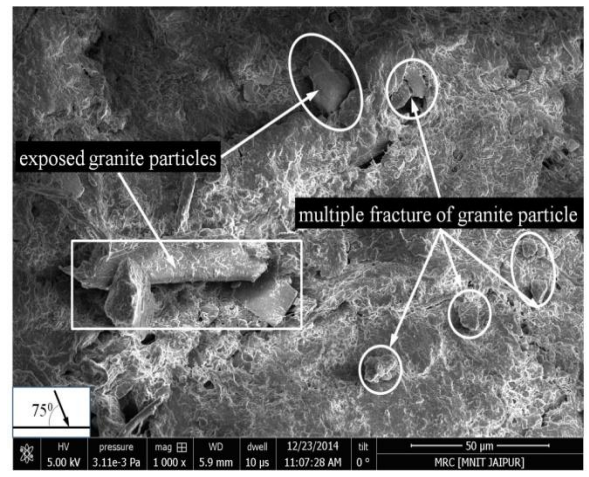
(j) 24 wt.% granite powder, 75º impingement angle
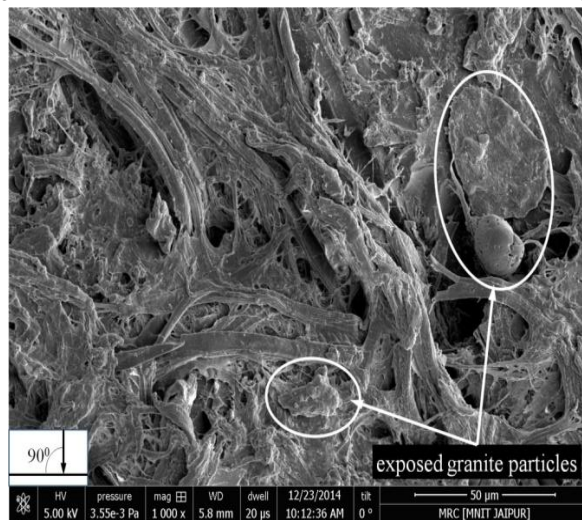
(k) 16 wt.% granite powder, 90º impingement angles

Figure 6.17 Scanning electron micrograph of unfilled and granite filled jute fiber-epoxy composites under steady state condition with varying impingement angle (impact velocity 30 m/s, erodent discharge 160 gm/min, erodent size 325 μm, stand-off distance 50mm and nozzle diameter 3mm)

Effect of addition of granite powder on wear mechanism and scanning electron micrograph at impact velocity 30 m/s, erodent discharge 160 gm/min, erodent size 325 μm and stand-off distance 50 mm is shown in Figures 6.17g to 6.17k. Figure 6.17g shows eroded surface of 8wt.% granite filled alkali treated jute epoxy composites at 30° impingement angle under steady state condition. Similar to unfilled composite the particulate filled composite at impingement angle of 30° the erodent material slides on the surface forming wear track and the removal of matrix material is taking place due to micro-plowing only. The effect of presence of granite powder is not predominant at lower filler content. Figure 6.17h shows 8 wt.% granite powder filled composite subjected to slurry jet at 45° impingement angle. It shows local removal of matrix material and on further impact of erodent material results in fracture of fiber.

Figure 6.17i shows eroded surface of 16 wt.% granite powder filled composite at 60° impingement angle. At higher granite powder content, the kinetic velocity of erodent material is significantly affected for debonding of granite particles from matrix material, which results in formation of few craters. Presence of hard particles in the matrix absorbs the considerable fraction of kinetic energy of erodent material and therefore the minimum energy is available for plastic deformation of matrix. Figure 6.17j shows the wear mechanism for 24 wt.% of granite powder filled jute epoxy composite at 75° impingement angle. The maximum kinetic energy of erodent material is absorbed by granite particles and results in exposure of granite particles. The micrograph also shows multiple fractures of granite particles that create crater due to complete removal of granite particles. Absence of sliding of erodent at normal impact results in utilization of kinetic energy fully for impact which causes the removal of granite particles earlier for composite with 16 wt.% granite powder (Figure 6.17k).

Figures 6.18a to 6.18f show surface morphology of unfilled and granite powder filled jute epoxy composites as observed from Taguchi experimental results (Table 6.4a and 6.4b). Figure 6.18a shows, at lower impact velocity (10 m/s) for 30wt.% jute epoxy composites at 60° impingement angle the eroded surface look like removal of upper surface and simultaneously the fiber which are aligned parallel with the matrix material also delimitation occurs between them (see Table 6.4a, Expt. run 3). However, with increase in impact velocity to 30 m/s (Figure 6.18b) the matrix is uniformly grooved with local removal of matrix materials and therefore a ploughing mechanism is developed which leads to removal of matrix material by micro-plowing. The micro-plowing is observed due to sliding of erodent particle at higher impact velocity (see Table 6.4a, Expt. run 12). Again on further increase in impact velocity to 40 m/s (Figure 6.18c) shows excessive removal of matrix material, crack

generation and propagation through fiber layer and simultaneously fiber breaking occurs which no longer bound with the matrix material (see Table 6.4a, Expt. run 15). Figure 6.18d shows the eroded surface of the 20 wt.% jute epoxy composite with lower impact velocity (20m/s) the formation of deep grooves due to repeated sliding of erodent at lower impingement angle (30°) (see Table 6.4a, Expt. run 6). With increase in granite content along with impact velocity (see Table 6.4b, Expt. run 11) the morphology of eroded surface shows distinct regions of matrix removal (Figure 6.18e). The material is removed from region of scarcity of granite particles. Surface morphology of composite reinforced with 24 wt.% granite powder at 40 m/s is shown in Figure 6.18f (see Table 6.4b, Expt. run 15). Due to high velocity the granite particles are completely exposed and the craters are formed due to removal of matrix material from the region of lack of granite.
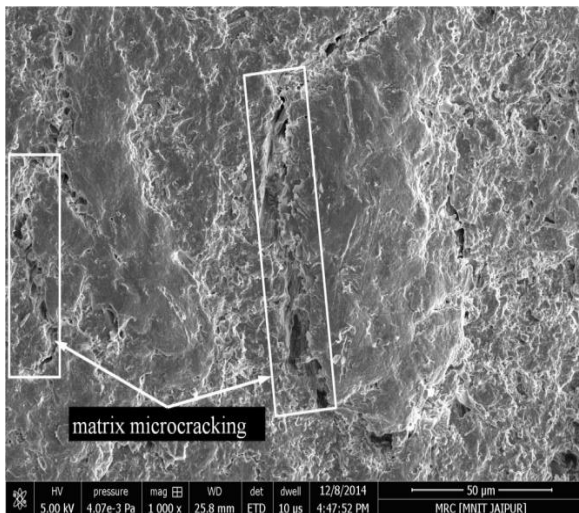
(a) 30 wt.% jute, 10m/s, 60˚, 250µm
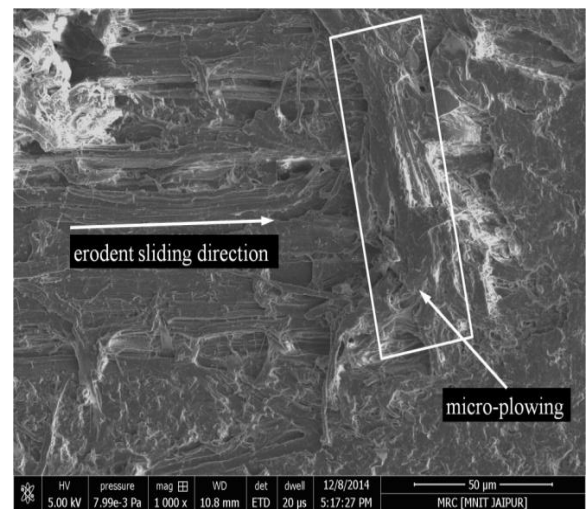
(b) 40 wt.% jute, 30m/s, 45˚, 100µm
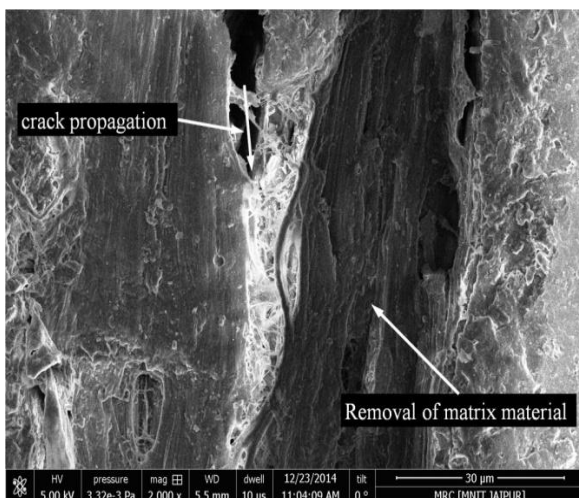
(c) 40 wt.% jute, 40m/s, 30˚, 250µm
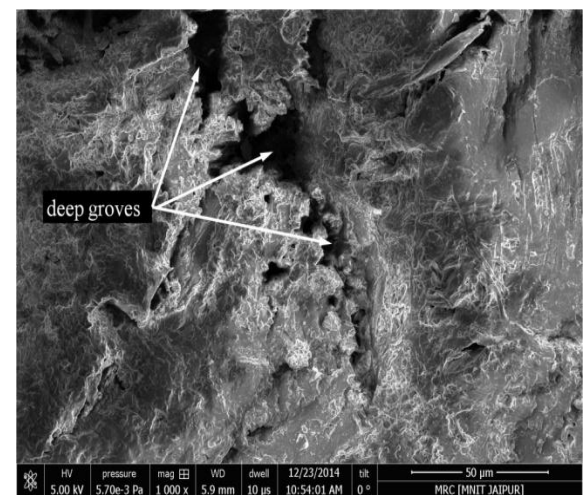
(d) 20 wt.% jute, 20m/s, 30˚, 325µm
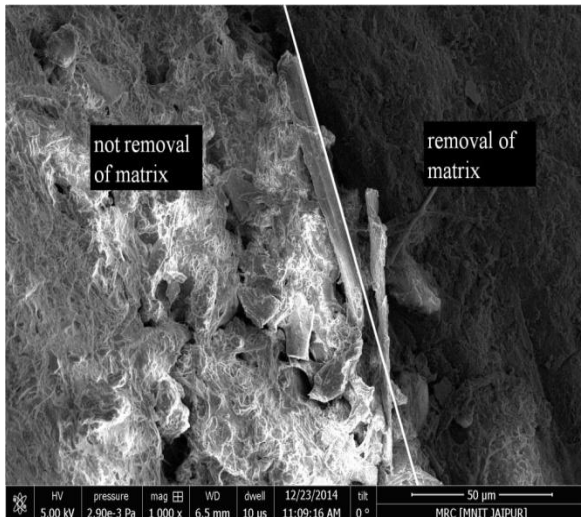
(e) 16 wt.% granite, 30m/s, 30˚, 175μm   (f) 24 wt.% granite, 40m/s, 45˚, 325μm
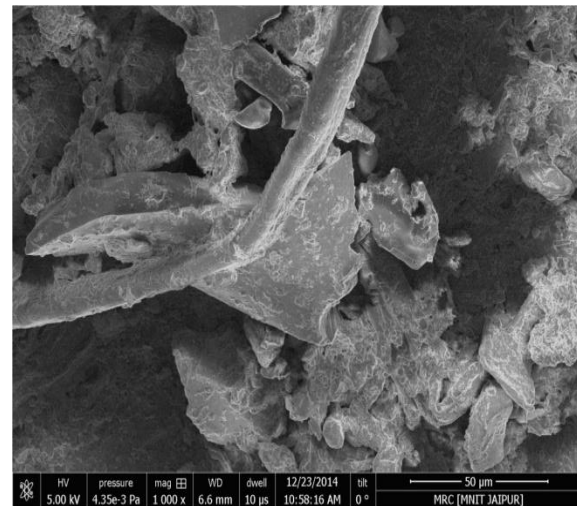
Figure 6.18 Scanning electron micrograph of unfilled and granite powder filled jute fiber-epoxy composites (Taguchi Design of Experiment)

Part-III

Slurry jet erosion wear analysis of unfilled and granite powder filled carbon-epoxy composites

6.7 Steady state slurry erosion rate

6.7.1 Influence of impingement angle on slurry erosion rate

Actual conditions to which the structural components are subjected due to impact of foreign particles along with rain droplets can be simulated by varying the impingement angle of slurry jet with respect to target material using slurry jet erosion tribometer. The impingement angle corresponding to peak erosion rate may be considered as an indication of material behavior. Figure 6.19a and 6.19b show the effect of impingement angle on erosion rate for different wt.% of fiber reinforced unfilled carbon epoxy composites respectively at impact velocity of 30 m/s, stand-off distance 50 mm, erodent size 325 μm and sand flow rate 160 g/min. Peak erosion rate is observed at 60º impingement angle for 10 wt.% fiber loading whereas, for higher amount of fiber loading the peak erosion is observed at 75º impingement angle (see Figure 6.19a). This may be indication of resistance of carbon fiber against abrasion by erodent particle but at higher impingement angle abrading action is less and maximum kinetic energy of erodent is used for cutting. Irrespective of impingement angle the slurry erosion resistance is significantly improved for reinforcement of fiber up to 30 wt.% and marginal improvement is observed for higher fiber loading. Peak erosion observed as 55.12, 39.75, 30.75, 25.72 and 24.75 mg/kg for 10, 20, 30, 40 and 50 wt.% fiber loading in unfilled carbon epoxy composites respectively.
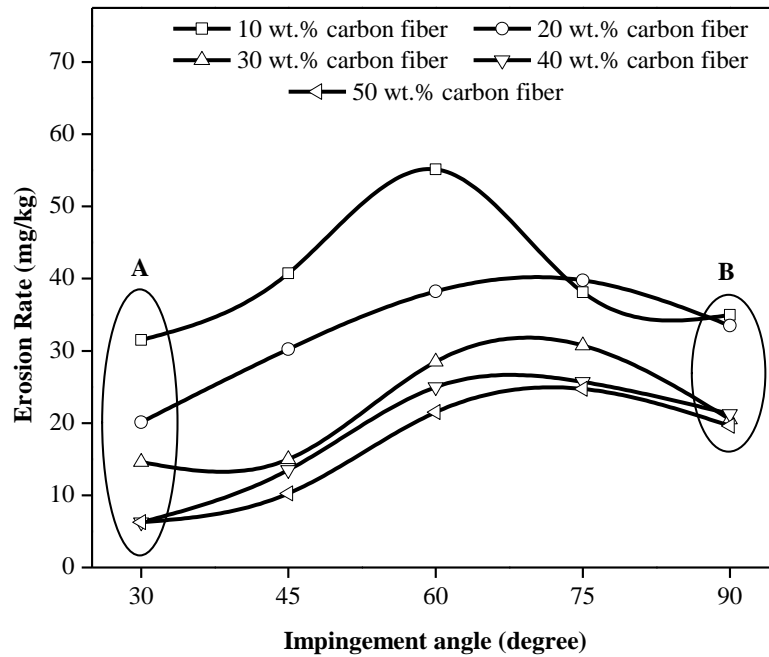
Figure 6.19a Influence of impingement angle on erosion rate for unfilled carbon epoxy composites
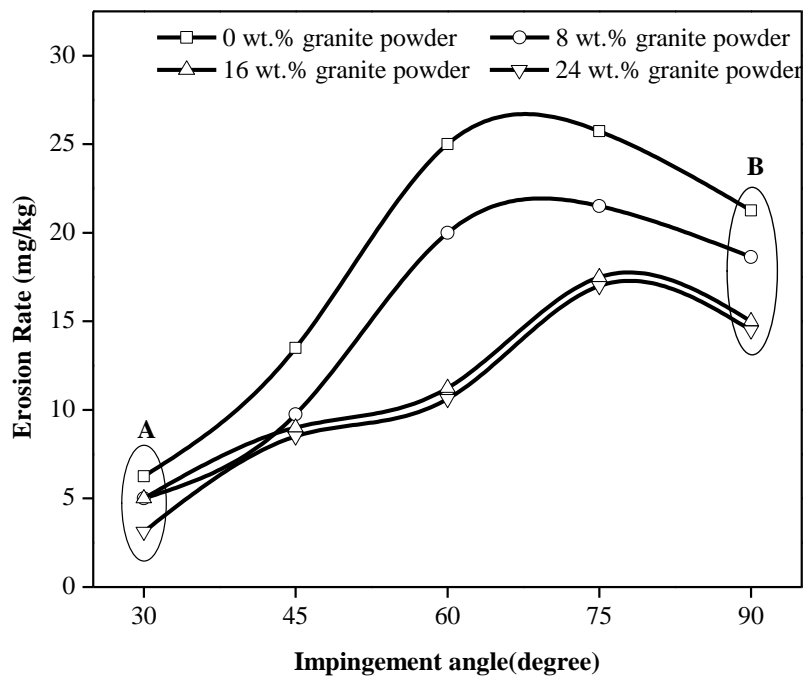
Figure 6.19b Influence of impingement angle on erosion rate for granite powder filled carbon epoxy composites

Figure 6.19b shows maximum resistance to slurry erosion wear at lower impingement angle (i.e 30 and 45º) for all granite powder filled carbon epoxy composites. At low

impingement angle, erodent particles tend to slide and remove minimum material from surface as compared to higher impingement angle. The slurry erosion rate is increased with increase in impingement angle up to 75º. This is due to material removal by cutting mechanism more than abrasion mechanism as impingement angle increased. Impact of erodent in normal direction slightly decreased the slurry erosion rate due to loss of part of kinetic energy of impacting erodent to displace the erodent particle impacted prior to it. Maximum influence of granite powder is observed at 60º impingement angle on slurry erosion rate. The slurry erosion rate for 8, 16 and 24 wt.% granite powder filled carbon epoxy composite is 20, 11.25 and 10.62 mg/kg as compared to 25 mg/kg for virgin carbon epoxy composite.

Addition of granite powder has less influence on slurry erosion rate at lower impingement angle (see region A in Figure 6.19b) as points are close to each other. Whereas, for higher impingement angle the granite filler plays important role in improving slurry erosion wear resistance (see region B in Figure 6.19b) as points spacious to each other. However, reinforcement of fiber has significant effect at lower impingement angle on slurry erosion rate of unfilled carbon epoxy composites (see region A in Figure 6.19a) as compared to influence of fiber reinforcement at higher impingement angle (see region B in Figure 6.19a). Thus the observations justify the use of fiber and filler material as reinforcement in epoxy matrix. For impingement of erodent at lower angle, granite powder particles resisted the material removal by abrading action. The fiber absorbed considerable energy of erodent before fracture at higher impingement angle.

6.7.2 Influence of impact velocity on slurry erosion rate

Figure 6.20a and 6.20b show influence of impact velocity on slurry erosion rate at impingement angle 60º, stand-off distance 50 mm, erodent size 325 μm and sand flow rate 160 g/min for unfilled and granite powder filled carbon epoxy composites respectively. Effect of impact velocity is insignificant for range 10 to 20 m/s for both the unfilled and granite powder filled carbon epoxy composites. Figure 6.20a shows the positive effect of fiber reinforcement on slurry erosion resistance of unfilled carbon epoxy composites. The result in reduction of slurry erosion rate is observed significant for impact velocity higher than 20 m/s. The erosion rate calculated at impact velocity of 40 m/s for 10, 20, 30, 40 and 50 wt.% carbon epoxy composites are observed in the decreasing order as 165.25, 133.75, 102.25, 81.87 and 70.32 mg/kg. The maximum reduction in slurry erosion rate (23.55%) is recorded for 30 wt.% carbon epoxy composite. Whereas, above 40 wt.% fiber loading the

reduction in erosion rate is not significant at entire range of impact velocity considered for present work.
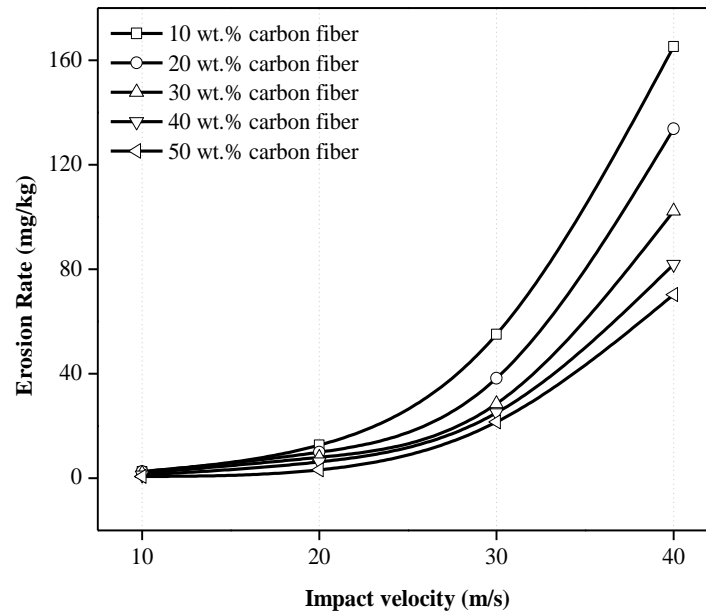
Figure 6.20a Influence of impact velocity on erosion rate for unfilled carbon epoxy composites
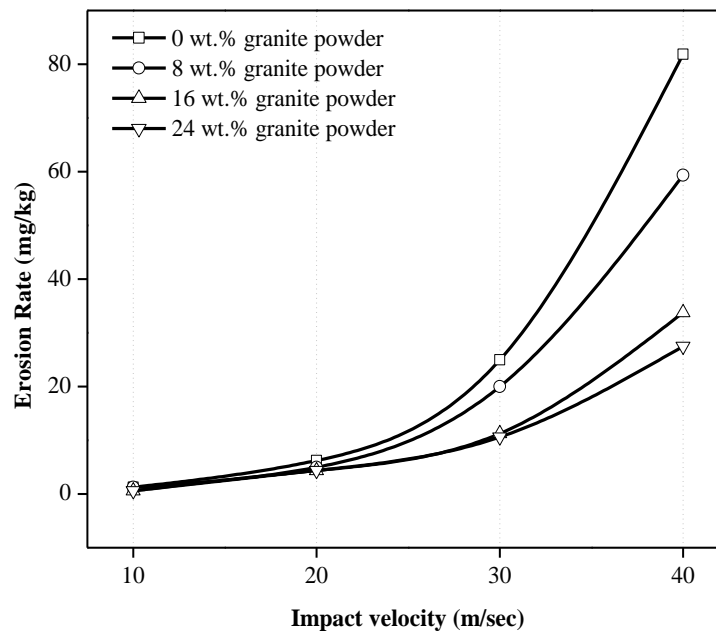
Figure 6.20b Influence of impingement angle on erosion rate for granite powder filled carbon epoxy composites

Influence of impact velocity on slurry erosion rate of granite powder filled carbon epoxy composites is shown in Figure 6.20b. Similar to unfilled composites, granite powder

filled composites show marginal increase in slurry erosion rate for increase in impact velocity from 10 to 20 m/s. Granite powder showed important role in improving slurry erosion resistance at higher velocity impact of erodent. At 30 m/s impact velocity the slurry erosion rate is decreased from 25 mg/kg for 0 wt.% granite content to 20, 11.25 and 10.62 mg/kg for 8, 16 and 24 wt.% granite filled carbon epoxy composites. However, at 40 m/s impact velocity the corresponding value is decrease from 81.87 mg/kg to 59.37, 33.75 and 27.5 mg/kg. The maximum reduction in slurry erosion rate is reported for addition of granite powder from 8 to 16 wt.%. At impact velocity 40 m/s

6.7.3 Slurry erosion profile

The cross section of scar generated due to impact of slurry jet in normal direction at impact velocity 30 m/s for granite powder filled carbon-epoxy composites are illustrated in Figure 6.21. Similar with the observations recorded for glass-epoxy and jute-epoxy composites the shape of scar is like letter 'W' with protruded island at the centre. Impact of water jet containing sand particles generated region of back pressure at the centre of impact. This caused to deflect the sand particles away from the centre and marginal material removed from the centre portion. Depth of 'W' scar is inversely proportional to granite powder content.
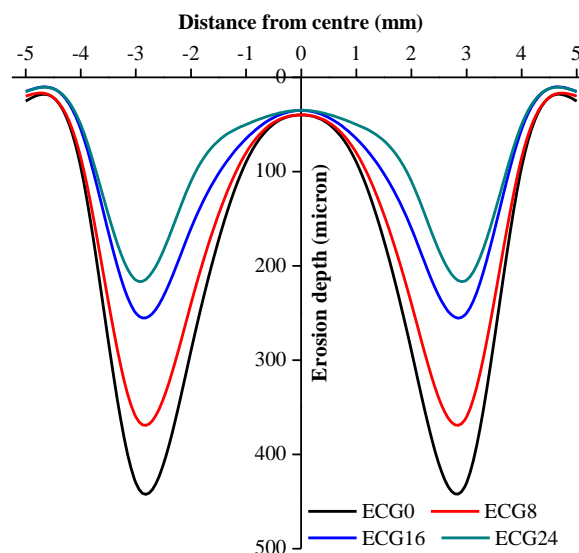
Figure 6.21 Profile of eroded surface for granite powder filled carbon epoxy composite

6.7.4 Numerical analysis

Figure 6.22a – 6.22d show the traces of particles and slurry erosion contours for unfilled and granite powder filled carbon epoxy composites. The impact of particles at lower impingement angle cause the particles to slide which may be confirmed by all traces in forward direction as illustrated in Figure 6.22a(i) and 6.22c(i). However, at higher impingement angle the particles are most prone to impact to cut the material rather than sliding which may be confirmed by few traces in reverse direction for impact angle of 60º (see Figure 6.22b(i) and 6.22d (ii)). With increase in impingement angle from 45º to 60º the slurry erosion rate is increased from 2.21×10^{-5} kg/m^{2}sec to 2.69×10^{-5} kg/m^{2}sec for unfilled 40 wt.% carbon fiber reinforced epoxy composites. Similarly, slurry erosion rate is increase from 1.99×10^{-5} kg/m^{2}sec to 2.49×10^{-5} kg/m^{2}sec for increase in impingement angle from 45º to 60º for 16 wt.% granite powder filled carbon epoxy composites. Figure 6.23 shows the similar trend for slurry erosion rate of unfilled and granite powder filled epoxy composites with peak erosion rate between 60 º to 75º impingement angle.

| (i) | (ii) |
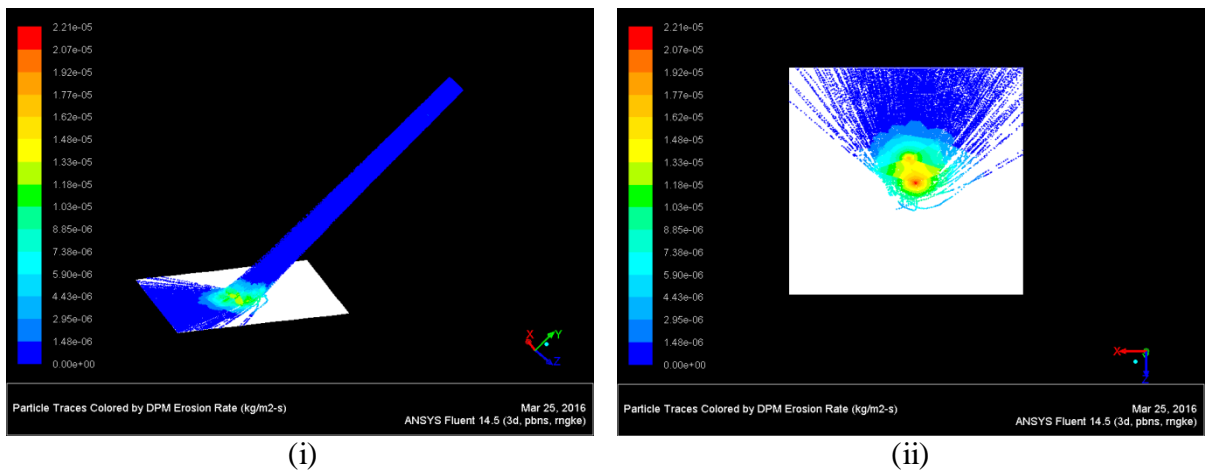
Figure 6.22a Particle traces and contour for erosion rate for jet impact velocity of 30 m/sec at 45º impingement angle for 40 wt.% carbon-epoxy composite

| (i) | (ii) |

Figure 6.22b Particle traces and contour for erosion rate for jet impact velocity of 30 m/sec at 60º impingement angle for 40 wt.% carbon-epoxy composite

Figure 6.22c Particle traces and contour for erosion rate for jet impact velocity of 30 m/sec at 45° impingement angle for 16 wt.% granite powder filled carbon-epoxy composite
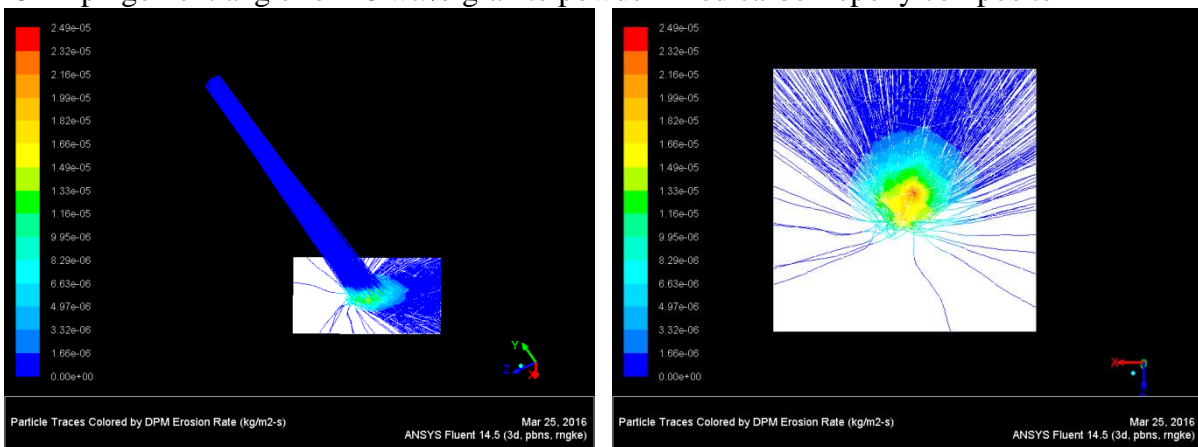
Figure 6.22d Particle traces and contour for erosion rate for jet impact velocity of 30 m/sec at 60° impingement angle for 16 wt.% granite powder carbon-epoxy composite
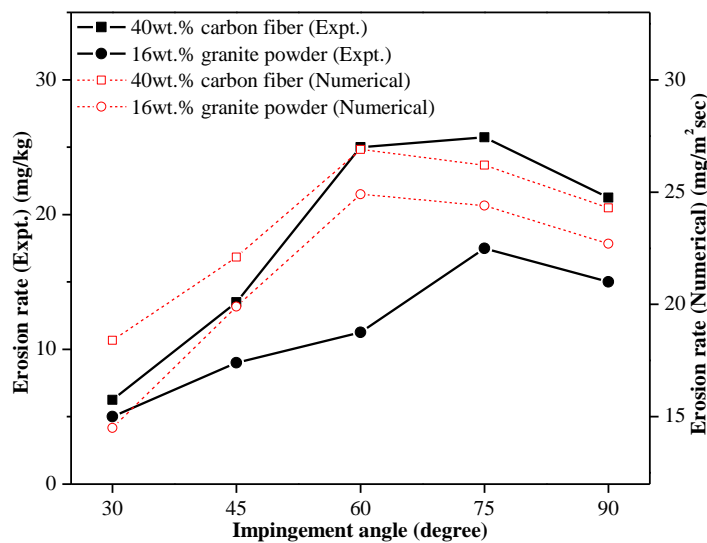
Figure 6.23 Correlation in the trend of slurry erosion rate for unfilled and granite powder filled carbon epoxy composites

6.8 Taguchi design of experiment for unfilled and granite powder filled carbon epoxy composites

Table 6.6a and 6.6b shows the slurry erosion rate of unfilled and particulate filled carbon epoxy composites respectively under slurry erosive environment using Taguchi design of experiment principle (MINITAB-16). The overall mean of S/N ratio for unfilled and granite filled jute epoxy composite is found to be -17.61 db and -16.80 db (decibel) respectively. Figures 6.2a and 6.2b show graphically the effect of all four control factors on slurry erosion rate. For unfilled jute-epoxy composite, the optimum factor combination is A1 (impact velocity of 10 m/s), B4 (fiber loading of 40 wt.%), C1 (impingement angle of $30^{°}$) and D3 (erodent size of 250 μm). Analysis of S/N plots for granite filled jute–epoxy composite leads to conclusion that factor combination of A1 (impact velocity of 10 m/s), B4 (filler content 24 wt.%), C1 (impingement angle of $30^{°}$), D1 (erodent size of 100 μm) gives minimum erosion rate.

It is cleared from the Figures 6.24a and 6.24b that factor A (impact velocity) and factor B (fiber loading/filler content) are the significant factor while factor C (impingement angle) and factor D (erodent size) have relatively less significant influence. Although, S/N plots obtained from Taguchi analysis are indicators of the relative significance of various control factors, this can be confirmed after performing the analysis of variance (ANOVA).

Table 6.6a Experimental design using L_{16} orthogonal array (unfilled carbon-epoxy composites)

Sl. No.	Impact velocity (A) (m/s)	Fiber loading (B) (%)	Impingement angle(C) (degree)	Erodent size (D) (μm)	Erosion rate (Er) (mg/kg)	S/N ratio (db)
1	10	10	30	100	2.50	-7.95
2	10	20	45	175	1.25	-1.93
3	10	30	60	250	1.25	-1.93
4	10	40	75	325	0.63	4.08
5	20	10	45	275	11.25	-21.02
6	20	20	30	325	4.50	-13.06
7	20	30	75	100	3.75	-11.48
8	20	40	60	175	3.25	-10.23
9	30	10	60	325	55.12	-34.82
10	30	20	75	250	24.75	-27.87
11	30	30	30	175	12.38	-21.85
12	30	40	45	100	8.25	-18.32
13	40	10	75	175	64.13	-36.14
14	40	20	60	100	52.50	-34.40
15	40	30	45	325	28.38	-29.05
16	40	40	30	250	6.13	-15.74

Table 6.6b Experimental design using L_{16} orthogonal array (granite powder filled carbon-epoxy composites)

Sl. No.	Impact velocity (A) (m/s)	Filler content (B) (%)	Impingement angle (C) (degree)	Erodent size (D) (μm)	Erosion rate (Er) (mg/kg)	S/N ratio (db)
1	10	0	30	100	2.50	-7.95
2	10	8	45	175	3.75	-11.48
3	10	16	60	250	2.50	-7.95
4	10	24	75	325	1.50	-3.52
5	20	0	45	275	8.25	-18.32
6	20	8	30	325	6.38	-16.08
7	20	16	75	100	3.25	-10.23
8	20	24	60	175	2.50	-7.95
9	30	0	60	325	25.00	-27.95
10	30	8	75	250	13.75	-22.76
11	30	16	30	175	13.13	-22.36
12	30	24	45	100	2.50	-7.95
13	40	0	75	175	56.75	-35.07
14	40	8	60	100	37.50	-31.48
15	40	16	45	325	19.75	-25.91
16	40	24	30	250	3.88	-11.76
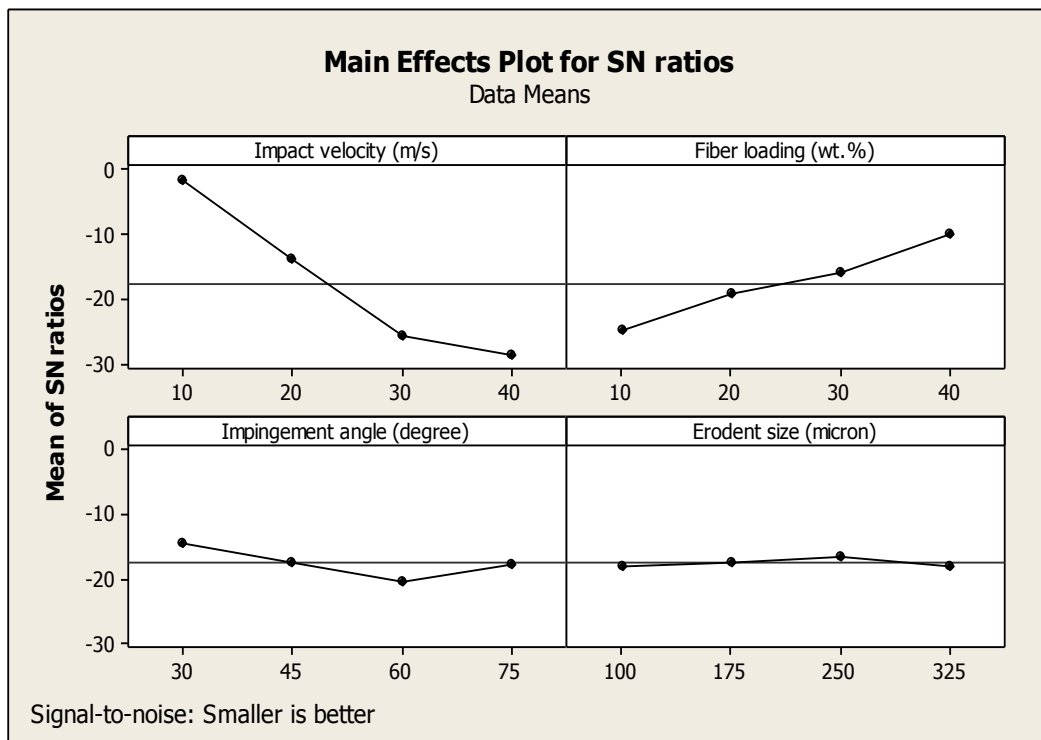
Figure 6.24a Effect of control factors on erosion rate unfilled carbon epoxy composite
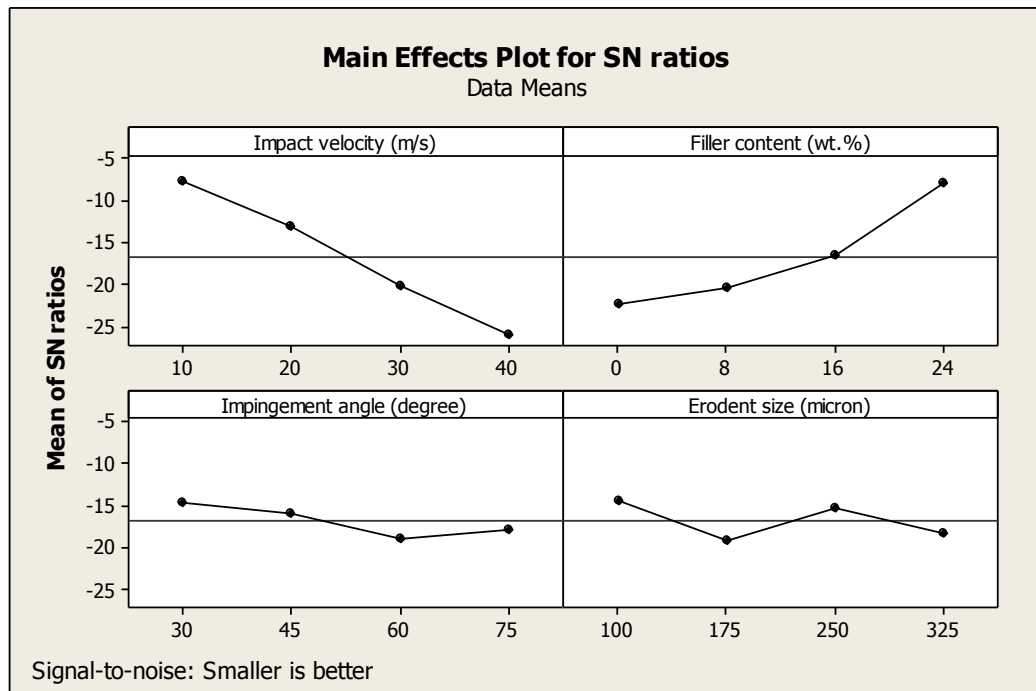
Figure 6.24b Effect of control factors on erosion rate granite powder filled carbon epoxy composite

Significance of various factors can be determined by performing analysis of variance (ANOVA). ANOVA results for erosion rate of composites with different weight percentage of alkali treated jute fiber loading and granite powder content are presented in Tables 6.7a and 6.7b respectively. The last column of each table indicates significance of individual control factor on erosion rate. The ANOVA results for unfilled jute epoxy composites (Table 6.7a) shows that, the impact velocity (p = 0.002) and fiber loading (p = 0.012) have great significance on erosion rate and impingement angle (p = 0.159) and erodent size (p = 0.806) presents less significance on erosion rate. For granite filled jute epoxy composite similar trend of significance is observed from Table 6.7b. The factor impact velocity (p = 0.011) and filler content (p = 0.02) shows more significance and impingement angle (p = 0.354) and erodent size (p = 0.249) have less significance on erosion rate.

Table 6.7a ANOVA table for slurry erosion rate: unfilled carbon epoxy composite

Source	DF	Seq SS	Adj SS	Adj MS	F	P
A: Impact velocity	3	1803.12	1803.12	601.04	99.99	0.002
B: Fiber loading	3	466.93	466.93	155.64	25.89	0.012
C: Impingement angle	3	65.25	65.25	21.75	3.62	0.159
D: Erodent size	3	5.98	5.98	1.99	0.33	0.806
Error	3	18.03	18.03	6.01		
Total	15	2359.30				

Table 6.7b ANOVA table for slurry erosion rate: granite powder filled carbon epoxy composite

Source	DF	Seq SS	Adj SS	Adj MS	F	P
A: Impact velocity	3	773.09	773.09	257.70	27.59	0.011
B: Filler content	3	499.85	499.85	166.62	17.84	0.020
C: Impingement angle	3	44.94	44.94	14.98	1.60	0.354
D: Erodent size	3	66.34	66.34	22.11	2.37	0.249
Error	3	28.02	28.02	9.34		
Total	15	1412.25				

6.9 Surface morphology

The Figure 6.25 shows the SEM micrographs of unfilled 40 wt.% carbon epoxy composites respectively at impact velocity of 60 m/sec. The images revealed that the erosion mechanism of carbon epoxy composites is a complex process involving matrix removal, fiber damages, ploughing, crater formation and micro cracking [289].
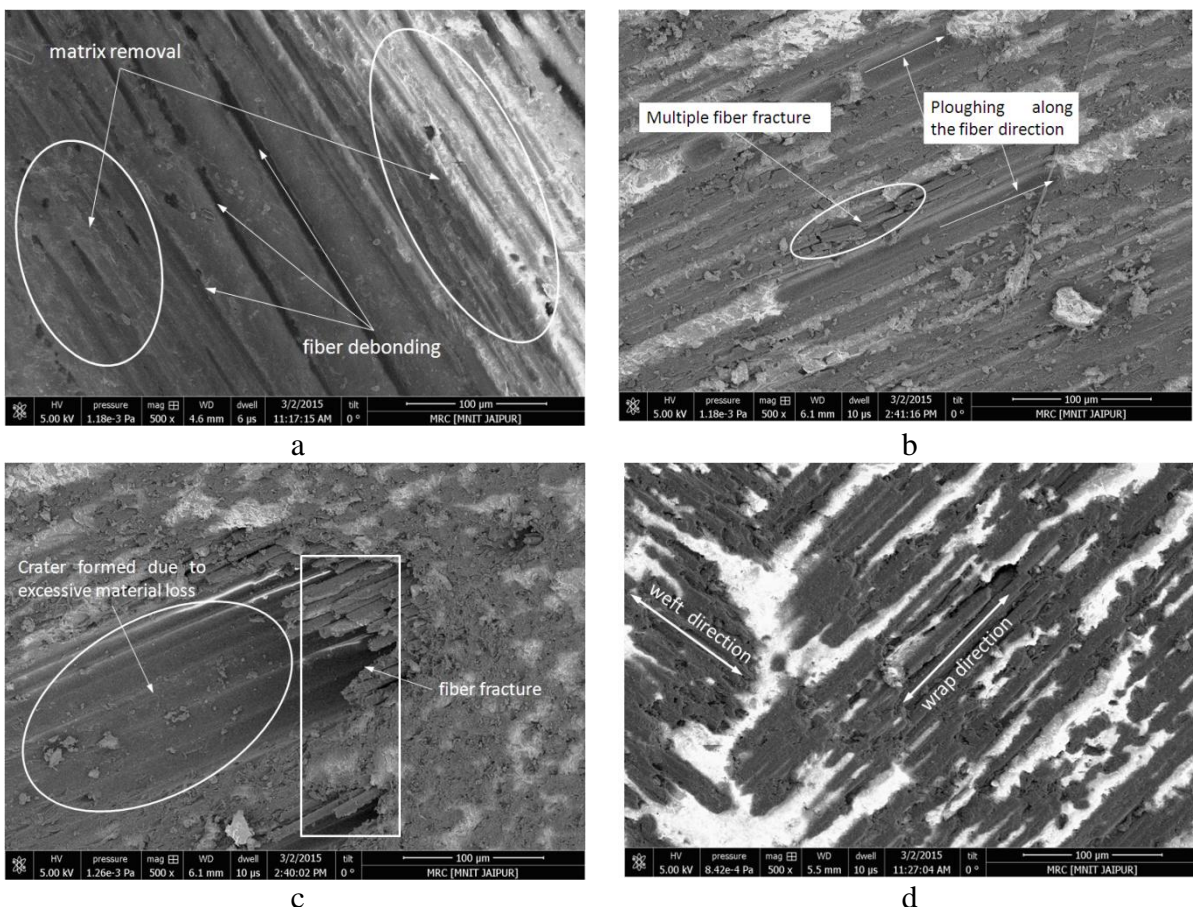
Figure 6.25 SEM micrographs for 40 wt.% carbon epoxy composites at impact velocity 60 m/sec at impingement angle a) 30º, b) 60º, c) 75º and d) 90º

Figure 6.25a demonstrate local removal of matrix material with few fibers debonded from composite at low impingement angle of 30º. This local removal of matrix material is result of abrading action of erodent particle due to slidindg. However, multiple fiber fracture alongwith excessive matrix removal is observed at impingement angle of 60º (see Figure 6.25b). Ploughing mechanism is also obsreved along the fiber direction. The array of matrix is exposed due to remoal of matrix convering it. Matrix removal is result of parrallel component of kinetic energy while fiber fracture is result of normal component of kinetic energy. Figure 6.25c illustrates severe material loss on the surface of target material at impingement angle of 75º. Fibers are damaged and completely taken off from the composite matrial which generates crater. Fiber fracture and crater generation while surrounding unaffected area is marginally agrred with utilization of kinetic energy of erodent for impacting more compared to sliding at relatively higher impact angle. At normal impingement angle kinetic energy is utilized for impacting which results in local damage of layered structure of composite as shown in. Perpendicular directions of wrap and weft is the charactristic of woven fabric can be seen from Figure 6.25d.
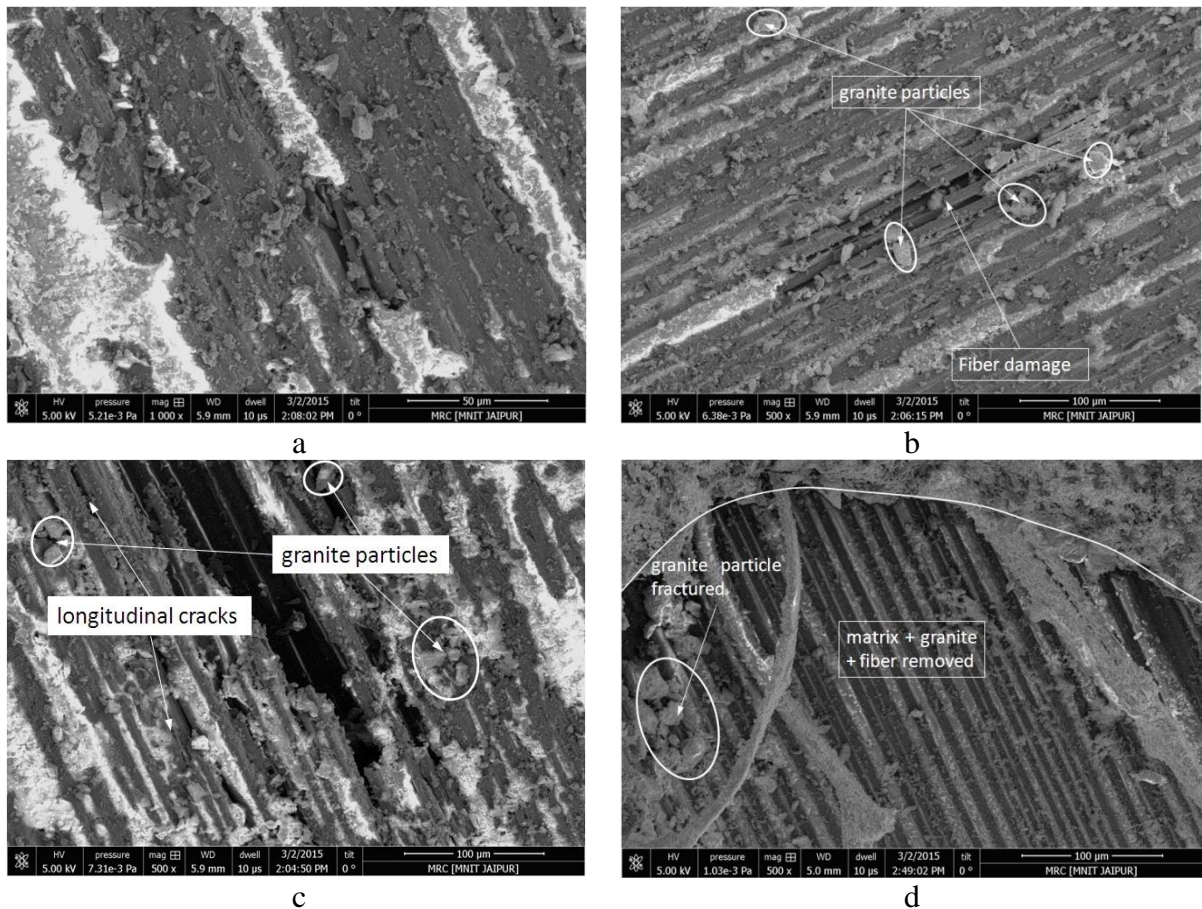
Figure 6.26 SEM micrographs for 16 wt.% granite powder filled carbon epoxy composites at impact velocity 60 m/sec at impingement angle a) 45º, b) 60º, c) 75º and d) 90º

Presence of granite particles positively influence the material removal rate which can be seen from the SEM micrograph in Figure 6.26 for eroded surfaces of 16 wt.% granite powder filled carbon epoxy at impact velocity of 60 m/sec. Relatively lower impingement angle of 45º offer resistance by hard granite particle and only matrix material is removed which results in exposure of granite particles on the surface (Figure 6.26a). At few places fiber shearing is also observed. Figure 6.26b illustrates eroded surface at impingement angle of 60º. The matrix material along with granite particles are removed from the surface. Due to higher impacting energy the granite particles are damaged in to small pieces and the entire array of fibers is exposed. Figure 6.26 c and 6.26d show harsh material removal with formation of scar which is in close agreement with higher erosion rate of 16 wt.% granite powder filled carbon epoxy composite at 75º and 90º compared to 60º impingement angle (see Figure 6.19b). Lack of sliding of erodent at impingement angle 75º, cause concentrated damage on the surface in form of heavy matrix removal. The longitudinal cracks are observed as well as few particles of granite are also visible in Figure 6.26c. Figure 6.26d demonstrates removal of matrix, granite powder and fibers owing to normal impact of erodent material. The generated scar is also visible due to concentrated impacting of erodent material.

Section B: Solid particle erosion wear

The behavior of polymer composites subjected to solid particle erosion has been reported exhaustively in the past literatures. Solid particle erosion is clearly different class as compared to other forms of erosion like liquid impact erosion, slurry erosion and cavitation. Material loss owing to solid particle erosion is result of series of independent but similar impact [289].

Part-I

Solid particle erosion wear analysis of unfilled and granite powder filled glass-epoxy composites

6.10 Steady state solid particle erosion

6.10.1 Influence of impingement angle on solid particle erosion

Solid particle erosion behavior as function of impingement angle is largely determined by nature of target material. Ductile materials show peak erosion at lower impingement angle (i.e 15º to 30º) and brittle materials wear maximum at normal (i.e 90º) impingement angle [289]. Solid particle erosion rate as a function of glass fiber loading granite powder content at different impingement angle are illustrated in Figure 6.27a and 6.27b respectively (impact velocity 60 m/s, stand-off distance 10 mm, erodent size 150 μm and sand flow rate 2 g/min).

With increase in fiber loading up to 30 wt.% the solid particle erosion rate is significantly decreased. Further, increase in fiber loading (40 and 50 wt.%) marginally increased the solid particle erosion rate. This result is on good agreement with results reported by Mahapatra at al [227] for glass fiber reinforced polyester composites. Article presented linear increase in erosion rate for composites reinforced with 40 wt.% glass fiber or more. Figure 6.27a also illustrated peak erosion rate at 60° impingement angle for all the unfilled glass epoxy composites with minimum erosion rate at lower impingement angle (30°). This shows the material loss is combined result of impact (cutting) and abrasion action at 60°. The composites show resistance to material removal when either impact (cutting) at higher angle or abrasion at lower angle observed individually.
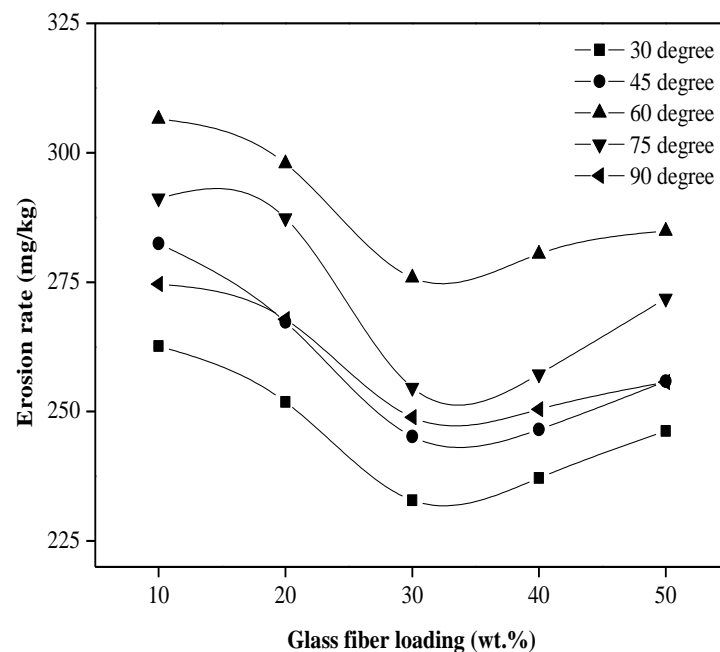
Figure 6.27a Solid particle erosion rate with impingement angle for different wt.% glass fiber loading

Positive influence of conventional filler materials on solid particle erosion characteristics of glass epoxy composites was reported [290-292]. Figure 6.27b show effect of addition of granite powder on solid particle erosion rate for glass epoxy composites. Solid particle erosion rate is decreased with increase in granite powder content at all considered impingement angle as compared to unfilled glass epoxy composites. This reduction in erosion rate is attributed to hardness of granite powder due to presence of oxides of silicon which resisted to impacting and abrading action of erodent material. Similar reduction in erosion rate at impingement angle from 15° to 90° was observed for 20 wt.% titanium carbide filled

glass epoxy composites by Mohapatra et al [292]. It is interested to note that, at impingement angle 60º the erosion rate is drastically influenced with incorporation of granite powder as compared to other impingement angle. Addition of granite powder in glass epoxy composites illustrated peak erosion rate at multiple angle. Maximum erosion occurred at 60º impingement angle for unfilled and 8 wt.% granite filled glass epoxy composites. Whereas, for 16 and 24 wt.% granite filled glass epoxy composites the peak erosion shifted to 75º impingement angle. This shift in peak erosion rate towards higher impingement angle shows transition from semi-ductile to brittle erosion behavior of composites [291].
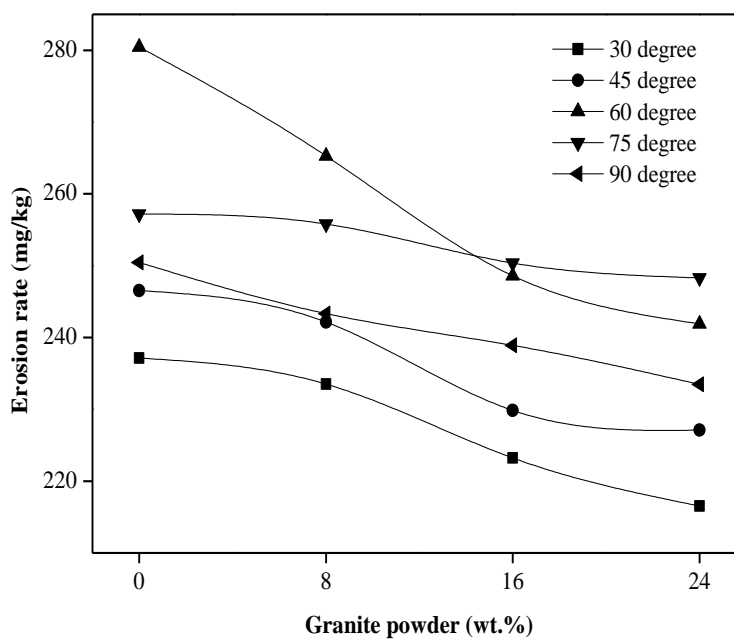
Figure 6.27b Solid particle erosion rate with impingement angle for granite powder filled glass epoxy composites

6.10.2 Influence of impact velocity on solid particle erosion

Impact velocity of erodent has remarkable effect on the solid particle erosion of materials. The influence of impact velocity (V) on erosion rate (E) is given by velocity exponent 'p' in the eq.

$$E \alpha V^p$$

The value reported for velocity exponent for is 2.4 to 2.55 for metals, 3 for ceramics and 5 polymer composites [290]. Figure 6.28a shows influence of impact velocity from 30 to 75 m/sec for glass fiber loading from 10 to 50 wt.% while maintaining other parameters constant (impingement angle of 60º, stand-off distance 10mm, erodent size 150 micron and erodent discharge rate 2 g/min). Erosion rate for impact velocity of 30 m/sec for all the composites is

in the range of 87 to 96 mg/kg which drastically increased to range of 148 to 181 mg/kg for impact velocity of 45 m/sec. Further, this trend continued to increase the erosion rate to the range of 275 to 307 mg/kg for 60m/sec impact velocity of erodent. This drastic increase in the rate of solid particle erosion is in agreement with increase in erosion rate exponentially with increase in impact velocity [290]. However, increase in impact velocity to 75 m/sec marginally increased the erosion rate. The unfilled glass epoxy composite filled with 30 wt.% fiber depicted optimum performance as far as minimum erosion rate is concerned. The influence of 30 wt.% fiber loading on erosion rate is becoming significant at higher impact velocity as compared to lower impact velocity.
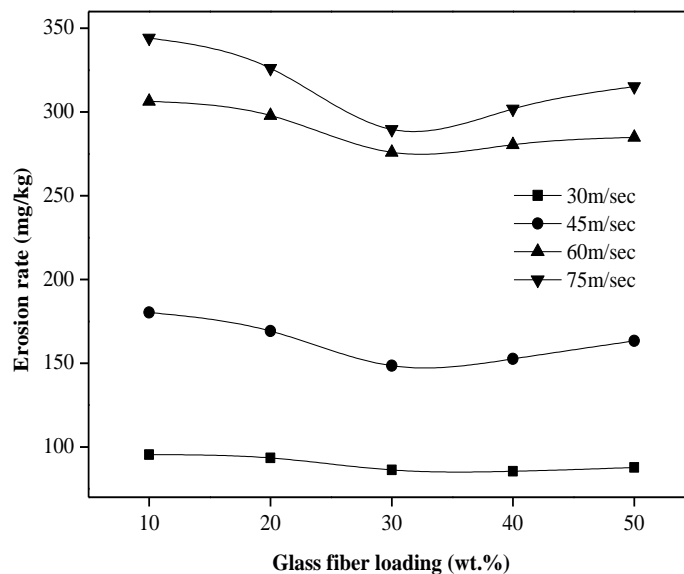
Figure 6.28a Solid particle erosion rate with impact velocity for different wt.% glass fiber loading

Figure 6.28b illustrated effect of granite powder addition on erosion rate for glass epoxy composites at different impact velocities (impingement angle of 60º, stand-off distance 10mm, erodent size 150 micron and erodent discharge rate 2 g/min). Reduction of erosion rate is more or less linear for addition of granite powder at different impact velocities. Influence of addition of granite powder is observed significant on erosion rate at higher impact velocity as compared to erosion rate at lower velocity (observed by different slope of lines in Figure 6.28b). These may be attributed to absorption of more fraction of kinetic energy of erodent particles by granite powder before getting eroded from the target material. With increase in impact velocity the trend of granite powder filled glass epoxy composites show similarity with unfilled glass epoxy composites. The erosion rate is exponentially

increased up to impact velocity of 60 m/sec and at velocity higher than 60 m/sec the marginal increase in erosion rate is observed.
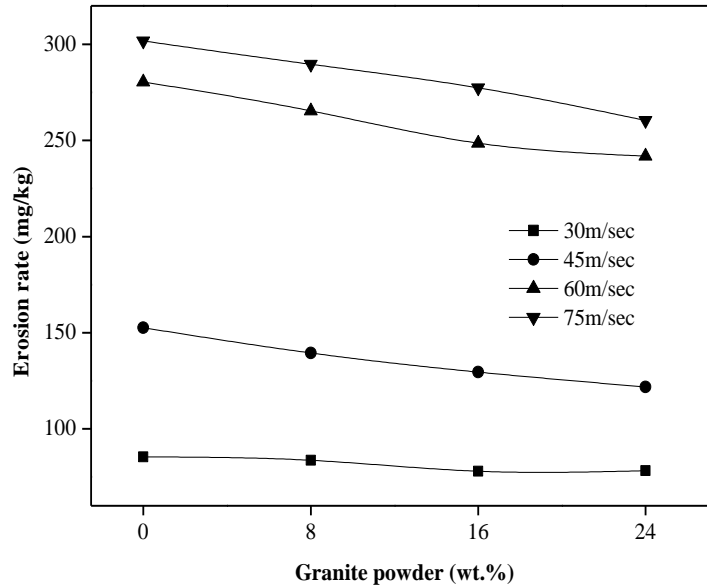
Figure 6.28b Solid particle erosion rate with impact velocity for granite powder filled glass epoxy composites

6.11 Taguchi design of experiment for unfilled and granite powder filled glass epoxy composites

Table 6.8a and 6.8b shows the solid particle erosion rate of unfilled and particulate filled glass epoxy composites respectively using Taguchi design of experiment orthogonal array-L_{16}. The overall mean of S/N ratio for unfilled and granite filled jute epoxy composite is found to be -47.69 db and -47.04 db (decibel) respectively. Figures 6.29a and 6.29b show graphically the effect of all five control factors on slurry erosion rate. For unfilled glass-epoxy composite, the optimum factor combination for minimum solid particle erosion rate is A1 (impact velocity of 10 m/s), B4 (fiber loading of 40 wt.%), C1 (impingement angle of 30°), D2 (erodent size of 100 μm) and E1 (temperature 25℃). Analysis of S/N plots for granite filled glass–epoxy composite leads to conclusion that factor combination of A1 (impact velocity of 10 m/s), B4 (filler content 24 wt.%), C1 (impingement angle of 45°), D3 (erodent size of 150 μm) and E1 (temperature 25℃) resulted in minimum erosion rate. It is clear from the Figures 6.29a and 6.29b that factor A (impact velocity) and factor B (fiber loading/filler content) are the significant factor as S/N plot for these factors are more inclined with horizontal while factor C (impingement angle) factor D (erodent size) and factor E

(temperature) have relatively less significant influence as the plot for these factors are more or less parallel with horizontal.

Table 6.8a Experimental design using L_{16} orthogonal array (unfilled glass-epoxy composites)

Sl. No.	Impact velocity (A) (m/s)	Fiber loading (B) (%)	Impingement angle(C) (degree)	Erodent size (D) (μm)	Temperature (E) C	Erosion rate (Er) (mg/kg)	S/N ratio (db)
1	30	10	30	50	25	191.51	-45.64
2	30	20	45	100	35	184.66	-45.32
3	30	30	60	150	45	187.12	-45.44
4	30	40	75	200	55	182.54	-45.22
5	45	10	45	150	55	237.84	-47.52
6	45	20	30	200	45	221.24	-46.89
7	45	30	75	50	35	217.57	-46.75
8	45	40	60	100	25	209.14	-46.40
9	60	10	60	200	35	301.21	-49.57
10	60	20	75	150	25	287.36	-49.16
11	60	30	30	100	55	266.34	-48.50
12	60	40	45	50	45	257.95	-48.23
13	75	10	75	100	45	318.41	-50.05
14	75	20	60	50	55	318.85	-50.07
15	75	30	45	200	25	294.10	-49.36
16	75	40	30	150	35	280.91	-48.97

Table 6.8b Experimental design using L_{16} orthogonal array (granite powder filled glass-epoxy composites)

| Sl. No.	Impact velocity (A) (m/s)	Filler content (B) (%)	Impingement angle (C) (degree)	Erodent size (D) (μm)	Temperature (E) C	Erosion rate (Er) (mg/kg)	S/N ratio (db)
1	30	0	30	50	25	206.45	-46.29
2	30	8	45	100	35	196.60	-45.87
3	30	16	60	150	45	187.12	-45.44
4	30	24	75	200	55	180.50	-45.12
5	45	0	45	150	55	228.58	-47.18
6	45	8	30	200	45	212.45	-46.54
7	45	16	75	50	35	199.45	-45.99
8	45	24	60	100	25	194.32	-45.77
9	60	0	60	200	35	273.30	-48.73
10	60	8	75	150	25	249.81	-47.95
11	60	16	30	100	55	229.61	-47.21
12	60	24	45	50	45	217.14	-46.73
13	75	0	75	100	45	297.28	-49.46
14	75	8	60	50	55	278.40	-48.89
15	75	16	45	200	25	248.84	-47.91
16	75	24	30	150	35	241.54	-47.65
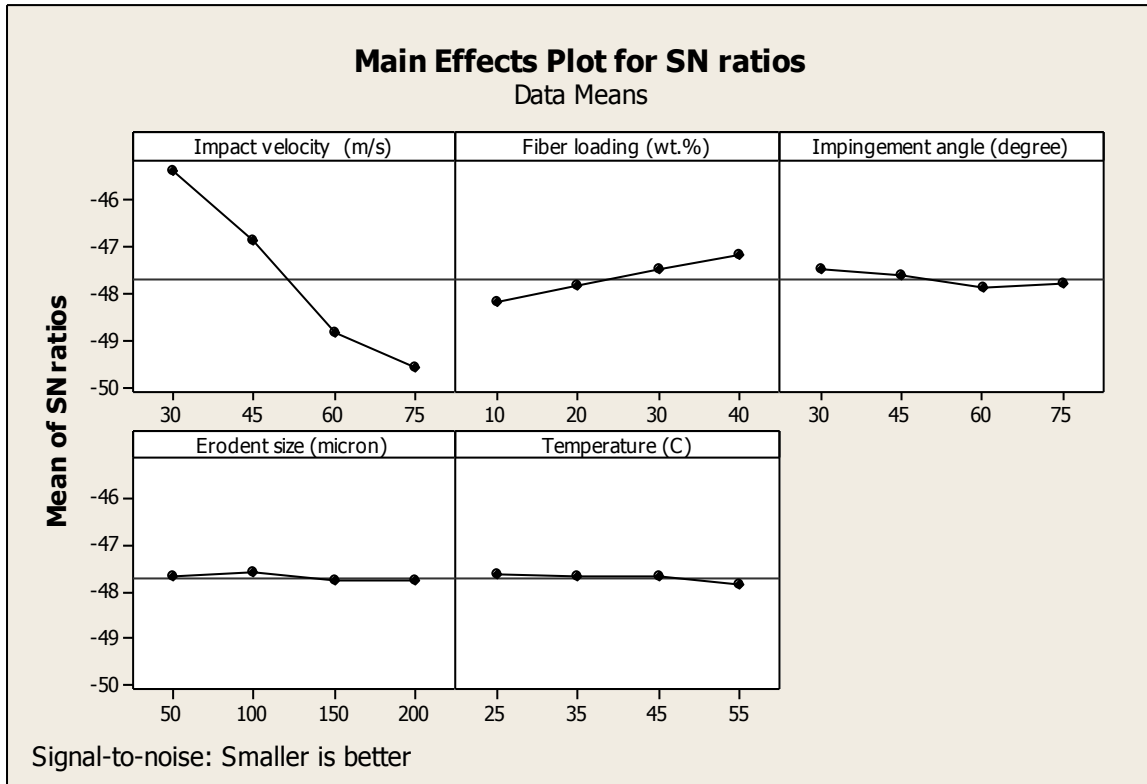
Figure 6.29a Effect of control factors on erosion rate of unfilled glass epoxy composite

Figure 6.29b Effect of control factors on erosion rate granite powder filled glass epoxy composite

The rank of individual control parameter can be determined from Table 6.9a and 6.9b also. Maximum value of delta is indication of maximum influence while minimum value of delta is indication of minimum influence. For unfilled glass epoxy composites the ranking of the parameters are in the sequence of Impact velocity (Δ= 4.21), fiber loading (Δ= 0.99), impingement angle (Δ = 0.37), erodent size (Δ = 0.2) and temperature (Δ = 0.19). The ranking of control parameters for granite powder filled glass epoxy composites are in the sequence of Impact velocity (Δ = 2.80), filler content (Δ = 1.59), impingement angle (Δ = 0.28), temperature (Δ = 0.12) and erodent size (Δ = 0.10). It is interesting to note that both the fiber loading and filler content is at second rank for unfilled and granite powder filled glass epoxy composites. Influence of filler content (Δ = 1.59) on minimizing solid particle erosion rate is more significant than fiber loading (Δ= 0.99).

Table 6.9a Response table for S/N ratio (unfilled glass epoxy composite)

Level	Impact velocity	Fiber loading	Impingement angle	Erodent size	Temperature
1	-45.41	-48.21	-47.51	-47.67	-47.65
2	-46.90	-47.87	-47.61	-47.58	-47.66
3	-48.87	-47.52	-47.88	-47.78	-47.66
4	-49.62	-47.21	-47.80	-47.77	-47.83
Delta (Δ)	4.21	0.99	0.37	0.2	0.19
Rank	1	2	3	4	5

Table 6.9b Response table for S/N ratio (granite powder filled glass epoxy composite)

Level	Impact velocity	Filler content	Impingement angle	Erodent size	Temperature
1	-45.68	-47.92	-46.93	-46.98	-46.98
2	-46.37	-47.32	-46.93	-47.08	-47.07
3	-47.66	-46.64	-47.21	-47.06	-47.05
4	-48.48	-46.32	-47.14	-47.08	-47.11
Delta (Δ)	2.80	1.59	0.28	0.10	0.12
Rank	1	2	3	5	4

6.12 Surface morphology

Unfilled glass fiber reinforced epoxy composites exhibits several stages of erosion and material removal. Initially, local removal of resin material from the impacted surface is observed. As a result of this local removal of resin, the fibers are exposed to erosive environment [241]. Figure 6.30 illustrates change in erosion mechanism of 40 wt.% glass epoxy composite with variation in impact velocity at impingement angle of 60º. Eroded surface at low impact velocity (30 m/sec) shows local removal of epoxy resin which fails in brittle manner indicating numerous micro-cracks and ploughing mechanism in resin (Figure 6.30a). Increase in impact velocity to 45 m/sec resulted in excessive removal of resin material and fibers are exposed to erosive environment. In addition to resin failure, micro-cracks are observed at the fiber matrix interface as shown in Figure 6.30b. Further increase in impact velocity (60 m/sec) shows severe material removal with fiber matrix interface damage and fibers are completely de-bonded from the surface. Longitudinal cracks are clearly visible which may be the result of impacting erodent particle with high kinetic energy (Figure 6.30c). At highest velocity of 75 m/sec this trend of material removal continues showing longitudinal intra-fiber cracks. High kinetic energy of erodent particles cause bending
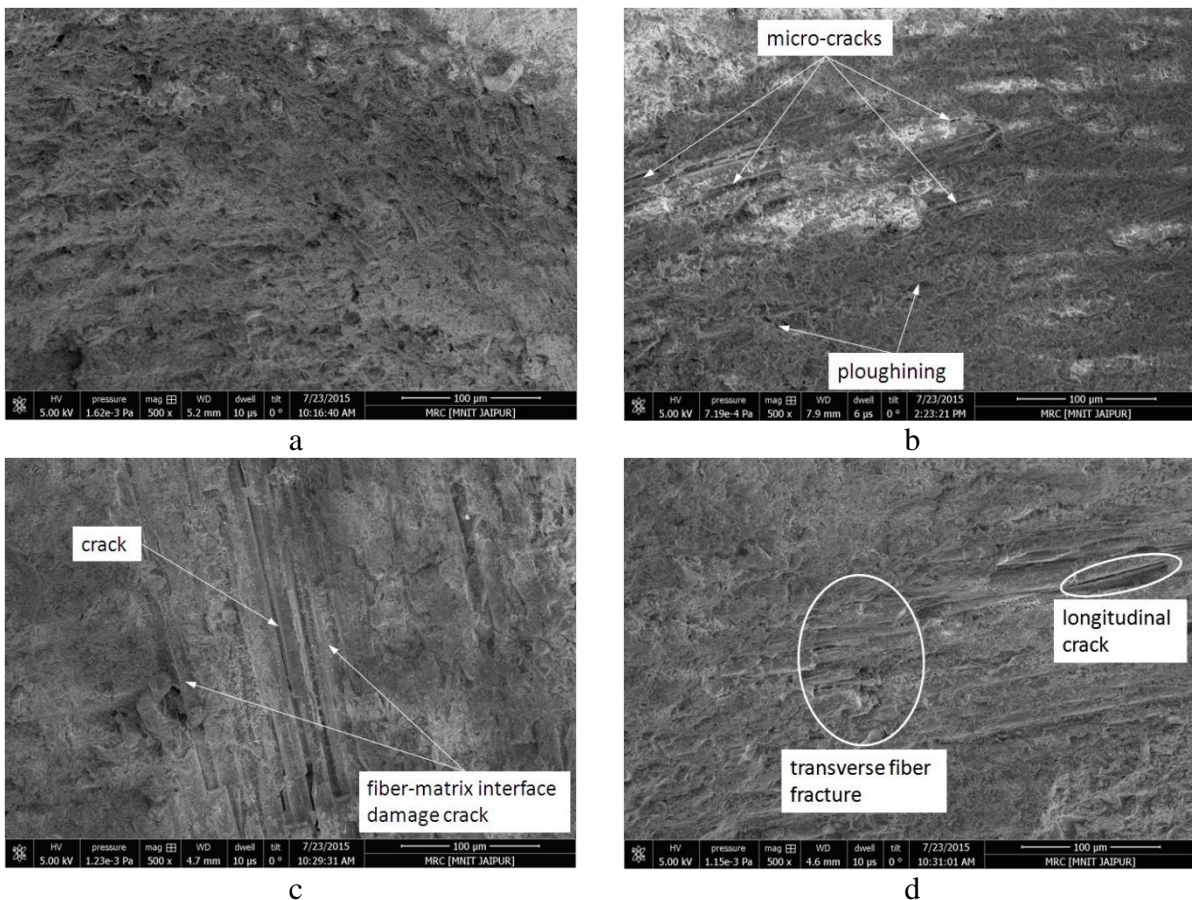
Figure 6.30 SEM images showing erosion mechanism for unfilled glass epoxy composites

Figure 6.31 illustrated damage mechanism using SEM micrographs for granite powder filled glass epoxy composites at impingement angle 60º. Figure 6.31a showed micrograph of 8 wt.% granite powder filled glass epoxy composite at impact velocity of 60 m/sec. Lower amount of granite particles get eroded from the surface along with matrix resin and further bombardment of erodent material result in fiber and fiber matrix interface damage. Few traces of de-bonded granite particles are also visible on the surface of eroded sample. Further addition of 16 wt.% granite particles effectively resist the kinetic energy of erodent particles and prevent complete exposure of fiber array. The erosion mechanism is observed in the form of local removal of matrix, micro-cracks and exposed granite particles (see Figure 6.31b). Higher content of granite powder (i.e. 24 wt.%) result in much exposure of fiber array at limited area only and remaining area is subjected to local removal of matrix as shown in Figure 6.31c. With increase in velocity from 60 m/sec to 75 m/sec for 24 wt.% granite powder filled glass epoxy composite depicted the erosion mechanisms such as multiple fiber fracture, micro-cracks and removal of matrix material as shown in Figure 6.31d. The SEM micrograps also agreed with experimental results which illustrate improvement in erosion resistance with incorporation of granite powder as filler material.

a

b

c

d
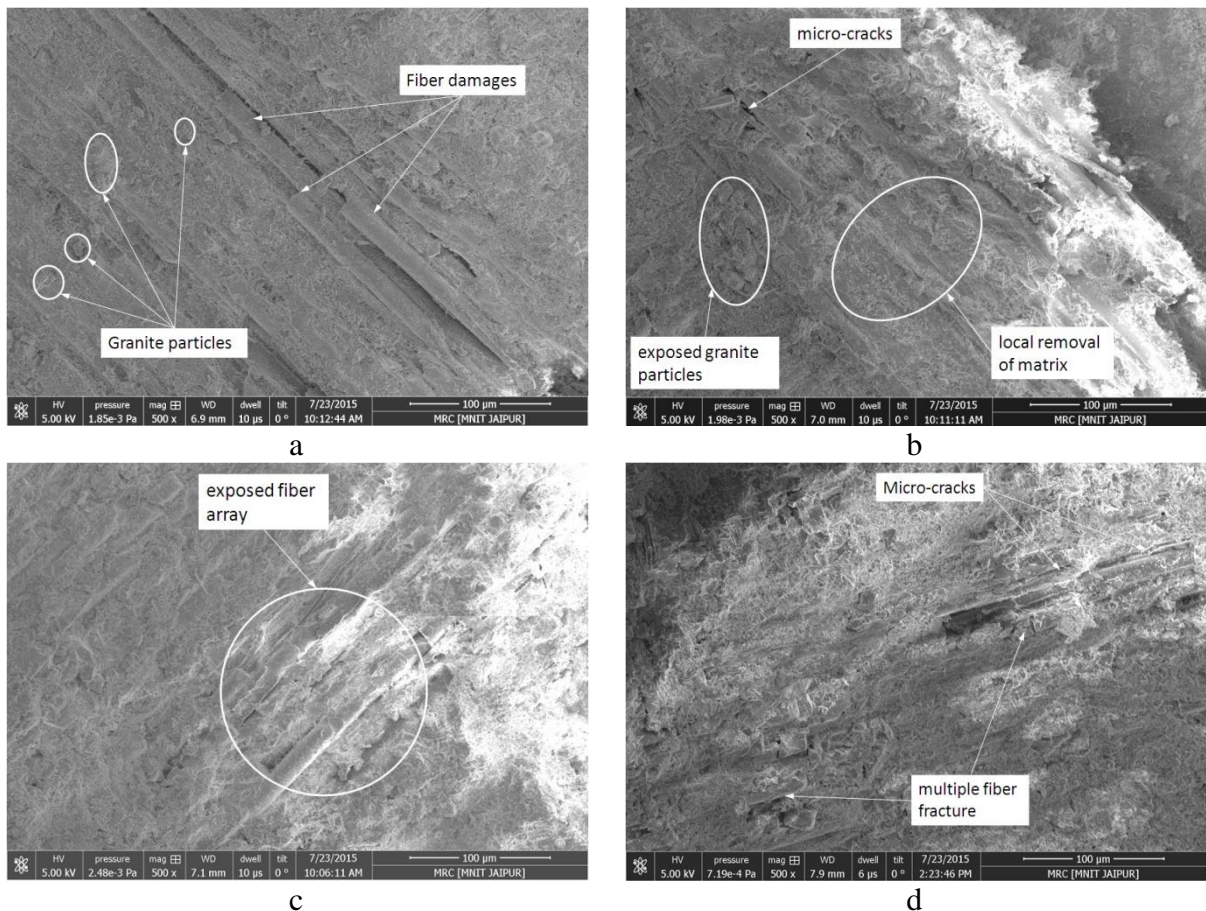
Figure 6.31 SEM images showing erosion mechanism for granite powder filled glass epoxy

composites

Part-II

Solid particle erosion wear analysis of unfilled and granite powder filled jute-epoxy composites

6.13 Steady state solid particle erosion

6.13.1 Influence of impingement angle on solid particle erosion

The thermoplastic composites show ductile behavior with maximum erosion at lower impingement angle. However, the thermosetting plastic composites behave in brittle manner with maximum erosion rate at normal incidence. While this classification of erosion behavior is point of dispute as erosion is influenced by composition of target material and experimental conditions [293]. The Figure 6.32a and 6.32b show influence of impingement angle on erosion rate of unfilled and granite powder filled jute epoxy composites respectively, keeping other control parameters constant (impact velocity of 60 m/sec, stand-off distance 10mm, erodent size 150 micron and erodent discharge rate 2 g/min).
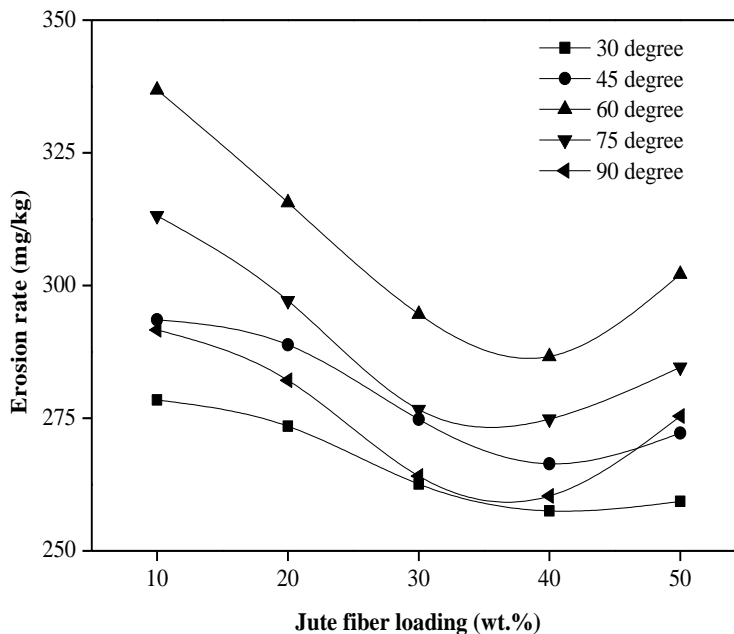
Figure 6.32a Solid particle erosion rate with impingement angle for different wt.% jute fiber loading

The solid particle erosion rate is observed significantly lower for impingement angles other than 60º for unfilled jute epoxy composites (see Figure 6.32a). Peak erosion is reported at 60º impingement angle which confirms to semi-ductile behavior of jute epoxy composites [294]. Minimum erosion rate is observed for impingement angle 30º due to resistance of

brittle phase for abrasion by erodent material. Jute fiber reinforcement up to 30 wt.% has significant positive effect on erosion rate. While, fiber loading of 40 wt.% shows marginal reduction in erosion rate for unfilled jute epoxy composites. Beyond 40 wt.% of jute fiber loading the unfilled composites depicted undesirable effect on erosion rate. Similar to unfilled composites, granite powder addition in to jute epoxy composites exhibits peak erosion rate at 60 ° impingement angles which agreed with semi-ductile failure under erosive environment (see Figure 6.32b). Erosion rate is continually decreasing with addition of granite powder at all the impingement angles under investigation except to composite filled with 24 wt.% granite powder at 75° impingement angle. This reduction in erosion rate is attributing to improvement in hardness of composite with incorporation of hard granite particles. The granite powder also absorbs part kinetic energy associated with erodent material [11]. The exceptional case of increase in erosion rate for 24 wt.% granite powder shows the loss of ductility and shift towards brittle failure.
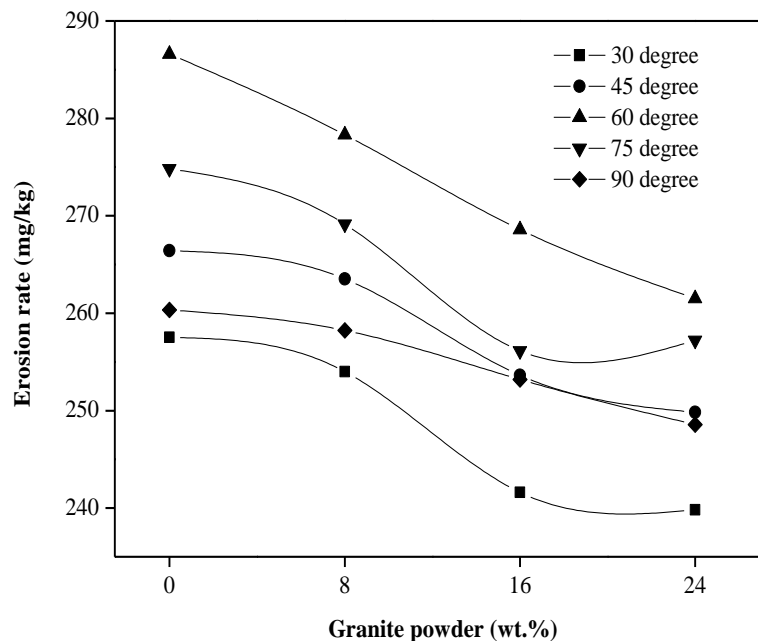
Figure 6.32b Solid particle erosion rate with impingement angle for granite powder filled jute epoxy composites

6.13.2 Influence of impact velocity on solid particle erosion

Figure 6.33a and 6.33b show influence of impact velocity on solid particle erosion rate for unfilled and granite powder filled jute epoxy composite respectively keeping other control

parameters constant (impact velocity of 60 m/sec, stand-off distance 10mm, erodent size 150 micron and erodent discharge rate 2 g/min). The lines in the both the graphs are spacious to each other which show significant effect of impact velocity on erosion rate. While, most significant increase in erosion rate is observed for increase in impact velocity from 45 to 60 m/sec. For any velocity under consideration the erosion rate is found to be reduced up to 40 wt.% jute fiber loading and for 50 wt.% jute epoxy composite the erosion rate is further slightly increased. This reduction in erosion rate up to 40 wt.% jute fiber loading is very marginal for 30 m/sec impact velocity whereas, it becomes significant when impact velocity reaches to 75 m/sec. This is evident from the erosion rate of 108.15 mg/kg and 94.3 mg/kg for 10 wt.% jute fiber loading and 40 wt.% jute fiber loading respectively at impact velocity 30/ sec as compared to the corresponding erosion rate of 367.64 mg/kg to 317.65 mg/kg at impact velocity of 75 m/sec

Figure 6.33b illustrated very marginal reduction in erosion rate from 94.14 mg/kg for unfilled jute epoxy composite to 88.12 mg/kg for 24 wt.% granite powder filled jute epoxy composite at impact velocity 30 m/sec. In the same context erosion rate is reduced from 161.74 mg/kg to 137.84 mg/kg and 286.61 mg/kg to 261.5 mg/kg for 45 m/sec and 60 m/sec impact velocity respectively. Significant decrease in erosion rate is observed at impact velocity of 75 m/sec from 317.65 mg/kg to 275.18 mg/kg with increase in granite powder content from 0 wt.% to 24 wt.% respectively.
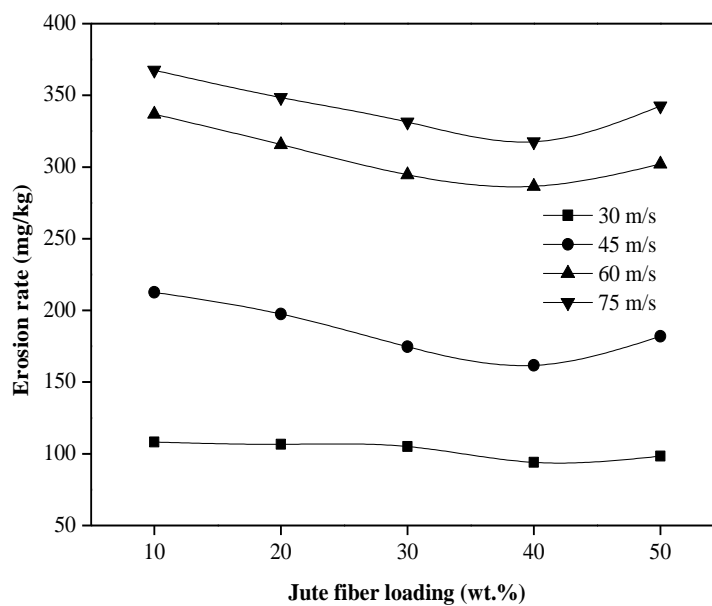
Figure 6.33a Solid particle erosion rate with impact velocity for different wt.% jute fiber loading
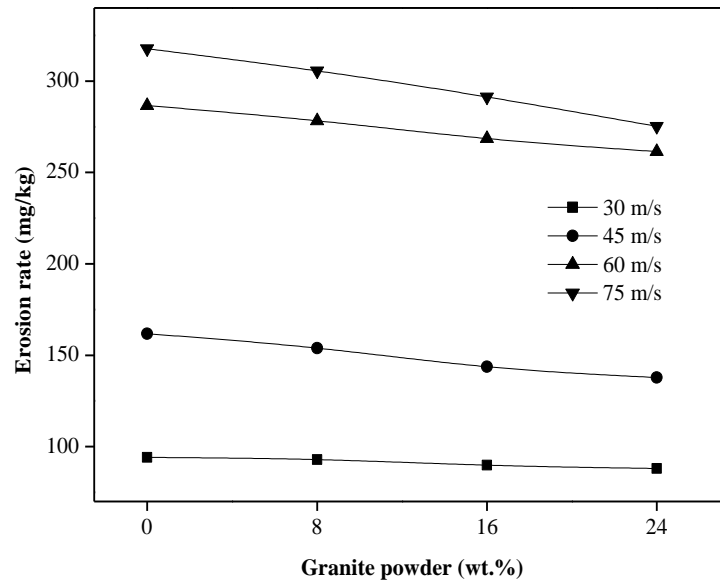
Figure 6.33b Solid particle erosion rate with impact velocity for granite powder filled jute epoxy composites

6.14 Taguchi design of experiment for unfilled and granite powder filled jute epoxy composites

Table 6.10a and 6.10b shows the solid particle erosion rate of unfilled and particulate filled jute epoxy composites respectively using Taguchi design of experiment orthogonal array-L_{16}. The overall mean of S/N ratio for unfilled and granite filled jute epoxy composite is found to be -48.02 db and -47.70 db (decibel) respectively. Figures 6.34a and 6.34b show graphically the effect of all five control factors on slurry erosion rate. For unfilled jute-epoxy composite, the optimum factor combination for minimum solid particle erosion rate is A1 (impact velocity of 10 m/s), B4 (fiber loading of 40 wt.%), C2 (impingement angle of 45°), D2 (erodent size of 100 µm) and E1 (temperature 25°C).

Analysis of S/N plots for granite filled jute–epoxy composites leads to conclusion that factor combination of A1 (impact velocity of 10 m/s), B4 (filler content 24 wt.%), C2 (impingement angle of 45°), D1 (erodent size of 50 µm) and E1 (temperature 25°C) resulted in minimum erosion rate. It is clear from the Figures 6.34a and 6.34b show that factor A (impact velocity) and factor B (fiber loading/filler content) are the significant factor as S/N plot for these factors are more inclined with horizontal while factor C (impingement angle) factor D (erodent size) and factor E (temperature) have relatively less significant influence as the plot for these factors are more or less parallel with horizontal.

Table 6.10a Experimental design using L_{16} orthogonal array (unfilled jute-epoxy composites)

Sl. No.	Impact velocity (A) (m/s)	Fiber loading (B) (%)	Impingement angle(C) (degree)	Erodent size (D) (μm)	Temperature (E) C	Erosion rate (Er) (mg/kg)	S/N ratio (db)
1	30	10	30	50	25	205.60	-46.26
2	30	20	45	100	35	201.45	-46.08
3	30	30	60	150	45	199.00	-45.97
4	30	40	75	200	55	190.56	-45.60
5	45	10	45	150	55	242.10	-47.69
6	45	20	30	200	45	237.21	-47.50
7	45	30	75	50	35	225.71	-47.07
8	45	40	60	100	25	210.60	-46.46
9	60	10	60	200	35	305.55	-49.70
10	60	20	75	150	25	297.15	-49.45
11	60	30	30	100	55	287.25	-49.16
12	60	40	45	50	45	261.20	-48.33
13	75	10	75	100	45	317.15	-50.02
14	75	20	60	50	55	330.45	-50.38
15	75	30	45	200	25	303.80	-49.65
16	75	40	30	150	35	285.15	-49.10

Table 6.10b Experimental design using L_{16} orthogonal array (granite powder filled jute-epoxy composites)

| Sl. No.	Impact velocity (A) (m/s)	Filler content (B) (%)	Impingement angle (C) (degree)	Erodent size (D) (μm)	Temperature (E) C	Erosion rate (Er) (mg/kg)	S/N ratio (db)
1	30	0	30	50	25	217.51	-46.74
2	30	8	45	100	35	210.80	-46.47
3	30	16	60	150	45	203.45	-46.16
4	30	24	75	200	55	189.25	-45.54
5	45	0	45	150	55	245.10	-47.78
6	45	8	30	200	45	236.48	-47.47
7	45	16	75	50	35	219.45	-46.82
8	45	24	60	100	25	207.60	-46.34
9	60	0	60	200	35	282.10	-49.00
10	60	8	75	150	25	269.15	-48.59
11	60	16	30	100	55	256.56	-48.18
12	60	24	45	50	45	229.47	-47.21
13	75	0	75	100	45	314.45	-49.95
14	75	8	60	50	55	305.50	-49.70
15	75	16	45	200	25	278.75	-48.90
16	75	24	30	150	35	264.85	-48.46
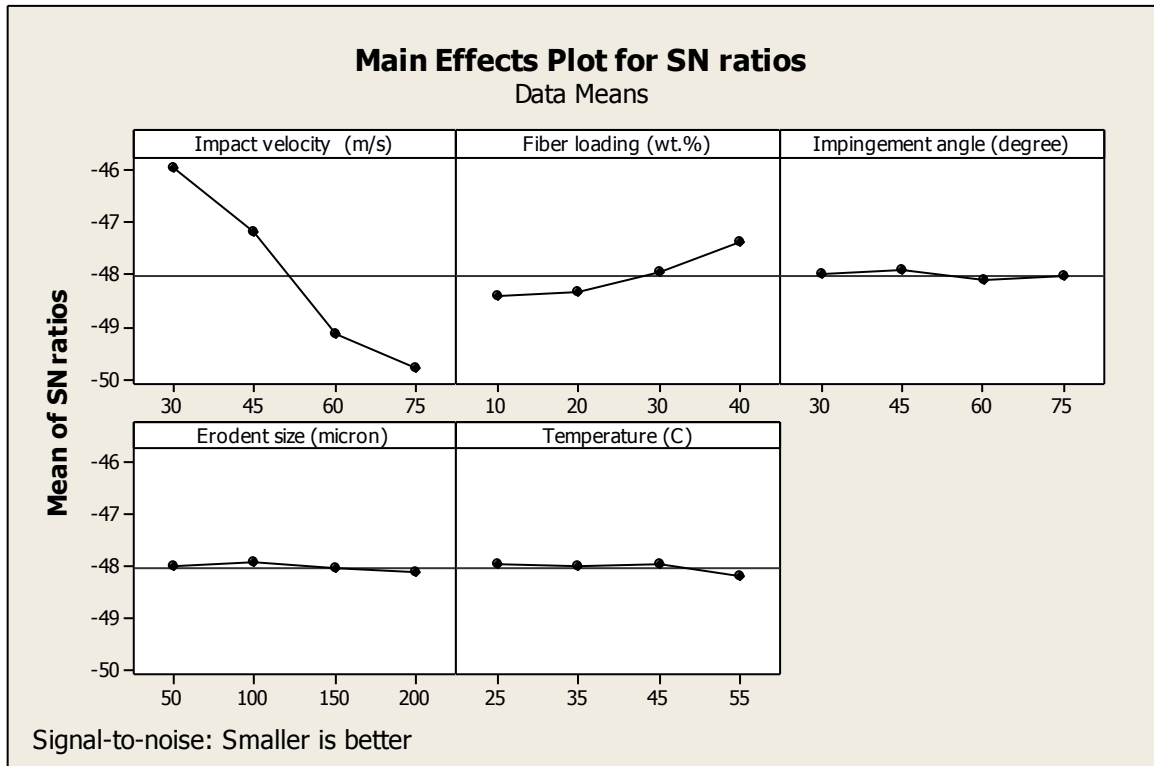
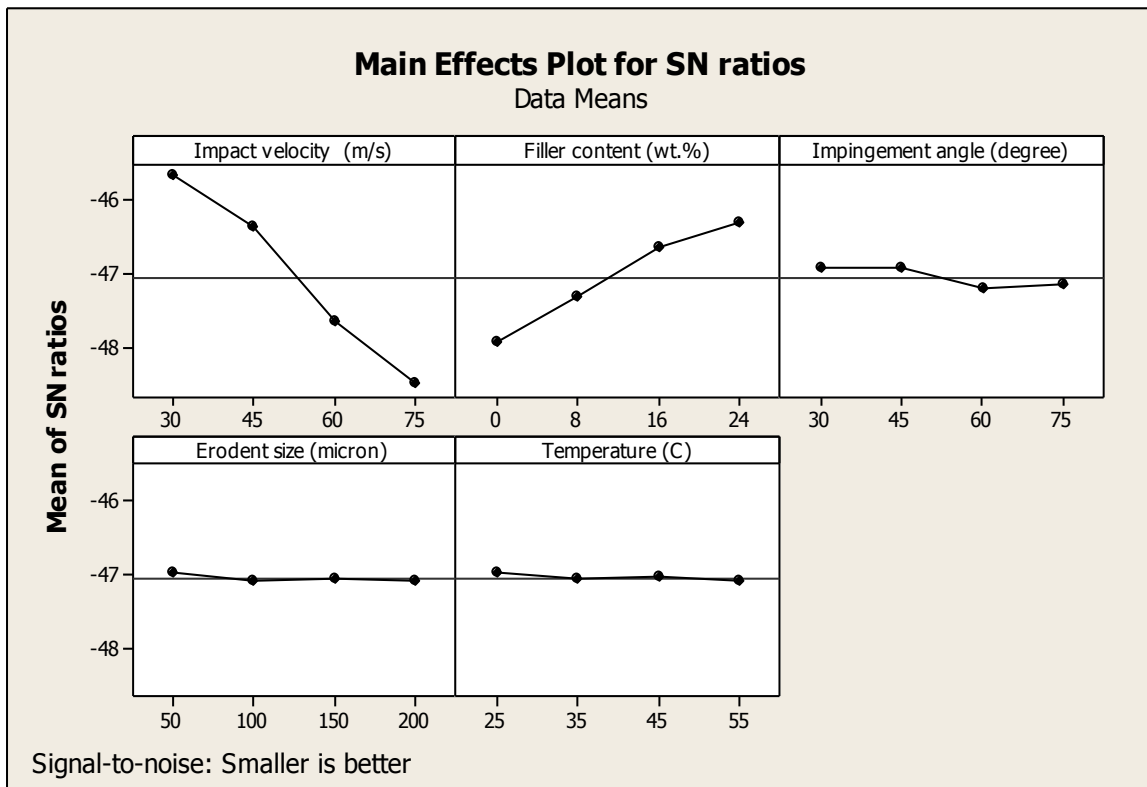Figure 6.34a Effect of control factors on erosion rate of unfilled jute epoxy composite

Figure 6.34b Effect of control factors on erosion rate of unfilled jute epoxy composite

The rank of individual control parameter can be determined from Table 6.11a and 6.11b also. Maximum value of delta is indication of maximum influence while minimum value of delta is indication of minimum influence. For unfilled glass epoxy composites the ranking of the parameters are in the sequence of Impact velocity (Δ= 3.81), fiber loading (Δ= 1.04), temperature (Δ = 0.25), impingement angle (Δ = 0.19) and erodent size (Δ = 0.18). The ranking of control parameters for granite powder filled glass epoxy composites are in the sequence of Impact velocity (Δ = 3.02), filler content (Δ = 1.48), impingement angle (Δ = 0.21), temperature (Δ = 0.15) and erodent size (Δ = 0.13). Similar to glass epoxy composites both the fiber loading and filler content is at second rank for unfilled and granite powder filled jute epoxy composites. Influence of filler content (Δ = 1.48) on minimizing solid particle erosion rate is more significant than fiber loading (Δ= 1.04).

Table 6.11a Response table for S/N ratio (unfilled jute epoxy composite)

Level	Impact velocity	Filler loading	Impingement angle	Erodent size	Temperature
1	-45.98	-48.42	-48.01	-48.01	-47.96
2	-47.18	-48.36	-47.94	-47.94	-47.99
3	-49.17	-47.97	-48.13	-48.05	-47.96
4	-49.79	-47.38	-48.04	-48.11	-48.21
Delta	3.81	1.04	0.19	0.18	0.25
Rank	1	2	4	5	3

Table 6.11b Response table for S/N ratio (granite powder filled jute epoxy composite)

Level	Impact velocity	Filler loading	Impingement angle	Erodent size	Temperature
1	-46.23	-48.37	-47.72	-47.62	-47.65
2	-47.11	-48.06	-47.60	-47.74	-47.69
3	-48.25	-47.52	-47.81	-47.75	-47.70
4	-49.25	-46.89	-47.73	-47.73	-47.80
Delta	3.02	1.48	0.21	0.13	0.15
Rank	1	2	3	5	4

6.15 Surface morphology

Morphology of surfaces of specimen after solid particle erosion for unfilled jute epoxy composites for varying impingement angle is shown in Figure 6.35 (fiber loading: 40 wt.%, impact velocity: 60 m/sec, stand of distance: 10 mm, erodent size: 150 μm, erodent discharge: 2 gm/min etc.). At lower impingement angle of 30° the surface of eroded sample show cracks on matrix material (see Figure 6.35a). With increase in impingement angle to

45° the damage on the eroded surface show micro-ploughing, this resulted in exposure of fiber layer as shown in Figure 6.35b. It is also observed that the removal of matrix takes place at impingement angle of 45°. Higher impingement angle of 60° leads to more impact of erodent particle rather than sliding of erodent particle. Severe fiber damage is observed at impingement angle of 60° and it is in agreement with peak erosion rate obtained experimentally. Also few deep groves are observed as a result of major cracks generated due to interface damage as shown in Figure 6.35c. Further, increase in impact angle to 75° continues the trend of erosion mechanism in form of severe fiber damage as shown in Figure 6.35d. Impact of erodent particle at higher impact angle resulted in concentrated removal of matrix material and formation of micro crater.
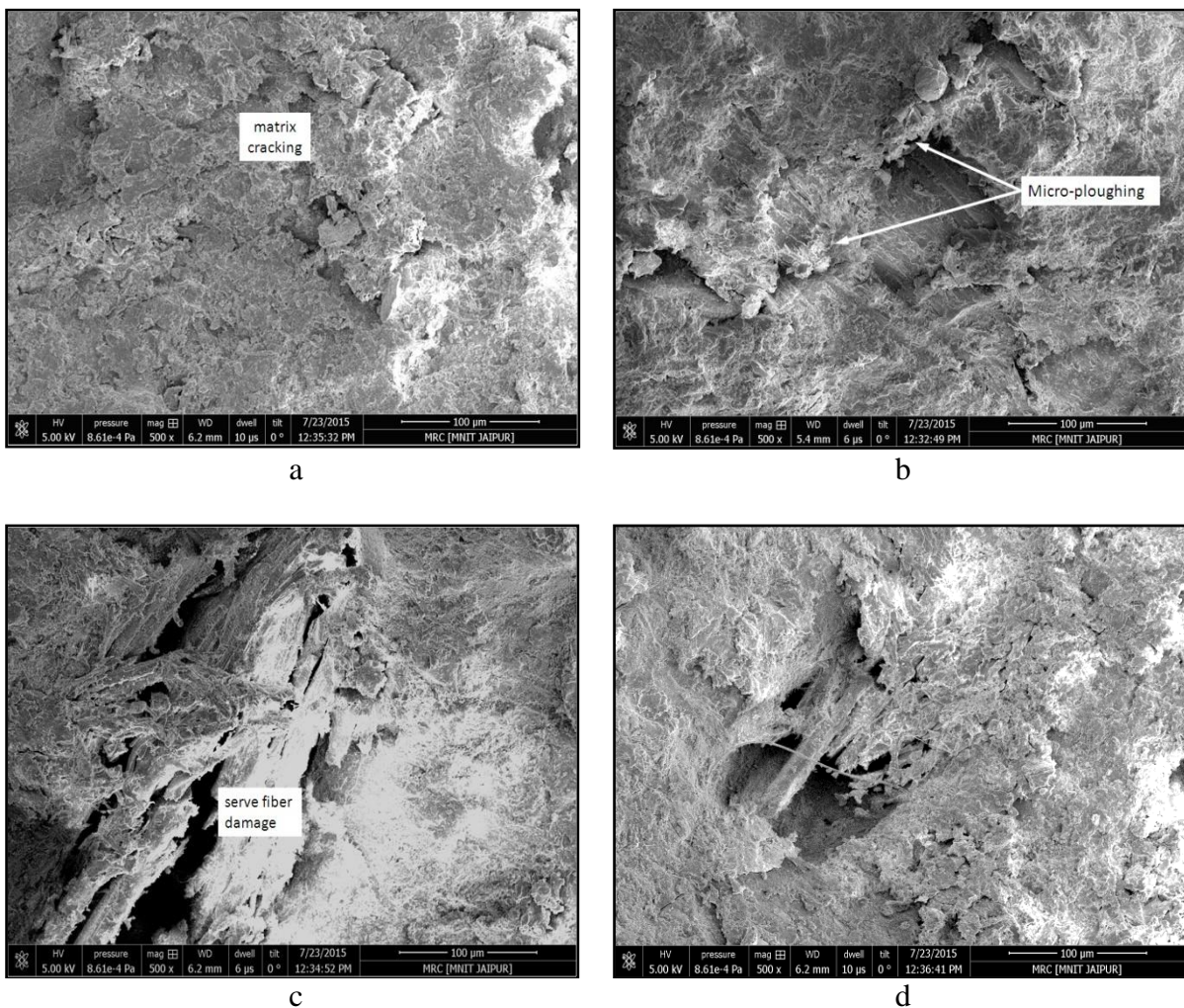
Figure 6.35 SEM images for eroded surfaces for unfilled jute epoxy composites

Incorporation of granite powder resulted in different morphology of eroded surface compared to unfilled jute epoxy composites. The differences in damage mechanisms are

clearly visible from Figure 6.35 and 6.36. In case of addition of granite powder in jute epoxy composites show micro-ploughing and matrix cracking. The granite powder particles absorbed the kinetic energy of erodent particles and prevent the fiber exposure. Figure 6.36a to 3.36d shows morphology of eroded surface of 16 wt.% granite powder filled jute epoxy composites at impingement angle of 30, 45, 60 and 90° respectively (impact velocity: 60 m/sec, stand of distance: 10 mm, erodent size: 150 μm, erodent discharge: 2 gm/min etc.). Local removal matrix material is observed at lower impingement angle of 30 and 45°. Some particles of granite powder are also visible on the surface of eroded samples. For impingement angle of 60°, deep groves are reported along with micro-cracks. Matrix material is completely removed and fiber layer is exposed to bombardment of erodent material. Normal incidences of erodent particles severely damage the surface of material.

a

b

c

d
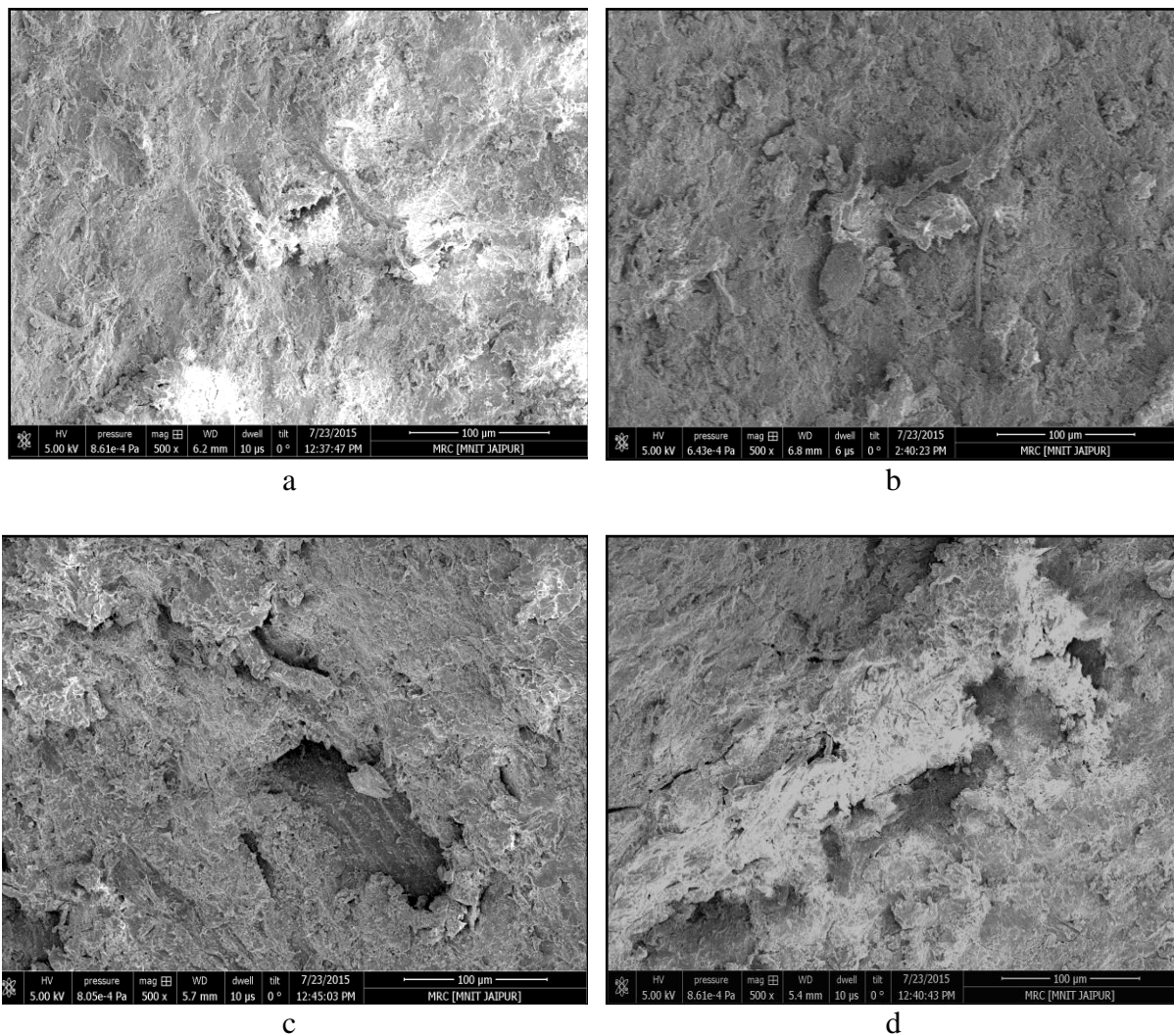
Figure 6.36 SEM images for eroded surfaces for granite powder filled jute epoxy composites

Part-III

Solid particle erosion wear analysis of unfilled and granite powder filled carbon-epoxy composites

6.16 Steady state solid particle erosion

6.16.1 Influence of impingement angle on solid particle erosion

Influence of impingement angle on the solid particle erosion rate for unfilled carbon epoxy composite is shown in Figure 3.37a. Peak erosion rate is reported for impingement angle of 60° irrespective of fiber loading percentage. This shows semi-ductile erosion behavior of carbon fiber reinforced epoxy composites. Figure 6.37a clearly show that erosion rate at 60° impingement angle is at much higher side than any other impingement angle under consideration. With addition of carbon fiber the erosion rate is linearly decreased up to 40 wt.% fiber reinforcement. Further with addition of carbon fiber beyond 40 wt.% erosion rate is in show increased trend at all the impingement angle under consideration. Erosion rate at 60° impingement angle decreased from 294.22 mg/kg for 10 wt.% carbon epoxy composites to 282.1, 259.6 and 249.3 mg/kg for reinforcement of 20, 30 and 40 wt.% of carbon fiber. However, the erosion rate is further increased to 271.2 mg/kg for reinforcement of 50 wt.% carbon fiber. Surprisingly, the value of erosion rate for 50 wt.% carbon fiber is higher than erosion rate of carbon epoxy composite reinforced with 30 wt.% and 40 wt.% carbon fiber. This indicate that proper wetting ability of epoxy for carbon fiber is limited by 40 wt.% carbon fiber addition. Further addition of carbon fiber result in fiber-fiber interaction and initiate the cracks.

Figure 6.37b depicted the erosion rate of granite powder filled carbon epoxy composites. Unfilled carbon epoxy composite show peak erosion rate at 60° impingement angle. However, for composite with granite addition, peak erosion rate is shifted to higher impingement angle (i.e. 75°). This shift in peak erosion rate from 60° to 75° impingement angle shows loss of ductility and shift towards brittle failure of composite material with incorporation of granite powder. It is visible from Figure 6.37b that the erosion rate is constantly decreasing with increase in granite powder. This is attributed to higher amount of kinetic energy absorbed by hard granite powder before detached from the surface. Minimum erosion rate for unfilled and granite powder filled carbon epoxy composites is reported at impingement angle of 30°. This is due to sliding of erodent particle with minimum material removal from the surface of target material at lower impingement angle.
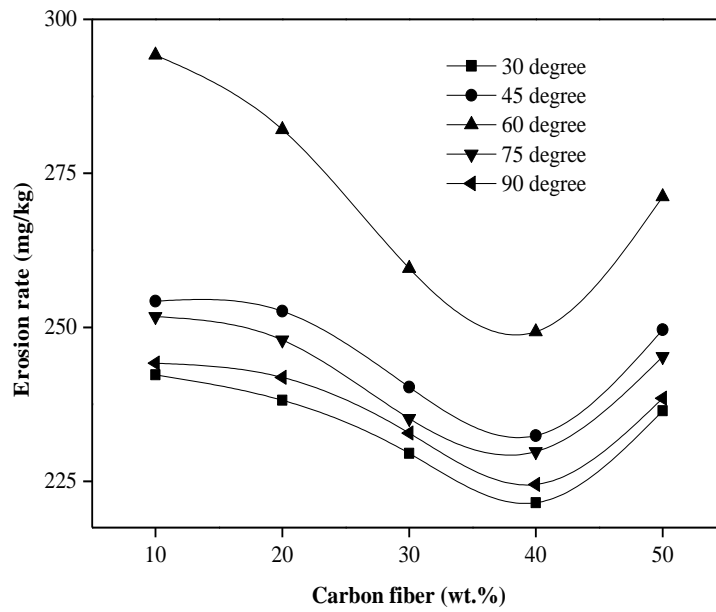
Figure 6.37a Solid particle erosion rate with impingement angle for different wt.% carbon fiber loading
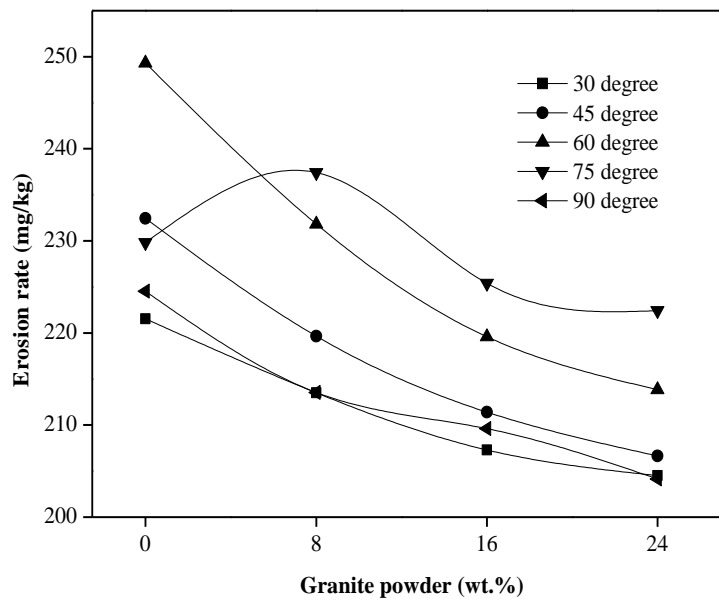
Figure 6.37b Solid particle erosion rate with impingement angle for granite powder filled carbon epoxy composites

6.16.2 Influence of impact velocity on solid particle erosion

Impact velocity is one of the most influencing control parameter on the solid particle erosion performance of polymer composite. Figure 6.38a illustrated the solid particle erosion rate at varying impact velocity as function of wt.% of carbon fiber reinforcement. Spacious lines in

the graph show the increase in erosion rate with increase in impact velocity of erodent particles. Influence of fiber reinforcement on erosion rate is significant at higher impact velocity compared to erosion rate at lower impact velocity. At impact velocity 75 m/sec the erosion rates are 315.3, 296.12, 276.84, 268.82 and 289.14 mg/kg with increase in carbon fiber loading from 10 to 50 wt.% in the interval of 10 wt.%. Lower value of erosion rate is reported for the carbon epoxy composite reinforced with 40 wt.% fiber irrespective of value of impact velocity. Harsh increase in erosion rate for series of unfilled carbon epoxy composites is observed for increase in impact velocity from 45 m/sec to 60 m/sec.

Effect of impact velocity on erosion rate as function of granite powder content is given in Figure 6.38b. Erosion rate is marginally affected with addition of granite powder at lower impact velocity. At impact velocity of 30 m/sec the erosion rate is decreased from 83.84 mg/kg for unfilled carbon epoxy composite to 80.15, 78.16 and 75.81 mg/kg for addition of 8, 16 and 24 wt.% granite powder respectively. However, at higher impact velocity the reduction in erosion rate with addition of granite powder is significant. At impact velocity 75 m/sec the erosion rate is significantly reduced from 268.62 mg/kg for unfilled carbon epoxy composite to 252.41, 245.69 and 229.81 mg/kg for addition of 8, 16 and 24 wt.% granite powder.
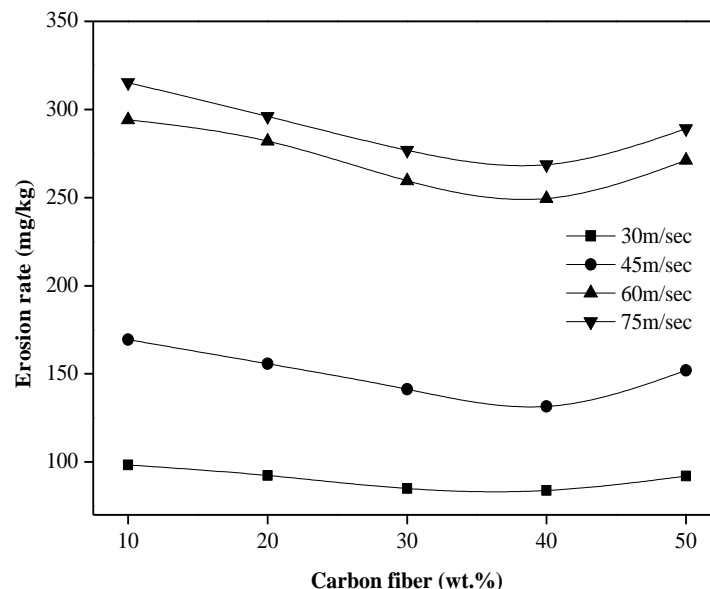
Figure 6.38a Solid particle erosion rate with impact velocity for different wt.% carbon fiber loading
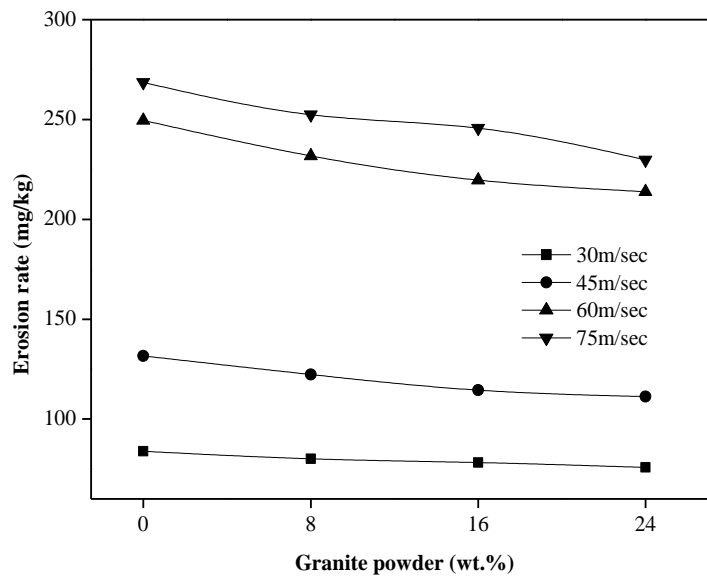
Figure 6.38b Solid particle erosion rate with impact velocity for granite powder filled carbon epoxy loading

6.17 Taguchi design of experiment for unfilled and granite powder filled carbon epoxy composites

Table 6.12a and 6.12b show the solid particle erosion rate of unfilled and particulate filled carbon epoxy composites respectively using Taguchi design of experiment orthogonal array-L_{16}. The overall mean of S/N ratio for unfilled and granite filled jute epoxy composite is found to be -46.92 db and -46.67 db (decibel) respectively. Figures 6.39a and 6.39b show graphically the effect of all five control factors on slurry erosion rate.

For unfilled carbon-epoxy composite, the optimum factor combination for minimum solid particle erosion rate is A1 (impact velocity of 10 m/s), B4 (fiber loading of 40 wt.%), C1 (impingement angle of 30º), D2 (erodent size of 100 μm) and E1 (temperature 25ºC). Analysis of S/N plots for granite filled carbon–epoxy composites leads to conclusion that factor combination of A1 (impact velocity of 10 m/s), B4 (filler content 24 wt.%), C2 (impingement angle of 45º), D1 (erodent size of 50 μm) and E1 (temperature 25ºC) resulted in minimum erosion rate. It is clear from the Figures 6.39a and 6.39b show that factor A (impact velocity) and factor B (fiber loading/filler content) are the significant factor as S/N plot for these factors are more inclined with horizontal while factor C (impingement angle) factor D (erodent size) and factor E (temperature) have relatively less significant influence as the plot for these factors are more or less parallel with horizontal.

Table 6.12a Experimental design using L_{16} orthogonal array (unfilled carbon-epoxy composites)

Sl. No.	Impact velocity (A) (m/s)	Fiber loading (B) (%)	Impingement angle(C) (degree)	Erodent size (D) (μm)	Temperature (E) C	Erosion rate (Er) (mg/kg)	S/N ratio (db)
1	30	10	30	50	25	191.47	-45.64
2	30	20	45	100	35	182.56	-45.22
3	30	30	60	150	45	186.20	-45.39
4	30	40	75	200	55	172.00	-44.71
5	45	10	45	150	55	213.54	-46.58
6	45	20	30	200	45	205.40	-46.25
7	45	30	75	50	35	197.14	-45.89
8	45	40	60	100	25	179.12	-45.06
9	60	10	60	200	35	259.33	-48.27
10	60	20	75	150	25	247.94	-47.88
11	60	30	30	100	55	231.85	-47.30
12	60	40	45	50	45	216.75	-46.71
13	75	10	75	100	45	304.80	-49.68
14	75	20	60	50	55	289.14	-49.22
15	75	30	45	200	25	276.30	-48.82
16	75	40	30	150	35	254.12	-48.10

Table 6.12b Experimental design using L_{16} orthogonal array (granite powder filled carbon-epoxy composites)

| Sl. No.	Impact velocity (A) (m/s)	Filler content (B) (%)	Impingement angle (C) (degree)	Erodent size (D) (μm)	Temperature (E) C	Erosion rate (Er) (mg/kg)	S/N ratio (db)
1	30	0	30	50	25	205.10	-46.23
2	30	8	45	100	35	192.40	-45.68
3	30	16	60	150	45	183.92	-45.29
4	30	24	75	200	55	175.18	-44.86
5	45	0	45	150	55	225.87	-47.07
6	45	8	30	200	45	209.48	-46.42
7	45	16	75	50	35	192.84	-45.70
8	45	24	60	100	25	188.42	-45.50
9	60	0	60	200	35	270.21	-48.63
10	60	8	75	150	25	237.41	-47.51
11	60	16	30	100	55	221.52	-46.90
12	60	24	45	50	45	210.50	-46.46
13	75	0	75	100	45	272.78	-48.71
14	75	8	60	50	55	251.45	-48.00
15	75	16	45	200	25	224.80	-47.03
16	75	24	30	150	35	220.41	-46.86
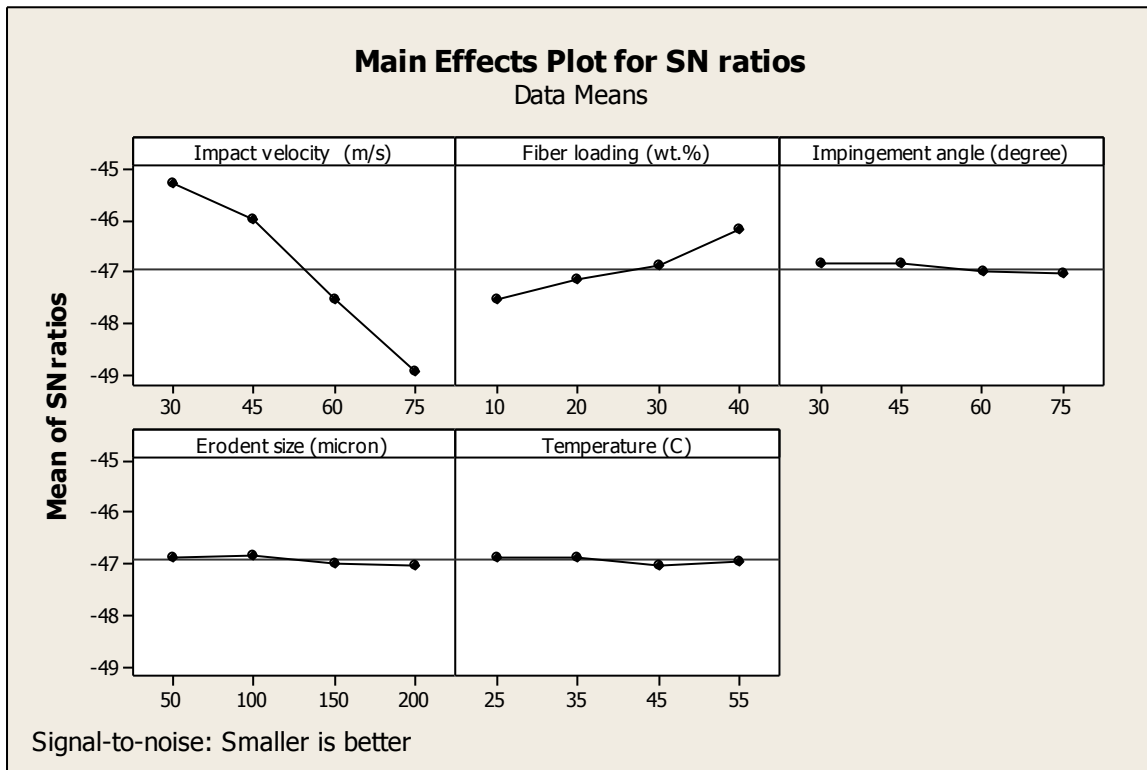
Figure 6.39a Effect of control factors on erosion rate of unfilled carbon epoxy composite
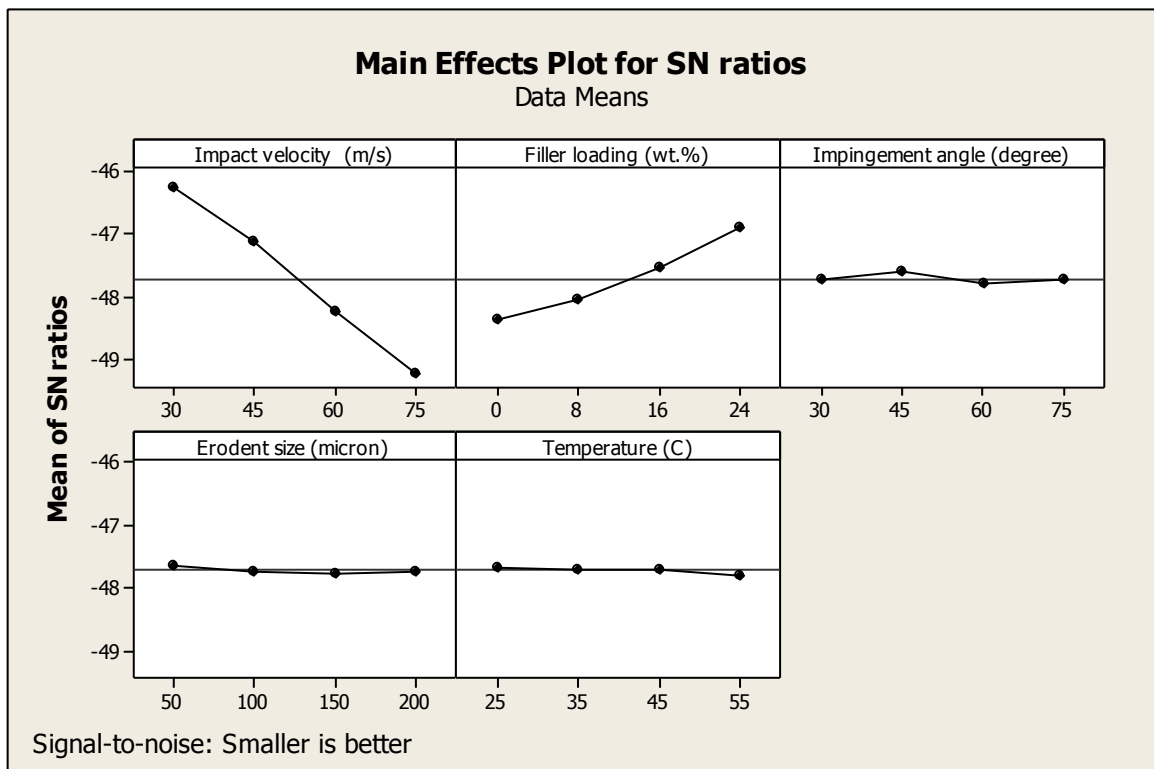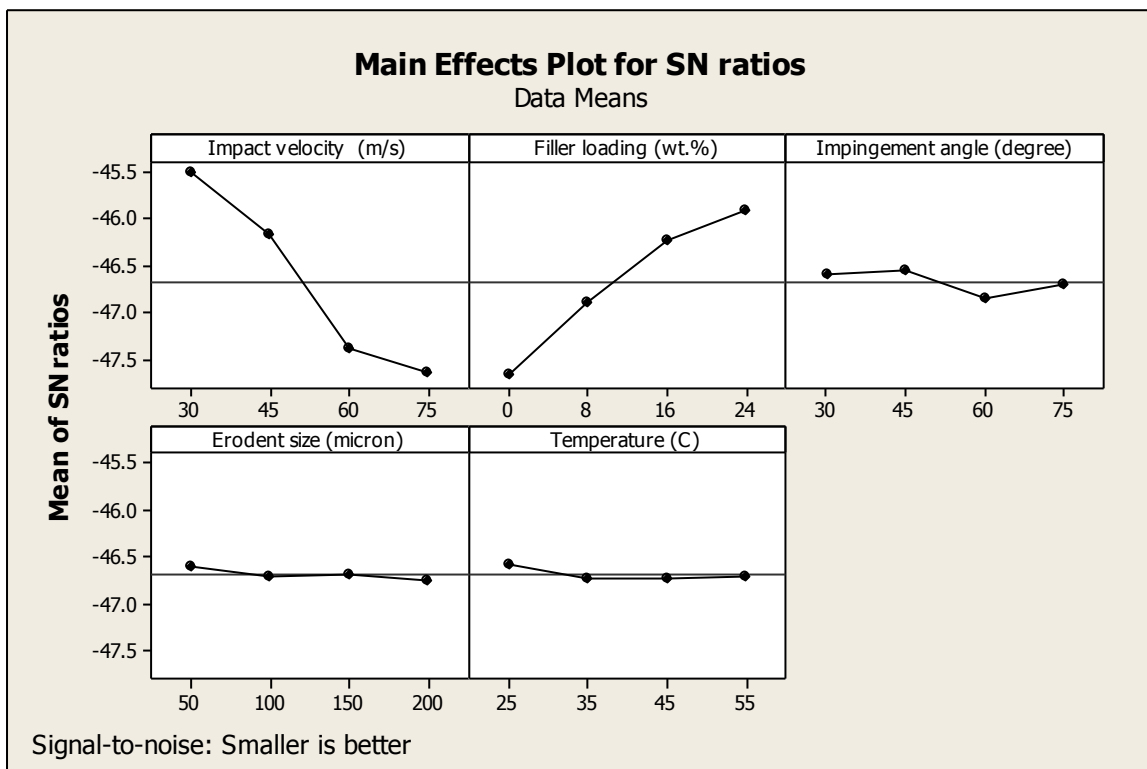

Figure 6.39b Effect of control factors on erosion rate of granite powder filled jute epoxy composite

The rank of individual control parameter can be determined from Table 6.13a and 6.13b also. Maximum value of delta is indication of maximum influence while minimum value of delta is indication of minimum influence. For unfilled carbon epoxy composites the ranking of the parameters are in the sequence of Impact velocity (Δ= 3.71), fiber loading (Δ= 1.40), impingement angle (Δ = 0.22), erodent size (Δ = 0.2) and temperature (Δ = 0.16). The ranking of control parameters for granite powder filled carbon epoxy composites are in the sequence of Impact velocity (Δ = 2.14), filler content (Δ = 1.74), impingement angle (Δ = 0.29), temperature (Δ = 0.15) and erodent size (Δ = 0.14). Similar to glass epoxy composites both the fiber loading and filler content is at second rank for unfilled and granite powder filled jute epoxy composites. Influence of filler content (Δ = 1.74) on minimizing solid particle erosion rate is more significant than fiber loading (Δ= 1.40). Influence of fiber loading in case of carbon epoxy (Δ= 1.40) composite is more significant compared to glass epoxy (Δ= 0.99) and jute epoxy (Δ= 1.04) composites.

Table 6.13a Response table for S/N ratio (unfilled carbon epoxy composite)

Level	Impact velocity	Filler loading	Impingement angle	Erodent size	Temperature
1	-45.25	-47.55	-46.82	-46.87	-46.85
2	-45.95	-47.15	-46.84	-46.82	-46.88
3	-47.55	-46.86	-46.99	-46.99	-47.01
4	-48.96	-46.15	-47.04	-47.02	-46.96
Delta	3.71	1.40	0.22	0.2	0.16
Rank	1	2	3	4	5

Table 6.13b Response table for S/N ratio (granite powder filled carbon epoxy composite)

Level	Impact velocity	Filler loading	Impingement angle	Erodent size	Temperature
1	-45.52	-47.67	-46.61	-46.60	-46.57
2	-46.18	-46.91	-46.57	-46.70	-46.72
3	-47.38	-46.24	-46.86	46.69	-46.72
4	-47.66	-45.93	-46.70	46.74	-46.72
Delta	2.14	1.74	0.29	0.14	0.15
Rank	1	2	3	5	4
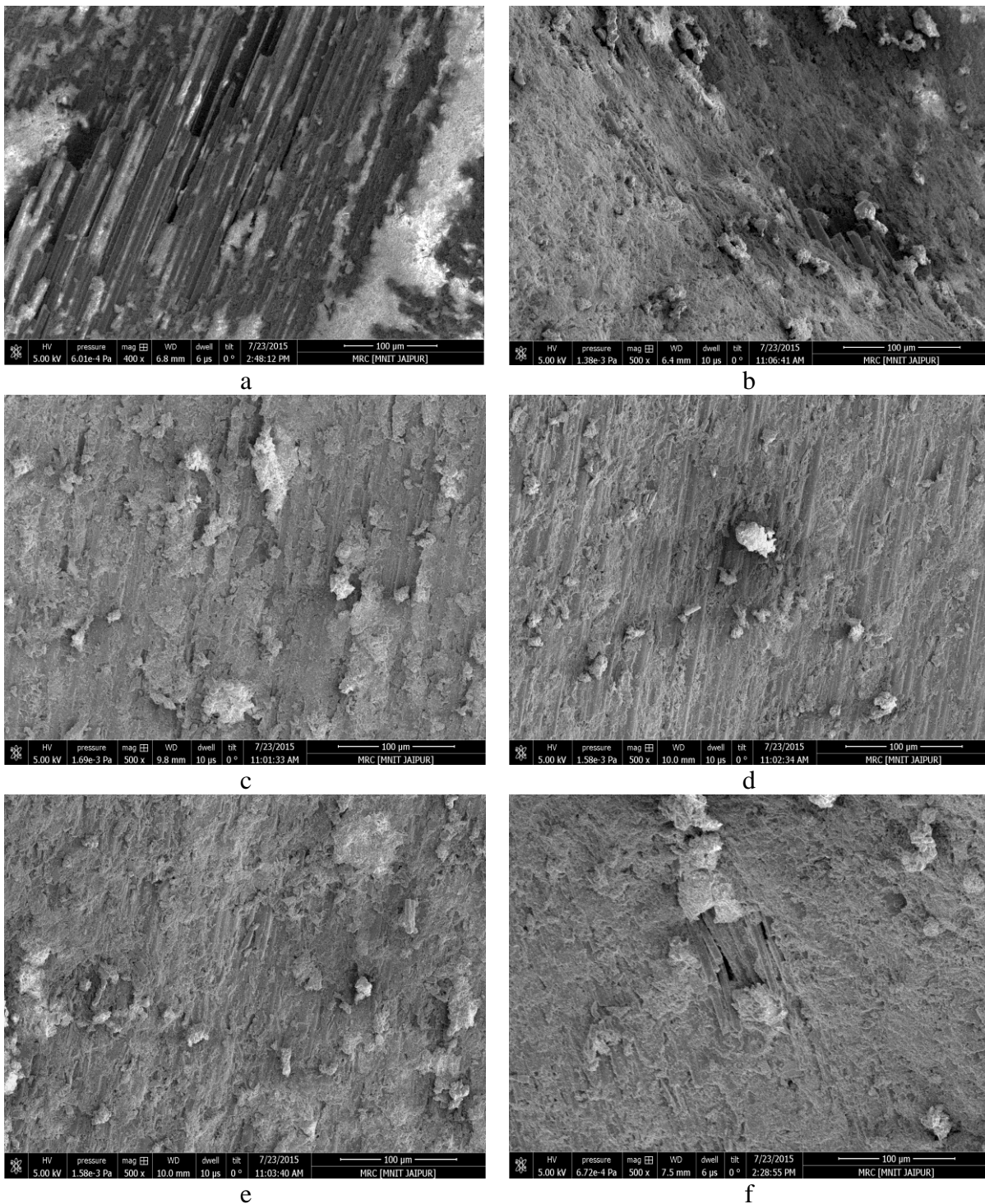
Figure 6.40 SEM micrographs for unfilled and granite powder filled carbon epoxy composite

6.18 Surface morphology

The surface morphology of unfilled and granite powder filled carbon epoxy composite specimens subjected solid particle erosion is shown in Figure 6.40 (stand of distance: 10 mm, erodent size: 150 µm, erodent discharge: 2 gm/min etc.). Unfilled 40 wt.% carbon fiber reinforced epoxy composite subjected to erodent attack at 60° angle and impact velocity of 75 m/sec shows micrograph in Figure 6.40a. Impact at higher kinetic energy resulted in

removal of matrix and complete exposure of fibers to bombardment of erodent particles. Also, fiber breakage normal to length is observed due to excessive bending force on the fiber. Severe kinetic energy of erodent particle at velocity of 75 m/sec caused few longitudinal inter-fiber cracks. Whereas, lower fiber loaded (20 wt.%) carbon epoxy composite subjected to lower impact velocity of 45 m/sec at impingement angle of 45° resulted in sliding of erodent particles and removed matrix material along with small amount of fibers as shown in Figure 6.40b.

Figure 6.40c and 6.40d depicted the micrographs of 16 wt.% granite powder filled carbon epoxy composites subjected to impact of erodent particles at impact velocity of 45 and 60 m/sec respectively at impingement angle of 45°. Both images clearly show the influence of impact velocity on solid particle erosion. Erosion is directly proportional to impact velocity which is evident from more removal of matrix material at impact velocity of 60 m/sec (see Figure 6.40d) as compared to impact velocity of 45 m/sec (see Figure 6.40c). Figure 6.40 e and 6.40f illustrated influence of impingement angle on eroded surface morphology of 16 wt.% granite powder filled carbon epoxy composites at 30° and 75° impingement angles respectively. At impingement angle of 30° maximum kinetic energy of erodent particle is utilized for abrading the surface resulting in removal of matrix material. Maximum part of component of kinetic energy along the surface is absorbed by hard granite powder. However, 75° impingement angle resulted in complete penetration of surface up to fiber layer and breakage of fibers.

Section C: Ranking of alternatives

6.19 Implementation of TOPSIS method for ranking of alternatives

Multi Criteria Decision Making (MCDM) methods are the statistical tools which help the designer or engineer to set the requisite material properties as a function and then finding the best alternative among the available materials that would fulfil the function at its best. The technique for order of preference by similarity to ideal solution (TOPSIS) is base on idea of determining alternative with minimum deviation from best alternative (positive ideal solution) and maximum deviation from worst alternative (negative ideal solution) [295]. TOPSIS is one of the fast methods used for ranking the alternatives with numerical output value for each alternative which facilitate comparison of suitability between alternatives [296].

The selected performance defining criterion (PDC) for considered alternatives is tabulated in the form of decision matrix. Initially, the values in the decision matrix are

normalized to eliminate influence of units and the weight criteria for each alternative are decided. Then, based on the benefit or cost criteria the positive and negative ideal solutions are determined (i.e. in case of strength property benefit criteria is applied where maximum value is set as positive ideal solution and minimum value is assigned as negative ideal solution. Whereas, for wear rate the cost criteria is applied where minimum value is considered as positive ideal solution and maximum value is considered as negative ideal solution). Distances of each alternative from positive ideal solution and negative ideal solution are calculated thereafter. In this thesis work, twenty four PDCs are considered (see Table 3.13) and their experimental data and its corresponding normalized values for twenty four different alternatives are mentioned in the Table 6.14 and Table 6.15 respectively. Evaluated weight for each alternative and weighted normalised matrix is illustrated in Table 6.16 and 6.17 respectively. Closeness index and ranking of different alternatives are mentioned in the Table 6.18.

All the alternatives are then arranged in descending order according to the value of their closeness index. The alternative at the top of the list is the optimum one. The ranking is given based on the descending value of closeness index.

Chapter Summary

This chapter has provided:

- ❖ The experimental results of slurry jet erosion tests and solid particle erosion tests unfilled and granite powder filled three different fiber reinforced polymer composites.

- ❖ The influence of addition of granite powder as filler material with regard to the steady state erosion (slurry jet and solid particle) performance of composites under similar test conditions.

- ❖ The analysis of the experimental results using Taguchi experimental design orthogonal array L_{16}.

- ❖ The effect of impingement angle and impact velocity on slurry jet erosion and solid particle erosion response of composites.

- ❖ The surface morphologies of eroded composites using scanning electron microscope.

- ❖ The numerical prediction of slurry jet erosion rate using computational fluid dynamics code.

- ❖ Finally, TOPSIS method is applied for sequencing the overall performance of series of composites considering physical, mechanical and erosive wear characteristics of composites.

Table 6.14 Experimental data of PDCs

PDC	PDC 1	PDC 2	PDC3	PDC 4	PDC 5	PDC 6	PDC 7	PDC 8	PDC 9	PDC 10	PDC 11	PDC 12	PDC 13	PDC 14	PDC 15	PDC 16	PDC 17	PDC 18	PDC 19	PDC 20	PDC 21	PDC 22	PDC 23	PDC 24
EG10	1.08	7.72	30	276.2	189.38	9.47	22.65	2.98	2.5	11.25	67.5	174.37	30	43.75	41.87	38.75	95.45	180.35	306.54	344.15	262.64	282.48	291.2	274.63
EG20	1.16	6.60	34	304.6	206.56	10.33	24.45	4.50	2.5	9.37	47.5	153.75	23.75	31.87	42.5	35	93.47	168.14	297.91	326.18	251.84	267.29	287.36	267.84
EG30	1.27	4.55	35	346.1	294.38	14.72	29.12	6.05	2.5	7.5	40	131.87	16.25	23.12	40	22.52	86.29	148.46	275.87	289.18	232.84	245.21	254.62	248.91
EG40	1.37	4.18	37	361.8	320.31	16.02	31.56	11.00	1.87	6.87	29.38	85.62	7.5	16.25	33.75	22.5	85.41	152.67	280.45	301.81	237.15	246.52	257.21	250.46
EG50	1.50	3.18	38	362.3	325.63	16.28	33.11	11.50	1.87	3.12	34.37	92.5	4.37	17.5	38.12	24.37	87.82	163.4	284.91	315.23	246.27	255.86	271.85	255.67
EGG8	1.41	7.26	41	367.2	327.81	16.39	32.26	11.64	1.25	6.25	26.87	66.25	6.25	15	31.87	21.87	83.65	139.53	265.3	289.64	233.5	242.14	249.81	243.34
EGG16	1.49	8.23	44	358.2	309.06	15.45	35.81	12.57	1.25	5.62	22.5	48.75	5	11.87	26.25	17.5	77.94	129.49	248.61	277.37	223.24	229.84	254.36	238.91
EGG24	1.58	9.24	47	346.9	300.31	15.02	37.2	12.21	1.25	6.25	21.25	44.37	5	10.62	23.75	15	78.24	121.81	241.9	260.41	216.54	227.7	252.29	233.47
EJ10	1.05	6.37	29	28.33	44.20	2.76	20.35	2.13	3.125	14.37	64.37	185.62	37.5	40	32.5	31.87	108.15	212.61	336.84	367.64	278.41	293.52	313.14	291.62
EJ20	1.09	4.31	30	31.71	49.60	3.10	20.98	4.20	2.5	10.62	55.62	168.75	28.12	38.12	26.25	30.25	106.54	197.54	315.61	348.47	273.51	288.84	297.15	282.15
EJ30	1.12	2.97	32	33.04	68.80	4.30	21.84	6.05	2.5	8.125	51.25	161.87	20	29.37	25.25	28.75	105.54	197.54	315.61	348.47	262.57	274.78	276.61	264.12
EJ40	1.14	3.00	35	33.72	81.80	5.11	22.65	7.79	2.5	8	39.37	100	13.87	27.5	25	23.12	94.14	161.74	286.61	317.65	257.51	266.41	274.84	260.34
EJ50	1.16	3.08	37	34.26	97.80	6.11	23.87	8.75	0.625	8.125	40.25	93.12	14.37	28.75	31.25	24.5	98.3	181.84	302.15	342.51	259.32	272.2	284.61	275.42
EJG8	1.18	4.55	38	33.13	75.20	4.83	23.27	9.18	1.25	10	33.75	68.12	8.75	25	20	22.75	92.89	153.89	278.32	305.59	254	263.51	269.15	258.25
EJG16	1.20	7.67	42	32.6	72.80	4.55	25.02	7.70	1.25	9.37	30	54.37	8.15	21.25	15	18.12	89.84	143.68	268.58	291.37	241.61	253.64	256.15	253.21
EJG24	1.24	9.69	44	32.27	66.40	4.28	25.51	8.33	1.25	6.87	12.12	40	8	16.25	12.5	8.44	88.12	137.84	261.5	275.18	239.81	249.84	257.21	248.58
EC10	1.06	7.03	29	305.26	180.63	9.03	21.51	3.83	2.5	12.625	55.12	165.25	31.5	40.75	38.125	35	98.25	169.36	294.22	315.3	242.3	254.26	251.74	244.21
EC20	1.11	6.69	31	323.21	212.18	10.61	23.63	5.55	2.5	10	38.25	133.75	20.12	30.25	39.75	33.5	92.3	155.78	282.1	296.12	238.15	252.65	247.94	241.86
EC30	1.21	2.83	36	358.14	299.38	14.97	30.46	8.90	1.87	8	28.5	102.25	14.62	15	30.75	20.5	84.9	141.26	259.6	276.84	229.54	240.3	235.21	232.85
EC40	1.27	2.66	39	375.25	356.56	17.83	32.81	12.95	1.87	6.25	21.75	73.25	6.25	13.5	25.725	21.25	83.84	131.54	249.3	268.62	221.54	232.43	229.81	224.52
EC50	1.33	2.38	40	381.84	361.88	18.09	33.2	13.40	0.625	3.125	21.5	70.325	6.25	10.25	24.75	19.625	91.91	151.62	271.2	289.14	236.47	249.62	245.24	238.51
ECG8	1.35	2.42	42	379.2	360.94	18.05	33.47	14.91	1.87	6.25	19.25	60.625	5	9.75	21.5	18.625	80.15	122.3	231.82	252.41	213.5	219.65	237.41	213.54
ECG16	1.40	4.20	46	374.41	343.44	17.17	34.2	16.19	1.25	5.625	16.325	46.25	5	9	17.5	15	78.16	114.52	219.58	245.69	207.3	211.41	225.4	209.62
ECG24	1.46	6.34	47	368.28	325.31	16.27	34.91	14.31	1.25	5.625	16	44	3.125	8.5	17	14.5	75.81	111.27	213.84	229.81	204.51	206.65	222.42	204.15

Table 6.15 Normalised Decision matrix

PDC	PDC 1	PDC 2	PDC3	PDC 4	PDC 5	PDC 6	PDC 7	PDC 8	PDC 9	PDC 10	PDC 11	PDC 12	PDC 13	PDC 14	PDC 15	PDC 16	PDC 17	PDC 18	PDC 19	PDC 20	PDC 21	PDC 22	PDC 23	PDC 24
EG10	0.036	0.061	0.033	0.047	0.036	0.035	0.034	0.014	0.057	0.059	0.081	0.074	0.091	0.082	0.061	0.069	0.044	0.049	0.047	0.048	0.046	0.047	0.047	0.046
EG20	0.038	0.052	0.038	0.052	0.039	0.038	0.036	0.021	0.057	0.050	0.057	0.065	0.072	0.060	0.062	0.062	0.043	0.046	0.045	0.045	0.044	0.044	0.046	0.045
EG30	0.042	0.036	0.039	0.059	0.056	0.054	0.043	0.028	0.057	0.040	0.048	0.056	0.049	0.043	0.059	0.040	0.040	0.040	0.042	0.040	0.040	0.041	0.041	0.042
EG40	0.045	0.033	0.041	0.062	0.061	0.059	0.047	0.051	0.043	0.036	0.035	0.036	0.023	0.030	0.050	0.040	0.040	0.041	0.043	0.042	0.041	0.041	0.041	0.042
EG50	0.049	0.025	0.042	0.062	0.062	0.060	0.049	0.053	0.043	0.016	0.041	0.039	0.013	0.033	0.056	0.043	0.041	0.044	0.043	0.044	0.043	0.042	0.044	0.043
EGG8	0.047	0.057	0.045	0.063	0.062	0.061	0.048	0.054	0.029	0.033	0.032	0.028	0.019	0.028	0.047	0.039	0.039	0.038	0.040	0.040	0.041	0.040	0.040	0.041
EGG16	0.049	0.065	0.049	0.061	0.059	0.057	0.053	0.058	0.029	0.030	0.027	0.021	0.015	0.022	0.039	0.031	0.036	0.035	0.038	0.039	0.039	0.038	0.041	0.040
EGG24	0.052	0.073	0.052	0.059	0.057	0.055	0.055	0.056	0.029	0.033	0.026	0.019	0.015	0.020	0.035	0.027	0.036	0.033	0.037	0.036	0.038	0.038	0.040	0.039
EJ10	0.035	0.050	0.032	0.005	0.008	0.010	0.030	0.010	0.071	0.076	0.077	0.078	0.114	0.075	0.048	0.057	0.050	0.058	0.051	0.051	0.048	0.049	0.050	0.049
EJ20	0.036	0.034	0.033	0.005	0.009	0.011	0.031	0.019	0.057	0.056	0.067	0.071	0.086	0.071	0.039	0.054	0.049	0.054	0.048	0.049	0.047	0.048	0.048	0.047
EJ30	0.037	0.023	0.035	0.006	0.013	0.016	0.032	0.028	0.057	0.043	0.062	0.068	0.061	0.055	0.037	0.051	0.049	0.054	0.048	0.049	0.046	0.046	0.044	0.044
EJ40	0.038	0.024	0.039	0.006	0.016	0.019	0.034	0.036	0.057	0.042	0.047	0.042	0.042	0.052	0.037	0.041	0.044	0.044	0.044	0.044	0.045	0.044	0.044	0.044
EJ50	0.038	0.024	0.041	0.006	0.019	0.023	0.035	0.040	0.014	0.043	0.048	0.039	0.044	0.054	0.046	0.043	0.046	0.049	0.046	0.048	0.045	0.045	0.046	0.046
EJG8	0.039	0.036	0.042	0.006	0.014	0.018	0.035	0.042	0.029	0.053	0.041	0.029	0.027	0.047	0.029	0.040	0.043	0.042	0.042	0.043	0.044	0.044	0.043	0.043
EJG16	0.040	0.060	0.047	0.006	0.014	0.017	0.037	0.036	0.029	0.050	0.036	0.023	0.025	0.040	0.022	0.032	0.042	0.039	0.041	0.041	0.042	0.042	0.041	0.043
EJG24	0.041	0.076	0.049	0.006	0.013	0.016	0.038	0.038	0.029	0.036	0.015	0.017	0.024	0.030	0.018	0.015	0.041	0.037	0.040	0.038	0.042	0.041	0.041	0.042
EC10	0.035	0.055	0.032	0.052	0.034	0.033	0.032	0.018	0.057	0.067	0.066	0.070	0.096	0.076	0.056	0.062	0.046	0.046	0.045	0.044	0.042	0.042	0.040	0.041
EC20	0.037	0.053	0.034	0.055	0.040	0.039	0.035	0.026	0.057	0.053	0.046	0.057	0.061	0.057	0.058	0.059	0.043	0.042	0.043	0.041	0.041	0.042	0.040	0.041
EC30	0.040	0.022	0.040	0.061	0.057	0.055	0.045	0.041	0.043	0.042	0.034	0.043	0.044	0.028	0.045	0.036	0.039	0.038	0.039	0.039	0.040	0.040	0.038	0.039
EC40	0.042	0.021	0.043	0.064	0.068	0.066	0.049	0.060	0.043	0.033	0.026	0.031	0.019	0.025	0.038	0.038	0.039	0.036	0.038	0.037	0.038	0.039	0.037	0.038
EC50	0.044	0.019	0.044	0.065	0.069	0.067	0.049	0.062	0.014	0.017	0.026	0.030	0.019	0.019	0.036	0.035	0.043	0.041	0.041	0.040	0.041	0.041	0.039	0.040
ECG8	0.045	0.019	0.047	0.065	0.068	0.067	0.050	0.069	0.043	0.033	0.023	0.026	0.015	0.018	0.032	0.033	0.037	0.033	0.035	0.035	0.037	0.036	0.038	0.036
ECG16	0.046	0.033	0.051	0.064	0.065	0.063	0.051	0.075	0.029	0.030	0.020	0.020	0.015	0.017	0.026	0.027	0.036	0.031	0.033	0.034	0.036	0.035	0.036	0.035
ECG24	0.048	0.050	0.052	0.063	0.062	0.060	0.052	0.066	0.029	0.030	0.019	0.019	0.010	0.016	0.025	0.026	0.035	0.030	0.032	0.032	0.035	0.034	0.036	0.034

Table 6.16 Evaluation of criteria weights by entropy method

PDC	Entropy, E_j	Weight, W_j
1	0.996731	0.006093
2	0.970355	0.055256
3	0.9955	0.008387
4	0.917749	0.153310
5	0.947386	0.098070
6	0.957267	0.079651
7	0.993121	0.012822
8	0.966428	0.062575
9	0.976337	0.044106
10	0.980907	0.035589
11	0.969083	0.057628
12	0.963336	0.068340
13	0.923223	0.143106
14	0.961693	0.071403
15	0.984083	0.029669
16	0.983123	0.031457
17	0.997463	0.004729
18	0.994471	0.010306
19	0.9971	0.005405
20	0.996859	0.005855
21	0.997974	0.003776
22	0.997752	0.004190
23	0.997803	0.004094
24	0.997795	0.004110

Table 6.17 Weighted normalized decision matrix

PDC	PDC 1	PDC 2	PDC3	PDC 4	PDC 5	PDC 6	PDC 7	PDC 8	PDC 9	PDC 10	PDC 11	PDC 12	PDC 13	PDC 14	PDC 15	PDC 16	PDC 17	PDC 18	PDC 19	PDC 20	PDC 21	PDC 22	PDC 23	PDC 24
EG10	0.0011	0.0151	0.0014	0.0301	0.0015	0.0123	0.0021	0.0039	0.0116	0.0098	0.0209	0.0223	0.0519	0.0258	0.0086	0.0101	0.0010	0.0024	0.0012	0.0014	0.0008	0.0010	0.0009	0.0009
EG20	0.0011	0.0129	0.0015	0.0332	0.0017	0.0134	0.0022	0.0058	0.0116	0.0082	0.0147	0.0196	0.0411	0.0188	0.0087	0.0091	0.0010	0.0023	0.0012	0.0013	0.0008	0.0009	0.0009	0.0009
EG30	0.0012	0.0089	0.0016	0.0378	0.0024	0.0191	0.0027	0.0078	0.0116	0.0065	0.0124	0.0168	0.0281	0.0136	0.0082	0.0059	0.0009	0.0020	0.0011	0.0011	0.0007	0.0008	0.0008	0.0008
EG40	0.0013	0.0082	0.0017	0.0395	0.0026	0.0208	0.0029	0.0143	0.0087	0.0060	0.0091	0.0109	0.0130	0.0096	0.0069	0.0059	0.0009	0.0021	0.0011	0.0012	0.0008	0.0008	0.0008	0.0008
EG50	0.0015	0.0062	0.0017	0.0395	0.0026	0.0211	0.0030	0.0149	0.0087	0.0027	0.0107	0.0118	0.0076	0.0103	0.0078	0.0064	0.0009	0.0022	0.0011	0.0013	0.0008	0.0009	0.0009	0.0009
EGG8	0.0014	0.0142	0.0018	0.0401	0.0026	0.0212	0.0030	0.0151	0.0058	0.0055	0.0083	0.0085	0.0108	0.0088	0.0065	0.0057	0.0009	0.0019	0.0011	0.0012	0.0007	0.0008	0.0008	0.0008
EGG16	0.0015	0.0161	0.0020	0.0391	0.0025	0.0200	0.0033	0.0163	0.0058	0.0049	0.0070	0.0062	0.0086	0.0070	0.0054	0.0046	0.0008	0.0017	0.0010	0.0011	0.0007	0.0008	0.0008	0.0008
EGG24	0.0016	0.0181	0.0021	0.0378	0.0024	0.0195	0.0034	0.0158	0.0058	0.0055	0.0066	0.0057	0.0086	0.0063	0.0049	0.0039	0.0008	0.0016	0.0010	0.0010	0.0007	0.0008	0.0008	0.0008
EJ10	0.0010	0.0125	0.0013	0.0031	0.0004	0.0036	0.0019	0.0028	0.0145	0.0125	0.0200	0.0237	0.0649	0.0236	0.0066	0.0083	0.0012	0.0029	0.0013	0.0015	0.0009	0.0010	0.0010	0.0010
EJ20	0.0011	0.0084	0.0014	0.0035	0.0004	0.0040	0.0019	0.0054	0.0116	0.0093	0.0173	0.0215	0.0486	0.0225	0.0054	0.0079	0.0011	0.0027	0.0013	0.0014	0.0009	0.0010	0.0010	0.0010
EJ30	0.0011	0.0058	0.0014	0.0036	0.0006	0.0056	0.0020	0.0078	0.0116	0.0071	0.0159	0.0207	0.0346	0.0173	0.0052	0.0075	0.0011	0.0027	0.0013	0.0014	0.0008	0.0009	0.0009	0.0009
EJ40	0.0011	0.0059	0.0016	0.0037	0.0007	0.0066	0.0021	0.0101	0.0116	0.0070	0.0122	0.0128	0.0240	0.0162	0.0051	0.0060	0.0010	0.0022	0.0011	0.0013	0.0008	0.0009	0.0009	0.0009
EJ50	0.0011	0.0060	0.0017	0.0037	0.0008	0.0079	0.0022	0.0113	0.0029	0.0071	0.0125	0.0119	0.0249	0.0169	0.0064	0.0064	0.0011	0.0025	0.0012	0.0014	0.0008	0.0009	0.0009	0.0009
EJG8	0.0012	0.0089	0.0017	0.0036	0.0006	0.0063	0.0021	0.0119	0.0058	0.0087	0.0105	0.0087	0.0151	0.0147	0.0041	0.0059	0.0010	0.0021	0.0011	0.0012	0.0008	0.0009	0.0009	0.0009
EJG16	0.0012	0.0150	0.0019	0.0036	0.0006	0.0059	0.0023	0.0100	0.0058	0.0082	0.0093	0.0069	0.0141	0.0125	0.0031	0.0047	0.0010	0.0019	0.0011	0.0012	0.0008	0.0009	0.0008	0.0009
EJG24	0.0012	0.0190	0.0020	0.0035	0.0005	0.0055	0.0023	0.0108	0.0058	0.0060	0.0038	0.0051	0.0138	0.0096	0.0026	0.0022	0.0009	0.0019	0.0010	0.0011	0.0008	0.0008	0.0008	0.0008
EC10	0.0010	0.0138	0.0013	0.0333	0.0015	0.0117	0.0020	0.0050	0.0116	0.0110	0.0171	0.0211	0.0545	0.0240	0.0078	0.0091	0.0011	0.0023	0.0012	0.0013	0.0008	0.0009	0.0008	0.0008
EC20	0.0011	0.0131	0.0014	0.0353	0.0017	0.0137	0.0022	0.0072	0.0116	0.0087	0.0119	0.0171	0.0348	0.0178	0.0081	0.0087	0.0010	0.0021	0.0011	0.0012	0.0008	0.0009	0.0008	0.0008
EC30	0.0012	0.0055	0.0016	0.0391	0.0024	0.0194	0.0028	0.0115	0.0087	0.0070	0.0088	0.0130	0.0253	0.0088	0.0063	0.0053	0.0009	0.0019	0.0010	0.0011	0.0007	0.0008	0.0008	0.0008
EC40	0.0012	0.0052	0.0018	0.0409	0.0029	0.0231	0.0030	0.0168	0.0087	0.0055	0.0067	0.0093	0.0108	0.0080	0.0053	0.0055	0.0009	0.0018	0.0010	0.0011	0.0007	0.0008	0.0007	0.0008
EC50	0.0013	0.0047	0.0018	0.0417	0.0029	0.0234	0.0030	0.0174	0.0029	0.0027	0.0067	0.0090	0.0108	0.0060	0.0051	0.0051	0.0010	0.0020	0.0011	0.0011	0.0008	0.0008	0.0008	0.0008
ECG8	0.0013	0.0047	0.0019	0.0414	0.0029	0.0234	0.0031	0.0193	0.0087	0.0055	0.0060	0.0077	0.0086	0.0057	0.0044	0.0049	0.0009	0.0017	0.0009	0.0010	0.0007	0.0007	0.0008	0.0007
ECG16	0.0014	0.0082	0.0021	0.0408	0.0028	0.0223	0.0031	0.0210	0.0058	0.0049	0.0051	0.0059	0.0086	0.0053	0.0036	0.0039	0.0008	0.0015	0.0009	0.0010	0.0007	0.0007	0.0007	0.0007
ECG24	0.0014	0.0124	0.0021	0.0402	0.0026	0.0211	0.0032	0.0185	0.0058	0.0049	0.0050	0.0056	0.0054	0.0050	0.0035	0.0038	0.0008	0.0015	0.0009	0.0009	0.0007	0.0007	0.0007	0.0007

Table 6.18 Closeness index and ranking of the alternatives

Composite designation	D_i^+	D_i^-	CI	Ranking
EG10	0.1091626	0.03179214	0.225548542	22
EG20	0.0966414	0.0418468	0.302168764	19
EG30	0.0694491	0.05706239	0.451045091	14
EG40	0.0627894	0.07231674	0.535258643	11
EG50	0.0662782	0.07659408	0.536101762	10
EGG8	0.0612036	0.07490561	0.55033445	9
EGG16	0.0508151	0.07716338	0.602940079	5
EGG24	0.0446183	0.07675821	0.632397552	3
EJ10	0.1146077	0.00746077	0.061119535	24
EJ20	0.1026922	0.02112454	0.170611405	23
EJ30	0.0935054	0.03582809	0.27702088	20
EJ40	0.079901	0.04756939	0.373180018	16
EJ50	0.0815348	0.04831261	0.372072195	17
EJG8	0.076668	0.05702399	0.426532657	15
EJG16	0.0687357	0.05830417	0.458943789	13
EJG24	0.0469212	0.0616143	0.567687854	8
EC10	0.1041984	0.03401945	0.24612922	21
EC20	0.091204	0.04810074	0.345291363	18
EC30	0.061846	0.06335523	0.50602737	12
EC40	0.0589398	0.077283	0.567327769	7
EC50	0.0546977	0.07943321	0.592206387	6
ECG8	0.0522223	0.08071525	0.607166764	4
ECG16	0.0418712	0.08110635	0.659521687	2
ECG24	0.0408744	0.08206109	0.667513601	1

The next chapter presents the summary of research findings and specific conclusions drawn from this investigation along with scope for future work.

<div align="center">*****</div>

<div align="right">

Chapter 7

SUMMARY AND CONCLUSIONS

</div>

The work reported in this thesis is a comparative experimental study on reinforcement of three different fibers in polymer composites with varying fiber loading identically. Also, effect of addition of granite powder as filler material on physical, mechanical, thermal and erosive wear characteristics of fiber reinforced polymer composites is reported. An attempt is made to predict the value of stress intensity factor and thermal conductivity of composites under this investigation using analysis software. Computational fluid dynamics approach is applied to validate the slurry jet erosion behavior of unfilled and granite powder filled fiber reinforced polymer composites. Taguchi design of experiment method is implemented to determine the significance of different control parameters on erosive wear characteristics of series of fiber reinforced polymer composites. Finally, based on the physical, mechanical and erosive were characteristics of composites are studied in present work, ranking has been done using MCDM technique TOPSIS to obtain best combination of material characteristics.

7.1 Summary of research findings

The world's growing appetite for wind energy is transforming wind blades into one of the hottest composite applications around. The huge build-up of wind-power generating capacity, particularly in the U.S, China, and Spain has raised a bumper crop of new plants for manufacturing these composite parts. The material used for wind turbine blade is decided based on the size and capacity of wind mill. Use of timber, polymer composites reinforced with natural fibers (bamboo, jute etc) is preferred for material of turbine blade of micro and mini wind mills. However, for large turbine blades high strength fiber (glass/carbon) reinforced polymer composites is used. It necessary to study mechanical performance of the material potentially developed specifically for wind turbine blade. Also, study related to effect of simultaneous thermal and mechanical stresses is suggested. There is need of improving the fracture toughness of polymer composite material with minimum penalties on other properties. Being structural component wind turbine blade material is subjected to continuous attack of sand along with either air or rain water. Hence, erosive wear performance assessment of potential material for wind turbine blade is decisive. The mechanical performance of unfilled fiber reinforced epoxy composites is observed to more or less linearly improve all the three types of fibers used in this investigation. This may be attributed to higher modulus of fiber compared to neat epoxy. Unfilled jute fiber reinforced epoxy composites show inferior mechanical performance compare to other two series of

composites reinforced with glass and carbon fibers. This result is obvious as mechanical properties of jute fibers are much lower compared to other synthetic fibers used in this study. Comparing the mechanical performance of unfilled synthetic fiber reinforced epoxy composites; the carbon epoxy composites are marginally superior to the glass epoxy composites. Surprisingly fracture toughness value of all the three series of unfilled fiber epoxy composites is comparable to each other.

Addition of granite powder in fiber reinforced epoxy composites by keeping fiber loading 40 wt.% constant resulted in improvement of properties such as: hardness, impact strength and fracture toughness respectively. However, the mechanical properties like tensile strength, flexural strength and inter-laminar shear strength are improved with the addition of 8 wt.% granite powder. Further, with the increasing in granite powder content beyond 8 wt.% the mentioned properties showed marginal decline in performance. The thermo-mechanical performance of unfilled and granite powder filled fiber (glass/jute/carbon) reinforced epoxy composite is compared with mechanical performance of corresponding composites at room temperature. Dynamic mechanical analysis is illustrated three distinct stages of behaviour when the composite subjected to simultaneous thermal and cyclic mechanical stresses. First stage (approximately below 50ºC) is indicated by stiff behaviour where elastic performance is higher and viscous performance is very low. This may be due to strong cross linking structure of epoxy over filler and/or fiber material. With the increase in temperature the cyclic stress applied cause start of mobility in cross linking structure in the second stage. This resulted in decrease in stiffness and increase in viscous response (ability to absorb energy in internal motion) of the composite.

Thermo-gravimetric analysis (TGA) indicated thermal degradation temperature of synthetic fiber reinforced epoxy composite is marginally higher as compared to natural fiber reinforced epoxy composite in this investigation. The residue content remaining after complete degradation of composite material is found higher for composite reinforced with glass and carbon fiber. This is due to high thermal stability of glass and carbon fiber above temperature used for TGA study. It is obvious to found more residue content for granite powder filled fiber epoxy composite than corresponding unfilled composite. The thermal conductivity of unfilled fiber reinforced composite is increased with reinforcement of glass and carbon fiber. However, the thermal conductivity for unfilled jute epoxy composites is decreased with the increase in fiber loading. The thermal conductivity of granite powder filled fiber reinforced epoxy composites is increased. The experimental values as obtained for thermal conductivity are in close agreement with predicted values.

The erosive wear performance of unfilled fiber reinforced epoxy composite is improved up to reinforcement of 30 to 40 wt.% fiber and beyond this performance is declining. This decline in erosive wear performance is due to improper wetting of fiber at higher fiber loading. Addition of granite powder has positive hybridizing effect on the slurry erosion and solid particle erosion response of composites irrespective to type of fiber reinforcement. The peak slurry erosion rate and solid particle rate in case of unfilled fiber epoxy composites are corresponds to 60º impingement angle. This shows semi-ductile behavior of composites. However, in few cases the peak erosion rate of granite powder filled fiber epoxy composites shifts to 75º impingement angle which show loss of ductility. Taguchi approach depicted the most influencing control parameter on both the erosion performance is impact velocity. The fiber or filler content is the second most influencing parameter with very few exceptions.

7.2 Conclusions

On the basis of work carried out in this study the following conclusions have been reported in this thesis as,

1. Addition of treated jute fiber has enhanced both tensile and flexural properties of the composites. The 40 wt.% jute epoxy composite has tensile strength and tensile modulus of 33.72 MPa and 1228.48 MPa respectively as compared to 28.33 MPa and 624.65 MPa for 10 wt.% jute epoxy composite. Whereas, the flexural strength and flexural modulus are improved to 81.8 MPa and 1258.37 MPa as compared to 44.2 MPa and 736 MPa for 10 wt.% jute epoxy composite. The incorporation of granite powder in the treated jute epoxy composites has marginal inferior effect on tensile and flexural properties of jute epoxy composites.

2. Impact strength and hardness of composites are shown effective potential with reinforcement of jute fiber as well as granite powder in the matrix material. The 24 wt.% of granite powder filled jute epoxy composite has 51% and 25% improvement in hardness and impact strength respectively in comparison with 10 wt.% jute epoxy composite.

3. The fracture toughness of the fiber reinforced epoxy composites is increased with the increase in jute fiber loading from 10 wt.% to 50 wt.% respectively. For the a/W ratio of 0.5, the K_{IC} increased to 4.19 MPa.m$^{1/2}$, 6.94 MPa.m$^{1/2}$, 7.79 MPa.m$^{1/2}$ and 8.74 MPa.m$^{1/2}$ for reinforcement of 20, 30, 40 and 50 wt.% of jute fiber respectively as compared to 2.13 MPa.m$^{1/2}$ for reinforcement of 10 wt.% jute fiber. It is evident that the value of K_{IC} increased for low filler loading (0 − 8 wt.%). For higher weight fraction of granite powder

reinforcement (more than 8 wt.%), a decreasing in trend is observed but the values are at higher side as compared to virgin composite.

4. Storage modulus has 88% and 11% improvement for 30 wt.% jute fiber reinforced and 16 wt.% granite powder filled jute epoxy composite as compared to 10 wt.% jute fiber reinforced and 0 wt.% granite powder reinforced jute epoxy composites respectively. The T_g obtained from loss modulus curve is less than T_g obtained from damping factor curve. Cole-Cole plot shows highest degree of homogeneity for 30 wt.% jute epoxy and 8 wt.% granite powder filled composites. Finally, the Cole–Cole diagram showed imperfect semi-circles, which is characteristic of heterogeneous system for particulate filled jute fiber reinforced epoxy composites.

5. Results depicted that both the tensile and flexural properties are significantly improved up to 40 wt.% glass fiber loading and beyond that improvement is insignificant. The tensile and flexural strength at 40 wt.% of glass fiber loading is 361.8 MPa and 320.31 MPa respectively. However, addition of 24 wt.% granite powder marginally reduces the values to 346.9 MPa and 300.31 MPa respectively.

6. Highest improvement in experimental value of stress intensity factor is observed for composite with 16 wt.% granite powder at all the a/W ratios. Whereas, the numerical results for fracture toughness is underestimated as compared to experimental results due to deficiency in modeling to find toughening of composite due to presence of reinforcement.

7. The storage modulus (E′) of the unfilled and granite powder filled glass epoxy composite at 30ºC is comparable with the flexural modulus. The minimum difference of 0.17 GPa in storage and flexural modulus is observed for unfilled 20 wt.% glass epoxy composite whereas, maximum difference of 0.71 GPa is recorded for unfilled 50 wt % glass epoxy composite. The measured thermal conductivity for unfilled 50 wt.% glass fiber reinforced epoxy composite and 24 wt.% granite powder filled glass epoxy composite are 0.523W/mK and 0.886 W/mK respectively.

8. The tensile strength, flexural strength and ILSS are significantly improved with the increase in carbon fiber loading whereas; properties are marginally decreased with increase in granite powder content. However, the impact strength of composite is show increasing trend for both the type of reinforcement (i.e. fiber and granite powder).

9. Experimental value of K_{IC} for unfilled composites is improved significantly with increase in carbon fiber loading because of extrinsic toughening mechanism. The significant improvement in experimental value of K_{IC} for addition of 8 and 16 wt.% of granite powder

is reported because of intrinsic toughening mechanism. Minimum variation for value of K_{IC} by experimental and numerical method is recorded as 0.23 MPa.m$^{1/2}$ for unfilled 10 wt.% carbon epoxy composite for a/W ratio of 0.1. Whereas, maximum variation of 5.43 MPa.m$^{1/2}$ is recorded for 16 wt.% granite powder filled carbon epoxy composite at a/W ratio of 0.5.

10. The storage modulus at 30°C of composite is comparable with the flexural modulus of the same composite. Highest closeness for storage modulus and flexural modulus of 0.17 GPa is observed for unfilled 10 wt.% carbon fiber epoxy composite and lowest closeness of 0.86 GPa is observed for 16 wt.% granite powder filled carbon epoxy composite. Both unfilled and filled composite are thermally stable below 300°C temperature and above 350°C rapid thermal degradation started.

11. A successful attempt is made for mechanical analysis of full scale model of wind turbine blade using Finite Element code (ANSYS R 14.5). The deflection predicted using numerical method is in agreement with past studies.

12. In case of unfilled jute epoxy composites the maximum slurry erosion rate is observed at 60° impingement angle as compared to other angles. This shows semi-ductile behavior of composites. However, with the incorporation of granite powder in the jute epoxy composites the maximum erosion rate is observed in 60° impingement angle only but slurry erosion rate reduced to 32% between 0 to 8wt. % granite powder filled jute epoxy composites. Similarly, reduction in slurry erosion rate is 20% between 8 to 16wt. % granite powder filled and 25% reduction in slurry erosion rate between 16 to 24wt. % granite powder filled respectively.

13. Granite powder filled glass epoxy composites possess comparatively good potential for application like engineering structures in dusty environment in deserts subjected to erosive environment. The content of granite powder is to be decided sensibly keeping the strength and wear attack in mind. These composites, in general may also be strongly recommended for applications like wind turbine blades, pipe lines carrying water, light weight vehicles structures, etc.

14. The peak slurry erosion rate for unfilled composite with 10 and 20 wt.% glass fiber is at 60° impingement angle whereas, for further addition of glass fiber to 30, 40 and 50 wt.% show peak erosion at 75° impingement angle . However, for all granite powder filled glass epoxy composites show peak erosion at 75° impingement angle. This show transition of composite failure from semi-ductile towards brittle failure with inclusion of reinforcement.

15. Slurry erosion rate at 40 m/s is reduced from 174.37 mg/kg to 153.75 mg/kg (i.e. 11%) for increase of glass fiber reinforcement from 10 m/s to 20 m/s. Further at 30 m/s erosion rate is reduced to 131.87 mg/kg (i.e reduced by 14%). Highest reduction from 131.87 to 85.62 mg/kg (i.e. 35%) is observed for increase in glass fiber loading from 30 wt.% to 40 wt.%. However, at higher velocity of 40 m/s the reduction in erosion rate for 8 wt.% granite powder filled glass epoxy composite is reduced from 85.62 mg/kg to 66.25 mg/kg (i.e. 22%). Addition of 16 wt.% granite powder further reduced the erosion rate to 48.75 mg/kg (i.e. 26%). Further addition of 24 wt.% granite powder reduced erosion rate marginally to 44.37 mg/kg (i.e. 8%).

16. The experimentally obtained slurry erosion rate is validated with the one obtained with CFD code. Simulation results and experimental results are in good agreement as far as trend of slurry erosion rate is concerned. Both the experimental as well as simulation results shows semi-ductile behaviour of composite material when subjected to high velocity impact of jet containing water and sand particles. Solid particle erosion behaviour also illustrates peak erosion rate at 60° to 75° impingement angle which confirms semi-ductile behaviour of composites.

17. For same wt.% of reinforcement/filler content carbon epoxy composite show better solid particle erosion performance. Subsequently, glass epoxy composite show inferior performance than carbon epoxy composite. Jute epoxy composite illustrated highest solid particle erosion rate for same wt.% of reinforcement/filler content.

18. The ranking obtained from implementation of TOPSIS method iss: ECG24 (Rank 1) > ECG16 (Rank 2) > EGG24 (Rank 3) >>……>> EJG24 (Rank 8) >>…… >> EJ10 (Rank 24).

7.3 Scope for future work

❖ There is need to feasibility of utilization of other stone waste powder in modifying properties of fiber reinforced polymer composites.

❖ In the present work, unfilled and particulate filled fiber reinforced polymer composites are fabricated by conventional hand lay-up technique. The other technique like vacuum assisted resin transfer moulding, vacuum bagging method etc could be possible.

❖ There is need of fabrication and testing of actual wind turbine blade for actual operating conditions.

❖ Cost analysis of these composites is required to assess their economic viability in industrial applications.

****

REFERENCES

[1]   N. Zhang, F. Yang, D. Guerra, C. Shen, J. Castro, J.L. Lee, Enhancing particle erosion resistance of glass-reinforced polymeric composites using carbon nanofiber-based nanopaper coatings, Journal of Applied Polymer Science, 129 (2013) 1875-1881.

[2]   K. Wood: Blade repair: Closing the maintenance gap. Composites Technology, 1 April 2011 (http://www.compositesworld.com/articles/blade-repair-closing-the-maintenance-gap)

[3]   A. Peacock, D.P. Jenkins, M. Ahadzi, A. Berry, S. Turan, Micro wind turbines in the UK domestic sector, Energy and Buildings 40 (2008) 1324–1333.

[4]   C. Jadranka, E.T. Horst, K. Syngellakis, M. Niel, P. Clement, R. Heppener, E.P. Pierano, Urban Wind Turbines: Guidelines for Small Wind Turbines in the Built Environment, Intelligent Energy Europe.
        http://www.urbanwind.net/pdf/SMALL_WIND_TURBINES_GUIDE_final.pdf.

[5]   N.M. Barkoula, J. Karger-Kocsis, Solid particle erosion of unidirectional GF reinforced EP composites with different fiber/matrix adhesion, Journal of Reinforced Plastics and Composites 21 (2002) 1377–1388.

[6]   K.V. Pool, C.K.H. Dharan, I. Finnie, Erosive wear of composite-materials, Wear 107 (1986) 1– 12.

[7]   A.P. Harsha, S.K. Jha, Erosive wear studies of epoxy-based composites at normal incidence, Wear 265 (2008)1129–1135.

[8]   A. Patnaik, A. Satapathy, N. Chand, N.M. Barkoula, S. Biswas, Solid particle erosion wear characteristics of fiber and particulate filled polymer composites: A review, Wear 268 (2010) 249–263.

[9]   Y. Fouad, M. El-Meniawi, A. Afifi, Erosion behaviour of epoxy based unidirectional (GFRP) composite materials, Alexandria Engineering Journal 50 (2011) 29-34.

[10]   R. Rattan, J. Bijwe, Influence of impingement angle on solid particle erosion of carbon fabric reinforced polyetherimide composite, Wear 262 (2007) 568–574.

[11]   S.S. Mahapatra, A. Patnaik, Study on mechanical and erosion wear behavior of hybrid composites using Taguchi experimental design, Materials and Design 30 (2009) 2791–2801.

[12]   M. Bagci, H. Imrek, Solid particle erosion behavior of glass fibre reinforced boric

acid filled epoxy resin composites, Tribology International 44 (2011) 1704–1710.

[13]   M. Bagci, H. Imrek, Application of Taguchi method on optimization of testing parameters for erosion of glass fiber reinforced epoxy composite materials, Materials and Design 46 (2013) 706–712.

[14]   J.S. Rajadurai, T. Christopher, G. Thanigaiyarasu, B. Nageswara Rao, Finite element analysis with an improved failure criterion for composite wind turbine blades, Forschung im Ingenieurwesen 72 (2008) 193-207.

[15]   W.H. Wu, W.B. Young, Structural Analysis and Design of the Composite Wind Turbine Blade, Applied Composite Materials 19 (2012) 247-257.

[16]   X. Chen, B.S. McLaury, S.A. Shirazi, Application and experimental validation of a computational fluid dynamics (CFD) based erosion prediction model in elbows and plugged tees, Computers and Fluids 33 (2004) 1251–1272.

[17]   Q.B. Nguyen, C.Y.H. Lim, V.B. Nguyen, Y.M. Wan, B. Nai, Y.W. Zhang, M. Gupta, Slurry erosion characteristics and erosion mechanisms of stainless steel, Tribology International 79 (2014) 1–7.

[18]   Q.B. Nguyen, V.B. Nguyen, C.Y.H. Lim, Q.T. Trinh, B. Nai, S. Sankaranarayanan, M. Gupta, Effect of impact angle and testing time on erosion of stainless steel at higher velocities, Wear 321 (2014) 87–93.

[19]   V.B. Nguyen, Q.B. Nguyen, Z.G. Liu, S. Wan, C.Y.H. Lim, Y.W. Zhang, A combined numerical-experimental study on the effect of surface evolution on the water-sand multiphase flow characteristics and the material erosion behavior, Wear 319 (2014) 96–109.

[20]   H. Zhu, Y. Lin, G. Feng, K. Deng, X. Kong, Q. Wang, D. Zeng, Numerical Analysis of Flow Erosion on Sand Discharge Pipe in Nitrogen Drilling, Advances in Mechanical Engineering (2013) Doi: 10.1155/2013/952652.

[21]   B. Bozzini, M.E. Ricotti, M. Boniardi, C. Mele, Evaluation of erosion–corrosion in multiphase flow via CFD and experimental analysis, Wear 255 (2003) 237–245.

[22]   J.A. Grande. Wind Power Blades Energize Composites Manufacturing, Plastics Technology, October 2008.

[23]   J.C. Watson, J.C. Serrano, Composite Materials for Wind Blades, Wind Systems, September 2010; 46-51.

[24]   D.H. Bowen, C.W.A.Maskell, D.C. Phillips, T.W. Thorpe, G.M. Wells, N.J.M. Wilkins, Materials Aspects of Large Aerogenerator Blades. Proceedings of the

European Wind Energy Conference – Hamburg (1984) 281-286.

[25]   B. Eker, A. Akdogan, A. Vardar, Using of Composite Material in Wind Turbine Blade, Journal of Applied Sciences 6 (2006) 2917-2921.

[26]   K. Debnath, I. Singh, A. Dvivedi, P. Kumar. Natural Fibre Reinforced-Polymer Composites for Wind Turbine Blades: Challenges and Opportunities, Dr. Brahim Attaf (Ed.) Recent Advances in Composite Materials for Wind Turbines Blades (2013) 25-38 (ISBN 978-0-9889190-0-6)

[27]   A. Corbyn, M. Little, Fibre glass wind turbine blade manufacturing guide, Engineers Without Borders (EWB - UK) & SIBAT – Philippines 1st May 2008.

[28]   N.M. Chikhradzea, F.D.S. Marquisc, G.S. Abashidze. Hybrid fiber and nanopowder reinforced composites for wind turbine blades. Journal of Material Research and Technology 4 (2015) 60–67.

[29]   P.K. Fossum, L. Freyd, O.G. Dahlhaug. Design and Fatigue Performance of Large utility-Scale Wind Turbine Blades. Journal of Solar Energy Engineering 135 (2013) 1-11.

[30]   B. Madsen, P. Brondsted, T.L. Andersen. Biobased composites: materials, properties and potential applications as wind turbine blade materials. Advances in wind turbine blade design and materials. Woodhead Publishing Limited (2013) 363-385 (doi:10.1533/9780857097286.3.363).

[31]   P. Bortolotti, Carbon Glass Hybrid Materials for Wind Turbine Rotor Blades, MS Thesis, Delft University of Technology, Netherland, 2012.

[32]   Q. Song, Design, Fabrication, and Testing of a New Small Wind Turbine Blade, MS Thesis, University of Guelph, Canada, 2012.

[33]   K. Cox, Structural Design and Analysis of a 10MW Wind Turbine Blade, Ph.D. Thesis, NTNU, Norwegian University of Science and Technology, Norway, 2012.

[34]   D.D. Samborsky, P. Agastra, J.F. Mandell, Fatigue Trends for Wind Blade Infusion Resins and Fabrics. 51st AIAA/ASME/ASCE/AHS/ASC Structures, Structural Dynamics, and Materials Conference, 12 - 15 April 2010, Orlando, Florida.

[35]   J.W. Holmes, P. Brondsted, B.F. Sorensen, Z. Jiang, Z. Sun, X. Chen, Development of a Bamboo-Based Composite as a Sustainable Green Material for Wind Turbine Blades, Wind Engineering 33 (2009) 197–210.

[36]   D.A. Griffin, T.D. Ashwill, Alternative Composite Material for Megawatt-Scale

Wind Turbine Blades: Design Considerations and Recommended Testing, Journal of Solar Energy Engineering 125 (2003) 515-521.

[37]   P.A. Joosse-Toward, Cost Effective Large Turbine Components with Carbon Fibres, European Wind Energy Conference and Exhibition, Copenhagen, Denmark, 2001.

[38]   L. Mishnaevsky Jr., P. Freere, R. Sinha, P. Acharya, R. Shrestha, P. Manandhar, Small wind turbines with timber blades for developing countries: Materials choice, development, installation and experiences. Renewable Energy 36 (2011) 2128-2138.

[39]   P. Brondsted, L.P. Mikkelsen. Challenges Testing Composite Materials for Wind Turbine Blades. Indo-Danish Workshop on Future Composites Technologies for Wind Turbine Blades, IIT Delhi, India, 8-9 Oct. 2012.

[40]   J.L. Tsaia, B.H. Huang, Y.L. Cheng. Enhancing Fracture Toughness of Glass/Epoxy Composites for Wind Blades Using Silica Nanoparticles and Rubber Particles, Procedia Engineering 14 (2011) 1982–1987.

[41]   R. Stewart, Wind turbine blade production – new products keep pace as scale increases, Reinforced Plastics 56 (2012) 18–25.

[42]   U. Javaid, Z. M. Khan, M. B. Khan, M. Bassyouni, S. M. S. Abdel-Hamid, M. H. Abdel-Aziz, S.W. Hasan, Fabrication and thermo-mechanical characterization of glass fiber/vinyl ester wind turbine rotor blade, Composites Part B: Engineering 91 (2016) 257-266.

[43]   N. Dalili, A. Edrisy, R. Carriveau, A review of surface engineering issues critical to wind turbine performance, Renewable and Sustainable Energy Reviews 13 (2019) 428–438.

[44]   H. M. Slot, E. R. M. Gelinck, C. Rentrop, E. van der Heide, Leading edge erosion of coated wind turbine blades: Review of coating life models, Renewable Energy 80 (2015) 837-848.

[45]   L. Rempel, Rotor Blade Leading Edge Erosion – Real Life Experiences, Wind Systems, October 2012; 22-24.

[46]   F. Sayer, A Antoniou, A van Wingerde, Investigation of structural bond lines in wind turbine blades by sub-component tests, International Journal of Adhesion & Adhesives 37 (2012) 129–135.

[47]   Y.H. Qiao, J. Han, C.Y. Zhang, J.P. Chen, Modeling Smart Structure of Wind

Turbine Blade, Applied Composite Material 19 (2012) 491-498.

[48]   B. Natarajan, J. Lee, J. Lim, S. Shin, Structural Analysis Of Composite Wind Turbine Blade Using Advanced Beam Model Approach, International Journal of Precision Engineering and Manufacturing 13 (2012) 2245-2250.

[49]   Y. Hu, S.S. Rao. Robust Design of Horizontal Axis Wind Turbines Using Taguchi Method, Journal of Machine Design 133 (2011) 1 – 15.

[50]   Z. Wang, X. Huang, L. Bai, R. Du, Y. Liu, Y. Zhang, G. Zhao, Effect of micro-Al2O3 contents on mechanical property of carbon fiber reinforced epoxy matrix composites, Composites Part B: Engineering 91 (2016) 392-398.

[51]   K.L. Pickering, M.G. Aruan Efendy, Preparation and mechanical properties of novel bio-composite madeof dynamically sheet formed discontinuous harakeke and hemp fibremat reinforced PLA composites for structural applications, Industrial Crops and Products 84 (2016) 139–150.

[52]   M.R. Petersen, A. Chen, M. Roll, S.J. Jung, M. Yossef, Mechanical properties of fire-retardant glass fiber-reinforced polymer materials with alumina tri-hydrate filler, Composites Part B: Engineering 78 (2015) 109-121.

[53]   R.A. Braga, P.A.A. Magalhaes Jr, Analysis of the mechanical and thermal properties of jute and glass fiber as reinforcement epoxy hybrid composites, Materials Science and Engineering 56 (2015) 269–273.

[54]   G.M. Arifuzzaman Khan, M. Terano, M.A. Gafur, M. Shamsul Alam, Studies on the mechanical properties of woven jute fabric reinforced poly(L-lactic acid) composites, Journal of King Saud University – Engineering Sciences 28 (2016) 69–74.

[55]   N. Hameed, P.A. Sreekumar, V.S. Valsaraj, S. Thomas, High-performance composite from epoxy and glass fibers: Morphology, mechanical, dynamic mechanical and thermal analysis, Polymer Composites 30 (2009) 982–992.

[56]   H.He, F. Gao, Resin modification on interlaminar shear property of carbon fiber/epoxy/nano-CaCO$_3$ hybrid composites, Polymer Composites (2015) doi: 10.1002/pc.23775.

[57]   R.K. Nayak, A. Dasha, B.C. Ray, Effect of epoxy modifiers (Al2O3/SiO2/TiO2) on mechanical performance of epoxy/glass fiber hybrid composites, Procedia Materials Science 6 (2014) 1359 – 1364.

[58]   T. Ahmad, O. Mamat, R. Ahmad, Studying the Effects of Adding Silica Sand

Nanoparticles on Epoxy Based Composites, Journal of Nanoparticles (2013) dx.doi.org/10.1155/2013/603069.

[59]   A. Satapathy, A.K. Jha, S. Mantry, S.K. Singh, A. Patnaik. Processing and Characterization of Jute–Epoxy Composites Reinforced with SiC Derived from Rice Husk, Journal of Reinforced Plastics and Composites. 29 (2010) 2869 - 2878.

[60]   F.O. Abas, R.O. Abas, S.I. Ibrahim, A Comparison Study of Different Ceramic Filler on Mechanical and Thermal Properties of Glass, Carbon, Kevlar / Polyester Composites, Engineering & Technology Journal, 28 (2010) 2469-2479.

[61]   R. Kaundal, A. Patnaik, A. Satapathy, Solid Particle Erosion of Short Glass Fiber Reinforced Polyester Composite, American Journal of Materials Science 2 (2012) 22-27.

[62]   A. Patnaik, A. Satapathy, S.S. Mahapatra, R.R. Dash, Implementation of Taguchi Design for Erosion of Fiber-Reinforced Polyester Composite Systems with Sic Filler, Journal of Reinforced Plastics and Composites 27 (2008) 1093 - 1111.

[63]   Y.H. Zhao, Y.F. Zhang, S.L. Bai, X.W. Yuan, Carbon fibre/graphene foam/polymer composites with enhanced mechanical and thermal properties, Composites Part B: Engineering 94 (2016) 102 - 108.

[64]   L. Yan, N. Chouw, L. Huang, B. Kasal, Effect of alkali treatment on microstructure and mechanical properties of coir fibres, coir fibre reinforced-polymer composites and reinforced-cementitious composites, Construction and Building Materials 112 (2016) 168–182.

[65]   H. Essabir, R. Boujmal, M.O. Bensalahb, D. Rodriguec, R. Bouhfida , A.K. Qaiss, Mechanical and thermal properties of hybrid composites: Oil-palm fiber/clay reinforced high density polyethylene, Mechanics of Materials 98 (2016) 36 – 43.

[66]   M. Boopalan, M.J. Umapathy, P. Jenyfer, A Comparative Study on the Mechanical Properties of Jute and Sisal Fiber Reinforced Polymer Composites, Silicon 4 (2012) 145–149.

[67]   J. Chaichanawong, C. Thongchuea, S. Areerat, Effect of moisture on the mechanical properties of glass fiber reinforced polyamide composites, Advanced Powder Technology 27 (2016) 898 -902.

[68]   K. Naresh, K. Shankar, B.S. Rao, R. Velmurugan, Effect of High Strain Rate on Glass/Carbon/Hybrid Fiber Reinforced Epoxy Laminated Composites, Composites Part B: Engineering (2016)

doi10.1016/j.compositesb.2016.06.007.

[69]   C. Dong, Uncertainties in flexural strength of carbon/glass fibre reinforced hybrid epoxy composites, Composites Part B: Engineering 98 (2016) 176-181.

[70]   R.M. Bajracharya, A.C. Manalo, W. Karunasena, K. Lau, Experimental and theoretical studies on the properties of injection moulded glass fibre reinforced mixed plastics composites, Composites: Part A: Applied Science and Manufacturing 84 (2016) 393–405.

[71]   Y. Dobah, M. Bourchak, A. Bezazi, A. Belaadi, F. Scarpa, Multi-axial mechanical characterization of jute fiber/polyester composite materials, Composites Part B: Engineering 90 (2016) 450 – 456.

[72]   Md.R. Rahman, Md.M. Huque, Md.N. Islam, M. Hasan, Improvement of physico-mechanical properties of jute fiber reinforced polypropylene composites by post-treatment, Composites: Part A: Applied Science and Manufacturing 39 (2008) 1739 – 1747.

[73]   A. Gopinatha, M. S. Kumar, A. Elayaperumal, Experimental Investigations on Mechanical Properties Of Jute Fiber Reinforced Composites with Polyester and Epoxy Resin Matrices, Procedia Engineering 97 (2014) 2052 – 2063.

[74]   A. Athijayamani, B. Stalin, S. Sidhardhan, C. Boopathi, Parametric analysis of mechanical properties of bagasse fiber-reinforced vinyl ester composites, Journal of Composite Materials 50 (2016) 481-493.

[75]   M. Manjunath, N.M. Renukappa, B. Suresha, Influence of micro and nanofillers on mechanical properties of pultruded unidirectional glass fiber reinforced epoxy composite systems, Journal of Composite Materials 50 (2016) 1109-1121.

[76]   N.E. Merter, G. Başer, M. Tanoglu, Effects of hybrid yarn preparation technique and fiber sizing on the mechanical properties of continuous glass fiber-reinforced polypropylene composites, Journal of Composite Materials 50 (2016) 1697-1706.

[77]   D.L. Motoc, S.F. Bou, R.B. Gimeno, Effects of fibre orientation and content on the mechanical, dynamic mechanical and thermal expansion properties of multi-layered glass/carbon fibre-reinforced polymer composites, Journal of Composite Materials 49 (2015) 1211-1221.

[78]   L.T. Harper, T.A. Turner, J.R.B. Martin, N.A. Warrior, Fiber Alignment in Directed Carbon Fiber Preforms – Mechanical Property Prediction, Journal of Composite Materials 44 (2010) 931-951.

[79]   C. Medina, C. Canales, C. Arango, P. Flores, The influence of carbon fabric weave on the in-plane shear mechanical performance of epoxy fiber-reinforced laminates, Journal of Composite Materials, 48 (2014) 2871-2878.

[80]   X.K. Zhu, J.A. Joyce, Review of fracture toughness (G, K, J, CTOD, CTOA) testing and standardization, Engineering Fracture Mechanics 85 (2012) 1–46.

[81]   M.E. Launey, R.O. Ritchie, On the Fracture Toughness of Advanced Materials, Advanced Materials 21 (2009) 2103 -2110.

[82]   A.J. Brunner, Experimental aspects of Mode I and Mode II fracture toughness testing of fibre-reinforced polymer-matrix composites, Computer Methods in Applied Mechanics and Engineering 185 (2000) 161-172.

[83]   A. Avcia, H. Arikanb, A. Akdemir, Fracture behavior of glass fiber reinforced polymer composite, Cement and Concrete Research 34 (2004) 429–434.

[84]   H. Arikan, A. Avci, A. Akdemir, Fracture behaviour of steel fibre reinforced polymer Composite, Polymer Testing 23 (2004) 615–619.

[85]   A. Samanci, Fracture behavior of woven steel fiber reinforced and sand particle filled polymer composites, Construction and Building Materials 26 (2012) 167–171.

[86]   Q. Liu, M. Hughes, The fracture behaviour and toughness of woven flax fibre reinforced epoxy composites, Composites: Part A: Applied Science and Manufacturing 39 (2008) 1644–1652.

[87]   E. Perez, V. Alvarez, C.J. Perez, C. Bernal, A comparative study of the effect of different rigid fillers on the fracture and failure behavior of polypropylene based composites, Composites: Part B: Engineering 52 (2013) 72–83.

[88]   S. Chandrasekaran, N. Sato, F. Tolle, R. Mulhaupt, B. Fiedler, K. Schulte, Fracture toughness and failure mechanism of graphene based epoxy Composites, Composites Science and Technology 97 (2014) 90–99.

[89]   B. Lauke, S.Y. Fu. Aspects of fracture toughness modelling of particle filled polymer composites, Composites: Part B: Engineering 45 (2013) 1569–1574.

[90]   J.A. DeSouza, S. Goutianos, M. Skovgaard, B.F. Sorensen, Fracture resistance curves and toughening mechanisms in polymer based dental composites, Journal of the Mechanical Behavior of Biomedical Materials 4 (2011) 558–571.

[91]   T. Kusaka, M. Hojo, Y.W. Mai, T. Kurokawa, T. Nojima, S. Ochiai, Rate Dependence of Mode I Fracture Behaviour in Carbon-Fibre/Epoxy Composite

Laminates, Composites Science and Technology 58 (1998) 591-602.

[92]   K.D. Cowley, P.W.R. Beaumont, The Interlaminar and Intralaminar Fracture Toughness of Carbon-Fibre/Polymer Composites: The Effect of Temperature, Composite Science and Technology 57 (1997) 1433-1444.

[93]   E.V. Morozov, S.A. Sylantiev, E.G. Evseev, H.G. Lessmann, Nonlinear fracture analysis of hybrid polymer composite materials and structures, Composite Structures 48 (2000) 135 – 138.

[94]   G. Gong, B.H. Xie, M.B. Yang, W. Yang, W.Q. Zhang, M. Zhao, Mechanical properties and fracture behavior of injection and compression molded polypropylene/coal gangue powder composites with and without a polymeric coupling agent, Composites: Part A: Applied Science and Manufacturing 38 (2007) 1683–1693.

[95]   Y. Zhang, A.P. Vassilopoulos, T. Keller, Mode I and II fracture behavior of adhesively-bonded pultruded composite joints, Engineering Fracture Mechanics 77 (2010) 128–143.

[96]   M.R. Ayatollahi, S. Shadlou, M.M. Shokrieh, Fracture toughness of epoxy/multi-walled carbon nanotube nano-composites under bending and shear loading conditions, Materials and Design 32 (2011) 2115–2124.

[97]   L. Sun, R.F. Gibson, F. Gordaninejad, Multiscale analysis of stiffness and fracture of nanoparticle-reinforced composites using micromechanics and global–local finite element models, Engineering Fracture Mechanics 78 (2011) 2645–2662.

[98]   M. Miura, Y. Shindo, T. Takeda, F. Narita, Interlaminar fracture characterization of woven glass/epoxy composites under mixed-mode II/III loading conditions at cryogenic temperatures, Engineering Fracture Mechanics 96 (2012) 615–625.

[99]   J.M.L. Reis, Sisal fiber polymer mortar composites: Introductory fracture mechanics approach, Construction and Building Materials 37 (2012) 177–180.

[100] E. Perez, L. Fama, S.G. Pardo, M.J. Abad, C. Bernal, Tensile and fracture behaviour of PP/wood flour composites, Composites: Part B: Engineering 43 (2012) 2795–2800.

[101] M.W. Czabaj, J.G. Ratcliffe, Comparison of intralaminar and interlaminar mode I fracture toughnesses of a unidirectional IM7/8552 carbon/epoxy composite, Composites Science and Technology 89 (2013) 15–23.

[102] V. Rizov, Mixed-mode I/II fracture study of polymer composites using Single

Edge Notched Bend specimens, Computational Materials Science 77 (2013) 1–6.

[103]   V. Kushvaha, H. Tippur, Effect of filler shape, volume fraction and loading rate on dynamic fracture behavior of glass-filled epoxy, Composites: Part B: Engineering 64 (2014) 126–137.

[104]   K.C. Jajam, M.M. Rahman, M.V. Hosur, H.V. Tippur, Fracture behavior of epoxy nanocomposites modified with polyol diluent and amino-functionalized multi-walled carbon nanotubes: A loading rate study, Composites: Part A: Applied Science and Manufacturing 59 (2014) 57–69.

[105]   S. Nekhlaoui, H. Essabir, M.O. Bensalah, O. Fassi-Fehri, A. Qaiss, R. Bouhfid, Fracture study of the composite using essential work of fracture method: PP–SEBS–g–MA/E1 clay, Materials and Design 53 (2014) 741–748.

[106]   P.S. Shivakumar Gouda, V. Chatterjee, P.K. Barhai, D. Jawali, S. Rahatekar, M.R. Wisnom, Improved fracture toughness in carbon fibre epoxy composite through novel pre-preg coating method using Epoxy Terminated Butadiene Nitrile rubber, Materials and Design 62 (2014) 320–326.

[107]   T. Matthews, M. Ali, A.J. Paris, Finite element analysis for large displacement J-integral test method for Mode I interlaminar fracture in composite materials, Finite Elements in Analysis and Design 83 (2014) 43–48.

[108]   Y.J. Wan, L.X. Gong, L.C. Tang, L.B. Wu, J.X. Jiang, Mechanical properties of epoxy composites filled with silane-functionalized graphene oxide, Composites: Part A: Applied Science and Manufacturing 64 (2014) 79–89.

[109]   H. Silva, J.A.M. Ferreira, C. Capela, M.O.W. Richardson, Mixed Mode interlayer fracture of glass fiber/nano-enhanced epoxy Composites, Composites: Part A: Applied Science and Manufacturing 64 (2014) 211–222.

[110]   D. Boyina, A. Banerjee, R. Velmurugan, Mixed-mode translaminar fracture of plain-weave composites, Composites: Part B: Applied Science and Manufacturing 60 (2014) 21–28.

[111]   R.B. Prime, Thermosets, Thermal Characterization of Polymeric Materials, Ed. A. Thuri, Academic Press, New York USA (1981) 435 -569.

[112]   N. Saba, M. Jawaid, O.Y. Alothman, M.T. Paridah. A review on dynamic mechanical properties of natural fibre reinforced polymer composites, Construction and Building Materials 106 (2016) 149–159.

[113]   V. Pistor, F.G. Ornaghi, H.L. Ornaghi, A.J. Zattera, Dynamic mechanical

characterization of epoxy/epoxycyclohexyl-POSS nanocomposites, Material Science and Engineering: A 532 (2012) 339–345.

[114]   H.L. Ornaghi, V. Pistor, A.J. Zattera, Effect of the epoxycyclohexyl polyhedral oligomeric silsesquioxane content on the dynamic fragility of an epoxy resin, Journal of Non-Crystlline Solids 358 (2012) 427–432.

[115]   N.T. Qazvini, N. Mohammadi, Dynamic mechanical analysis of segmental relaxation in unsaturated polyester resin networks: effect of styrene content, Polymer 46 (2005) 9088–9096,

[116]   M. Jawaid, H.P.S. Abdul Khalil, A. Hassan, R. Dungani, A. Hadiyane, Effect of jute fibre loading on tensile and dynamic mechanical properties of oil palm epoxy composites, Composites Part B: Engineering. 45 (2013) 619–624.

[117]   Z. Zhang, P. Wang, J. Wu, Dynamic mechanical properties of EVA polymer modified cement paste at early age, Physics Procedia 25 (2012) 305–310.

[118]   Y. Karaduman, M.M.A. Sayeed, L. Onal, A. Rawal, Viscoelastic properties of surface modified jute fiber/polypropylene nonwoven composites, Composites: Part B: Engineering 67 (2014) 111–118.

[119]   N. Naffakh, M. Dumon, J. Gérard, Study of a reactive epoxy-amine resin enabling in situ dissolution of thermoplastic films during resin transfer moulding for toughening composites, Composites Science and Technology, 66 (2006) 1376-1384.

[120]   H.L. Ornaghi, H.S.P. da-Silva, A.J. Zattera, S.C. Amico, Dynamic mechanical properties of curaua composites, Journal of Applied Polymer Science, 125 (2012) E110-E116.

[121]   T.F. Scott, W.D. Cook, J.S. Forsythe, Kinetics and network structure of thermally cured vinyl ester resins, European Polymer Journal, 38 (2002) 705-716.

[122]   W.D. Cook, T.F. Scott, S. Quay-Thevenon, J.S. Forsythe, Dynamic mechanical thermal analysis of thermally stable and thermally reactive network polymers, Journal of Applied Polymer Science 93 (2004) 1348-1359.

[123]   D. Ray, B.K. Sarkara, S. Dasb, A.K. Rana, Dynamic mechanical and thermal analysis of vinylester-resin-matrix composites reinforced with untreated and alkali-treated jute fibres, Composites Science and Technology 62 (2002) 62: 911–917.

[124]   D. Ray, N.R. Bose, A.K. Mohanty, M. Misra, Modification of the dynamic damping behaviour of jute/vinylester composites with latex interlayer, Composites:

Part B: Engineering 38 (2007) 380–385.

[125] D. Shanmugam, M. Thiruchitrambalam, Static and dynamic mechanical properties of alkali treated unidirectional continuous Palmyra Palm Leaf Stalk Fiber/jute fiber reinforced hybrid polyester composites, Materials and Design 50 (2013) 533–542.

[126] V.S. Sreenivasan, N. Rajini, A. Alavudeen, V. Arumugaprabu, Dynamic mechanical and thermo-gravimetric analysis of Sansevieria cylindrica/polyester composite: Effect of fiber length, fiber loading and chemical treatment, Composites: Part B: Engineering 69 (2015) 76–86.

[127] S.M.S. Kumar, D. Duraibabu, K. Subramanian, Studies on mechanical, thermal and dynamic mechanical properties of untreated (raw) and treated coconut sheath fiber reinforced epoxy composites, Materials and Design 59 (2014) 63–69.

[128] S. Mohanty, S.K. Verma, S.K. Nayak, Dynamic mechanical and thermal properties of MAPE treated jute/HDPE composites, Composites Science and Technology 66 (2006) 538–547.

[129] G. George, E.T. Jose, D. Akesson, M. Skrifvars, E.R. Nagarajan, K. Joseph. Viscoelastic behaviour of novel commingled biocomposites based on polypropylene/jute yarns, Composites: Part A: Applied Science and Manufacturing 43 (2012) 893–902.

[130] V. Baheti, J. Militky, R. Mishra, B.K. Behera, Thermo-mechanical properties of glass fabric/epoxy composites filled with fly ash, Composites Part B: Engineering 85 (2016) 268-276.

[131] R. Kaundal, A. Patnaik, A. Satapathy, Comparison of the Mechanical and Thermo-Mechanical Properties of Unfilled and SiC Filled Short Glass Polyester Composites, Silicon 4 (2012) 175–188.

[132] S. Kumar, B.K. Satapathy, A. Patnaik, Thermo-mechanical correlations to erosion performance of short glass/carbon fiber reinforced vinyl ester resin hybrid composites, Computational Materials Science 60 (2012) 250–260.

[133] S. Kumar, B.K. Satapathy, A. Patnaik, Thermo-mechanical correlations to erosion performance of short carbon fibre reinforced vinyl ester resin composites, Materials and Design 32 (2011) 2260–2268.

[134] W. Stark, Investigation of the curing behaviour of carbon fibre epoxy prepreg by Dynamic Mechanical Analysis DMA, Polymer Testing 32 (2013) 231–239.

[135] W. Stark, M. Jaunich, J. McHugh, Carbon-fibre epoxy prepreg (CFC) curing in an

autoclave analogue process controlled by Dynamic Mechanical Analysis (DMA), Polymer Testing 32 (2013) 1487–1494.

[136]   W. Stark, M. Jaunich, J. McHugh, Dynamic Mechanical Analysis (DMA) of epoxy carbon-fibre prepregs partially cured in a discontinued autoclave analogue process, Polymer Testing 41 (2015) 140-148.

[137]   L.D. Landro, W. Lorenzi, Mechanical Properties and Dynamic Mechanical Analysis of Thermoplastic-Natural Fiber/Glass Reinforced Composites, Macromolecular Symposia 286 (2009) 145–155.

[138]   H.L. Ornaghi, A.S. Bolner, R. Fiorio, A.J. Zattera, S.C. Amico. Mechanical and Dynamic Mechanical Analysis of Hybrid Composites Molded by Resin Transfer Molding, Journal of Applied Polymer Science 118 (2010) 887–896.

[139]   S. Mandal, S. Alam, Dynamic mechanical analysis and morphological studies of glass/bamboo fiber reinforced unsaturated polyester resin-based hybrid composites, Journal of Applied Polymer Science 125 (2012) E382 - E387.

[140]   K. Kumaresan, G. Chandramohan, M. Senthilkumar, B. Suresha, Dynamic mechanical analysis and three-body wear of carbon–epoxy composite filled with SiC particles, Journal of Reinforced Plastics and Composites, 31 (2012) 1435-1448.

[141]   A.Hassan, N.M. Salleh, R. Yahya, M.R.K. Sheikh, Fiber length, thermal, mechanical, and dynamic mechanical properties of injection-molded glass-fiber/polyamide 6,6: plasticization effect, Journal of Reinforced Plastics and Composites, 30 (2011) 488-498.

[142]   D. Ray, Modification of the Dynamic Damping Behavior of Fly Ash Filled Unsaturated Polyester Resin/SBR Latex Blend Composites, Journal of Reinforced Plastics and Composites, 28 (2009) 1537-1552.

[143]   H.S. Shen, J.J. Zheng, X.L. Huang, Dynamic response of shear deformable laminated plates under thermomechanical loading and resting on elastic foundations, Composite Structures 60 (2003) 57 - 66.

[144]   A.P. Mouritz, Post-fire flexural properties of fibre-reinforced polyester, epoxy and phenolic composites, Journal of Materials Science 37 (2002) 1377 - 1386.

[145]   J. Kim, W. Lee, S.W. Tsai, Modeling of mechanical property degradation by short-term aging at high temperatures, Composites Part B: Engineering 33 (2002) 531 - 543.

[146] M.R.E. Looyeh, A. Samanta, S. Jihan, J. McConnachie, Modelling of reinforced polymer composites subject to thermo-mechanical loading, International Journal for Numerical Methods in Engineering 63 (2005) 898 - 925.

[147] L. Torre, J.M. Kenny, A.M. Maffezzoli, Degradation behaviour of a composite material for thermal protection systems Part II Process simulation, Journal of Materials Science 33 (1998) 3145 - 3149.

[148] D. Cho, B. Yoon, Microstructural interpretation of the effect of various matrices on the ablation properties of carbon-fiber-reinforced composites, Composites Science and Technology 61 (2001) 271 - 280.

[149] J. Staggs, Simple mathematical models of char-forming polymers, Polymer International 49 (2000) 1147 - 1152.

[150] A.W. Coats, J.P. Redfern, Thermogravimetric Analysis: A Review, Analyst 88 (1963) 906–924.

[151] X. Liu, W. Yu, Evaluating the Thermal Stability of High Performance Fibers by TGA, Journal of Applied Polymer Science 99 (2006) 937–944.

[152] J.M. Ferreiraa, O.A.Z. Errajhib, M.O.W. Richardson, Thermogravimetric analysis of aluminised E-glass fibre reinforced unsaturated polyester composites, Polymer Testing 25, (2006) 1091–1094.

[153] G.P. Tilly, A two stage mechanisms of ductile erosion, Wear 23 (1973) 87–96.

[154] C.K. Lee, Corrosion and wear-corrosion resistance properties of electroless Ni–P coatings on GFRP composite in wind turbine blades, Surface & Coatings Technology 202 (2008) 4868–4874.

[155] A.W. Ruff, S.M. Wiederhorn, Erosion by solid particle impact, in: C.M. Preece (Ed.), Treatise on Materials Science and Technology, Academic Press, New York, 16 (1979) 69–125.

[156] J.A.C. Humphrey, Fundamentals of fluid motion in erosion by solid particle impact, International Journal of Heat and Fluid Flow 11 (1990) 170–195.

[157] I. Finnie, Some reflections on the past and future of erosion, Wear 186/187 (1995) 1 - 10.

[158] S. Soderberg, S. Hogmark, H. Swahn, Mechanisms of material removal during erosion of a stainless steel, A S L E Transactions 26 (1983) 161 – 172.

[159] S. Soderberg, S. Hogmark, U. Engman, H. Swahn, Erosion classification of materials using a centrifugal erosion tester, Tribology International 14 (1981) 333–

343.

[160]   I.M. Hutchings, Monograph on Erosion of Materials by Solid Particle Impact, MTI
         Publication, Columbus OH, (1983).

[161]   I.M. Hutchings, Introduction to the microscopy of erosion, Journal of Microscopy
         130 (1983) 331–338.

[162]   B.S. McLaury, J. Wang, S.A Shirazi, J.R. Shadley, E.F. Rybicki, Solid particle
         erosion in long radius elbows and straight pipes, SPE Annual Technical
         Conference and Exhibition, San Antonio, Texas, 5-8 October 1997.
         http://dx.doi.org/10.2118/38842-MS

[163]   H.C. Meng, K.C. Ludema, Wear models and predictive equations: their form and
         content, Wear 181–183 (1995) 443 - 457.

[164]   A. Patnaik, A. Satapathy, Erosion Wear Response of Flyash-Glass Fiber-Polyester
         Composites: A Study using Taguchi Experimental Design, Malaysian Polymer
         Journal 4 (2009) 13-28.

[165]   S. Biswas A. Satapathy, A Comparative Study on Erosion Characteristics of Red
         Mud Filled Bamboo-Epoxy and Glass-Epoxy Composites, Journal of Materials
         and Design 31 (2010) 1752-1767.

[166]   S. Biswas, A. Patnaik, P. Kumar, Silicon Carbide Filled Polymer Composite for
         Erosive Environment Application: A Comparative Analysis of Experimental and
         FE Simulation Results, Dr. Moumita Mukherjee (Ed.) Silicon Carbide – Materials,
         Processing and Applications in Electronic Devices. (2011) 453-468.

[167]   S.K. Mishra, S. Biswas, A. Satapathy, A. Patnaik, Erosion Wear Analysis of Al_2O_3
         Particles Reinforced ZA-27 Alloy Metal Matrix Composite Using ANN,
         International Journal of Materials, Manufacturing and Design 1 (2012) 1: 65-76.

[168]   A. Patnaik, A. Satapathy, S.S. Mahapatra, R.R. Dash, A Taguchi Approach for
         Investigation of Erosion of Glass Fiber – Polyester Composites. Journal of
         Reinforced Plastics and Composites 27 (2008) 871 - 888.

[169]   S. Zhang, K. Dam-Johansen, P.L. Bernad, S. Kiil, Rain erosion of wind turbine
         blade coatings using discrete water jets: Effects of water cushioning, substrate
         geometry, impact distance, and coating properties, Wear 328-329 (2015) 140–148.

[170]   S. Zhang, K. Dam-Johansen, S. Norkjaerb, P.L. Bernad, S. Kiil. Erosion of wind
         turbine blade coatings – Design and analysis of jet-based laboratory equipment for
         performance evaluation, Progress in Organic Coatings 78 (2015) 103–115.

[171] A. Patnaik, A. Satapathy, S.S. Mahapatra, R.R. Dash, Parametric Optimization Erosion Wear of Polyester-GF-Alumina Hybrid Composites using the Taguchi Method, Journal of Reinforced Plastics and Composites 27 (2008) 1039 - 1058.

[172] A.P. Harsha, U.S. Tewari, B. Venkatraman, Solid particle erosion behaviour of various polyaryletherketone composites, Wear 254 (2003) 693–712.

[173] A. Patnaik, S. Tejyan, A Taguchi approach for investigation of solid particle erosion response of needle-punched nonwoven reinforced polymer composites: Part II, Journal of Industrial Textiles 43 (2014) 458 - 480. 2012.

[174] M. Bagci, Determination of solid particle erosion with Taguchi optimization approach of hybrid composite systems, Tribology International 94 (2016) 336–345.

[175] S. Biswas, A. Satapathy, Tribo-performance analysis of red mud filled glass-epoxy composites using Taguchi experimental design, Materials and Design 30 (2009) 2841–2853.

[176] A.K. Rout, A. Satapathy, Study on mechanical and tribo-performance of rice-husk filled glass–epoxy hybrid composites, Materials and Design 41 (2012) 131–141.

[177] J. Bijwe, R. Rattan, Influence of weave of carbon fabric in polyetherimide composites in various wear situations, Wear 263 (2007) 984–991.

[178] R. Rattan, J. Bijwe, Carbon fabric reinforced polyetherimide composites: Influence of weave of fabric and processing parameters on performance properties and erosive wear, Materials Science and Engineering: A 420 (2006) 342–350.

[179] Y.G. Zheng, Z.M. Yao, W. Ke, Erosion–corrosion resistant alloy development for aggressive slurry flows, Materials Letters 46 (2000) 362–368.

[180] K. Sugiyama, S. Nakahama, S. Hattori, K. Nakano, Slurry wear and cavitation erosion of thermal-sprayed cermets, Wear 258 (2005) 768–775.

[181] M.A. Al-Bukhaiti, S.M. Ahmed, F.M.F. Badran, K.M. Emara, Effect of impingement angle on slurry erosion behaviour and mechanisms of 1017 steel and high-chromium white cast iron, Wear 262 (2007) 1187–1198.

[182] K. Sugiyama, K. Harada, S. Hattori, Influence of impact angle of solid particles on erosion by slurry jet, Wear 265 (2008) 713–720.

[183] G.R. Desale, B.K. Gandhi, S.C. Jain, Slurry erosion of ductile materials under normal impact condition, Wear 264 (2008) 322–330.

[184] H.S. Grewal, H.S. Arora, A. Agrawal, H. Singh, S. Mukherjee, Slurry erosion of

thermal spray coatings: Effect of sand Concentration, Procedia Engineering 68 (2013) 484 – 490.

[185] H.M. Hawthorne, B. Arsenault, J.P. Immarigeon, J.G. Legoux, V.R. Parameswaran, Comparison of slurry and dry erosion behaviour of some HVOF thermal sprayed coatings, Wear 225–229 (1999) 825–834.

[186] Q. Fang, H. Xu, P.S. Sidky, M.G. Hocking, Erosion of ceramic materials by a sand/water slurry jet, Wear 224 (1999) 183–193.

[187] A.G. Joshi, M.P. Kumar, S. Basavarajappa, Influence of Al_2O_3 filler on Slurry Erosion Behavior of Glass/Epoxy Composites, Procedia Material Science 5 (2014) 863-872.

[188] T. Frosell, M. Fripp, E. Gutmark, Investigation of slurry concentration effects on solid particle erosion rate for an impinging jet, Wear 342-343 (2015) 33–43.

[189] A. Corsini, A. Marchegiani, F. Rispoli, P. Venturini, A.G. Sheard, Predicting Blade Leading Edge Erosion in an Axial Induced Draft Fan, Journal of Engineering for Gas Turbines and Power 134 (2012) 042601, doi:10.1115/1.4004724.

[190] Y.F. Wang, Z.G. Yang, Finite element model of erosive wear on ductile and brittle materials, Wear 265 (2008) 871–878.

[191] M. Liu, H. Liu, R. Kang, Similarity criteria of the solid particle erosion in elbows between model experiments and engineering for dry gas and gas–mist flows, Wear 360-361 (2016) 121–136.

[192] V. Hadavi, C.E. Moreno, M. Papini, Numerical and experimental analysis of particle fracture during solid particle erosion, part I: Modeling and experimental verification, Wear 356-357 (2016) 135–145.

[193] V. Hadavi, C.E. Moreno, M. Papini. Numerical and experimental analysis of particle fracture during solid particle erosion, Part II: Effect of incident angle, velocity and abrasive size, Wear 356-357 (2016) 146–157.

[194] R.E. Vieira, A. Mansouri, B.S. McLaury, S.A. Shirazi, Experimental and computational study of erosion in elbows due to sand particles in air flow, Powder Technology 288 (2016) 339–353.

[195] A. Gnanavelu, N. Kapur, A. Neville, J.F. Flores, N. Ghorbani, A numerical investigation of a geometry independent integrated method to predict erosion rates in slurry erosion, Wear 271 (2011) 712– 719.

[196]   M.H. Wanga, C. Huanga, K. Nandakumarb, P. Minevc, J. Luoa, S. Chiovelli, Computational fluid dynamics modelling and experimental study of erosion in slurry jet flows, International Journal of Computational Fluid Dynamics 23 (2009) 155–172.

[197]   S. Singh, R. Nagar, V. Agrawal, A review on Properties of Sustainable Concrete using granite dust as replacement for river sand, Journal of Cleaner Production 126 (2016) 74-87.

[198]   A. Rout, A. Satapathy, S. Mantry, A. Sahoo, T. Mohanty, Erosion Wear Performance Analysis of Polyester-GF-Granite Hybrid Composites using the Taguchi Method, Procedia Engineering 38 (2012) 1863-1882.

[199]   A.K. Rout, A. Satapathy, Study on mechanical and erosion wear performance of granite filled glass-epoxy hybrid composites, Proceedings of the Institution of Mechanical Engineers, Part L: Journal of Materials: Design and Applications 229 (2015) 38-50.

[200]   A. Piratelli-Filho, F. Levy-Neto, Behavior of Granite-Epoxy Composite Beams Subjected to Mechanical Vibrations, Materials Research 13 (2010) 497-503.

[201]   A.A. Kareem, Physical Properties of Polymer Filled with Inorganic (Granite) Filler, Global Journal of Science Frontier Research: B Chemistry 14 (2014) 23 - 26.

[202]   H. V. Ramakrishna, S. K Rai, Utilization of Granite Powder as a Filler for Polybutylene Terepthalate Toughened Epoxy Resin, Journal of Minerals & Materials Characterization & Engineering, 5 (2006) 1-19.

[203]   A.A. Kareem, Mechanical properties of granite powder as a filler for polycarbonate toughened epoxy resin, International Journal of Pharma Sciences, 3 (2013) 254-257.

[204]   R. Baskaran, M. Sarojadevi, C.T. Vijayakumar, Utilization of Granite Powder as Filler for Vinyl Ester Resin, Malaysian Polymer Journal 9 (2014) 39-44.

[205]   H.V. Ramakrishna, S.P. Priya, S.K. Rai, Utilization of Granite Powder as Filler in Epoxy Phenol Cashew Nut Shell Liquid-toughened Epoxy Resin for Impact and Compression Strength, Journal of Reinforced Plastics and Composites 25 (2006) 227-234.

[206]   S. Singh, R. Nagar, V. Agrawal, Performance of granite cutting waste concrete under adverse exposure conditions, Journal of Cleaner Production 127 (2016) 172-

182.

[207]   S. Singh, S. Khan, R. Khandelwal, A. Chugh, R. Nagar, Performance of sustainable concrete containing granite cutting waste, Journal of Cleaner Production 119 (2016) 86-98.

[208]   S. Singh, R. Nagar, V. Agrawal, A. Rana, A. Tiwari, Sustainable utilization of granite cutting waste in high strength concrete, Journal of Cleaner Production 116 (2016) 223-235.

[209]   P. Torres, H.R. Fernandes, S. Agathopoulos, D.U. Tulyaganov, J.M.F. Ferreira, Incorporation of granite cutting sludge in industrial porcelain tile formulations, Journal of the European Ceramic Society 24 (2004) 3177–3185.

[210]   P. Torres, R.S. Manjate, S. Quaresma, H.R. Fernandes, J.M.F. Ferreira. Development of ceramic floor tile compositions based on quartzite and granite sludges, Journal of the European Ceramic Society 27 (2007) 4649–4655.

[211]   P. Torres, H.R. Fernandes, S. Olhero, J.M.F. Ferreira. Incorporation of wastes from granite rock cutting and polishing industries to produce roof tiles, Journal of the European Ceramic Society 29 (2009) 23–30.

[212]   S. Spuzic, M. Zec, K. Abhary, R. Ghomashchi, I. Reid, Fractional design of experiments applied to a wear simulation, Wear 212 (1997) 131-139.

[213]   B.K. Prasad Abrasive wear characteristics of a zinc-based alloy and zinc-alloy/ SiC composite, Wear 252 (2002) 250-263.

[214]   R.L. Deuis, C. Subramanian, J.M. Yellup. Three-body abrasive wear of composite coatings in dry and wet environments, Wear 214 (1998) 112-130.

[215]   A. Banerji, S.V. Prasad, M.K. Surappa P.K. Rohatgi. Abrasive wear of cast aluminium alloy-zircon particle composites, Wear 82 (1982) 141-151.

[216]   D.P. Mondal, S. Das, A.K. Jha, A.H. Yegneswaran, Abrasive wear of Al alloy– Al_2O_3 particle composite: a study on the combined effect of load and size of abrasive, Wear 223 (1998) 131-138.

[217]   G. Taguchi, S. Konishi, Taguchi Methods: Orthogonal Arrays and Linear Graphs; Tools for Quality Engineering, American Supplier Institute Inc., Dearborn, MI. (1987).

[218]   G. Taguchi, Introduction to Quality Engineering, Asian Productivity Organization, Tokyo (1990).

[219]   M.S. Phadke, Quality Engineering using Robost Design, Prentice- Hall,

Englewood Cliffs, NJ (1989).

[220]   Y. Wu, W.H. Moore Quality Engineering: Product & Process Design Optimization, American Supplier Institute Inc., Dearborn, MI (1986).

[221]   A.C. Shoemaker, R.N. Kackar,. A methodology for planning experiments in robust product and process design, Quality and Reliability Engineering International 4 (1988) 95–103.

[222]   M.S. Phadke, K.Dehnad. Optimization of product and process design for quality and cost, Quality and Reliability Engineering International 4 (1988) 105–112.

[223]   V. Gautam, A. Patnaik, I.K. Bhat, Microstructure and Wear Behavior of Single layer (CrN) and Multilayered (SiN/CrN) Coatings on Particulate Filled Aluminum Alloy Composites, Silicon 8 (2016) 417 – 435.

[224]   A. Satapathy, A. Patnaik, M.K. Pradhan, A study on processing, characterization and erosion behavior of fish (Labeo-rohita) scale filled epoxy matrix composites, Materials and Design 30 (2009) 2359–2371.

[225]   M.E. Amine, J. Pailhes, N. Perry, Selection and use of a multi-criteria decision aiding method in the context of conceptual design with imprecise information: Application to a solar collector development, Concurrent Engineering 24 (2016) 35-47.

[226]   M. Ohring, Engineering Material Science, Academic Press Inc, California (1995).

[227]   S.S. Mahapatra, A. Patnaik, A. Satapathy, Taguchi method applied to parametric appraisal of erosion behavior of GF-reinforced polyester composites, Wear 265 (2008) 214–222.

[228]   www.matweb.com/search/carbon fiber

[229]   M. Hojamberdiev, A. Eminov, Y. Xu, Utilization of muscovite granite waste in the manufacture of ceramic tiles, Ceramics International, 37 (2010) 871–876.

[230]   B.D. Agarwal, L.J. Broutman, Analysis and performance of fiber composites, 2nd edition, Jhon wieley and Sons, New York (1990).

[231]   A. Patnaik, A. Satapathy, S.S. Mahapatra, Study on Erosion Response of Hybrid Composites using Taguchi Experimental Design, Journal of Engineering Materials and Technology 131 (2009) 1-16.

[232]   A.R. Shahani, M.R.A. Fasakhodi, Finite element analysis of dynamic crack propagation using remeshing technique, Materials and Design 30 (2009) 1032–1041.

[233] H. Yu, L. Wu, L. Guo, H. Wu, S. Du, An interaction integral method for 3D curved cracks in nonhomogeneous materials with complex interfaces, International Journal of Solids and Structures 47 (2010) 2178–2189.

[234] B. Harris, O.G. Braddell, D.P. Almond, C. Lefebvre, J. Verbist, Study of carbon fibre surface treatments by dynamic mechanical analysis, Journal of Material Science 28 (1993) 3353 - 3366.

[235] Y. Wu, Z. Yu, Thermal conductivity of in situ epoxy composites filled with ZrB_2 Particles, Composites Science and Technology 107 (2015) 61–66.

[236] A. Shojaei, M. Fahimian, B. Derakhshandeh, Thermally conductive rubber- based composite friction materials for railroad brakes-Thermal conduction characteristics, Composites Science and Technology 67 (2007) 2665-2674.

[237] A. Korjenic, V. Petranek, J. Zachb, J. Hroudova, Development and performance evaluation of natural thermal-insulation materials composed of renewable resources, Energy and Buildings 43 (2011) 2518–2523.

[238] J.J. Gou, Y.J. Dai, S. Li, W.Q. Tao, Numerical study of effective thermal conductivities of plain woven composites by unit cells of different sizes, International Journal of Heat and Mass Transfer 91 (2015) 829–840.

[239] L. Eppelbaum, I. Kutasov, A. Pilchin, Thermal Properties of Rocks and Density of Fluids, Applied Geothermics, Springer-Verlag Berlin Heidelberg (2014) 99-149.

[240] G. Taguchi, S. Choudhury, Y. Wu, Tagughi's Quality Engineering Handbook, John Wiley and Sons Inc., New Jersey (2005).

[241] V.K. Srivastava, A.G. Pawar, Solid particle erosion of glass fiber reinforced flyash filled epoxy resin composites, Composite Science and Technology, 66 (2006) 3021-3028.

[242] A. Suresh, A.P. Harsha, Study of erosion efficiency of polymers and polymer composites, Polymer Testing 25 (2006) 188-196.

[243] P.J. Schubel, R.J. Crossley, Wind Turbine Blade Design, Energies 5 (2012) 3425-3449.

[244] C.L. Hwang, K.Yoon, Multiple Attribute Decision Making: Methods and Applications, Springer-Verlag, New York (1981).

[245] K. Yoon, A reconciliation among discrete compromise situations. Journal of Operational Research Society 38 (1987) 277–286.

[246] C.L. Hwang, Y.J. Lai, T.Y. Liu, A new approach for multiple objective decision

making, Computers and Operational Research 20 (1993) 889–899.

[247]   L. Liu, Y. Zhang, F. Lv, B. Yang, X. Meng, Effects of red mud on rheological, crystalline, and mechanical properties of red mud/PBAT composites, Polymer Composite. 37 (2015) 2001 -2007.

[248]   Z.S. Guo, L. Liu, B.M. Zhang, S. Du. Critical Void Content for Thermoset Composite Laminates, Journal of Composite Materials 43 (2009) 1775 – 1790.

[249]   B.R. Raju, B. Suresha, R.P. Swamy, B.S.G. Kanthraju. Investigations on Mechanical and Tribological Behaviour of Particulate Filled Glass Fabric Reinforced Epoxy Composites, Journal of Minerals and Materials Characterization and Engineering 1, (2013) 160 - 167.

[250]   H. Iba, T. Chang and Y. Kagawa, Optically transparent continuous glass fibre-reinforced epoxy matrix composite: fabrication, optical and mechanical properties, Composites Science and Technology 62 (2002) 2043–2052.

[251]   S.Y. Fu, B. Lauke. Characterization of tensile behaviour of hybrid short glass fibre/calcite particle/ABS composites, Composites Part A: Applied Science and Manufacturing 29A (1998) 575-583.

[252]   J.L. Thomason, M.A. Vlug, G. Schipper, H.G.L.T. Krikor, Influence of fibre length and concentration on the properties of glass fibre-reinforced polypropylene: Part 3. Strength and strain at failure, Composites Part A: Applied Science and Manufacturing 27A (1996) 1075-1084.

[253]   A.A. Abdulmajeed, T.O. Narhi, P.K. Vallittu,L.V. Lassila, The effect of high fiber fraction on some mechanical properties of unidirectional glass fiber-reinforced composite Dental Material 27 (2011) 313 -321.

[254]   M.M. Rahman, S. Zainuddin, M.V. Hosur, C.J. Robertson, A. Kumar, J. Trovillion, S. Jeelani, Effect of NH2-MWCNTs on crosslink density of epoxy matrix and ILSS properties of e-glass/epoxy composites, Composite Structures. 95, (2013) 213 – 221.

[255]   S.J. Park, J. S. Jin, Effect of Silane Coupling Agent on Interphase and Performance of Glass Fibers/Unsaturated Polyester Composites, Journal of Colloid and Interface Science 242 (2001) 174–179.

[256]   C. Yilmaz, T. Korkmaz, The reinforcement effect of nano and microfillers on fracture toughness of two provisional resin materials Materials and Design 28 (2007) 2063–2070.

[257]   J. Yang, C. Peng, J. Xiao, J. Zeng, S. Xing, J. Jin, H. Deng, Structural investigation of composite wind turbine blade considering structural collapse in full-scale static tests, Composite Structures 97 (2013) 15–29.

[258]   R. Mohan, Kishore, Jute-Glass Sandwich Composites, Journal of Reinforced Plastics and Composites, 4 (1985) 186-194.

[259]   P.S. Chua, S.R. Dai, M.R. Piggot, Mechanical properties of the glass fibre-polyester interphase, Journal of Material Science, 27 (1992) 913 - 918.

[260]   A.C. deAlbuquerque, K. Joseph, L.H. deCarvalho, J. Roberto, M. Almeida, Composites Science and Technology, 60 (2000) 833 - 844.

[261]   H.A. Sharifah, P.A. Martin, The effect of alkalization and fibre alignment on the mechanical and thermal properties of kenaf and hemp bast fibre composites: part 2 – cashew nut shell liquid matrix, Composites Science and Technology 64 (2004) 1231–1238.

[262]   B.F. Yousif, A. Shaiwan, C.W. Chin, K.C. Ming, Flexural properties of treated and untreated kenaf/epoxy composites, Materials and Design 40 (2012) 378 - 385.

[263]   W.K. Chin, H.T. Liu, Y.D. Lee, Effects of fiber length and orientation distribution on the elastic modulus of short fiber reinforced thermoplastics, Polymer Composites 9 (1988) 27 – 35.

[264]   K.J. Bowles, S. Frimpong, Relationship Between Voids and Interlaminar Shear Strength of Polymer Matrix Composites. NASA Technical Memorandum 103643, 36th International Symposium and Exhibition sponsored by the Society for the Advancement of Materials and Process Engineering. San Diego, California, April 15-18, 1991.

[265]   S.R. Ghiorse, A Comparison of Void Measurement Methods for Carbon/Epoxy Composites, Report number: MTL TR 91-13, U.S. Army Materials Technology Laboratory Watertown, Massachusetts 02172-0001. April 1991.

[266]   J. Brunbauer, H. Stadler, G. Pinter, Mechanical properties, fatigue damage and microstructure of carbon/epoxy laminates depending on fibre volume content, International Journal of Fatigue, 70 (2015) 85–92

[267]   H.W. He and F. Gao, Effect of Fiber Volume Fraction on the Flexural Properties of Unidirectional Carbon Fiber/Epoxy Composites, International Journal of Polymer Analysis and Characterization, 20 (2015) 180-189.

[268]   A.L. Martinez-Hernandez, C. Velasco-Santos, M. De-Icaza, V.M. Castano,

Dynamical–mechanical and thermal analysis of polymeric composites reinforced with keratin biofibers from chicken feathers, Composite Part B: Engineering 38 (2007) 405–410.

[269]   M. Jawaid, H.P.S. Abdul Khalil, O.S. Alattas, Woven hybrid biocomposites: Dynamic mechanical and thermal properties. Composite Part A: Applied Science 43 (2012) 288–293.

[270]   S. Kumar, B.K. Satapathy, A. Patnaik, Viscoelastic interpretations of erosion performance of short aramid fibre reinforced vinyl ester resin composites, Journal of Material Science, 46 (2011) 7489 – 7500.

[271]   L.A. Pothan, Z. Oommen, S. Thomas, Dynamic mechanical analysis of banana fiber reinforced polyester composites, Composites Science and Technology 63 (2003) 283–293.

[272]   J.D. Ferry, Viscoelastic properties of polymers, John Wiley and Sons, Inc. New York (1980).

[273]   A. Vanaja, R.M.V.G.K. Rao, Fibre fraction effects on thermal degradation behaviour of GFRP, CFRP and hybrid composites. Journal of Reinforced Plastics and Composites 21 (2002) 1389–1398.

[274]   S. Keusch, R. Haessler, Influence of surface treatment of glass fibres on the dynamic mechanical properties of epoxy resin composites, Composites: Part A: Applied Science and Manufacturing 30 (1999) 997–1002.

[275]   N. Hameed, P.A. Sreekumar, B. Francis, W. Yang, S. Thomas, Morphology, dynamic mechanical and thermal studies on poly(styrene-co-acrylonitrile) modified epoxy resin/glass fibre composites, Composites: Part A: Applied Science and Manufacturing 38 (2007) 2422–2432.

[276]   S. Tejyan, A. Patnaik, A. Rawal, B.K. Satapathy, Structural and mechanical properties of needle-punched nonwoven reinforced composites in erosive environment, Journal of Applied Polymer Science 123 (2012) 1698 - 1707.

[277]   V. Fiore, T. Scalici, G. Vitale, A. Valenza, Static and dynamic mechanical properties of Arundo Donax fillers-epoxy composites, Materials and Design 57 (2014) 456–464.

[278]   A.K. Saha, S. Das, D. Bhatta, B.C. Mitra. Journal of Applied Polymer Science, 71 (1999) 1505 – 1513.

[279]   I. Hutchings, Ductile–brittle transitions and wear maps for the erosion and abrasion

of brittle materials, Journal of Physics D: Applied Physics, 25 (1992) A212–A221.

[280]   K. Tsuda, M. Kubouchi, T. Sakaia, A. H. Saputra, N. Mitomo, General method for predicting the sand erosion rate of GFRP, Wear 260 (2006) 1045–1052.

[281]   A. Gnanavelu, N. Kapur, A. Neville, J. F. Flores, An integrated methodology for predicting material wear rates due to erosion, Wear 267 (2009) 1935–1944.

[282]   D.W. Wheeler, R.J.K. Wood, Erosion of hard surface coatings for use in offshore gate valves, Wear 258 (2005) 526–536.

[283]   A.J. Speyer, R.J.K. Wood, K.R. Stokes, Erosion of aluminium-based claddings on steel by sand in water, Wear 250 (2001) 802–808.

[284]   D.C. Montgomery, Design and Analysis of Experiments, fifth ed., John Wiley & Sons (Asia), Singapore (2005).

[285]   A.Gupta, A.Kumar, A.Patnaik, S.Biswas, Effect of Different Parameters on Mechanical and Erosion Wear Behavior of Bamboo Fiber Reinforced Epoxy Composites, International Journal of Polymer Science (2011) doi: 10.1155/2011/592906.

[286]   R.S. Lynn, K.K. Wong, H.M. Clark, On the particle size effect in slurry erosion, Wear 149 (1991) 55–71 (1991).

[287]   S. Turenne, M. Fiset, Modelling of abrasive particle trajectories during erosion by a slurry jet, Wear 162–164 Part B (1993) 679–687.

[288]   H.M. Clark, A comparison of particle impact in gas–solid and liquid–solid erosion, Wear 186–187 Part 2 (1995) 465–472.

[289]   U.S. Tewari, A.P. Harsha , A.M. Hager, K. Friedrich, Solid particle erosion of carbon fibre– and glass fibre–epoxy composites, Composites Science and Technology 63 (2003) 549–557.

[290]   G. Sundararajan, M. Roy, Solid particle erosion behaviour of metallic materials at room and elevated temperatures, Tribology International 30 (1997) 339-359.

[291]   A. Aktas, Solid particle erosion of glass epoxy composite strengthened by metal powder, Journal of Thermoplastic Composite Materials, 25 (2011) 949–963.

[292]   S. Mohapatra, S. Mantry, S.K. Singh, Performance Evaluation of Glass-Epoxy-TiC Hybrid Composites Using Design of Experiment, Journal of Composites (2014) doi.org/10.1155/2014/670659.

[293]   J. Zahavi, G.F. Schmitt Solid particle erosion of reinforced composite materials, Wear 71 (1981) 179–190.

[294] S. Mantry, A. Satapathy, A.K. Jha, S. K. Singh, A. Patnaik. Preparation, characterization and erosion response of jute-epoxy composites reinforced with SiC derived from rice husk, International Journal of Plastic Technology 15 (2011) S69–S76.

[295] S. Opricovic, G. Tzeng, Compromise solution by MCDM methods: A comparative analysis of VIKOR and TOPSIS, European Journal of Operational Research 156 (2002) 445-455.

[296] A. Shanian, O. Savadogo, TOPSIS multiple-criteria decision support analysis for material selection of metallic bipolar plates for polymer electrolyte fuel cell, Journal of Power Sources, 159 (2006) 1095-1104.

LIST OF PUBLICATIONS

Papers published in international journals

1. **M. J. Pawar**, Amar Patnaik, Ravindra Nagar, Mechanical and Thermo-Mechanical Analysis Based Numerical Simulation of Granite Powder Filled Polymer Composites for Wind Turbine Blade, Fibers and Polymers 17 (2016) 1078-1089 **(SCI).**

2. **M. J. Pawar**, Amar Patnaik, Ravindra Nagar, Experimental investigation and numerical simulation of granite powder filled polymer composites for wind turbine blade: A comparative analysis, Polymer Composites (2015) DOI 10.1002/pc.23700 **(SCI).**

3. **M. J. Pawar**, Amar Patnaik, Ravindra Nagar, Investigation on Mechanical and Thermo-Mechanical Properties of Granite Powder Filled Treated Jute Fiber Reinforced Epoxy Composite, Polymer Composites (2015) DOI 10.1002/pc.23633 **(SCI).**

4. **M. J. Pawar**, Amar Patnaik, Ravindra Nagar, Numerical Simulation and Experimental Validation of Granite Powder Filled Jute Epoxy Composite for Slurry Jet Erosive Wear, International Polymer Processing 31 (2016) 37-50 **(SCI).**

Papers presented in international conferences

1. **M. J. Pawar**, Ravindra Nagar, Amar Patnaik, Parametric Optimizations for Wind Turbine Blade Applications: A Statistical Analysis, NIT-MTMI International Conference on Emerging Paradigms and Practices in Global Technology, Management & Business Issues, NIT Hamirpur, December 22-24, 2014.

2. **M. J. Pawar**, Amar Patnaik, Ravindra, Nagar Investigation on Mechanical Properties of Granite Dust Filled Glass Epoxy Composite for Wind Turbine Blade, International Conference on Emerging and Futuristic Trends in Engineering & Technology at Maharja Agrasen Institute of Technology, Solal, Baddi (HP), May 8-9, 2015.

Patent

1. **M. J. Pawar**, Dr. Amar Patnaik, Prof. Ravindra Nagar, Erosion Wear Resistant Polymer Composite Laminate Filled with Granite Powder Waste, Patent application number 1322/DEL/2015A (patent awaiting for examination).

A2

BRIEF BIO-DATA OF THE AUTHOR

Mr. Manoj Janardhan Pawar born on 20th August 1982, completed bachelors' degree in Automobile Engineering with first class with distinction from Rajarambapu Institute of Technology, Sakhrale, Sangli, Maharashtra, India and post graduate degree in Mechanical Engineering with first class from Government College of Engineering, Karad, Maharashtra, India. He has academic experience in the capacity of Lecturer, Sr. Lecturer and Assistant Professor for more than 8 years in the various institutes from Jan 2005 to July 2013.

Since July 2013, he has been engaged in his Doctoral research in the area of mechanical, thermal and erosive wear studies of polymer composites at Mechanical Engineering Department, Malaviya National Institute of Technology Jaipur, Rajasthan, India under the Institute Research Fellowship scheme by Ministry of Human Resource Development, Government of India. He has four research papers published in Science Citation Indexed (SCI) journals and presented two research papers in international conferences in reputed institutes. He has one patent filed/published (current status is awaiting for examination) to his credit. At present he is working as Associate Professor in the Department of Production Engineering at Kolhapur Institute Technology's College of Engineering, Kolhapur, Maharashtra, India.